Durham University
Department of Chemistry

^{1}H PARASHIFT Probes for Magnetic Resonance

Katie-Louise Natasha Amanda Finney

A thesis submitted for the degree of Doctor of Philosophy

December 2015

Abstract

The strong ^{1}H NMR signals from water and fat impose significant limitations to magnetic resonance spectroscopic imaging *in vivo*. Herein, novel paramagnetic lanthanide probes for ^{1}H magnetic resonance imaging and spectroscopy studies are described, in which a *tert*-butyl reporter group is incorporated and placed about 6 to 7 Å from a lanthanide(III) ion in a kinetically stable macrocyclic complex. At such a distance, the *tert*-butyl reporter is shifted to a ^{1}H NMR window that is well removed from the diamagnetic range, allowing its selective observation. Additionally, prudent selection of the lanthanide(III) ion, in accord with magnetic field strength, leads to an enhancement in the longitudinal relaxation rates, R_1, permitting faster data acquisition per unit time in spectroscopy and imaging protocols. Further sensitivity gains are achieved by selecting a *tert*-butyl reporter group, within which the number of magnetically equivalent nuclei is maximised.

As a result, the development of ^{1}H PARASHIFT probes with carboxylate chelating arms possess *tert*-butyl groups that are shifted up to 25 ppm away from the water signal. At such frequencies, the enhanced sensitivity associated with the zero-background signal *in vivo,* allows the detection of these complexes in live mice, and due to the achievement of the required R_1 values, data acquisition occurs within a few minutes following tail vein injection of well-tolerated doses that are of the same size as clinically administered contrast agents (0.1 mmol kg^{-1}).

Remarkable *tert*-butyl chemical shift enhancements up to 85 ppm away from the water signal are observed for ^{1}H PARASHIFT probes possessing phosphinate chelating arms, moving the goal posts *further still* for ^{1}H MRS studies. Such a shift magnitude means that larger spectral imaging bandwidths (such as 20 kHz) can be used, to further reduce data acquisition times.

Minimal structural modifications, in the 4-position of the coordinated pyridyl moiety, have led to the development of 'smart' pH responsive ^{1}H PARASHIFT probes, and also a covalently bound high-molecular weight glycol chitosan adduct. In the latter case, a strategy for increasing the retention time of these complexes is presented.

Declaration

The research described herein was carried out at the Department of Chemistry, Durham University between October 2012 and December 2015. All of the work is my own, except where otherwise stated. No part has been previously submitted for a degree at this, or any other, university.

Statement of Copyright

Ethics Declaration

All animal experiments were reviewed and approved by the Newcastle University (UK) animal welfare committee, and were performed according to the guidelines for the welfare and use of animals in cancer research 34 and national law, under project license (PPL60/4442) issued by the UK Government Home Office under the animals (scientific procedure) act 1986.

Acknowledgements

First of all, I would like to thank my supervisor, Professor David Parker, for giving me this opportunity. Over the years, the wisdom he has shared, the inspiration he has provided and the encouragement he has offered have been greatly appreciated.

Next, special thanks go to *Team PARASHIFT*. I thank Dr. Nicola Rogers, for her constant help, expertise and friendship; and Kanthi, for her invaluable experience and encouragement throughout, especially regarding *that* reaction. Naturally, I would also like to thank the past and present members of CG 27 for their friendship and support, in particular Sergey and Andrew for messing up the office; Rachel for the fume-cupboard chats; Steve for the synthetic advice; and Robek for letting me pink-up his office.

At Durham, I'd like to thank the solution state NMR service, Dr. Alan Kenwright, Catherine Heffernan, Dr. Juan Aguilar Malavia and Dr. Raquel Belda-Vidal, for letting me loose on their beloved magnets; the mass spectrometry service, Dr. Jackie Moseley, Dr. Dave Parker and Peter Stokes, for putting up with me at 9 a.m. every morning; the team at stores, past and present, for providing a service with a smile; and finally, the laboratory attendants for the endless cups of tea and gossip.

Further afield, I'd like to thank Prof. Andrew Blamire, Dr. Ian Wilson and Dr. Dara O'Hogain, at the Newcastle Magnetic Resonance Centre, for the phantom and *in vivo* imaging studies; and Dr. Nicholas Chilton at the EPRSC EPR National Facility at the University of Manchester, for the EPR spectra and SQUID data.

I must also mention my best friends Laura and Anna, who always make time for me when I'm home in Birmingham; Sam, for the Sunday morning Skype chats; and Emily, for the wonderful year a half at 4 Grove Terrace.

A very special thanks to my Mom and Dad for not giving up on me even when I gave up on myself; my sister, Emma, for being everything I'm not, my true inspiration and my best friend; and my two guardian angels, Nan and Grandad, it's all for you.

Finally, to Neil for going through this amazing journey with me, and his heart.

For Rita Gascoigne

4th January 1932 – 22nd January 2011

&

John Gascoigne

17th September 1928 – 11th March 2013

Abbreviations

12-N_4	1,4,7,10-tetraazacyclododecane
2,3-DPG	2,3-diphosphoglycerate
2D	two-dimension(al)
3-APP	3-aminopropylphosphonate
3D	three-dimension(al)
a.u.	arbitrary units
Ar	aromatic
Asp	aspartic acid
at	acquisition time
ATP	adenosine triphosphate
$\boldsymbol{B_0}$	applied magnetic field
BM	Bohr Magneton
BMS	bulk magnetic susceptibility
BOC	*tert*-butoxycarbonyl
br	broad
BRW	Bloch-Redfield-Wangsness
C_3 or C3	tri-carboxylate
CEST	Chemical Saturation Transfer
$\boldsymbol{C_J}$	Bleaney coefficient
cm	centrimetre
cm^{-1}	inverse centrimetres or wavenumbers
C_n	an *n*-fold rotational axis
CF	crystal fieldΦ
CSI	chemical shift imaging
cyclen	1,4,7,10-tetraazacyclododecane
CyDTA	1,2-cyclohexylenedinitrilotetraacetic acid
d	doublet
DCM	dichloromethane
dd	doublet of doublets
DFT	Density Functional Theory
DIPEA	*N,N*-diisopropylethylamine

DMF	*N,N*-dimethylformamide
DO2A	1,7-bis(carboxymethyl)-1,4,7,10-tetraazacyclododecane
DO3A	1,4,7-tris(carboxymethyl)-1,4,7,10-tetraazacyclododecane
DOTA	1,4,7,10-tetraazacyclododecane-1,4,7,10-tetraacetic acid
DOTAM	1,4,7,10-tetraazacyclododecane-1,4,7,10-tetraacetic acid amide
DOTMA	tetramethyl-1,4,7,10-tetraazacyclododecane- 1,4,7,10-tetraacetic acid
DOTP	1,4,7,10-tetraazacyclododecane-1,4,7,10-tetrakis(methylene phosphinate)
DPA	dipicolinic acid
DSS	sodium 3-(trimethylsilyl)-1-propanesulfonate
dt	delay time (*not to be confused with dead time)*
DTPA	diethylenetriaminepentaacetic acid
EDTA	ethylenediaminetetraacetic acid
EPR	Electron Paramagnetic Resonance *or* enhanced permeability and retention
EPSRC	The Engineering and Physical Sciences Research Council
ESI	Electrospray Ionisation
FDA	Food and Drug Administration
FOV	Field of View
g	gram
G	Gauss
Glu	glutamic acid
g_J	Landé factor/ effective electron *g*-factor
GPC	gel permeation chromotography
h	hour(s)
HATU	1-[bis(dimethylamino)methylene]-1*H*-1,2,3-triazolo[4,5-*b*]pyridinium 3-oxidhexafluorophosphate
HEDTA	*N*-{2-[bis(carboxymethyl)amino]ethyl}-*N*-(2-hydroxyethyl)glycine
HMBC	heteronuclear multiple-bond correlation spectroscopy
HP-DO3A	hydroxypropyl-1,4,7,10-tetraazacyclododecane-1,4,7-triacetic acid
HPLC	high pressure liquid chromotography
HRMS	high resolution mass spectrometry
I	spin angular momentum
ICP-MS	inductively coupled plasma mass spectrometry

IS	inner-sphere
J	Total angular momentum *or* coupling constant
K	Kelvin
k	rank parameter
k_n	Boltzmann constant (n = B) *or* other rate constant
kg	kilogram
kHz	kilohertz
L	orbital angular momentum
LD_{50}	lethal dose, 50%
LG	leaving group
LIS	lanthanide(III) induced shift
Ln or Ln^{3+}	lanthanide or lanthanide(III) ion
K_{ML}	the metal ligand dissociation constant
LRMS	low resolution mass spectrometry
m	multiplet
M_0	net magnetisation vector
m.p.	melting point
***m*CPBA**	*meta*-chloroperoxybenzoic acid
mg	milligram
MHz	megahertz
min	minute(s)
mM	millimolar
mm	millimetre
mmol	millimole
MOE-DO3A	10-(2-methoxyethyl)-1,4,7,10-tetraaza-cyclododecane-1,4,7-triacetic acid
MOPS	3-(*N*-morpholino)propanesulfonic acid
MR	magnetic resonance
MRI	magnetic resonance imaging
MRS	magnetic resonance spectroscopy
ms	millisecond(s)
µs	microsecond(s)
mV	millivolt
MW	molecular weight

MWCO	molecular weight cut-off
$\boldsymbol{M_z}$	magnetisation along the *z*-aix
nm	nanometre
NMM	*N*-methylmorpholine
NMR	Nuclear Magnetic Resonance
NOE	Nuclear Overhauser effect
NOESY	Nuclear Overhauser effect spectroscopy
NOTA	1,4,7-triazacyclononane-1,4,7-triacetic acid
NSF	nephrogenic system fibrosis
nt	number of transients
NTA	nitrilotriacetic acid
OECD	Organisation for Economic Co-operation and Development
OS	outer-sphere
PARACEST	PARAmagnetic Chemical Saturation Transfer
PARASHIFT	PARAmagnetically SHIFTed
PCS	pseudocontact shift
pD	= pH + 0.41
PFC	perfluorocarbon
PFOB	perfluorooctylbromide
PFTA	perfluorotributylamine
$\mathbf{p}\boldsymbol{K_a}$	acid dissociation constant
$\mathbf{PMe_3}$	tri-phosphinate
PPA	phenylphosphonic acid
ppm	parts per million
PRESS	Point RESolved Spectroscopy
ps	picosecond(s)
q	quartet
$\boldsymbol{q}$	component parameter *or* the complex hydration number
$\boldsymbol{r}$	distance between the lanthanide(III) ion and the reporter nucleus/i
$\boldsymbol{R_1}$	longitudinal relaxation rate, = $1/T_1$
$\boldsymbol{r_{1p}}$	relaxivity
$\boldsymbol{R_2}$	transverse relaxation rate, = $1/T_2$
$\mathbf{R^2}$	coefficient of determination
$\boldsymbol{R_f}$	retention factor

RF	radio frequency
R_{icon}	contact contribution to paramagnetic relaxation
R_{id}	diamagnetic contribution to paramagnetic relaxation
R_{idip}	dipolar contribution to paramagnetic relaxation
R_{iM}	paramagnetic contribution to paramagnetic relaxation
R_{iobs}	observed paramagnetic relaxation rate
R_{iX}	Curie contribution to paramagnetic relaxation
ROI	Region of Interest
rt	room temperature
s	second(s) *or* singlet
S	spin angular momentum
SAP	square antiprism
SBM	Soloman-Bloembergen-Morgan
SNR	signal-to-noise
SQUID	Super Conducting Quantum Interference Device
SS	second-sphere
STEAM	Stimulated Echo Acquisition Mode
SW	sweepwidth
T	Temperature *or* Tesla
t	time
T_1	longitudinal relaxation time
T_{1e}	electronic relaxation time
T_2	transverse relaxation time
TBTU	*O*-(benzotriazol-1-yl)-*N,N,N',N'*-tetramethyluronium tetrafluoroborate
TETA	1,4,8,11-tetraazacyclotetradecane-*N,N',N''*-tetraacetic acid
TFA	trifluoroacetic acid
THF	tetrahydrofuran
TLC	thin layer chromotography
TR	repetition time
t_R	retention time
tri-BOC	1,4,7-tris-*tert*-butoxycarbonyl-1,4,7,10-tetraazacyclododecane
TSAP	twisted square antiprism
UV	ultra violet

vs.	versus
X-ray	X-radiography

Terms and Symbols

°	degrees
Å	Angstrom
B_q^k	crystal field parameters
C_q^k	spherical tensor operators
γ_N	gyromagnetic ratio
ΔE_{CF}	crystal field splitting
δ	delta
$\lvert\delta_{para}\rvert$	corrected total paramagnetic shift
θ	angle between the nucleus and the lanthanide(III)
λ	wavelength
m_l	magnetic quantum number
m_J	total quantum number
m_S	spin quantum number
μ_0	vacuum permeability
μ_B	Bohr magneton
μ_{eff}	effective magnetic moment
π	constant pi
τ_{D_2O}	emissive lifetime in D_2O
τ_{H_2O}	emissive lifetime in H_2O
τ_R or τ_r	rotational correlation time
$\omega_{½}$	linewidth half-height
ω_e	electron Larmor frequency
ω_N	nuclear Larmor frequency
ϕ	angle between the nucleus and the lanthanide(III)

Table of Contents

Chapter Five: Conclusions and Future Work

Chapter Six: Experimental

Appendix

Chapter One: Introduction

1.1 Magnetic Resonance Imaging: a historical overview

In 1937, Columbia University Professor Isidor I. Rabi first observed the quantum phenomenon renowned to be nuclear magnetic resonance (NMR). Within a decade, NMR spectroscopy was adopted for the analysis of substances by chemists, but a remarkable 30 years elapsed before the advent of nuclear medical imaging (renamed MRI in 1984).

Those three decades saw many investigations into both non-biological and biological samples within the field of NMR spectroscopy, but without doubt the most notable discovery came from the work of physician Raymond Damadian. In 1970, spurred on by his own medical non-diagnoses, Damadian surmised that the ^{1}H NMR signal of water in cancerous tissue might be different from that of healthy tissue, because the tumour contained more water. Despite his weak reasoning, he found that the longitudinal relaxation time (T_1) of the ^{1}H NMR signal of water in malignant tumour tissue (1.08 ± 0.08 s) was markedly longer than in healthy tissue (0.37 ± 0.08 s), and with it he had found 'the ultimate technology to detect cancer'.[1,2] In 1972, he filed a patent claim for the idea, entitled 'Apparatus and Method for Detecting Cancer in Tissue'.[3] All of the NMR experiments carried out until then were one-dimensional, with no mention made of a technique or method capable of using NMR spectroscopy to scan the human body.

It was at the same time, that Paul C. Lauterbur and Peter Mansfield, unaware of each other's work, concurrently described the answer: using magnetic field gradients and mathematical analyses for the two-dimensional spatial localisation of NMR signals.[4] Lauterbur christened his imaging technique *zeugmatography* (Greek for 'I excite') and persevered to publish the first ever proof-of-concept NMR image of two capillary tubes of H_2O, in a background of D_2O (*Figure 1.0*).[5]

Whilst Lauterbur's gradient approach gathered followers, Damadian set about building his large-scale human scanner. In 1977, the instrument named *Indomitable* carried out the world's first human MRI scan, of a graduate student's chest, and became the first

MRI machine prototype.[6] The technology's success was ashamedly short-lived, however, with detractors favouring Lauterbur's approach soon, and forever after.

1.1.1 ^{1}H MRI and MRS

Almost forty years on, ^{1}H MRI is widely regarded as one of the most significant tools in clinical diagnostics, with 6 MRI units per million population and nearly 42 MRI exams being carried out per thousand population every year, in the UK, according to the OECD (Organisation for Economic Co-operation and Development) Health Data 2013.[7] It is a powerful diagnostic technique, generating detailed three-dimensional anatomical images with impressive sub-millimetre resolution (*Figure 1.0*). The non-invasive nature of the technique also negates the use of harmful ionising radiation, typically associated with other imaging modalities, such as X-radiography.[8] Following its rapid rise to universal importance, the 2003 Nobel Prize in Physiology or Medicine was jointly awarded to Lauterbur and Mansfield for their pioneering efforts, with 12 additional Nobel Prizes being directly and indirectly linked to the advent of MRI.[9]

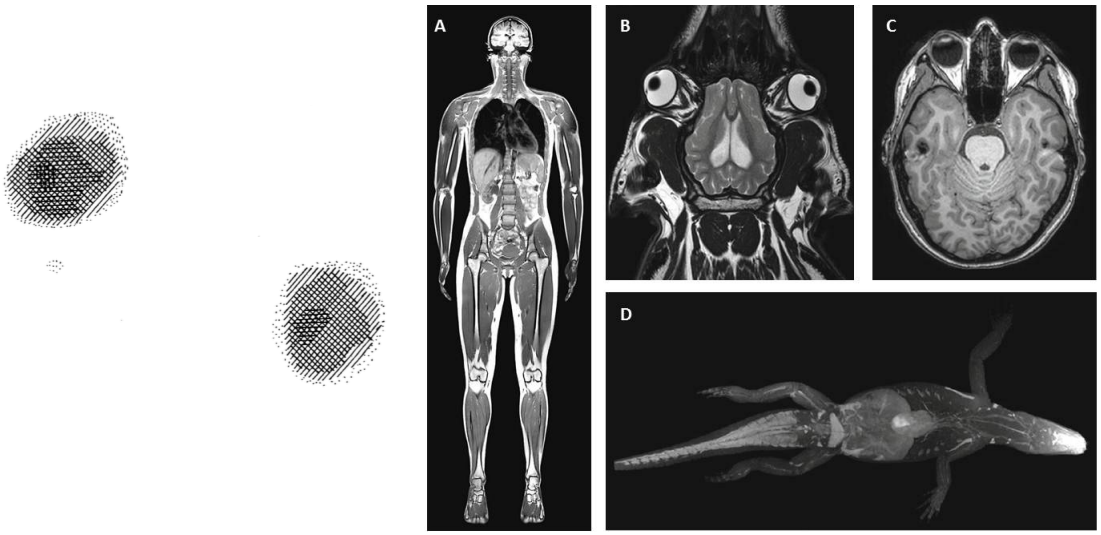

Figure 1.0 ^{1}H MRI images *then* and *now*: *left* Lauterbur's 'zeugmatogram' of two H_2O-filled capillary tubes and *right* A) vertical section through a human; B) horizontal section through the head of a pig; C) horizontal section through the head of a human; and D) horizontal image through an alligator.[5,10,11]

^{1}H MRI utilises the strong ^{1}H NMR signal of water in living systems to generate images, after deconvolution and reconstruction. Protons have a spin angular momentum, $I = ½$, and a magnetic moment, μ, due to a positively charged nucleus. When protons are placed inside an external magnetic field, the nuclear spins orientate themselves in discrete directions, either parallel (+½) or anti-parallel (-½) to the field, and precess

around B_0 at the Larmor frequency (*Figure 1.1A*). The difference in energy between these spin states is directly proportional to the strength of the external magnetic field, with the majority of spins adopting the more energetically favourable parallel orientation. The resulting net magnetisation vector, M_0, arising from the sum of the magnetic moments, is aligned along the *z*-axis, so that M_z is non-zero (*Figure 1.1B*). Following the application of a 90° radiofrequency (RF)-pulse along the *x*-axis, the spins in the low energy state absorb energy and adopt the high energy state, causing M_z to tilt into the *xy* plane (*Figure 1.1C and D*).

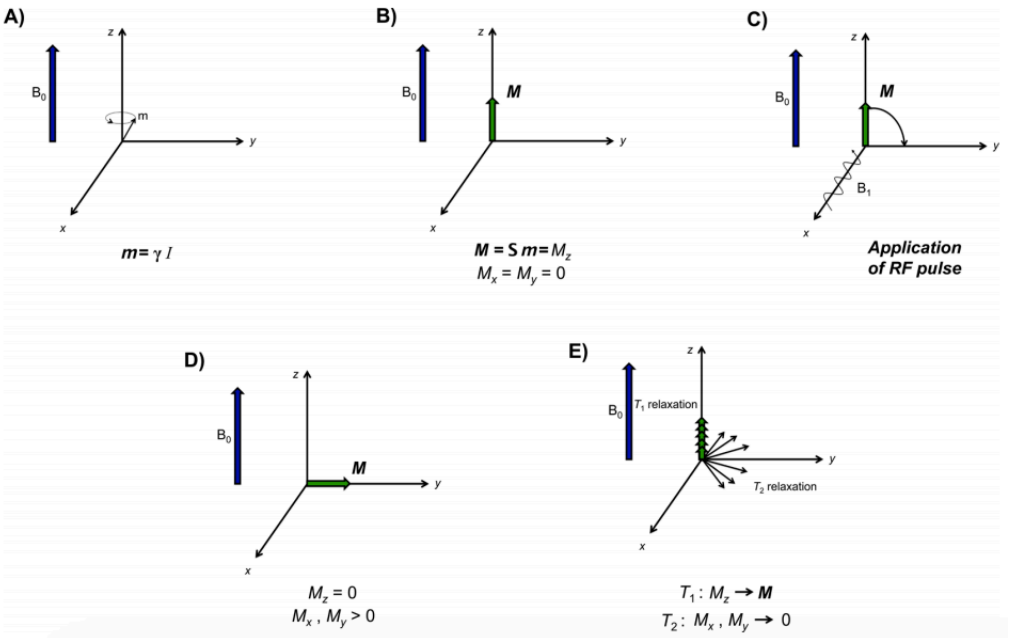

Figure 1.1 (A) The magnetic moment, μ, of each proton precesses around B_0 at the Larmor frequency. (B) The sum of magnetic moments generates a net macroscopic magnetisation, M_0, along the *z*-axis. (C) Application of an RF pulse along the *x*-axis causes M_z to tilt away from the *z*-axis. (D) Assuming a 90° pulse, the net magnetisation will lie in the *xy* plane. (E) Over time, the magnetisation recovers to its equilibrium value. This relaxation process is characterised by the time constants T_1 and T_2.[12]

When the RF-pulse is removed, the thermodynamic instability attributed to the perturbed magnetic states is such that the net magnetisation relaxes back to its equilibrium alignment in the *z*-direction (*Figure 1.1E*). This relaxation process is characterised by the time constants T_1 and T_2. The spin-lattice relaxation time, T_1, corresponds to the random processes whereby the excited spin states achieve stimulated emission of energy *via* interactions with proximal fluctuating magnetic fields within the lattice. The recovery of M_0 occurs exponentially such that at t = T_1, 63% of the original net magnetisation value has been recovered, with virtually 100% recovery at t = 5 ×

T_1.[13] The spin-spin relaxation time, T_2, refers to the loss of phase of the nuclear spins, arising from inhomogeneities in the local magnetic field they experience as a result of interactions with each other, following a 90° RF-pulse. Lauterbur first discovered that the protons of water molecules in different tissue types relaxed back to equilibrium at different rates and it is these differences in T_1 and T_2 that form the basis of ^{1}H MRI, whereby image contrast is achieved and the detailed elucidation of soft tissue morphology is made possible.

The modest sensitivity associated with low clinical field strengths, typically 1.5 or 3 T, led to the rapid introduction of contrast agents; a class of synthetic agents responsible for increasing signal intensity in MRI by either shortening T_1 (increasing R_1 since $R_1 = 1/T_1$), or shortening T_2 (increasing R_2 since $R_2 = 1/T_1$). This shortening of T_1 and T_2 arises due to the dipolar interaction between the nuclear magnetic moment of the water protons and the electronic magnetic moment of the contrast agent. A contrast agent can be classified as a T_1 or T_2 agent, depending on the relaxation time it affects predominantly.[14] The majority of commercially available contrast agents are T_1 agents, and induce positive image contrast. The use of T_2 agents is less common, owed largely to the inherent reduction in signal intensity and negative image contrast.

Gadolinium(III) based contrast agents represent the largest class of lanthanide T_1 agents currently in clinical use, with 40% of MRI scans typically using a 0.1 mM kg^{-1} body weight dose of contrast agent.[15] The Gd(III) ion might be considered an obvious choice, because it possesses the highest spin paramagnetism of any stable ion, but both dysprosium(III) and holmium(III) display larger magnetic moments due to orbital contributions to electron angular momentum. The isotropic nature of the electron distribution in Gd(III) means that it has a slower electronic relaxation time than the asymmetric Dy(III) and Ho(III), and so is more in tune with the proton Larmor frequency of water, leading to enhanced relaxation times.[16,17] The free Gd(III) ion is toxic, however, with an LD_{50} value of around 0.1 mM kg^{-1}, and so must be encapsulated within a multidentate ligand forming a complex that is kinetically and thermodynamically stable with respect to metal ion dissociation, if it is to be administered as an MRI contrast agent.[18,19] In 1988, the first Gd(III)-based contrast agent, **[Gd(DTPA)(H$_2$O)]$^{2-}$**(officially marketed as Magnevist®), was approved for clinical use ($\log K_{ML}$ thermodynamic stability constant 22.2).[17,20] Since then, eight

additional Gd(III)-based contrast agents have been approved for MRI applications (*Figure 1.2*).

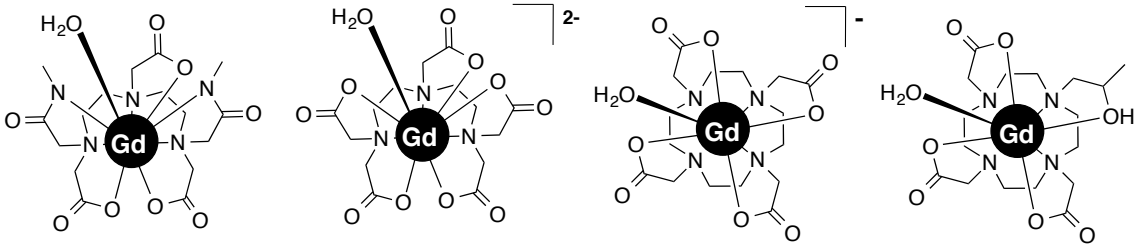

Figure 1.2 Structures of selected clinically approved Gd(III)-based contrast agents.

Recently, the cause of the debilitating disease nephrogenic system fibrosis (NSF) has been linked to the premature dissociation of Gd(III) ions from DTPA-based systems, especially the diamide species Omniscan®, in renal system compromised patients.[21] Earlier conclusive works had in fact highlighted such stark differences in stability between DTPA-based ligands and macrocyclic DOTA-based ligands,[22,23] and revised guidance warning radiographers about the use of contrast agents in patients with slow renal clearance was issued by the FDA in December 2010.[24]

Magnetic resonance spectroscopy (MRS) is the clinically appropriate name for NMR spectroscopy. It is markedly different from MRI, in that it acquires an NMR spectrum of a region of interest (ROI), which can range in size from a 2 cm^3 section to a single 1 mm^3 voxel, for example. MRS has been vying for commercial exploitation with MRI since the 1970's, but the emergence of stable magnetic fields, wide-bore magnets and contrast agents has made MRI the pre-eminent clinical imaging technique. Despite the scope for targeted and higher relaxivity contrast agents, economic and health risk factors have contributed to a plateau in their development. MRS offers inherently richer information content, but the prevalent reason why MRS has not been more widely utilised can be attributed to the intrinsically low sensitivity of the NMR experiment. MRI uses the intense proton signal from water *in vivo*, which is present at a concentration of 55 M.[14] The presence of other endogenous analytes typically lies in the millimolar range so their direct detection is problematic.

1.1.2 Heteronuclear MRI and MRS

An alternative approach, using heteronuclei, presents one possible means of improving sensitivity in MRS because there is no endogenous background signal. Among the earliest reported work in the field of MRS is the use of ^{31}P magnetic resonance. ^{31}P is considered an attractive nucleus due to its 100% natural abundance, favourable nuclear spin, large NMR shift range and biological relevance (*Table 1.0*).

Table 1.0 Comparison between ^{1}H, ^{31}P and ^{19}F nuclei.

	^{1}H	**^{31}P**	**^{19}F**
Spin, *I*	½	½	½
Natural abundance (%)	100	100	100
Atomic abundance in humans[a] (%)	63	0.14	0.0012
NMR shift range (ppm)	12	430	700
Gyromagnetic ratio, γ (MHz T^{-1})	42.6	17.2	40.1
NMR Sensitivity, relative to ^{1}H	1	0.00663	0.83

(a) As a percentage of the total atoms.[25,26]

Moon and Richards first reported the non-invasive determination of intracellular pH using ^{31}P MRS.[27] The separation between the two ^{31}P chemical shifts of 2,3-diphosphoglycerate (2,3-DPG, *Figure 1.3A*) is dependent on pH, with a maximum shift difference of 1 ppm around pH 6.5. Typical physiological concentrations of 5 mM, in human red blood cells, and 7 mM, in rabbit red blood cells, coupled with a zero background signal means that 2,3-DPG is easily visible by ^{31}P MRS. Although relatively agreeable pH results were presented in carbon monoxide treated rabbit blood and rabbit hemolysate, the authors cautiously warned how using 2,3-DPG as a pH probe is problematic, given that its strong interaction with deoxyhaemoglobin affects the chemical shift significantly. Therefore, 2,3-DPG can never be used in a living system.

The utility of phenylphosphonic acid (PPA, *Figure 1.3B*) as a ^{31}P MRS extracellular pH indicator has been demonstrated in perfused tissues.[28] The resonant frequency of PPA occurs at higher frequency relative to other cellular phosphorus-containing compounds and allows easy detection by NMR. It is pH sensitive with a shift of 1.12 ppm/ pH unit over the 6.4 to 7.6 range. However, phosphoryl containing compounds, namely ATP

and sugar phosphates, have displayed chemical shifts which are dependent on ionic effects from divalent cations and salt, and so absolute calibration and certain identification remains difficult.[29,30]

3-Aminopropylphosphonate (3-APP, *Figure 1.3C*) has also been used to measure the extracellular pH of tumours, by ^{31}P MRS.[31] Promising *in vitro* studies suggest the resonant frequency of 3-APP is not significantly affected by temperature or ionic strength, and the pH sensitivity of 1.5 ppm/ pH unit falls within the physiological range. Nevertheless, their *in vivo* work is restricted to the analysis of large tissue volumes, owing to the distinct lack of sensitivity associated with the multitude of endogenous ^{31}P NMR signals.

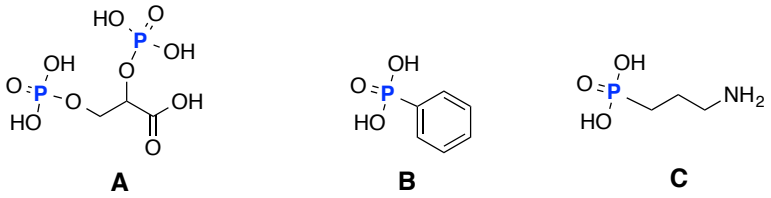

Figure 1.3 Structures of selected ^{31}P-MRS indicators, from *left* to *right*: (A) 2,3-DPG, (B) PPA and (C) 3-APP.[27,28,31]

Over the last thirty years, in an effort to overcome sensitivity limitations, the focus has moved away from imaging heteronuclei that are biologically prevalent and has promoted interest in those that have a zero background signal in living systems.[32–34] The leading example is ^{19}F, due to its 100% natural abundance, favourable nuclear spin, high NMR sensitivity and trace existence *in vivo* (*Table 1.0*).[35] Of course, there are higher concentrations of fluorinated salts in the bone and teeth, but a very short T_2 means it is not visible by conventional MRI methods. Also, the high gyromagnetic ratio of ^{19}F (only 6% lower than ^{1}H) means that spectral acquisition can occur on existing instrumentation, with minimal retuning of the RF coil. However, in order to produce an image of comparable quality to those produced in ^{1}H MRI, whose signal comprises almost two-thirds of all the atoms present in the body, a high density of ^{19}F nuclei is necessary.

Perfluorocarbons (PFCs) are simple organic compounds, in which all of the hydrogen atoms have been substituted with fluorine. Their potential was first recommended in the 1970's, when human ^{1}H MRI was in its infancy, after which they became one of the

earliest examples of contrast agents and the most prominent class of ^{19}F MRI agents to date.[36,37] The first documented example was perfluorotributylamine (PFTA, *Figure 1.4)*.[38]

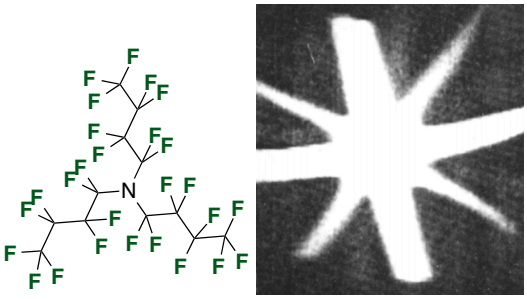

Figure 1.4 Structure of PFTA (*left*) and the first ^{19}F MRI image from 1977 (*right*), of a star-shaped 'Union Jack' phantom made from 2 and 6 mm tubes containing PFTA. The image took 400 s to acquire at 0.7 T using a steady-state free-precession (SSFP) MRI sequence, with a repetition time (TR) of the order of several ms.[38]

Almost a decade later, tumour detection by ^{19}F MRS was carried out using perfluorooctylbromide (PFOB, *Figure 1.5*).[39] Liquid PFCs typically have poor water solubility and must therefore be emulsified for clinical applications. Following intravenous administration of a PFOB suspension, leakage occurs through the tumour vascular endothelium, so that PFOB accumulates in the extracellular space. Since the local concentration of fluorine in the extracellular space is high, ^{19}F MRS can be used to detect the ^{19}F NMR signal. It is important to note that due to the inequivalent nature of the ^{19}F nuclei, more than one ^{19}F NMR signal is observed for PFOB. Therefore, chemical shift artefacts are observed, as the chemical shift and spatial frequency encoding information becomes entangled, so that the use of such agents is restricted. There is precedence for re-combining spatially close signals in the literature with the addition of selective excitation refocusing signals in Point RESolved Spectroscopy (PRESS)[40] and STimulated Echo Acquisition Mode (STEAM)[41] sequences. More recent examples have focused on the use of perfluoropolyethers, because the equivalence of the ^{19}F nuclei gives rise to one sharp resonance in the ^{19}F NMR.[36,42]

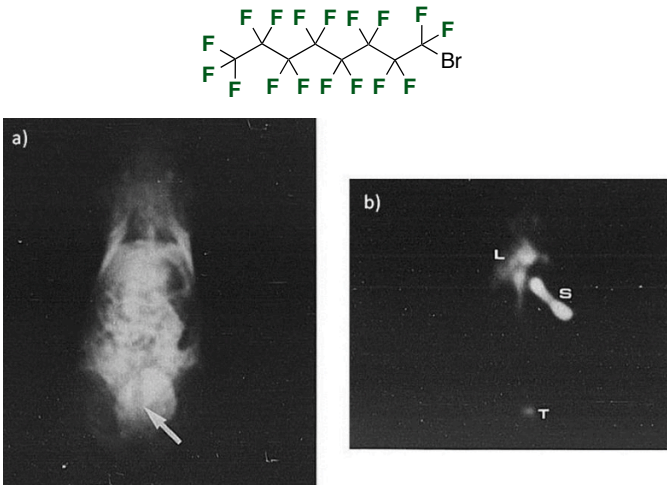

Figure 1.5 The chemical structure of PFOB (*top*); a) ^{1}H coronal image of a mouse, where the implanted tumour is indicated by an arrow; b) corresponding ^{19}F image with identical orientation, following the intravenous injection of 10 g/ kg body weight of PFOB emulsion. PFOB accumulates in the liver (L), spleen (S) and tumour (T).[39]

Despite dedicated imaging coils, this approach has achieved limited impact with only sporadic applications being reported. High ^{19}F spin density agents still need to be used at remarkably high concentrations, locally injected as a suspension due to poor water solubility. Injecting high concentrations of any agent is problematic, regardless of its apparent inertness or characterised clearance profile (*e.g.* for a typical human weighing 60 kg, 600 g of PFOB emulsion is required according to Ratner *et al.*). Additionally, the field relies heavily on stronger magnetic fields to increase the signal-to-noise ratio (SNR), but clinical operating fields are typically much lower than those reported. Despite these disadvantages, in 2005 Celsense Inc. developed a polymeric perfluorocarbon tracer agent, marketed as *Cell Sense*, which was used to label cells *ex vivo*, allowing for their visualisation by ^{19}F MRI/MRS after transfer.[43] *Cell Sense* was FDA approved in 2011, with its first clinical use in 2014, and represents the most successful PFC to date.[44]

It was mentioned previously that a high spin density of ^{19}F nuclei is essential and this is in some part due to the intrinsically slow relaxation rates of the ^{19}F nucleus. The T_1 of a ^{19}F nucleus, in a diamagnetic molecule, is typically 1 s, resulting in an R_1 of the order of 1 s^{-1}.[45] In an MRS experiment, it is obligatory to wait five times the magnitude of T_1 before applying another 90° pulse, in what is called the delay time (dt), so that full recovery of magnetisation in the *z*-direction (M_0) occurs (*Figure 1.6, left*). This propagates into exceedingly long repetition times (TR) and total scan times, which are

not clinically viable. A T_1 of this magnitude also means that the amount of 'dead time' in the experiment, the time where no data is being collected, is large (*Figure 1.6, top right*).

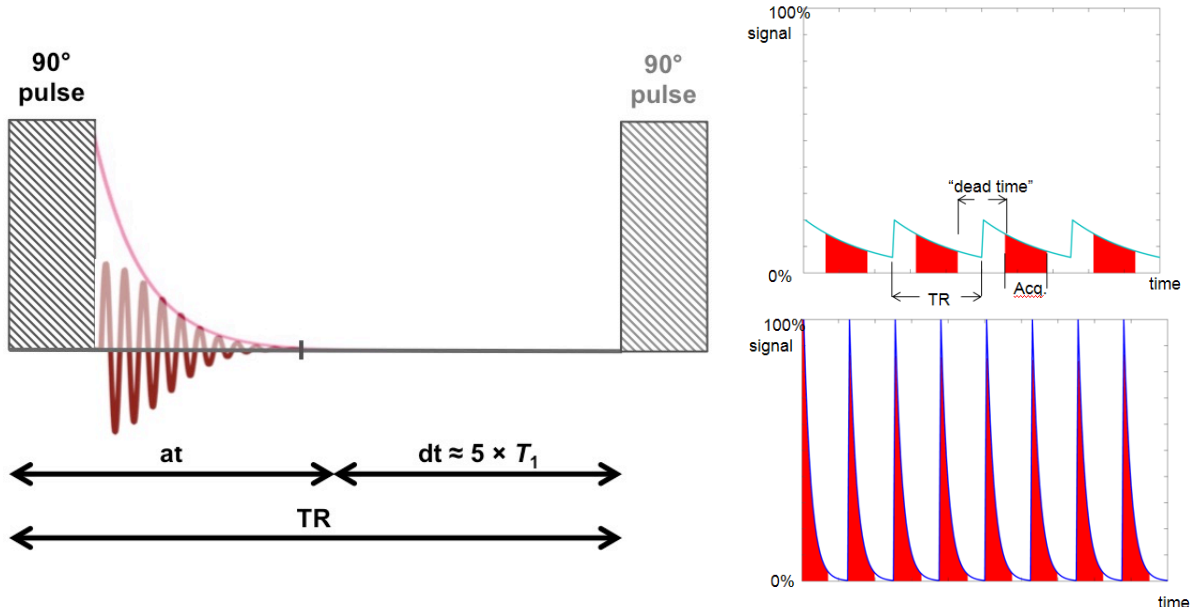

Figure 1.6 (*Left)* Example of a typical MRS pulse sequence where at = acquisition time, dt = delay time and TR = repetition time. The total scan time is given by n(TR). *(Right)* Representation of the signal intensity gained in an MRS experiment, where $T_1 = 1$ s^{-1} (*top*) and 4 ms^{-1} *(bottom)*.[46]

An obvious method therefore presents itself: increase the relaxation rates of the imaging nucleus so that a greater number of scans can be carried out in a given time frame, manifesting itself in a significantly reduced total scan time and increased signal intensity. Recently, ^{19}F relaxation rate enhancements between 10 and 25-fold have been achieved, by placing a CF_3 group in close proximity to a paramagnetic lanthanide(III) centre.[45,47–52] As a result, the delay times for MRS protocols were in the ms range, limiting the amount of 'dead time' and increasing the number of scans in a given time frame by allowing fast pulsing to occur (*Figure 1.6, bottom right*). Obvious therefore, is the requirement for an R_1 of the order of 100 to 200 s^{-1} at 7 T. However, the successes of ^{19}F MRI and MRS are limited, due to the far from trivial use in conventional ^{1}H MR operating systems. The work detailed within this thesis focuses on this methodology, but without the use of heteronuclei, offers a novel approach to alleviate the major disadvantages plaguing the fields of MRI and MRS, presented so far.

1.1.3 A novel approach to ^{1}H MRI and MRS: the use of PARASHIFT probes

In general, ^{1}H NMR chemical shifts for physiological compounds fall into the standard 0-12 ppm range, with the majority of signal intensity representing water (4.7 ppm) and fat (1.3 ppm). In this case, the operating practicality of ^{1}H MRI is its greatest drawback and so a method for circumventing the biological background signal has been devised. If the ^{1}H NMR signal of a probe can be shifted away from the interfering water and fat signals *in vivo*, then it is feasible to image this resonance selectively, in a region where there is zero-background signal (*Figure 1.7*). This new approach allows the commercial availability of sensitive ^{1}H MR imaging coils and the widespread understanding of ^{1}H MRI to be exploited, negating the major disadvantages associated with imaging heteronuclear probes, whilst taking advantage of the zero-background signal. In theory, placing a paramagnetic lanthanide(III) centre close to a probe reporter group can attain such shift magnitude, with potential chemical shifts ranging between +500 and -500 ppm. Herein derives the term PARASHIFT, meaning *paramagnetically shifted*. Before discussing applications further, the theoretical framework and practical aspects governing the design of these PARASHIFT probes should be addressed.

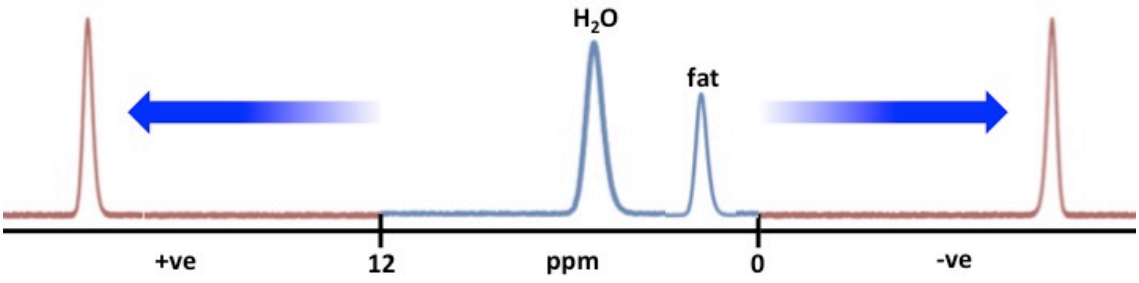

Figure 1.7 A schematic representation showing the concept of shifting a ^{1}H resonance outside the diamagnetic range, and away from the endogenous water and fat signals.

1.2 Critical design features of PARASHIFT probes

The design features of PARASHIFT probes, can be divided into two sub-sections, first, the physical theories that need to be considered in paramagnetic lanthanide(III) systems; and second, the practical features that need to be fulfilled when designing and synthesising PARASHIFT probes.

1.2.1 Theoretical considerations

In the early days of NMR spectroscopy, paramagnetic lanthanide(III) probes were used as shift agents, enhancing the limited shift dispersion of the NMR spectrum, and relaxation agents, by enhancing relaxation rates by providing additional relaxation pathways.[53–55] The following sub-section will explore the renowned theories underpinning the use of lanthanide(III) complexes as shift and relaxation agents.

1.2.1.1 Shift: Bleaney's theory of magnetic anisotropy

Magnetic susceptibility describes the degree of magnetisation of a material in response to an applied magnetic field. All of the lanthanide(III) ions, display anisotropic magnetic susceptibilities, due to the asymmetry of their electron density distributions, except Gd(III) which is isotropic with seven 4*f* electrons. This arises due to the strong spin-orbit coupling giving large orbital contributions to the ground state, which is orientation dependent. This anisotropy directly affects the chemical shift in an NMR spectrum of a lanthanide(III) complex, in what is termed the lanthanide induced shift (LIS). In the presence of a magnetic field, the induced magnetic field changes intensity with molecular orientation and the average over all orientations is net zero and so a shift is induced.

The LIS for a nucleus on a ligand that is coordinated to a lanthanide(III) ion can be explained as the sum of three contributions: a diamagnetic contribution (δ_d), the contact shift (δ_c) and the pseudocontact shift (δ_p) (*Equation 1*).

$$\delta_{obs} = \delta_d + \delta_c + \delta_p \qquad (1)$$

The diamagnetic contribution represents the change in shift of the ligand resonances upon coordination to a lanthanide(III) ion, typically arising from inductive effects, electrical field effects and conformational changes. These non-paramagnetic effects are negligible, typically, unless the nucleus is directly bound to the lanthanide(III) ion.[56]

Both the contact and pseudocontact shifts arise from the anisotropy of the magnetic susceptibility and provide more significant contributions to the overall shift enhancement. The contact shift emanates from the through-bond transmission of unpaired electron density from the 4*f* orbital to the nucleus in question. This means that the magnitude of the contact shift falls away considerably as the number of bonds

between the lanthanide(III) ion and the nucleus increases, such that for nuclei more than 5 Å or 3 bonds away from the lanthanide(III) ion the effect is usually near zero.

The pseudocontact shift (Δ_p or PCS) is a magnetic field induced, through-space dipolar interaction between the nucleus and the unpaired electron. Arising from the sum of the electron magnetisation and the applied magnetic field, the interaction results in additional chemical shielding or deshielding of the nuclei. Bleaney's theory of magnetic anisotropy has proved to be a reasonably reliable approximation for the PCS, defining it in terms of the ligand field, geometric coordinates, temperature and the nature of the lanthanide ion (*Equation 2*).[54]

$$\Delta_p = \frac{C_J \mu_B{}^2}{60(kT)^2}\left[\frac{(3\cos^2\theta - 1)}{r^3} B_0^2 + \frac{(\sin^2\theta \cos 2\varphi)}{r^3} B_2^2\right] \qquad (2)$$

where C_J is the Bleaney coefficient for a specific lanthanide ion (*Table 1.1)*, μ_B is the Bohr magneton, k is the Boltzmann constant, $\{\theta \text{ and } \varphi\}$ are the angles between the nucleus and the lanthanide(III) ion, r is the distance between the nucleus and the lanthanide(III) ion; and B_0^2 and B_2^2 are second order crystal field parameters.

Bleaney's theory presents us with three parameters to influence the overall PCS. For the work documented in this thesis, it is imperative to optimise these three parameters in order to induce a large PCS, and shift a reporter resonance outside the diamagnetic range. Firstly, through judicious lanthanide(III) ion selection, it is possible to influence both the direction and the magnitude of the PCS due to the varying values of the Bleaney coefficient (C_J) across selected lanthanide(III) ions (*Table 1.1),* and will be discussed later, in more detail (*Section 1.2.2.1*).

Table 1.1 Overview of Bleaney coefficients (C_J) for selected lanthanide(III) ions.

Ln(III)	C_J	C_J normalised[a]
Tb	-157.5	-87
Dy	-181	-100
Ho	-71.2	-49
Er	58.8	33
Tm	95.3	53
Yb	39.2	22

(a) The normalised values (to Dy) are typically quoted.

The second way is to exploit the strong dependence of the PCS upon the positioning of the nucleus of interest with respect to the principal magnetic axis and the lanthanide(III) ion. For a given probe nucleus, the typical distribution of the PCS can be represented as a 3D scalar field (*Figure 1.8*). In practice, a conformational change 4 to 5 Å away from the lanthanide(III) ion can result in a chemical shift change of approximately 50 ppm.[57] This is shown in *Figure 1.8*, where different nuclei in the archetypal **[Ln(DOTA)H_2O]$^-$** complex can resonate in an area of strong positive PCS (*red*) or an area of strong negative PCS (*blue*). Depending upon their location, they can be shifted in opposite directions of the ^{1}H NMR spectrum.

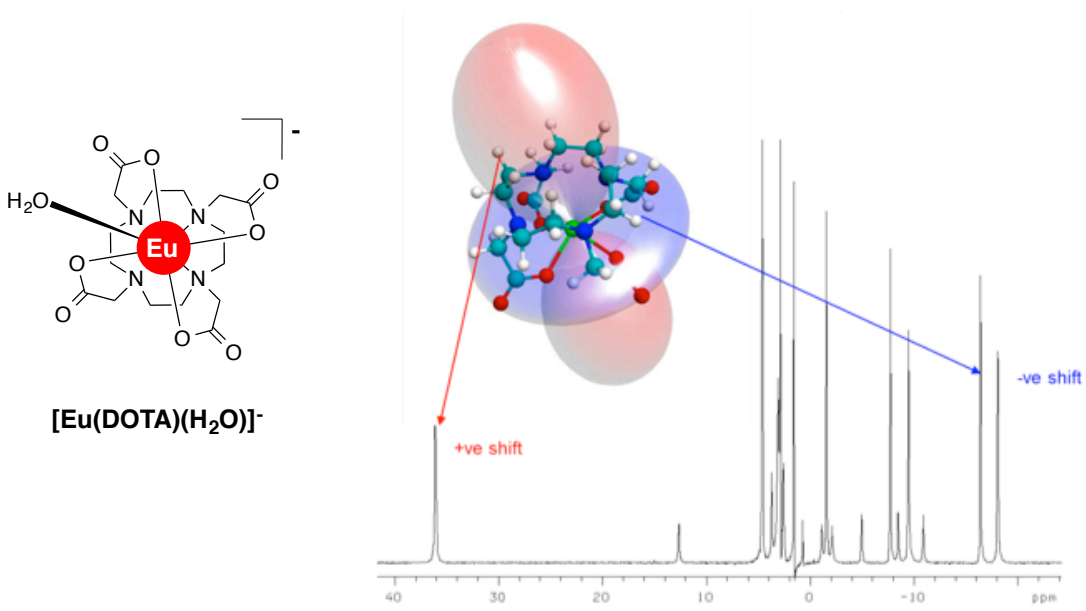

Figure 1.8 Schematic representation of the PCS field distribution around an archetypal **[Ln(DOTA)H_2O]$^-$** complex, with predominant axial magnetic susceptibility; and the effect it has on the corresponding **Eu** ^{1}H NMR spectrum (D_2O, 298 K, 9.4 T). Taken and adapted from reference [51].

The last variable that determines the PCS, relates to the local ligand field and is described by various crystal field splitting parameters, in the form B_q^k. As discussed previously, the PCS of a given nucleus occurs due to the magnetic anisotropy of the lanthanide(III) ion under investigation. The lanthanide(III) ion electron cloud is disturbed upon coordination to chelating ligands, resulting in splitting of the energy levels. Firstly, the electronic energy levels of the lanthanide(III) ions are split by electron-electron repulsions. These are then further divided into *J* energy levels, due to spin-orbit coupling; and finally, into *2J+1* magnetic states due to the crystal field.

Generally, the crystal field splitting is assumed to be smaller than the spin-orbit coupling, as defined by the Russell-Saunders coupling scheme (*Figure 1.9*).[16]

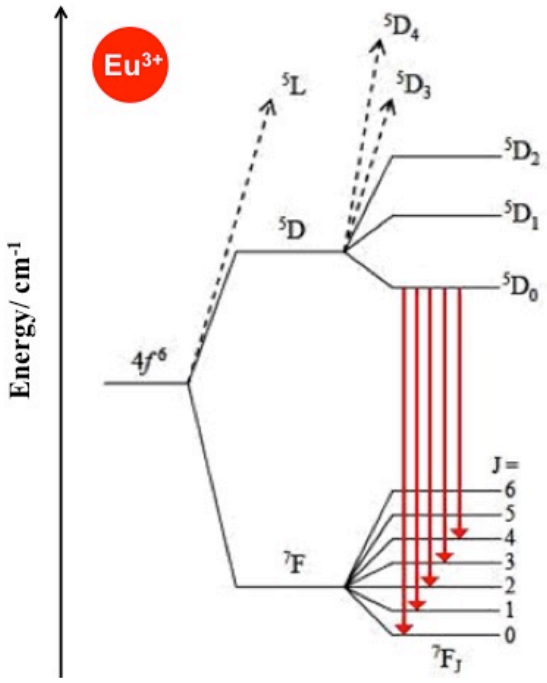

Figure 1.9 A schematic representation of the electronic energy levels of a model Eu(III) complex.

The crystal field states of lanthanide(III) complexes can be derived using the total Hamiltonian $H = H_0 + H_{CF}$, where H_0 is the free-ion Hamiltonian and H_{CF} is the crystal field Hamiltonian (*Equation 3*):

$$H_{CF} = \sum_{kq} B_q^k C_q^k \qquad (3)$$

where B_q^k are the crystal field parameters and C_q^k are the spherical tensor operators of rank k, with components q.[58]

Despite Bleaney's theory being the basis for current understanding relating magnetic anisotropy and paramagnetic NMR shifts, subsequent discussions have questioned its applicability, citing three main assumptions and approximations.

First, is the assumption that the electrons on the lanthanide(III) ion and the nucleus are point dipoles. A recent advance in the area by Charnock and Kuprov, describes a mathematical procedure to model the positions of the electrons on the lanthanide(III) ion as a non-point electron probability distribution, which is more realistic and can be

theoretically justified.[59] This alteration primarily affects the quality of shift prediction for nuclei that are closest to the lanthanide(III) ion.

Secondly, in his paper, Bleaney had assumed that the energy of the crystal field splitting of the lowest *J* state in a lanthanide complex, ΔE_{CF}, is smaller than $k_B T$ ie. $\frac{\Delta E_{CF}}{k_B T} \leq 1$.[54] The theory has been found to conform to a number of experimental observations. Bleaney originally investigated aqua-complexes, with small crystal field splittings around 100 cm^{-1}. However, at 295 K, $k_B T$ = 205 cm^{-1} and crystal field parameters exceeding this have been widely reported since, with a selection shown in *Table 1.2*. When the $\frac{\Delta E_{CF}}{k_B T} < 1$ condition is not fulfilled, the different *J* levels overlap and '*J*-mixing' occurs, so that *J* is no longer a good quantum number to describe the effects of spin-orbit coupling on the system. As a result, this has an impact on the validity of the C_J term in *Equation 2*. Clearly, Bleaney's assumption does not hold true for all lanthanide(III) complexes and so further clarification is needed. [60,61]

Table 1.2 Overview of reported crystal field splitting parameters for Eu(III) complexes of selected ligands.[51,62,63]

Ligand	B_0^2 **/ cm^{-1}**
aqua	-133
$(DPA)_3$	-367
NTA	+200
$(NTA)_2$	+333
EDTA	-267
DTPA	-500
CyDTA	+300
HEDTA	+467
NOTA	+467
DOTA	-633
TETA	+767

(a) Values of B_0^2 were estimated using the approximation $B_0^2 = \frac{10}{3}[\Delta J = 1]$ (*vide infra*).[64]

Lastly, only the second-rank crystal field splitting parameters, B_0^2 and B_2^2, are considered, but varying possible values of *k* and *q* mean that a large number of higher order crystal field splitting parameters exist. The rank tensor label, *k*, has allowed values of between 0 and 7. The even numbers represent the electrostatic interactions of electrons in specific orbitals, for example, $k = 0$ describes the *s*-orbital contribution. The odd numbers denote the intensities of induced electric-dipole transitions. The component tensor label, *q*, is defined by the point-group symmetry of the lanthanide(III) complex, which has allowed values between $-k$ and k.[65] The complexity of the crystal field splitting increases with reducing symmetry, such that higher order parameters play a more important role in low symmetry lanthanide(III) complexes. With up to 27 parameters possible, the sign and magnitude of the crystal field splitting can vary dramatically.[66,67] Bleaney's theory, however, assumes that the main contribution to the crystal field splitting comes from the second-rank parameters, B_0^2 and B_2^2, where B_2^2 is found to be typically smaller than B_0^2 (e.g. 20 cm^{-1} *vs.* 110 cm^{-1}) and neglects these potentially large higher-rank parameters (where $k_B T < B_q^k$).[65,68] The works of McGarvey and Golding *et al.* extended Bleaney's theory to include higher-rank parameters, albeit with limited impact.[55,69] Definite in their conclusions, however, was the limited applicability of Bleaney's theory to all lanthanide(III) systems, where it is clear the theory is violated.

The splitting of energy levels can be directly observed, in some cases, through examination of lanthanide(III) emission spectra. Binnemans proposed a method for estimating a numerical value for the crystal field splitting, using the emission spectra of Eu(III) complexes.[64,65] This, of course, assumes that the crystal field does not change between lanthanide(III) ions across an isostructural series. Excited Eu(III) ions emit visible light when energy is lost in transitions from the $^5D_0$ excited state to various *J* levels of the ground state. The $\Delta J = 1$ band, representing the $^5D_0 \rightarrow {}^7F_1$ transition, is split into a maximum of 3 bands in the presence of a ligand crystal field (*Figure 1.10*). In a C_n symmetric system, the $^7F_1$ energy level splits into an *A* state and a doubly degenerate *E* state. The proportionality constant, *x*, relating the $\Delta J = 1$ splitting value, ΔE, and the second-order crystal field parameter, B_0^2 (*Equation 4*), is believed to be somewhere between 3.3 and 4.1.

$$B_0^2 \approx x\,\Delta E \qquad (4)$$

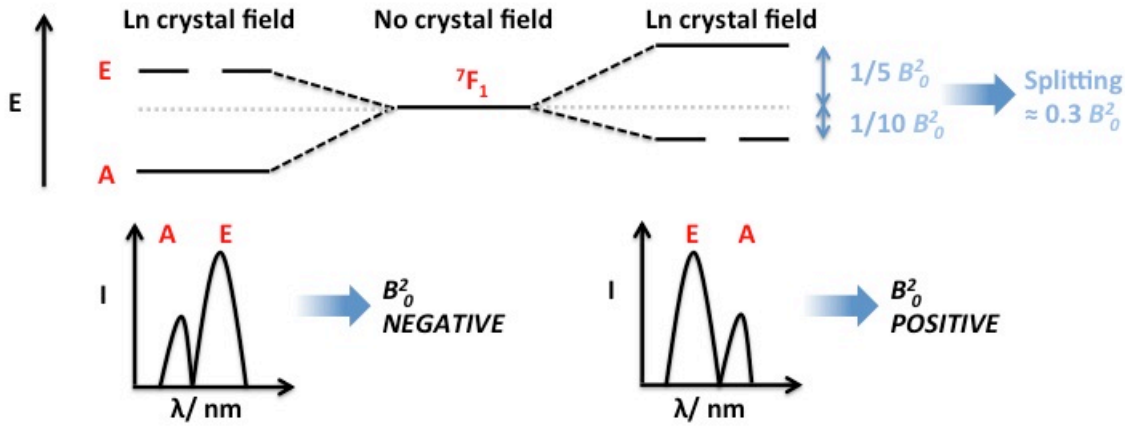

Figure 1.10 Energy level diagram, depicting the crystal field splitting of the $^7F_1$ state, in the presence of a lanthanide crystal field, with C_n symmetry and the model $\Delta J = 1$ bands.

1.2.1.2 Relaxation: Solomon-Bloembergen-Morgan theory

At the end of *Section 1.1.2*, the method of increasing the relaxation rates of the imaging nucleus using a paramagnetic lanthanide(III) ion was described, and a required R_1 of the order of 100 to 200 s^{-1} at 7 T, was derived. The standard NMR experiment and classical relaxation theory are explained in detail in *Section 1.1.1 vide supra*, and elsewhere in standard NMR textbooks.[35,70] For relaxation studies involving paramagnetic systems, the relaxation rates, R_1 and R_2, are typically analysed.

The unpaired *f* electrons present in paramagnetic lanthanide(III) ions provide nuclei with additional relaxation mechanisms, leading to substantially enhanced relaxation rates compared with diamagnetic systems. In such systems, the observed relaxation rate (R_{iobs}) can be expressed as the sum of the diamagnetic contribution (R_{id}) and the paramagnetic contribution (R_{iM}) (*Equation 5*), where i = 1, 2.

$$R_{iobs} = R_{id} + R_{iM} \quad (5)$$

The diamagnetic contribution represents the relaxation rate of solvent nuclei in the absence of a paramagnetic solute, and is found by comparison with diamagnetic complexes of La(III), Lu(III) and Y(III). The paramagnetic contribution occurs due to the electron-nuclear interaction between the fluctuating magnetic field, generated by the unpaired *f* electrons of the lanthanide ion, and the nuclear spins of the nucleus under study. This interaction is described as the sum of the contact contribution (R_{icon}), and the pseudocontact contribution, which is split into dipolar (R_{idip}) and Curie contributions (R_{iX}) (*Equation 6*).

$$R_{iM} = R_{icon} + R_{idip} + R_{i\chi} \quad (6)$$

The contact contribution stems from fluctuating electron spin density located at the resonating nucleus. However, this contribution to relaxation is typically deemed insignificant for the lanthanide(III) ions (except Gd(III)), and is largely ignored.[71] The pseudocontact contribution is the main contribution to relaxation, and describes two through-space relaxation mechanisms. Dipolar relaxation refers to the electronic relaxation of the nucleus due to fluctuations in the electronic magnetic field (*Figure 1.11a*). Curie relaxation originates from the interaction between the nuclear spin and the thermal average of the electronic spin, and depends on the rotational motion of the complex (*Figure 1.11b*).

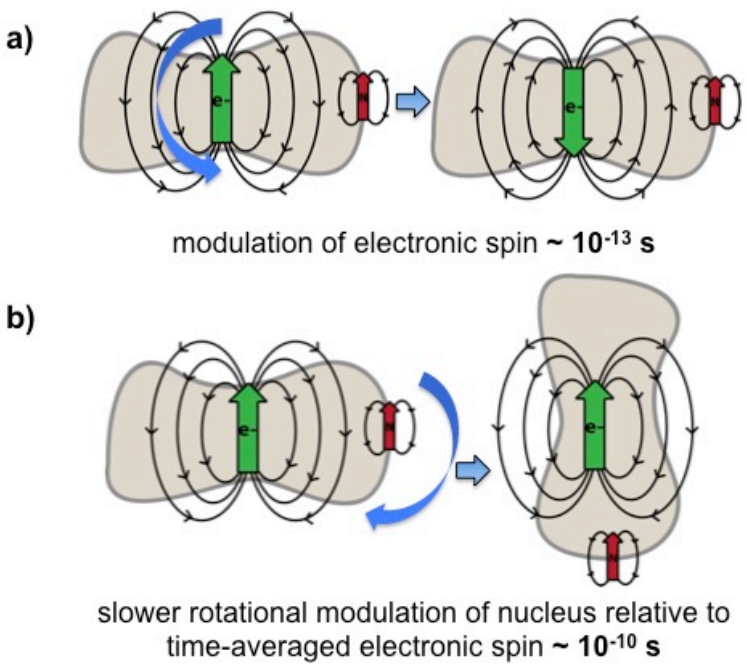

Figure 1.11 Schematic diagrams showing the two components of the pseudocontact relaxation mechanism, where a) is the dipolar contribution and b) is the Curie contribution.

The Solomon-Bloembergen-Morgan (SBM) equations (*7 and 8*), derived from Bloch-Redfield-Wangsness (BRW) theory, best describe the R_1 and R_2 of resonances in paramagnetic lanthanide(III) complexes, representing a summation of the dipolar and Curie relaxation terms.[72,73] These equations only apply within the limit that the energy of the coupling between the nucleus and the electrons, is smaller than the reciprocal of τ_R. This, the Redfield limit, is expressed as $1 / T_1 << 1 / \tau_R$ and all the lanthanide(III) complexes discussed within this thesis are expected to fall below it.[51,53,74,75]

$$R_1 = \frac{2}{15}\left(\frac{\mu_0}{4\pi}\right)^2 \frac{\gamma_N^2 \mu_{eff}^2}{r^6}\left[\frac{7\tau_{r+e}}{1+\omega_e^2\tau_{r+e}^2} + \frac{3\tau_{r+e}}{1+\omega_N^2\tau_{r+e}^2}\right] + \frac{2}{5}\left(\frac{\mu_0}{4\pi}\right)\frac{\omega_N^2\mu_{eff}^4}{(3kT)^2 r^6}\frac{3\tau_r}{1+\omega_N^2\tau_r^2}$$

(7)

$$R_2 = \frac{1}{15}\left(\frac{\mu_0}{4\pi}\right)^2 \frac{\gamma_N^2 \mu_{eff}^2}{r^6}\left[4\tau_{r+e} + \frac{3\tau_{r+e}}{1+\omega_N^2\tau_{r+e}^2} + \frac{13\tau_{r+e}}{1+\omega_e^2\tau_{r+e}^2}\right] + \frac{1}{5}\left(\frac{\mu_0}{4\pi}\right)^2 \frac{\omega_N^2\mu_{eff}^4}{(3kT)^2 r^6}\left[4\tau_r + \frac{3\tau_r}{1+\omega_N^2\tau_r^2}\right]$$

(8)

where μ_0 is the vacuum permeability, γ_N is the gyromagnetic ratio of the nucleus, μ_{eff} is the effective magnetic moment, r is the electron-nuclear distance, τ_r is the rotational correlation time, ω_N is the nuclear Larmor frequency, T is the absolute temperature and k is the Boltzmann constant and the remaining symbols are defined as:

$$\text{where } \mu_{eff}^2 = g_j^2\mu_B^2 J(J+1),\ \tau_{R+e} = (\tau_R^{-1} + T_{1e}^{-1})^{-1},\ \omega_e = (\tfrac{g_J\mu_B}{\hbar})B_0$$

in which g_J is the effective electron g-factor, μ_B is the Bohr magneton, $J(J+1)$ is the effective electron angular momentum, and T_{1e} is the longitudinal relaxation time of the electron spin.

In order to design a paramagnetic lanthanide(III) complex with desirable relaxation properties (R_1 = 100 to 200 s^{-1}), at a given field (7 T), there are four contributions to SBM theory that can be varied; the distance between the nucleus under observation and the lanthanide(III) ion, r, the effective magnetic moment of the lanthanide(III) ion, μ_{eff}, the rotational correlation time of the complex, τ_R, and the electronic longitudinal relaxation time, T_{1e}.

1.2.2 Practical considerations

The aforementioned analyses of Bleaney's theory of magnetic anisotropy and SBM theory present us with the following controllable practical design criteria for ^{1}H PARASHIFT probes, defined within this thesis:

- The choice of lanthanide(III) ion.
- The nature of ^{1}H reporter group.
- The position of the ^{1}H reporter group within the complex.

- And, the nature of the ligand framework.

The following section will discuss the advantages of optimising these criteria, with reference to the theories relating to their derivation.

1.2.2.1 Lanthanide(III) ion selection

The choice of lanthanide(III) ion has perhaps the most influential impact because it affects both the shift and relaxation behaviour. The Bleaney constant gives a good indication regarding the sign and the magnitude of the pseudocontact shift (*Table 1.3*). For example, Dy(III), Tb(III) and Tm(III) are typically employed due to their large shift ranges, arising from their high magnetic susceptibilities. The Bleaney constant for Tm(III) is the largest positive value, +53, whereas Dy(III) possesses the largest negative value, normalised to -100. Due to the difference in sign and magnitude, we expect their resonances to be shifted in opposite directions, with the Dy(III) resonances typically being shifted further. The pseudocontact shift does not always follow the magnitude of the Bleaney coefficient, however, with some Tm(III) resonances being reported with larger shifts than expected.[76,77]

Table 1.3 Magnetic and relaxation properties of selected lanthanide(III) ions, where the xenon core, [Xe], corresponds to $1s^2 2s^2 2p^6 3s^2 3p^6 3d^{10} 4s^2 4p^6 4d^{10} 5s^2 5p^6$.

Ln(III)	**Electronic configuration**	**Ground state term**	**μ_{eff}/BM[a]**	**T_{1e}[b] (aqua ion, 2.1 T) / 10^{-13} s**	**C_J[c] normalised**
Eu	[Xe] $4f^6$	$^7F_0$	3.5	0.09	4.0
Gd	[Xe] $4f^7$	$^8S_{7/2}$	7.9	10^4-10^5	0
Tb	[Xe] $4f^8$	$^7F_6$	9.8	2.03	-87
Dy	[Xe] $4f^9$	$^6H_{15/2}$	10.3	2.99	-100
Ho	[Xe] $4f^{10}$	$^5I_8$	10.4	1.94	-39
Er	[Xe] $4f^{11}$	$^4I_{15/2}$	9.4	2.38	32
Tm	[Xe] $4f^{12}$	$^3H_6$	7.6	3.69	53
Yb	[Xe] $4f^{13}$	$^2F_{7/2}$	4.3	1.37	22

(a) Taken from reference [78]. (b) Taken from references [79–81]. (c) As in *Table 1.1*.

The magnetic moment (*Table 1.3*) of the lanthanide(III) ion is also important when seeking to optimise nuclear relaxation rate enhancement. The higher the magnetic moment, the more significant effect it has on the nuclear relaxation, especially at high field (*Figure 1.12*). This renders Tm(III) a less attractive candidate than Dy(III), under normal circumstances.

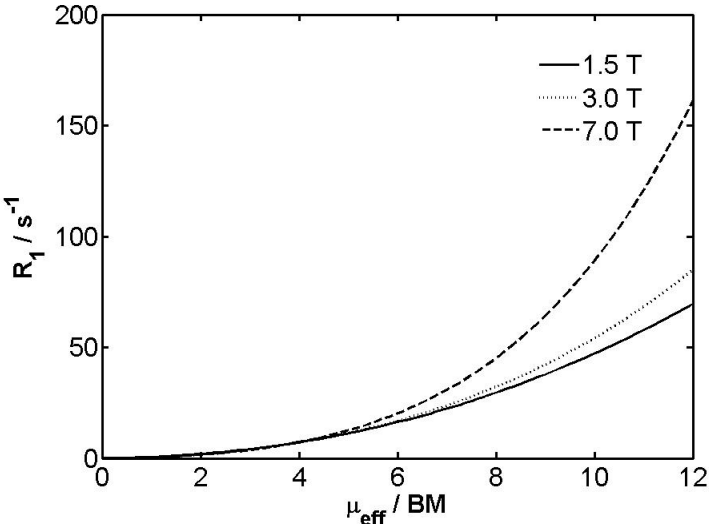

Figure 1.12 Simulation of the longitudinal relaxation rate, R_1, of a hypothetical ^{1}H resonance in an idealised system with the magnetic moment, μ_{eff}, at three different clinically relevant field strengths (B = 1.5, 3.0 and 7.0 T) (295 K, T_{1e} = 0.45 ps, r = 6.6 Å, τ_R = 250 ps).

The electronic relaxation time, T_{1e}, also features in SBM theory and varies amongst the lanthanide(III) ions (*Table 1.3*).[82] Values of T_{1e} tend to be *ca.* 10^{-12} to 10^{-13} s for fast relaxing lanthanide(III) complexes, except in the case of Gd(III).[83] These values are deemed to be independent of magnetic field, and display small temperature dependencies, increasing slightly with decreasing T due to the small activation energy for the electron spin relaxation process. Fries and Belorizky summated that T_{1e} can be interpreted as the fluctuation in the static and transient ligand fields because the strong spin-orbit coupling in lanthanide(III) complexes implies that such modulations promote electronic spin transitions.[83]

For relaxation rates at low field, T_{1e} has a significant impact. At low field, the dipolar term dominates the SBM equations (*7 and 8*), resulting in perturbation of the relaxation rates by almost one order of magnitude (*Figure 1.13).* This analysis highlights the importance of the consideration of T_{1e} at clinically relevant field strengths (0.1 to 3.0 T) for MRI applications. Unfortunately, however, the physical basis of T_{1e} is not properly

understood, and it is not yet possible to predict when designing a novel paramagnetic lanthanide(III) complex.

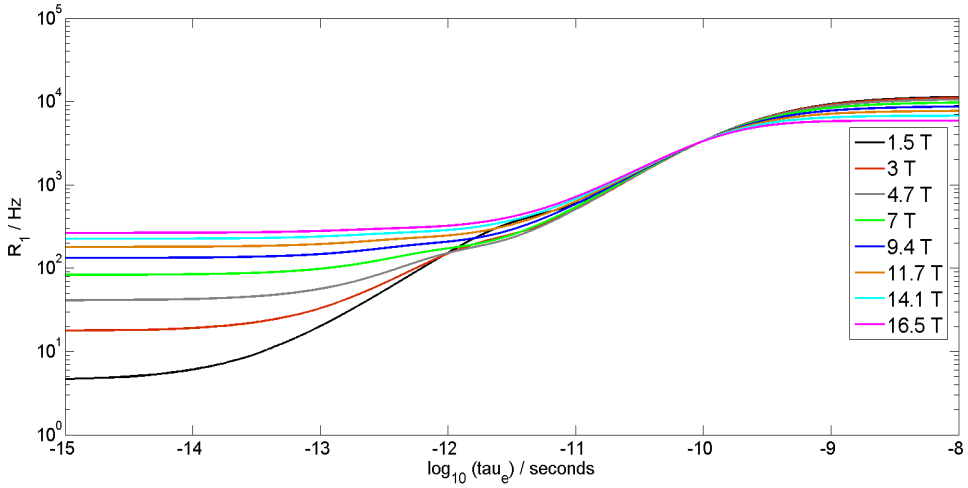

Figure 1.13 Simulation of the dependence of R_1 on T_{1e} at a variety of fields (295 K, μ_{eff} = 10 BM, r = 6.5 Å, τ_R = 250 ps).[82]

1.2.2.2 Ligand design

Any NMR based spectroscopic technique suffers from low SNR, and hence low sensitivity. Acquiring more scans is the most straightforward method for improving SNR, since SNR increases with the square root of the number of scans/transients (SNR ~ $\sqrt{nt}$), but is time consuming and therefore not clinically attractive. Recent advances in ^{19}F MRI (*Section 1.1.2*) saw a shift towards using high spin density perfluorinated probes, in an effort to increase signal intensity. Of those reported, the probes possessing a large number of magnetically equivalent nuclei were the most promising, affording a single sharp peak in the ^{19}F NMR spectrum. Evidently, the number of magnetically equivalent nuclei contributing to the ^{1}H reporter group in PARASHIFT probes should be optimised.

The time limiting constraint hindering clinical acceptance can be alleviated, however, by enhancing the relaxation rates of the reporter group so that more signal intensity can be acquired in a shorter imaging time frame. This methodology has yielded sensitivity gains between 10 and 25-fold using lanthanide(III)-based systems in ^{19}F MRI. In order to emulate these enhancements, the distance between the reporter nuclei and the lanthanide(III) ion, r, needs to be assessed. Since r appears on the denominator in the equations for both Bleaney and SBM theory (r^{-3} and r^{-6} respectively), the positioning of

the reporter group can have a dramatic impact on the shift and the relaxation behaviour, and warrants careful consideration. Consider the cases of Dy(III) and Tm(III), since they possess the largest pseudocontact shifts with opposing senses. Using literature values for the rotational correlation time, τ_R, and the electronic relaxation times,[82] T_{1e}, of Dy(III) and Tm(III) it is possible to simulate the rate of relaxation, R_1, as a function of the internuclear distance, r, at varying field strengths (*Figure 1.14*). This analysis reveals that for a Dy(III) complex, a distance between 6 and 7 Å is required to achieve a 100 to 200 s^{-1} enhancement in R_1. For Tm(III), however, these R_1 enhancements are only observed at shorter distances (5 Å at 4.7 T), due to its lower magnetic susceptibility. Similarly, the rate of transverse relaxation, R_2, is enhanced with respect to distance and so a balance needs to be struck. When R_2 increases, concomitant broadening of the NMR signal limits the sensitivity gain and inhibits signal detection. If the reporter nuclei are too close to the lanthanide(III) ion then line-broadening can be too severe; if they are too distant, then the effect on R_1 will be much too small. Therefore, in an effort to maximise signal intensity, an R_1/R_2 ratio as close to unity as possible is desirable for PARASHIFT systems.

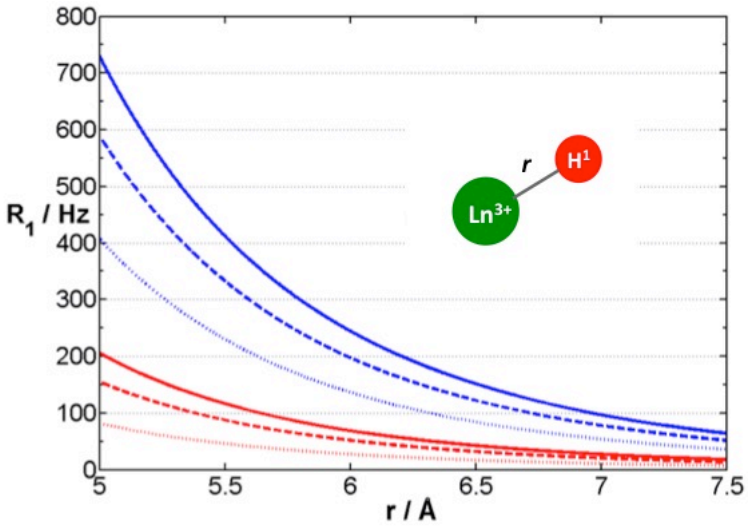

Figure 1.14 Simulated variation of the ^{1}H longitudinal relaxation rate, R_1, with Ln^{3+}-^{1}H internuclear distance, r, at for Ln^{3+} = Dy^{3+} (upper, blue) and Tm^{3+} (lower, red) at three different magnetic field strengths (B = 4.7, dot; 7.0, dash; and 9.4 T, line) (295 K, T_{1e} = 0.5 and 0.3 ps, τ_R = 250 ps).[84]

Finally, the nature of the ligand framework must also be considered. The 4*f* lanthanide orbitals have a small radial extension and are shielded by the filled 5*s* and 5*p* orbitals. Their resulting 'core-like' nature means they are less available to form covalent bonds with ligands. As a result of this, and coupled with their large ionic radii, the

lanthanide(III) ions prefer higher coordination numbers of typically 8 or 9. In the majority of examples, macrocyclic multidentate ligands are used to satisfy such high coordination environments such as 12-N_4 (1,4,7,10-tetraazacyclododecane) (*Figure 1.15*). In the cases where the ligands do not fully saturate the lanthanide(III) ion, additional water molecules can coordinate. It is not uncommon for the hydration number to decrease across an isostructural series of lanthanide(III) complexes due to the decreasing coordinative demand brought about by the lanthanide contraction. The number of water molecules on a lanthanide(III) complex can be estimated and is represented with the hydration number, *q*. In order to maximise the affinity of the ligand for the hard positive lanthanide(III) ion, donor atoms such as oxygen and nitrogen are favoured.

When designing a PARASHIFT probe for MR applications, it is imperative that the resulting lanthanide(III) complex is kinetically and thermodynamically stable with respect to metal ion dissociation. Much like free Gd(III) (LD_{50} = 0.1 mM kg^{-1}), other free lanthanide(III) ions are toxic. In 2011, the chemistry and applications of DOTA had been published in over one thousand papers, reflecting its suitability for use in PARASHIFT systems.[76] DOTA is a tetra-acetate modified 12-N_4 system, possessing both nitrogen and oxygen donors (*Figure 1.15*). Its affinity for Y(III) was determined by Cox *et al.*, with a thermodynamic binding constant, $logK_{ML}$, of 24.9.[85] The PARASHIFT complexes in this discussion will be based on either H_4DOTA or H_4DOTPMe.

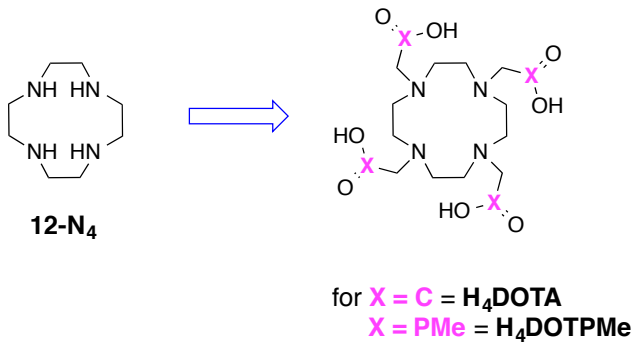

Figure 1.15 Structures of 12-N_4-based ligands reported in this thesis.

1.3 Applications of paramagnetic lanthanide(III) complexes in magnetic resonance: PARASHIFT and PARACEST

The two main avenues of research, embracing paramagnetic lanthanide(III) complexes, are to be discussed in this section. The first is the focus of this thesis, and explores the idea of examining a shifted ^{1}H reporter resonance on a paramagnetic lanthanide(III) complex (*i.e.* a PARASHIFT agent). There is some precedence in the literature regarding the development of ^{1}H PARASHIFT probes, with early work focusing mainly on the Yb(III), Tm(III) and Pr(III) complexes of DOTMA, DOTP and MOE-DO3A (*Figure 1.16*).

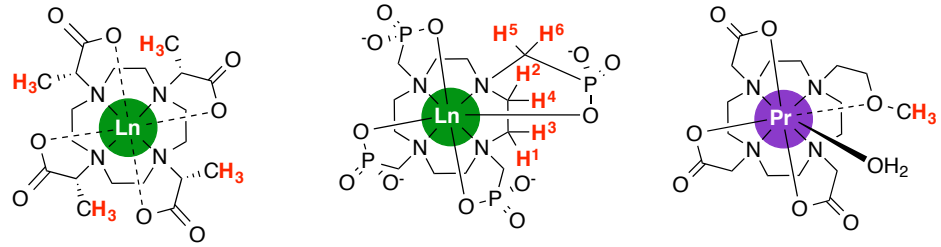

Figure 1.16 Previous examples of ^{1}H PARASHIFT probes, in which the ^{1}H reporter nuclei are highlighted in red (*NB.* all phosphinate arms in **[Ln.DOTP]$^{5-}$** are equivalent; one is drawn as shown for clarity).[86–93]

The first example of interest is the C_4-symmetric complex **[Yb.DOTMA]$^{-}$**, which possesses four equivalent methyl groups (*Figure 1.16*).[86] The 12 magnetically equivalent methyl ^{1}H nuclei resonate at -14.2 ppm (*Figure 1.17*). It was possible to observe this intense signal selectively, in a phantom imaging experiment, but it took over 6 h to observe a 3 mM aqueous solution of the complex at 4.7 T and 300 K. Under these conditions, R_1 = 15 s^{-1} and R_2 = 30 s^{-1}. Evidently, the relaxation rate enhancement is too small to allow fast data acquisition, leading to clinically impractical acquisition times. Nevertheless, as a prototypical PARASHIFT probe, **[Yb.DOTMA]$^{-}$** has demonstrated one of the aforementioned criteria: the high equivalent spin density of the ^{1}H reporter group. The pseudocontact shift exhibits a T^{-2} temperature dependency and as a result, all paramagnetic lanthanide(III)-based complexes possess T dependent chemical shifts. In light of this, the authors selected a pair of resonances and followed the chemical separation between them as a function of temperature. When looking at the change in chemical shift difference between an axial ring proton and a carboxylate arm

proton, a linear change of 0.41 ppm/K over the 308 to 318 K range was observed, in human serum. However, when observing the temperature dependence of the methyl signal under the same conditions, a meagre change of 0.04 ppm/K was found, the lowest of the resonances on **[Yb.DOTMA]**$^{-}$.

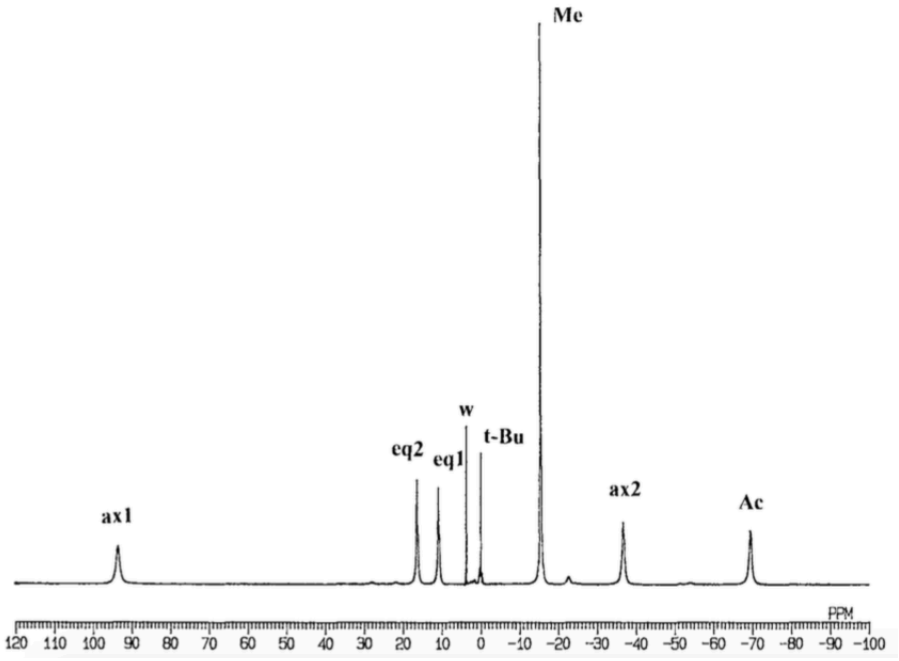

Figure 1.17 ^{1}H NMR spectrum of **Na[Yb.DOTMA]**, where w and t-Bu refer to the solvent and the *tert*-butyl reference, respectively (D_2O, 300 K, pH 7.4).[86]

Further responsive behaviour was sought and the same research group developed **[Yb.DOTP]**$^{5-}$.[87] The six ligand protons (highlighted in *Figure 1.16* for clarity) are magnetically non-equivalent and result in six distinguishable resonances that resonate outside the diamagnetic range (*Figure 1.18*). Its pH dependent chemical shift behaviour was investigated by measuring the chemical shift separation between the *ax1* (H^1) and *ac1* (H^5) resonances as a function of pH. This allowed linear shift difference dependencies to be established, with an observed change of 7 ppm/pH unit, over the physiologically relevant 5 to 7.5 pH range. The main advantage of this work is that by using two probe signals the need for internal calibration is negated. However, calibration at different temperatures will need to be assessed before **[Yb.DOTP]**$^{5-}$ can be considered for *in vivo* applications, since the chemical shift is also very temperature sensitive.

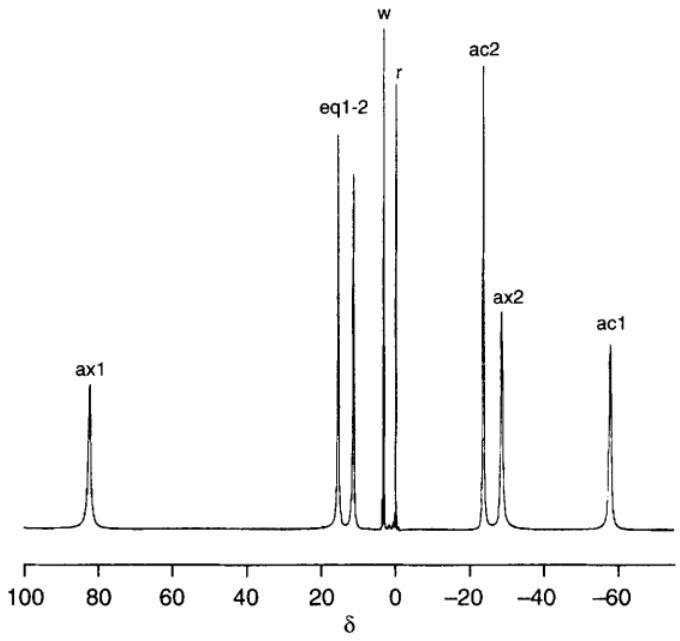

Figure 1.18 ^{1}H NMR spectrum of **Na_5[Yb.DOTP]**, where w and r refer to the solvent and the *tert*-butyl reference, respectively (D_2O, 312 K, pH 7.1, 90 MHz).[87]

Concurrently, Frenzel and co-workers developed a similar approach towards a potential *in vivo* NMR thermometer.[88,89] The methoxy group on **[Pr.MOE-DO3A]** (*Figure 1.16*) resonates at -24.1 ppm (relative to HOD), at 295 K. The change in chemical shift difference between the methoxy resonance and the water signal was measured in bovine serum, over the range 296 to 321 K, and a dependence of 0.13 ppm/K was established. The chemical shift remained unaffected by changes in pH between 5.6 and 9.6. However, an increase in linewidth was noted with increasing pH. A notable increase in linewidth is also evident when the NMR solvent is changed from D_2O to plasma. Following this, however, the usefulness of **[Pr.MOE-DO3A]** as an NMR thermometer was successfully demonstrated *in vivo*, reporting temperature increases in the livers of anaesthetised rats with an accuracy of ±1 K. The signal intensity was sufficient to obtain spectra 30 min after complex administration, but the methoxy signal becomes increasingly broad over time due to chemical exchange broadening. This is probably associated with protein side chain ligation of Asp and Glu resides, competing with displacement of the bound water and the weakly coordinated methoxy group. Also, the dose administered of 1 mmol/kg led the authors to admit it was rather high when compared with commercial Gd(III)-based MRI contrast agents (*ca.* 0.1 mmol/kg), although they argued that the LD_{50} of 12.5 mmol/kg gave them a margin of safety. An acquisition time of 2.7 min per spectrum was reported but it is clear that more time will be required if the signal intensity continues to decrease over time, and in the presence of

endogenous protein. Additionally, the R_1 of the methoxy signal in plasma was reported to be 23 s^{-1}, and offers no improvements on the relaxation rates observed with **[Yb.DOTMA]**$^-$. Finally, the complex was injected directly into the liver, rather than the tail vein. If it is administered intraveneously, it is likely that the hydrophilic complex would clear more quickly *via* the kidneys, localising in the bladder within a few minutes.

In more recent work, Bansal and co-workers examined the methyl shift at -102 ppm of the major isomer of **[Tm.DOTMA]**$^-$ (*Figure 1.16*).[90] The magnitude of this shift, compared to the Yb(III) analogue, resulted in dramatic improvements in phantom imaging experiments. Selective imaging of the strong methyl signal took just over 4 min at 9.4 T, for a 0.5 mM solution (*ca.* 6 h for 3 mM of the Yb(III) analogue). Their previous studies had demonstrated that **[Tm.DOTMA]**$^-$ was a good candidate for MR thermometry, with a temperature coefficient of 0.57 ppm/K, and a chemical shift that remains unaffected by variations in pH, [Ca^{2+}] or plasma protein levels.[91] Following these promising results, temperature mapping studies were successfully carried out *in vivo*, using doses of 0.5-0.6 mmol/kg. Images were acquired in about 3 min but due to rapid kidney clearance, the rats were nephrectomised beforehand. **[Tm.DOTMA]**$^-$ is without doubt the leading example of a ^{1}H PARASHIFT probe to date, but the work detailed in this publication is not without flaw. The authors themselves admit that little was done to modify the pulse sequence in order to optimise signal intensity acquisition. For example, because the methyl resonance is so far away from the H_2O signal, a much larger bandwidth for imaging could have been used to increase the SNR. With no such detail reported, it is unclear how long the complex takes to clear in a non-nephrectomised rat, but it is assumed to be too fast to allow practicable image acquisition. The nephrectomy approach used here limits the applicability of these studies. Another fundamental problem is that it is impossible to modify the structure of **[Tm.DOTMA]**$^-$ to incorporate a targeting or responsive moiety, without disturbing the magnetic equivalence of the four methyl groups.

More practically, the feasibility of tracking **[Tm.DOTMA]**$^-$ *in vivo* using the principle of PARASHIFT MR imaging as an alternative to established cell-tracking methods, has been explored.[94] Macrophages were directly and unambiguously detected, following labeling with **[Tm.DOTMA]**$^-$, in a mouse model. Due to the shift magnitude of the methyl signal, the complex was successfully imaged without interference from the

background water signal *in vivo*, using excitation and acquisition bandwidths centred at the resonant frequency (*Figure 1.19*). The method was extended *in vitro*, to **[Dy.DOTMA]**$^{-}$, and the practicality of imaging two separate resonant frequencies was demonstrated, without interference from the water signal or each other.

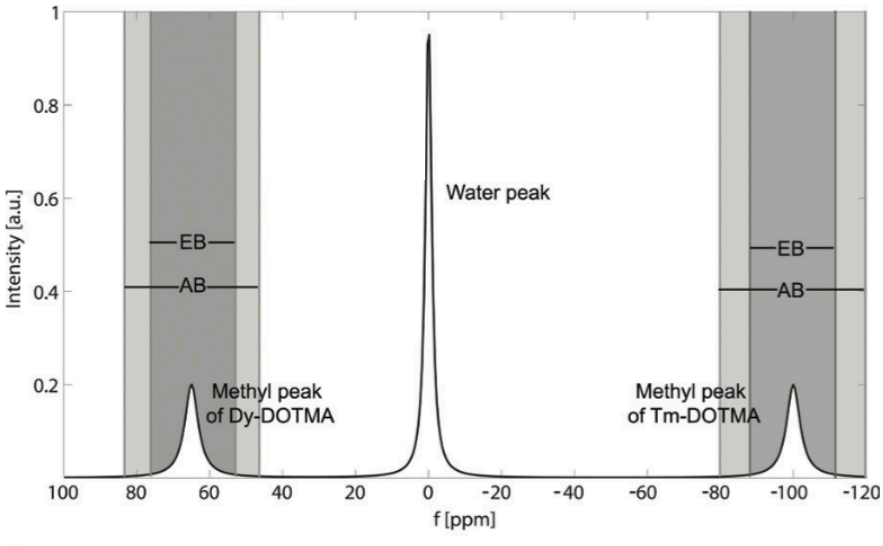

Figure 1.19 Schematic demonstrating the principle of PARASHIFT MR imaging. The resonant frequency of the methyl groups of **[Tm.DOTMA]**$^{-}$ and **[Dy.DOTMA]**$^{-}$ can be excited and detected separately and independently from the tissue water signal and each other. Dark grey bars indicate the typical excitation bandwidth (*EB*) and light grey bars indicate the acquisition bandwidth (*AB*).[94]

Related work by Hyder *et al.* demonstrated the use of **[Tm.DOTP]**$^{5-}$ to generate temperature and pH maps of rat brains *in vivo*.[92] The H^6 proton on **[Tm.DOTP]**$^{5-}$ (labeled in *Figure 1.16*), displays a temperature dependent chemical shift of 0.93 ppm/K, which is a 2-fold improvement on the behaviour of the methyl resonance in **[Tm.DOTMA]**$^{-}$.[93] The work, described earlier, for the Yb(III) analogue means that the chemical shifts are also pH dependent. Hyder *et al.* have previously proved that **[Tm.DOTP]**$^{5-}$ accumulates in the brain's extracellular space, presenting a potential method for temperature and pH mapping. The authors acknowledged that extensive calibration was required prior to *in vivo* studies, so they monitored the chemical shift of H^1, H^2, H^3 and H^6 as a function of temperature and pH (H^4 and H^5 were omitted due to their far removed resonant frequencies of +500 and -385 ppm, respectively). Each resonance showed a unique dependence towards both parameters. Subsequent *in vivo* studies, following the continuous infusion of complex over a 2 h period, allowed temperature and pH maps to be constructed of rat brains, with images taking 'at most a few minutes' to acquire. Although this work is thorough, there are a few drawbacks,

which must be scrutinised. Firstly, the doses of complex used *in vivo* are five to ten times higher than related Gd(III)-based contrast agents. This high dosage is probably due to the fact that the reporter signals in **[Tm.DOTP]$^{5-}$** only comprise four nuclei. Moreover, the rats used in these studies were nephrectomised to prevent complex clearance *via* the kidneys.

Another example has reported the use of Dy(III), Tb(III) and Tm(III) tetra-propargyl amide complexes as potential candidates for MR thermometry (*Figure 1.20*).[95] Due to the large Bleaney coefficients and the close proximity of the labeled nuclei to the lanathanide(III) ion, highly-shifted resonances are achieved: Dy (H^4) at -333 ppm, Tb (H^4) at -287 ppm, Tm (H^4) at 224 ppm and Tm (H^5) at -148 ppm. These same nuclei report high temperature dependencies, between 1.05 ppm/K (Tm (H^5)) and 1.76 ppm/K (Dy (H^4)), representing a 2 to 3-fold improvement in previously published examples. Unfortunately however, these promising results only got as far as being tested *in vitro*, where a slight decrease in the temperature dependence for the Tm(III) analogue was observed. Although the authors comment on negligible losses due to line-broadening, relaxation rates over 3000 s^{-1} were reported at 14.1 T and 308 K. Such fast rates are not surprising for resonances that are within 4 Å of the lanthanide(III) ion. Any attempts at *in vivo* studies will most certainly be hindered by the reactivity of the alkyne groups, supposedly present so that extension of the arms can be carried out using 'click' chemistry.

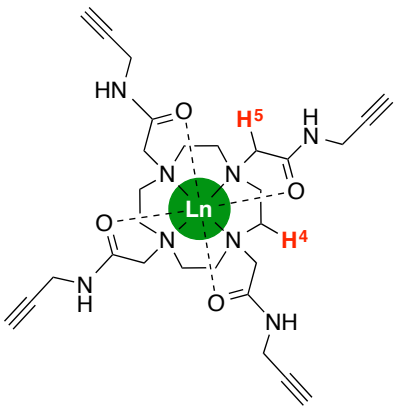

[Ln.tpDOTAM]$^{3+}$
where Ln = Tb, Dy and Tm

Figure 1.20 Example of the tetra-propargyl DOTAM complex, where Ln= Tb, Dy or Tm, and protons under discussion are highlighted in red.[95]

Work by Caravan *et al.*, sought to encapsulate **[Yb.DOTMA]**$^-$ inside liposomal nano-carriers with the diamagnetic ^{1}H shift probe, sodium 3-(trimethylsilyl)-1-propanesulfonate (DSS) (*Figure 1.21*).[96] Their aim was to demonstrate the potential for multiplex imaging using two different probes with chemical shift signatures (DSS at 0 ppm, **[Yb.DOTMA]**$^-$ at 14 ppm), with the added benefit of paramagnetic relaxation enhancement, to improve the detection sensitivity of DSS. However, the publication showed no results regarding **[Yb.DOTMA]**$^-$, seemingly noting it as a poor choice of relaxation agent, and opted for **[Gd(HP-DO3A)(H_2O)]** instead. Whilst, their conclusions ascertained that a wide variety of ^{1}H PARASHIFT probes can be used for this purpose, ultimately, this approach is completely invalidated because there are better examples of lanthanide(III)-based shift and relaxation agents in the literature. The only good idea to stem from this publication was to improve the biocompatibility of **[Yb.DOTMA]**$^-$ through encapsulation in a liposome, since without it; it has no specific biological target and is rapidly excreted.

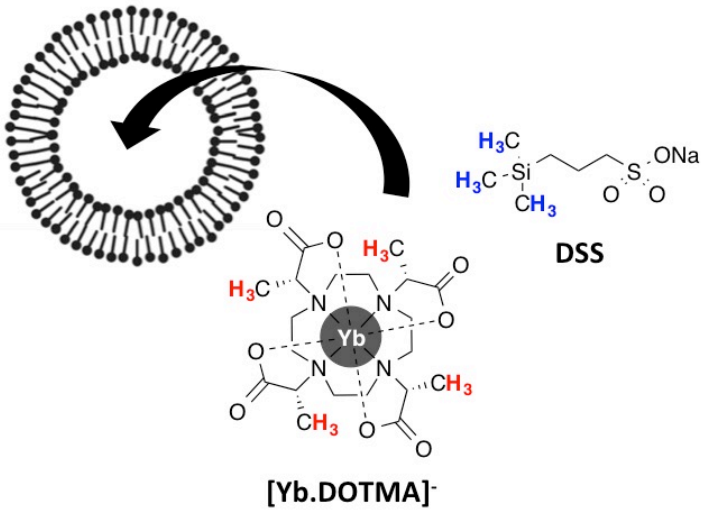

Figure 1.21 Schematic representation of the co-encapsulation of **[Yb.DOTMA]**$^-$ and DSS inside a liposome.

The second area of research, is the extension of the chemical exchange saturation transfer (CEST) experiment to include the use of paramagnetic lanthanide(III) complexes. Aime and co-workers discovered that compounds containing exchangeable protons (typically OH or NH) can act as T_2 agents, by reducing the water proton relaxation time *via* exchange processes.[97] Following this, substantial improvements were demonstrated when the RF irradiating field was applied at the exact resonant frequency of the exchanging protons, leading to a net decrease in the bulk water signal

intensity due to a saturation transfer effect.[98] In order for efficient saturation transfer to occur, the exchange rate between the mobile protons and the water, k_{ex}, must be optimised. This occurs as k_{ex} approaches the chemical shift separation between the two exchanging sites, $\Delta\nu$.[99] Consequently, larger $\Delta\nu$ values allow for larger k_{ex} values to be exploited, amounting in an enhanced CEST effect. The aforementioned research on ^{1}H PARASHIFT probes perfectly demonstrates the feasibility of shifting a ^{1}H resonance well away from the water signal and so offers an attractive class of probes for CEST applications, coined PARACEST.[100,101]

Paramagnetic lanthanide(III) complexes, such as **[Eu.DOTAM(H$_2$O)]** (*Figure 1.22*) and its variants, have been used as PARACEST agents.[102,103] Although interest in PARACEST has been growing in the last decade, due to the indirect nature of the technique the major limitation remains the need to determine the absolute concentration of the probe. As a result, there are few examples documented *in vivo*, and even then most cases report direct injection into the tissue of interest and/or a high injected dose (*ca.* 2 mmol/kg).[104,105] Following on from the successes regarding pH and temperature sensitivity, several ^{1}H PARASHIFT probes have been evaluated for sensitivity towards different physiological parameters, but once again only triumphs *in vitro* have been described. The main problems inherent to PARACEST are: the need to radiate continuously at high frequency, casting doubts over safety issues, and the need to collect multiple scans, meaning that acquisition times are long.

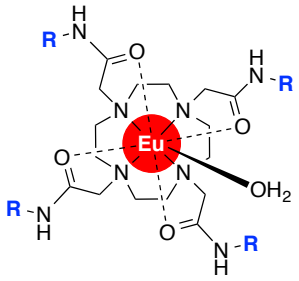

[Eu.DOTAM(H$_2$O)]$^{3+}$

Figure 1.22 Structure of a common PARACEST agent, **[Eu.DOTAM(H$_2$O)]$^{3+}$**, where functionalisation can occur by appending different R groups.

The examples of ^{1}H PARASHIFT probes discussed in this review, reinstate the need for the work in this thesis, and confirm that strict design criteria are required if any improvements are to be made moving forward. Of paramount importance is a ^{1}H

reporter resonance that is shifted well away from the diamagnetic range, so it can be imaged without interference from endogenous ^{1}H signals *in vivo*. Bleaney's theory of magnetic anisotropy proves that through careful lanthanide(III) ion selection (C_J and μ_{eff}), it is possible to influence the sign and magnitude of the paramagnetic shift. Most obvious, is the need for a strong signal, arising from more than one equivalent ^{1}H nucleus, permitting increased sensitivity. Also a necessity, but an idea not fully considered in these examples, is the benefit of longitudinal relaxation rate enhancement, and the hindrance of transverse relaxation rate enhancement; and their strong dependence on the Ln-nuclear distance (r) and lanthanide ion selection (μ_{eff} and T_{1e}), at a given magnetic field (B_0) (*Section 1.2.1.2*).

1.4 Aims and Objectives

The aim of this project is to synthesise and characterise novel ^{1}H PARASHIFT probes, with the definitive aim of developing systems that can be used for *in vivo* ^{1}H magnetic resonance imaging and spectroscopy studies. Therefore, it is important to improve on the successes and limitations of previous examples, detailed *vide supra Section 1.3*.

The design of these ^{1}H PARASHIFT probes must satisfy the following criteria:

- The probe must possess a reporter group with *high equivalent spin density*, so that one large signal dominates the ^{1}H NMR spectrum.
- The reporter group must be *located an appropriate distance away (r)* from the lanthanide(III) ion to benefit longitudinal relaxation rate enhancement; too close and line-broadening dominates; too distant and the enhancement is too small, such that the ratio of R_1/R_2 is close to unity.
- The probe must be based on a *12-N_4 macrocyclic framework* since it shows kinetic and thermodynamic stability with respect to lanthanide(III) ion dissociation.
- The *choice of lanthanide(III) ion* must optimise the shift (C_J) and relaxation (μ_{eff} and T_{1e}) behaviour of the reporter group.
- The probe must possess the *potential for functionalisation* with minimal modification, so that responsive behaviour can be readily incorporated.

Chapter 2 describes the design, synthesis and characterisation of a novel class of ^{1}H PARASHIFT probes, based on the abovementioned criteria. In *chapter 3*, a series of pH responsive ^{1}H PARASHIFT probes were synthesised in pursuit of non-invasive pH determination *in vivo*. Finally, *chapter 4* focuses on increasing the retention times of ^{1}H PARASHIFT probes *in vivo*, by altering their biodistributions and offering a longer period to image; as well as increasing local signal intensities, through the use of higher molecular weight materials.

1.5 References

1. R. Damadian, *Science*, 1971, **171**, 1151–1153.
2. R. Damadian, K. Zaner, D. Hor and T. DrMaio, *Proc. Nat. Acad. Sci. USA*, 1974, **71**, 1471–1473.
3. Patent no. 3789837, 1974.
4. P. Mansfield and P. K. Grannell, *J. Phys. Chem.: Solid State Phys.*, 1973, **6**, 422–426.
5. P. C. Lauterbur, *Nature*, 1973, **242**, 190–191.
6. R. Damadian, L. Goldsmith and L. Minkoff, *Physiol. Chem. Phys.*, 1977, **9**, 97–100.
7. OECD/ European Union, *Health at a Glance 2013. OECD Indicators*, 2013.
8. R. B. Lauffer, *Chem. Rev.*, 1987, **87**, 901–927.
9. C. L. Partain, *J. Magn. Reson. Imaging*, 2004, **19**, 515–526.
10. C. Cofield, *Symmetry*, 2008, **5**, 340.
11. A. Ziegler, M. Kunth, S. Mueller, C. Bock, R. Pohmann, L. Schroder, C. Faber and G. Giribet, *Zoomorphology*, 2011, **130**, 227–254.
12. M. C. Heffern, L. M. Matoszuick and T. J. Meade, *Chem. Rev.*, 2014, **114**, 4496–4539.
13. P. J. Hore, *Nuclear Magnetic Resonance*, Oxford University Press Inc. New York, 1995.
14. P. Caravan, *Chem. Soc. Rev.*, 2006, **35**, 512–523.
15. M. Bottrill, L. Kwok and N. J. Long, *Chem. Soc. Rev.*, 2006, **35**, 557–571.
16. N. Kaltsoyannis and P. Scott, *The f elements*, Oxford University Press Inc. New York, 1999.
17. P. Caravan, J. J. Ellison, T. J. McMurry and R. B. Lauffer, *Chem. Rev.*, 1999, **99**, 2293–2352.
18. I. Bertini, C. Luchinat and G. Parigi, *Solution NMR of Paramagnetic Molecules: Current Methods in Inorganic Chemistry*, Elsevier Science B. V. Amsterdam, 2001, vol. 2.
19. A. Sigel and H. Sigel, *Metal ions in biological systems. The lanthanides and their interrelations with biosystems*, Marcel Dekker Inc. Netherlands, 2003, vol. 40.
20. M. Botta, *Eur. J. Inorg. Chem.*, 2012, 1873–1874.
21. H. S. Thomsen, *Radiol. Clin. North Am.*, 2009, **47**, 827–831.
22. P. Wedeking, K. Kumar and M. F. Tweedle, *Magn. Reson. Imaging*, 1992, **10**, 641–648.
23. P. K. Pulukoddy, T. J. Norman, D. Parker, L. Royle and C. J. Broan, *J. Am. Chem. Soc., Perkin Trans. 2*, 1993, **2**, 605–620.
24. FDA, 2010.
25. H. J. M. Bowen, *Environmental chemistry of the elements*, Academic Press, 1979.
26. A. M. James and M. P. Lord, *Macmillan's chemical and physical data*, Macmillan, 1992.
27. R. B. Moon and J. H. Richards, *J. Biol. Chem.*, 1973, **248**, 7276–7278.
28. M. J. Fisher and P. F. Dillon, *Circulation Res.*, 1987, **60**, 472–477.
29. M. Cohn and T. R. Hughes, *J. Biol. Chem.*, 1962, **237**, 176–181.
30. C. T. Burt, T. Glonek and M. Barany, *J. Biol. Chem.*, 1976, **251**, 2584–2591.
31. R. J. Gillies, Z. Liu and Z. Bhujwalla, *Am. J. Physiol., Chem. Physiol. 36*, 1994, **267**, 195–203.
32. X.-H. Zhu, N. Zhang, Y. Zhang, X. Zhang, K. Ugurbil and W. Chen, *NMR Biomed.*, 2005, **18**, 83–103.

33. R. Gruetter, G. Adriany, I.-Y. Choi, P.-G. Henry, H. Lei and G. Oz, *NMR Biomed.*, 2003, **16**, 313–338.
34. M. Kitamura, T. Suzuki, R. Abe, T. Ueno and S. Aoki, *Inorg. Chem.*, 2011, **50**, 11568–11580.
35. M. H. Levitt, *Spin Dynamics: Basics of Nuclear Magnetic Resonance*, John Wiley & Sons Ltd., Chichester, 2001.
36. J. Ruiz-Cabello, B. P. Barnett, P. A. Bottomley and J. W. M. Bulte, *NMR Biomed.*, 2011, **24**, 114–129.
37. J. W. M. Bulte, *Nat. Biotech.*, 2005, **23**, 945–946.
38. G. N. Holland, P. A. Bottomley and W. S. Hinshaw, *J. Magn. Reson.*, 1977, **28**, 133–136.
39. A. Ratner, H. Muller and B. Bradley-Simpson, *Invest. Radiol.*, 1988, **23**, 361–364.
40. Patent no. US 4480228 A, 1984.
41. J. Frahm, K. D. Merboldt, W. Hanicke and A. Haase, *J. Magn. Reson.*, 1969, **64**, 81–93.
42. U. Flögel, Z. Ding, H. Hardung, S. Jander, G. Reichmann, C. Jacoby, R. Schubert and J. Schrader, *Circulation*, 2008, **118**, 140–148.
43. E. T. Ahrens, R. Flores, H. Xu and P. A. Morel, *Nat. Biotech.*, 2005, **23**, 983–987.
44. E. T. Ahrens, B. M. Helfer, C. F. O'Hanlon and C. Schirda, *Magn. Reson. Med.*, 2014, **72**, 1696–1701.
45. P. K. Senanayake, A. M. Kenwright, D. Parker and S. K. van der Hoorn, *Chem. Comm.*, 2007, 2923–2925.
46. F. Schmid, C. Holtke, D. Parker and C. Faber, *Magn. Reson. Med.*, 2013, **69**, 1056–1062.
47. A. M. Kenwright, I. Kuprov, E. De Luca, D. Parker, S. U. Pandya, P. K. Senanayake and D. G. Smith, *Chem. Comm.*, 2008, 2514–2516.
48. K. H. Chalmers, E. De Luca, N. H. M. Hogg, A. M. Kenwright, I. Kuprov, D. Parker, M. Botta, I. Wilson and A. M. Blamire, *Chem. Eur. J.*, 2010, **16**, 134–148.
49. K. H. Chalmers, M. Botta and D. Parker, *Dalton Trans.*, 2011, **40**, 904–913.
50. P. Harvey, K. H. Chalmers, E. De Luca, A. Mishra and D. Parker, *Chem. Eur. J.*, 2012, **18**, 8748–8757.
51. P. Harvey, I. Kuprov and D. Parker, *Eur. J. Inorg. Chem.*, 2012, **12**, 2015–2022.
52. E. De Luca, P. Harvey, K. H. Chalmers, A. Mishra, P. K. Senanayake, J. I. Wilson, M. Botta, M. Fekete, A. M. Blamire and D. Parker, *J. Biol. Inorg. Chem.*, 2014, **19**, 215–227.
53. N. Bloembergen and L. O. Morgan, *J. Chem. Phys.*, 1961, **34**, 842–850.
54. B. Bleaney, *J. Magn. Reson.*, 1972, **8**, 91–100.
55. R. M. Golding and P. Pyykkö, *Mol. Phys.*, 1973, **26**, 1389–1396.
56. J. Ren and A. D. Sherry, *J. Magn. Reson.*, 1996, **111**, 178–182.
57. J. A. Peters, J. Huskens and D. J. Raber, *Prog. Nucl. Magn. Reson. Spectrosc.*, 1996, **28**, 283–350.
58. C. Görller-Walrand, E. Huygen, K. Binnemans and L. Fluyt, *J. Phys. Condens. Matter*, 1994, **6**, 7797–7812.
59. G. T. P. Charnock and I. Kuprov, *Phys. Chem. Chem. Phys.*, 2014, 20184–20189.
60. V. S. Mironov, Y. G. Galyametdinov, A. Ceulemans, C. Görller-Walrand and K. Binnemans, *Chem. Phys. Lett.*, 2001, **345**, 132–140.
61. V. S. Mironov, Y. G. Galyametdinov, A. Ceulemans, C. Görller-Walrand and K. Binnemans, *J. Chem. Phys.*, 2002, **116**, 4673–4685.

62. R. S. Dickens, D. Parker, J. I. Bruce and D. J. Tozer, *Dalton Trans.*, 2003, 1264.
63. K. L. Gempf, S. J. Butler, A. M. Funk and D. Parker, *Chem. Comm.*, 2013, **49**, 9104–9106.
64. K. Binnemans and C. Görller-Walrand, *C. Chem. Phys. Lett.*, 1995, **245**, 75–78.
65. C. Görller-Walrand and K. Binnemans, in *Handbook on the Physics and Chemistry of Rare Earths*, eds. K. A. Gschneider Jnr. and Eyring, Elsevier, 1996, vol. 23, pp. 121–283.
66. D. J. Newman and Ng, *Crystal Field Handbook*, Cambridge University Press, Cambridge, 2000.
67. C.-K. Duan and P. A. Tanner, *J. Phys. Chem. A*, 2010, **114**, 6055–6062.
68. J.-G. Kang and T.-J. Kim, *Bull. Korean Chem. Soc.*, 2005, **26**, 1057–1064.
69. B. R. McGarvey, *J. Magn. Reson.*, 1979, **33**, 445–455.
70. J. Keeler, *Understanding NMR Spectroscopy*, John Wiley & Sons Ltd., Chichester, 2005.
71. L. P. Hwang and J. H. Freed, *J. Chem. Phys.*, 1975, **63**, 4017–4025.
72. M. R. Goldman, *J. Magn. Reson.*, 2001, **149**, 160–187.
73. M. Gueron, *J. Magn. Reson.*, 1969, **19**, 58–66.
74. I. Soloman, *Phys. Rev.*, 1955, **99**, 559–565.
75. N. Bloembergen, *J. Chem. Phys.*, 1957, **27**, 572–573.
76. S. Aime, M. Botta, Z. Garda, B. E. Kucera, G. Tireso, V. G. Young and M. Woods, *Inorg. Chem.*, 2011, **50**, 7955.
77. C. S. Zuo, A. Mahmood and A. D. Sherry, *J. Magn. Reson.*, 2001, **151**, 101–106.
78. H. Gysling and M. Tsutsui, *Adv. Organomet. Chem.*, 1971, **9**, 361–395.
79. B. Alsaadi, F. Rossotti and R. J. P. Williams, *J. Am. Chem. Soc., Dalton Trans.*, 1980, 2151–2154.
80. S. Aime, L. Barbero, M. Botta and G. Ermondi, *J. Am. Chem. Soc., Dalton Trans.*, 1992, 225–228.
81. I. Bertini, P. Turano and A. Vila, *Chem. Rev.*, 1993, **93**, 2833–2932.
82. A. M. Funk, P. H. Fries, P. Harvey, A. M. Kenwright and D. Parker, *J. Phys. Chem. A*, 2013, **117**, 905–917.
83. P. H. Fries and E. Belorizky, *J. Chem. Phys.*, 2012, **136**, 074513.
84. P. Harvey, A. M. Blamire, I. Wilson, K.-L. N. A. Finney, A. M. Funk, P. K. Senanayake and D. Parker, *Chem. Sci.*, 2013, **4**, 4251–4258.
85. J. P. L. Cox, K. J. Jankowski, R. Kataky, D. Parker, N. R. A. Beeley, B. A. Boyce, M. A. W. Eaton, K. Millar, A. T. Millican, A. Harrison and C. Walker, *J. Chem. Soc., Chem. Commun.*, 1989, 797–798.
86. S. Aime, M. Botta, M. Fasano, E. Terreno, P. Kinchesh, L. Calabi and L. Paleari, *Magn. Reson. Imaging*, 1996, **35**, 648–651.
87. S. Aime, M. Botta, L. Milone and E. Terreno, *Chem. Comm.*, 1996, 1265–1266.
88. T. Frenzel, K. Roth, S. Kossler, B. Raduchel, H. Bauer, J. Platzek and H.-J. Weinmann, *Magn. Reson. Med.*, 1996, **35**, 364–369.
89. K. Roth, G. Bartholomae, H. Bauer, T. Frenzel, S. Kossler, J. Platzek, B. Raduchel and H.-J. Weinmann, *Angew. Chem. Int. Ed. Engl.*, 1996, **35**, 655–657.
90. S. K. Pakin, S. K. Hekmatyar, P. Hopewell, A. Babsky and N. Bansal, *NMR Biomed.*, 2006, **19**, 116–124.
91. S. K. Hekmatyar, P. Hopewell, S. K. Pakin, A. Babsky and N. Bansal, *Magn. Reson. Med.*, 2005, **53**, 294–303.
92. D. Coman, H. K. Trubel, R. E. Rycyna and F. Hyder, *NMR Biomed.*, 2009, **22**, 229–239.

93. H. K. Trubel, P. K. Maciejewski, J. H. Faber and F. Hyder, *J. Appl. Physiol.*, 2003, **91**, 1641–1649.
94. R. Schmidt, N. Nippe, K. Strobel, M. Masthoff, O. Reifschneider, D. D. Castelli, C. Holtke, S. Aime, U. Karst, C. Sunderkotter, C. Bremer and C. Faber, *Radiol.*, 2014, **272**, 785–795.
95. M. Milne and R. H. E. Hudson, *Chem. Comm.*, 2011, **47**, 9194–9196.
96. Y. Yang, D. T. Schuhle, G. Dai, J. K. Alford and P. Caravan, *Contrast Media Mol. Imaging*, 2012, **7**, 276–279.
97. S. Aime, R. Nano and M. Grandi, *Invest. Radiol.*, 1998, **23**, 267–270.
98. K. M. Ward, A. H. Aletras and R. S. Balaban, *J. Magn. Reson.*, 2000, **143**, 79–87.
99. S. Aime, A. Barge, D. D. Castelli, F. Fedeli, A. Mortillaro, F. U. Nielsen and E. Terreno, *Magn. Reson. Med.*, 2002, **47**, 639–648.
100. S. Zhang, P. Winter, K. Wu and A. D. Sherry, *J. Am. Chem. Soc.*, 2001, **123**, 1517–1518.
101. Patent no. US20020127182 A1, 2002.
102. S. Zhang, M. Merritt, D. E. Woessner, R. E. Lenkinski and A. D. Sherry, *Acc. Chem. Res.*, 2003, **36**, 783–790.
103. A. X. Li, F. Wojciechowski, M. Suchy, C. K. Jones, R. H. E. Hudson, R. S. Menon and R. Bartha, *Magn. Reson. Med.*, 2008, **59**, 374–381.
104. N. McVicar, A. X. Li, M. Suchy, R. H. E. Hudson, R. S. Menon and R. Bartha, *Magn. Reson. Med.*, 2013, **70**, 1016–1025.
105. G. S. Liu, Y. G. Li, V. R. Sheth and M. D. Pagel, *Mol. Imaging*, 2012, **11**, 47–57.

Chapter Two: Parent ^{1}H PARASHIFT Probes

2.1 Introduction

The criteria at the end of *Chapter 1* outline key requirements for the design of PARASHIFT probes for ^{1}H MRS studies. Fundamentally, the shift of the ^{1}H reporter group needs to be well removed from the diamagnetic spectral window in order for it to be selectively imaged in ^{1}H MRS *in vivo* studies. In order to utilise practicable imaging pulse sequences, a spectral width of more than 20 kHz is required, and therefore the observed resonance must occur at least 10 kHz away from the water or fat signals.[1] Consequently, a shift of < -34 ppm or > +44 ppm is essential, at a magnetic field of 7 T. Bleaney's 40-year-old theory of magnetic anisotropy remains the most commonly used approximation for predicting paramagnetic lanthanide(III) induced shifts, and describes them in terms of the nature of the lanthanide(III) ion (C_J), the positioning of the reporter group (r, θ, φ) and the ligand field, assessed by the second order crystal field terms B_0^2 and B_2^2.[2]

Additionally, to enhance sensitivity in MRS protocols, the ^{1}H reporter group must still possess the required relaxation characteristics such that R_1 is in the 100 to 200 Hz range at 7 T, and minimal line broadening occurs so that the R_1/R_2 ratio is close to unity. The Solomon-Bloembergen-Morgan (SBM) equations,[3–5] derived from Bloch-Redfield-Wangsness (BRW) theory,[6] model the relaxation rates as a function of the distance between the lanthanide(III) ion and the ^{1}H reporter nuclei, r, the magnetic moment of the lanthanide(III) ion, μ_{eff}, the rotational correlation time of the complex, τ_r, and the electronic longitudinal relaxation time, T_{1e}. The steep r^{-6} dependence for both R_1 and R_2 means that strategic placement of the reporter group is a balance between being sufficiently close to induce sufficient R_1 enhancement, but not so close such that R_2 increases and too much line broadening occurs. Furthermore, the number of magnetically equivalent nuclei in the ^{1}H reporter group must be optimised, and one stereoisomeric complex must be preferred in solution, so that one large signal dominates the ^{1}H NMR spectrum.

With this background in mind, three target parent structures of ^{1}H PARASHIFT probes have been designed (*Figure 2.0*). Each system possesses a *tert*-butyl reporter group, since it introduces the maximum amount of equivalent spin density, and is based on a

macrocyclic 12-N_4-based ligand framework. Related work in the area estimates lanthanide(III) ion-reporter nuclei distances of about 6.5 Å, following inclusion of a reporter group on the *meta*-position of a coordinated pyridyl moiety.[7] The tri-carboxylate system, **[Ln.L^{1}(H$_2$O)]**, is in keeping with the design of many DO3A derivatives and as a result, presents the most straightforward synthetic route. Substitution of one carboxylate arm for a *tert*-butyl labeled pyridyl moiety to yield the C_2-symmetric system, **[Ln.L^{2}(H$_2$O)]$^{+}$**, has two added benefits: first, the resulting cationic nature will influence its biodistribution; second, the signal intensity of the ^{1}H reporter group will be doubled, providing that the *tert*-butyl groups are equivalent. Changing the chelating arms from carboxylate to phosphinate affords the PMe_3 parent system, **[Ln.L^{3}]**. Recent advances that incorporate such a structural change, have seen a reporter signal change from representing 50% of the total signal intensity, with carboxylate arms, to 87%, with the more sterically demanding phosphinate arms; along with remarkably large shift enhancements.[8]

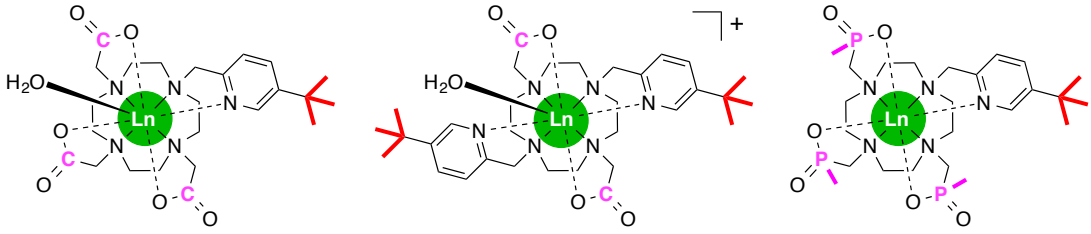

Figure 2.0 The target parent ^{1}H PARASHIFT probes: the model system, **[Ln.L^{1}(H$_2$O)]** (*left*); the C_2-symmetric system, **[Ln.L^{2}(H$_2$O)]$^{+}$** (*middle*) and the phosphinate system, **[Ln.L^{3}]** (*right*).

2.2 A Model Probe: The Tri-carboxylate Parent System

2.2.1 Synthetic procedure

The 12-N_4-based macrocyclic platform was synthesised following a literature method, using *tert*-butyl bromoacetate to alkylate 1,4,7,10-tetraazacyclododecane (cyclen) (*Scheme 2.0*).[9] Recrystallisation of the sticky residue, from toluene, yielded the target tri-carboxylate compound, ***1***, as a white solid.

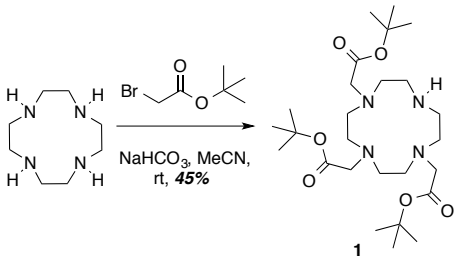

Scheme 2.0 General procedure for the synthesis of the 12-N_4-based macrocyclic platform, ***1***.

The synthesis of the *tert*-butyl labeled pyridyl moiety, ***5***, began with the introduction of the *tert*-butyl reporter group (*Scheme 2.1*), using a procedure adapted from the work of Bell and co-workers.[10,11] A small amount of copper(I) cyanide was required to catalyse the reaction between *tert*-butyl magnesium chloride and 5-bromo-2-methylpyridine, in THF. However, this procedure continually resulted in poor yields due to loss of the volatile product, ***2***, when removing THF under reduced pressure. In seeking to improve the procedure, diethyl ether was added to the solvent mixture, and losses were minimised by continuing the synthesis with ***2*** as a crude mixture. Subsequent oxidation of the pyridine ring nitrogen was achieved using *m*CPBA, and isolation of the *N*-oxide, ***3***, was achieved following purification by silica gel column chromotography.

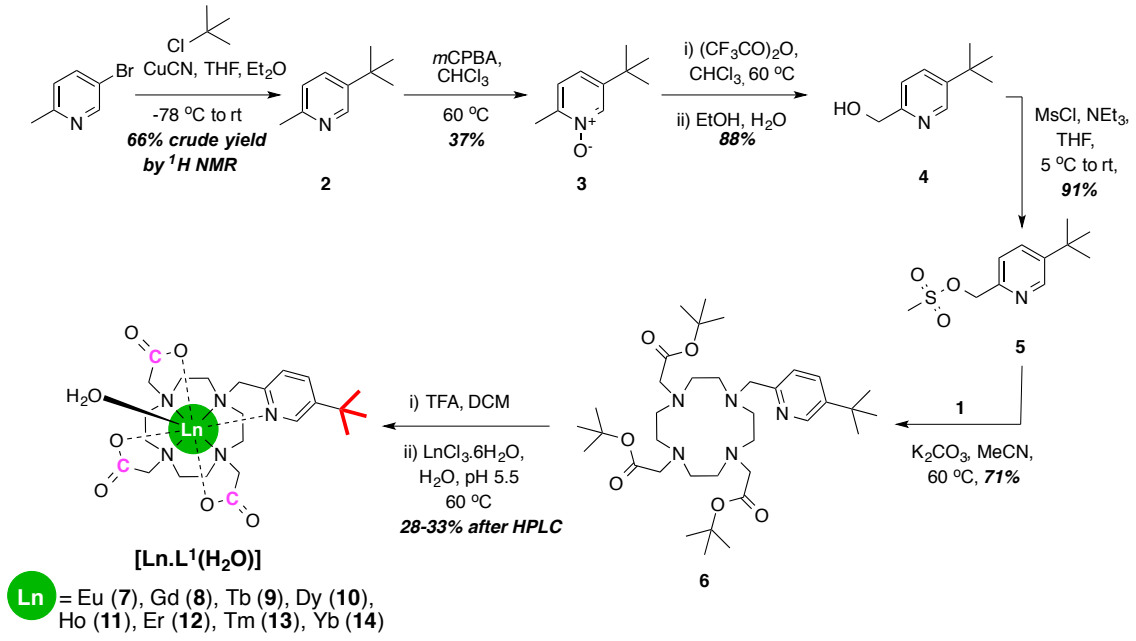

Scheme 2.1 General procedures for the synthesis of the model parent ^{1}H PARASHIFT probes, **[Ln.L^{1}(H$_2$O)]**, ***7-14***.

Treatment of the *N*-oxide, ***3***, with trifluoroacetic anhydride induced a [3,3]-sigmatropic shift, resulting in the formation of a trifluoroacetate ester intermediate, identifiable by both ^{1}H and ^{19}F NMR spectroscopy. Clean ester hydrolysis was performed *in situ*, using a 1:1 mixture of ethanol and water, and the identity of the desired alcohol, ***4***, was confirmed by a shift to lower frequency of the CH_2 resonance in the ^{1}H NMR spectrum (*Figure 2.1*). Nucleophilic substitution between the alcohol and methane sulfonyl chloride, in the presence of triethylamine, led to the formation of the mesylate precursor, ***5***.

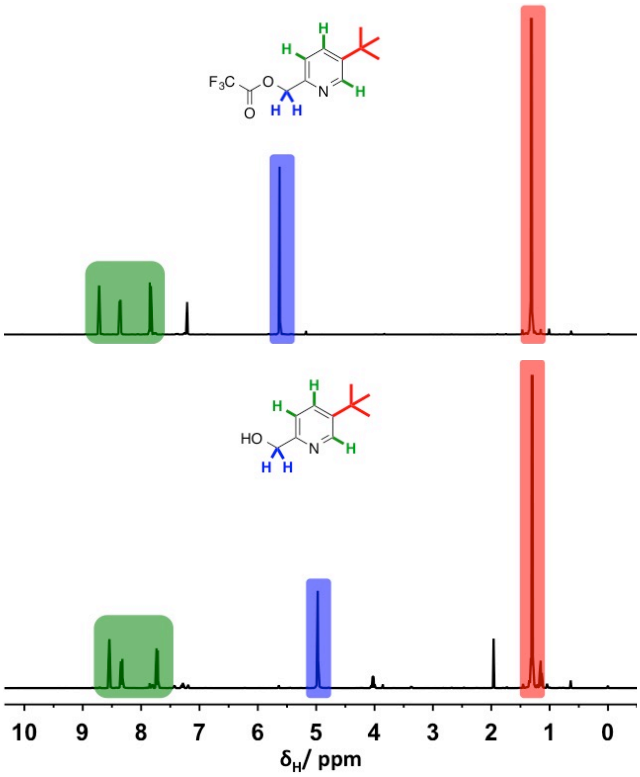

Figure 2.1 ^{1}H NMR spectrum of the trifluoroacetate intermediate (*top*) and the alcohol compound, ***4*** (*bottom*) showing the change in shift of the allylic CH_2 resonance (*blue*) ($CDCl_3$, 295 K, 9.4 T).

To avoid decomposition, the mesylate ***5*** was used immediately, in the *N*-alkylation of the secondary amine on ***1***. Purification by silica gel column chromatography allowed isolation of the protected ligand, ***6***. Removal of the *tert*-butyl protecting groups was achieved using a dilute mixture of trifluoroacetic acid and dichloromethane, and the resulting TFA salt was complexed in aqueous solution, held at pH 5.5, using the appropriate hydrated lanthanide(III) chloride. Preparative reverse-phase HPLC purification yielded the desired series of complex, **[Ln.L^{1}(H$_2$O)]**, where Ln = Eu to Yb (***7-14***).

2.2.2 Characterisation of the complexes

Firstly, the purity of each complex was assessed by analytical reverse-phase HPLC. Complexes ***7-14*** possessed one peak in the UV chromatogram (268 nm), with retention times (t_R) ranging between 8.3 and 9.3 min (*Figure 2.2* shows **[Yb.L^{1}(H$_2$O)]**). It is expected that an isostructural series of complexes, such as this, should exhibit similar retention times.

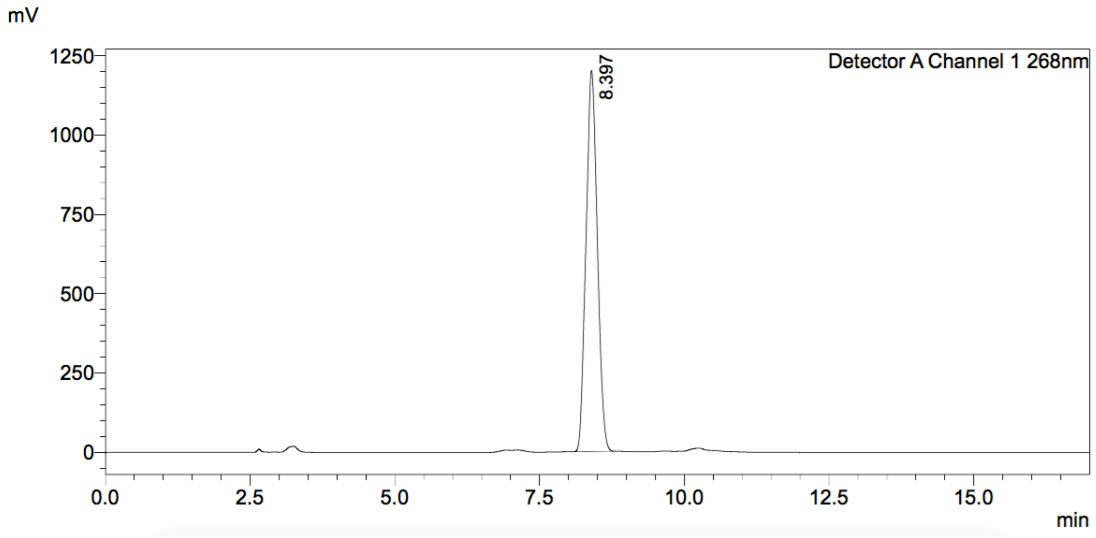

Figure 2.2 Observed analytical reverse-phase HPLC UV chromatogram of **[Yb.L^{1}(H$_2$O)]** (λ= 268 nm, 10-100% MeOH+0.1% formic acid in H_2O+0.1% formic acid over 10 min, t_R=8.4 min).

Secondly, the identity of the desired complexes was confirmed by low-resolution electrospray and high-resolution mass spectrometry, aided by the fact that each lanthanide possesses a distinctive isotope pattern. In each case, a characteristic isotope pattern was observed for complexes ***7-14*** (*Figure 2.3* shows the observed $[M+H]^+$ pattern for **[Dy.L^{1}(H$_2$O)]**), which corresponded well to their simulated isotope patterns (errors ≤ 5 ppm).

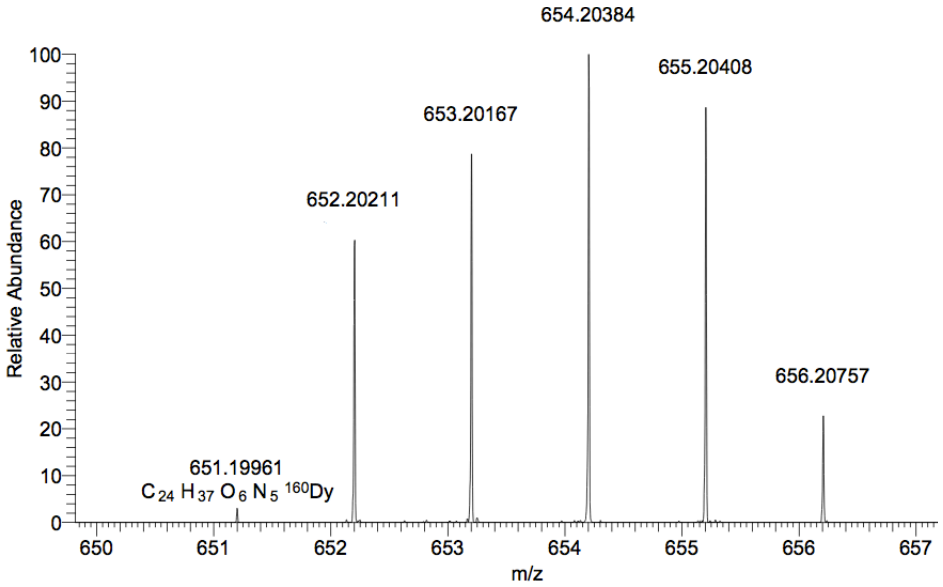

Figure 2.3 Observed ESI-HRMS (+) spectrum of **[Dy.L^{1}(H$_2$O)]**; where $[C_{24}H_{37}O_6N_5{}^{160}Dy]^+$ requires 651.1990, found 651.1996, error 0.9 ppm.

The metal hydration state of a lanthanide(III) complex (q value) can be calculated by measuring the radiative lifetime of the emissive excited state, k, in both H_2O and D_2O.[12] The attenuation of the metal-based emission intensity over time will always occur more slowly in D_2O than in H_2O, due to inefficient energy transfer between the lanthanide(III) excited state and X-D oscillators, in comparison to X-H oscillators.[12] In the cases of Eu(III) and Tb(III), the energy gap between the emissive state and the highest lying electronic energy level of the ground state manifold corresponds to emission in the visible region of the electromagnetic spectrum (Eu: 12,300 ($^5D_0 \rightarrow {}^7F_6$); Tb: 14,800 cm^{-1} ($^5D_4 \rightarrow {}^7F_0$)).[13] Hence, the difference between the radiative lifetimes in H_2O and D_2O can be readily measured for Eu(III) and Tb(III) complexes and exploited when estimating the number of bound water molecules:[12]

$$q_{Eu} = 1.2\left(k_{H_2O} - k_{D_2O} - 0.25\right) \qquad (1)$$

$$q_{Tb} = 5\left(k_{H_2O} - k_{D_2O} - 0.06\right) \qquad (2)$$

where k_{H_2O} and k_{D_2O} are the rate constants for the depopulation of the lanthanide(III) emissive excited state in each solvent (derived as the reciprocals of the luminescence lifetimes of the complex in each solvent, τ_{H_2O} and τ_{D_2O} respectively).

In order to calculate the q value, the decay of the lanthanide(III)-based emission intensity was initially recorded in H_2O, and subsequently in D_2O, following two cycles of dissolving and removing D_2O under reduced pressure. In each case, a mono-exponential decay was observed, and rate constants for the depopulation of the lanthanide(III) emissive excited state were calculated for each complex in each solvent. Estimations of the hydration state for each of the complexes were obtained using *equations 1 and 2* (*Table 2.0*). Based on ample literature precedent, the suggestion that the complexes in the **[Ln.L^1(H$_2$O)]** series possess one bound water molecule is expected for such carboxylate-12-N$_4$-based systems.

Table 2.0 Experimentally determined radiative rate constants, k, and derived values of q (±20%) for **[Eu.L^{1}(H$_2$O)]** and **[Tb.L^{1}(H$_2$O)]** (295 K, pH 7.0).

[Ln.L^{1}(H$_2$O)]	k_{H_2O}/ **ms^{-1}**	k_{D_2O}/ **ms^{-1}**	q
Eu	1.39	0.40	0.9
Tb	0.69	0.40	1.2

The hydration state of a lanthanide(III) complex can also be estimated from the relaxivity of the Gd(III) complex, *i.e.* its ability to enhance ($1/T_1$) and ($1/T_2$) of proximal nuclei per unit concentration, denoted by r_{1p} or r_{2p} respectively.[14] The relationship in *equation 3* allows the relaxivity to be calculated following the measurement of the relaxation rate, provided that the concentration of Gd(III) is known.[14]

$$\frac{1}{T_{i,obs}} = \frac{1}{T_{i,d}} + r_{i,p}[Gd(III)] \quad \text{where } i = 1, 2 \quad (3)$$

Relaxivity is most commonly used as a direct measure of the ability of a contrast agent to increase the rate of relaxation of the bulk water, where a large r_{1p} value denotes good image contrast. The presence of Gd(III) creates a strong local magnetic field, which interacts with the water proton nuclear spins to provide three relaxation mechanisms. The total relaxivity is given by the sum of these contributions in *equation 4*.[14,15] The first is inner-sphere relaxation (IS), and relates to relaxation enhancements due to the water molecule that is bound in the first coordination sphere of the Gd(III) ion (*Figure 2.4*). If this water molecule is in fast exchange, k_{ex}, with the bulk outer-sphere (OS) water then propagation of the magnetic field interaction ensues and relaxivity is increased. As a result, relaxivity values are much higher when there is a bound water molecule on the Gd(III) complex (*i.e.* such that q = 1) and so provides a method for estimating the q value.

$$r_{ip} = \left(r_{i,p}\right)^{IS} + \left(r_{i,p}\right)^{OS} + \left(r_{i,p}\right)^{SS} \quad \text{where } i = 1, 2 \quad (4)$$

The other two contributions are not considered when approximating the complex hydration state because they relate to outer-sphere (OS) and second-sphere (SS) effects, and are beyond the scope of this work as a result.

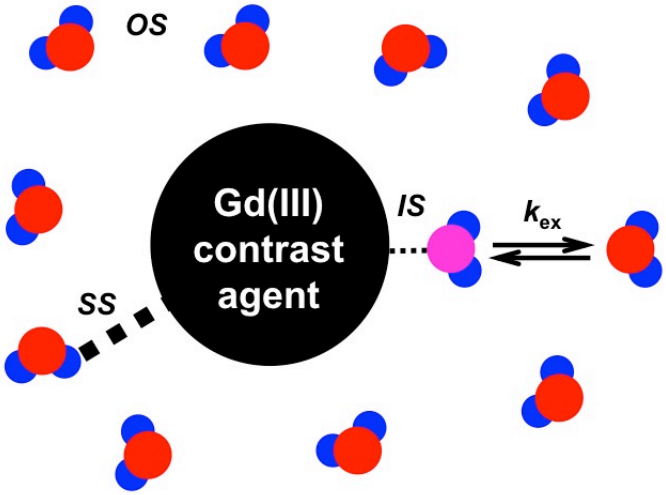

Figure 2.4 Schematic representation of a Gd(III) contrast agent in the presence of water, highlighting the inner-sphere (IS), outer-sphere (OS) and second-sphere (SS) relaxation mechanisms, where k_{ex} is the exchange between the coordinated IS water and the bulk OS water.

Using *equation 3*, the relaxivity of **[Gd.L^{1}(H$_2$O)]** was calculated to be 4.8±0.01 mM^{-1} s^{-1}. Such a value is consistent with the presence of one bound water molecule, based on analysis of numerous related DO3A-based Gd(III) complexes.[15] This analysis also corroborates well with the *q* value obtained by previously measuring the radiative lifetimes of the Eu(III) and Tb(III) emissive excited states.

2.2.3 ^{1}H NMR studies: shift behaviour

An initial investigation into the chemical shift behaviour of the *tert*-butyl reporter group on each complex was carried out using ^{1}H NMR spectroscopy (*Figure 2.5*). In each case, the *tert*-butyl reporter group gave rise to a strong sharp resonance, shifted away from the ligand *tert*-butyl resonance (1.5 ppm). In three of the complexes, this resonance possessed the required shift outside of the diamagnetic range, with an observed shift over 20 ppm away from the endogenous signals *in vivo* for the Dy(III) complex (*Figure 2.5*).

However, in order to interpret the observed *tert*-butyl chemical shifts, it is necessary to recall the origins of the pseudocontact shift in paramagnetic lanthanide(III) complexes, as discussed in *Section 1.2.1.1*:

$$\Delta_p = \frac{C_J \mu_B{}^2}{60(kT)^2}\left[\frac{(3\cos^2\theta - 1)}{r^3}B_0^2 + \frac{(\sin^2\theta\cos 2\varphi)}{r^3}B_2^2\right] \qquad (5)$$

where C_J is the Bleaney coefficient characteristic to each lanthanide(III) ion, μ_B is the Bohr magneton, $\{\theta \text{ and } \varphi\}$ are the angles between the nucleus and the lanthanide(III) ion, r is the distance between the nucleus and the lanthanide(III) ion; and B_0^2 and B_2^2 are second order crystal field parameters.

For an isostructural series of lanthanide(III) complexes, Bleaney theory assumes that the ligand crystal field is lanthanide(III) ion independent and invariant across the series. Therefore, if each ^{1}H NMR spectrum is acquired at the same temperature, it is expected that the resonant frequency of a given nucleus on each complex will be almost entirely determined by the respective Bleaney coefficients, since the spherical coordinates and the distance should remain relatively unchanged. The ^{1}H NMR spectra for complexes ***9-14*** are shown superimposed in *Figure 2.5*.

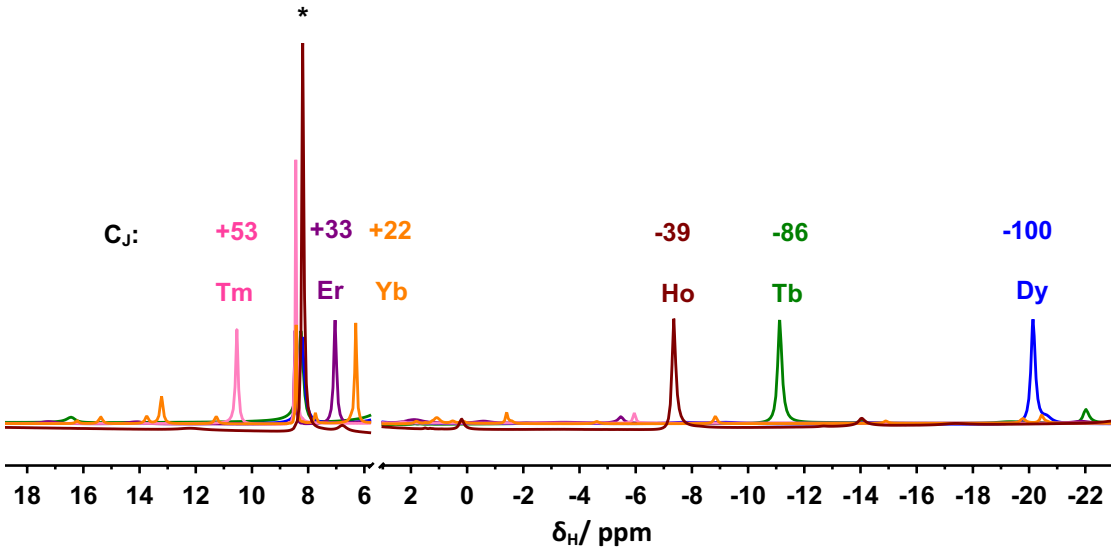

Figure 2.5 Superimposed ^{1}H NMR spectra of C_3 parent complexes, **[Ln.L^{1}(H$_2$O)]**, highlighting the shift in the *tert*-butyl reporter resonance for Ln = Tm, Er, Yb, Ho, Tb and Dy (D_2O, 9.4 T, 295 K), with respect to the corresponding Bleaney coefficients (C_J). The solvent water peak is omitted for clarity and * represents residual formate from HPLC purification and neutralisation.

Following this analysis, it is evident that the chemical shift behaviour of the *tert*-butyl group follows the sign and magnitude of the Bleaney coefficients, with positive C_J values shifting to higher frequency and negative C_J values shifting to lower frequency. The Dy(III) and Tm(III) complexes display the largest shifts in opposite directions, with the Dy(III) *tert*-butyl resonating at -20.1 ppm (C_J = -100) and the Tm *tert*-butyl resonating at +10.5 ppm (C_J = +53). Whilst the shifts show a reasonable agreement to the relative ordering predicted by the Bleaney coefficients, the magnitude does not fit to a linear trend, with the Tb(III) complex being the biggest outlier (*Figure 2.6*). It has

been previously noted that Bleaney theory has limited applicability,[16,17] and so a few more parameters need to be assessed for the **[Ln.L^{1}(H$_2$O)]** series, in order to gain a wider understanding.

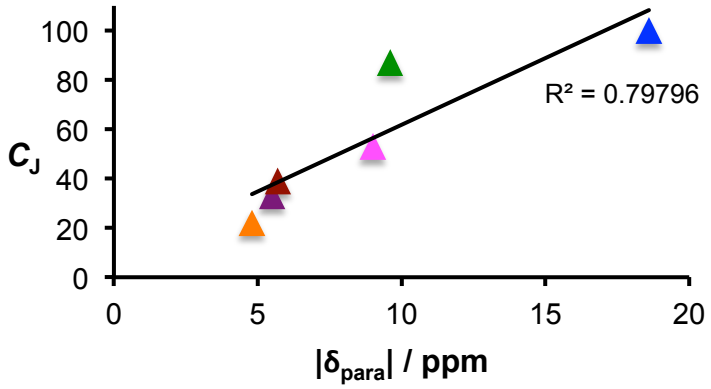

Figure 2.6 Relationship between the magnitude of the paramagnetic shift, $|\delta_{para}|$, of the *tert*-butyl reporter resonance for **[Ln.L^{1}(H$_2$O)]** and the Bleaney coefficients for each lanthanide(III) ion. *N.B.* All signs are positive for clarity, $|\delta_{para}|$ is estimated by assuming the diamagnetic complex has a shift of 1.5 ppm and the line shown is a line of best-fit to the data.

The temperature inside the NMR spectrometer was measured accurately after the acquisition of each NMR spectrum, using an ethylene glycol standard reference solution. Although, the distance between the lanthanide(III) ion and the *tert*-butyl reporter group, *r*, is likely to decrease slightly as a result of the lanthanide contraction, this variation would not contribute significantly to the overall shift (<0.05 Å across the series for the later lanthanide(III) ions).[18] The polar coordinates, $\{\theta \text{ and } \varphi\}$, cannot be properly alluded to without crystal structure information and knowledge of the principal axis.

The assumption in Bleaney's theory that the crystal field is constant for an isostructural series of lanthanide(III) complexes is not appropriate for many lanthanide(III) complexes. Research by Gruber and co-workers proved this, reporting an increase in B_0^2 and a decrease in B_2^2 from Tb(III) to Yb(III), for lanthanide(III) ions occupying the C_{3i} sites of Y_2O_3.[19] Owing to the work postulated by Binnemans, it is possible to roughly quantify B_0^2 by analysing the splitting in the $\Delta J = 1$ band in the Eu(III) emission spectrum.[20] Thus, the splitting of the $\Delta J = 1$ manifold was estimated for **[Eu.L^{1}(H$_2$O)]**, giving a B_0^2 value equal to -500 cm^{-1} (*Figure 2.7*). This value is comparable to related lanthanide(III) complexes, and provides further evidence to

nullify another assumption of Bleaney's theory that the crystal field terms are much smaller than k_BT (205 cm^{-1} at 295 K, addressed in *Section 1.2.1.1*). Further inspection of the Eu(III) emission spectrum, shows 3 bands in the $\Delta J = 1$ manifold, implying that the E states are not degenerate. Such behaviour is not surprising when the low symmetry of the **[Ln.L^1(H$_2$O)]** complex series is considered, leading to a significant error margin when estimating the crystal field splitting.

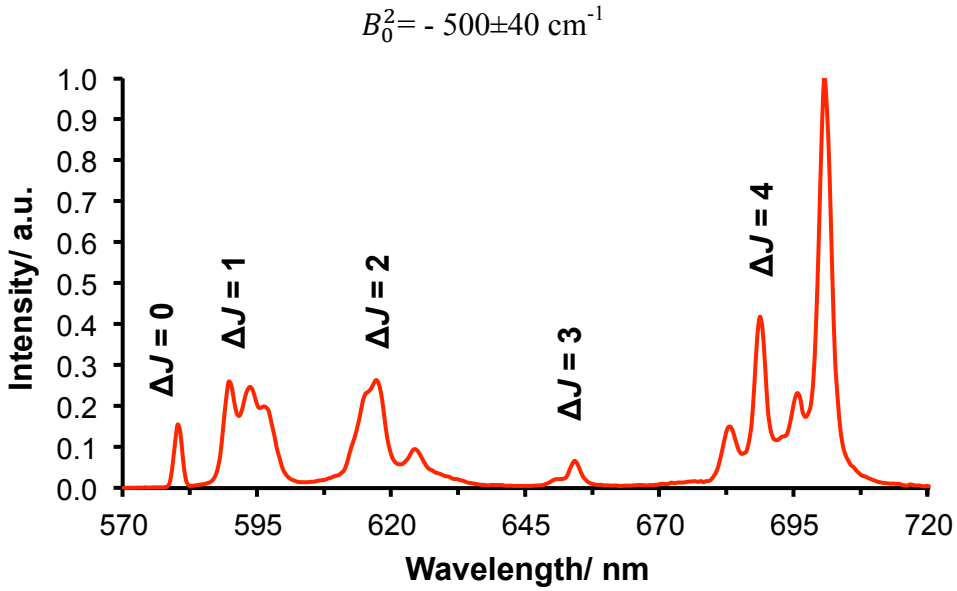

Figure 2.7 Emission spectrum of **[Eu.L^1(H$_2$O)]** (D$_2$O, 295 K, λ_{exc}= 270 nm), analysis of the $\Delta J = 1$ manifold at 590-595 nm allows the crystal field splitting parameter, B_0^2, to be estimated.

Yb(III) complexes, possess relatively sharp and well defined ^{1}H NMR spectra, although they do not allow considerable shifts to be achieved for the PARASHIFT work in this thesis. As a result, the ^{1}H NMR spectrum of **[Yb.L^1(H$_2$O)]** has been fully assigned, using relaxation rate data and a structurally related example as a guide (*Figure 2.8*).[21]

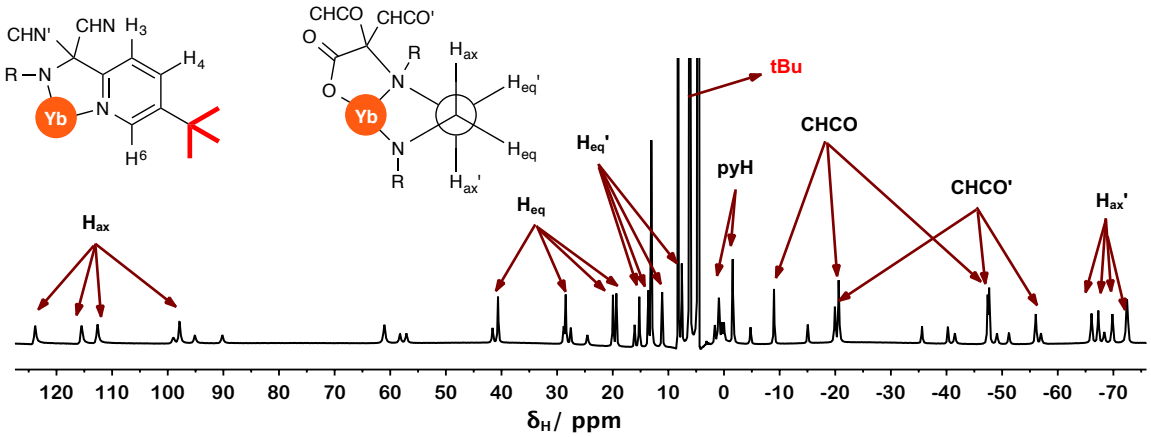

Figure 2.8 Annotated ^{1}H NMR spectrum of **[Yb.L^1(H$_2$O)]** (D$_2$O, 9.4 T, 295 K). The unassigned resonances correspond to the minor isomer, with twisted-square antiprismatic geometry.

The occurrence of isomers in solution can be seen from the ^{1}H NMR spectrum of **[Yb.L^{1}(H$_2$O)]**, and is a phenomenon expected for these pyridyl-based systems. The presence of isomers is not problematic, providing one species exists preferentially. This is indeed the case, with the major *tert*-butyl resonance accounting for over 80% of the observed signal intensity in each case.

There are two main elements of chirality for systems based on the complex **[Ln.DOTA(H$_2$O)]$^{-}$**, associated with the NCCN and NCCO chelate rings (*Figure 2.9*).[22,23] Each NCCN ring can have a torsion angle of +60° or -60°, denoted by δ and λ respectively. Similarly, each NCCO ring can have a torsion angle of *ca.* +30° or -30°, corresponding to Δ and Λ respectively. As a result, the occurrence of four stereoisomers is possible in solution. The larger lanthanide(III) ions typically adopt square antiprismatic (SAP) geometries whereas, the smaller lanthanide(III) ions form twisted-square antiprisms (TSAP).[22,23] Such a trend across the series is a result of the ligand twisting in conformation to accommodate the smaller metal. As a result, it is thought that the isomers of **[Dy.L^{1}(H$_2$O)]** are SAP and **[Tm.L^{1}(H$_2$O)]** are TSAP.

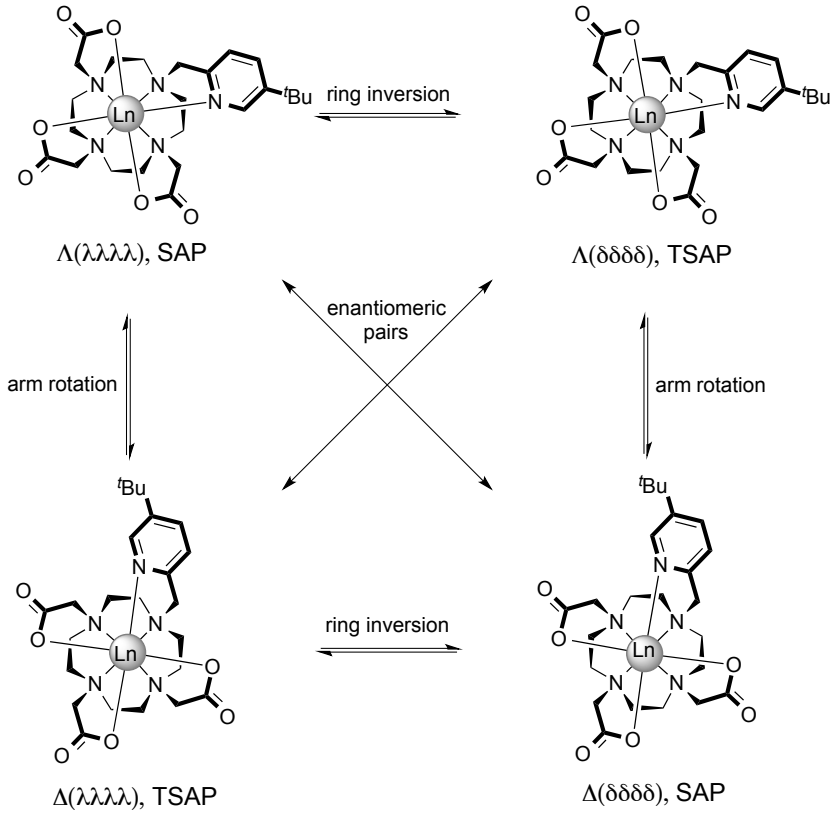

Figure 2.9 Schematic representation of the coordination geometries adopted by DOTA-based complexes, *e.g.* **[Ln.L^{1}(H$_2$O)],** through arm rotation and ring inversion: mono-capped square anti-prism (SAP) and twisted square anti-prism (TSAP). The bound water molecule has been omitted for clarity.

From this shift behaviour analysis, it can be surmised that **[Dy.L^{1}(H$_2$O)]** is a good candidate for a ^{1}H PARASHIFT probe. It possesses a *tert*-butyl shift that is over 20 ppm away from the biological window and should permit selective imaging. However, the relaxation behaviour must also be assessed before conclusions can be drawn concerning the suitability of this complex as a ^{1}H PARASHIFT probe for MRS applications.

2.2.4 ^{1}H NMR studies: relaxation behaviour

The longitudinal relaxation rate, R_1, for the major *tert*-butyl resonance of **[Ln.L^{1}(H$_2$O)]** was obtained using the inversion-recovery pulse sequence, at 6 different field strengths (*Table 2.1*). The complex characteristics detailed in *Section 2.1* stressed the importance of paramagnetic relaxation enhancement, with desired R_1 values of the order of 100 to 200 s^{-1} at 7 T. It is evident from this data, that R_1 exhibits the expected increase with increasing field, with enhancements most pronounced for the Dy(III) and Tb(III) complexes. In the case of Dy(III), the R_1 value falls into the desired range.

Table 2.1 Experimental longitudinal relaxation rate data for the major *tert*-butyl resonance of **[Ln.L^{1}(H$_2$O)]** at different magnetic field strengths (D_2O, 295 K[a]).

Ln	**R_1/ s^{-1} (± error)**						**R_1/R_2[b] (9.4 T)**
	1.0 T	**4.7 T**	**9.4 T**	**11.7 T**	**14.1 T**	**16.4 T**	
Tb	56 (1)	72 (1)	104 (2)	128 (1)	146 (1)	169 (1)	0.59
Dy	55 (2)	73 (1)	124 (1)	149 (1)	170 (1)	210 (2)	0.56
Ho	28 (1)	45 (1)	89 (1)	118 (1)	144 (1)	169 (1)	0.58
Er	21 (1)	29 (1)	59 (1)	80 (1)	97 (1)	120 (1)	0.55
Tm	18 (2)	31 (1)	54 (1)	64 (1)	71 (1)	82 (1)	0.57
Yb	6.1 (0.5)	6.4 (0.1)	7.6 (0.3)	8.6 (0.1)	9.5 (0.1)	10.7 (0.1)	0.12

(a) Temperature was monitored accurately, calibrating against an ethylene glycol shift thermometer; (b) R_2 values were estimated as ($\pi \times \omega_{1/2}$), for a Lorentzian line fit.

The variations in the measured R_1 values are consistent with the magnitude predicted by the effective magnetic moments, μ_{eff}, listed on *page 21*. For example, the Dy(III) complex shows the largest R_1 enhancement, with a μ_{eff} value of 10.3 BM, whereas the

corresponding Yb(III) complex has the smallest R_1 enhancement, possessing a μ_{eff} value of 4.3 BM.

Another important property when considering PARASHIFT probes for imaging applications is the relationship between the longitudinal relaxation rate, R_1, and the transverse relaxation rate, R_2. An increase in the latter results in an increase in linewidth, so it is imperative this is kept to a minimum. Therefore, it is suggested that in order to maximise signal intensity, the R_1/R_2 ratio should be as close to unity as possible, bearing in mind that R_2 is always greater than R_1. Values for R_2 were estimated from the individual peak linewidths (at half-height), using a $\pi \times \omega_{1/2}$ relationship in a Lorentzian fit. The data in *Table 2.1* shows that the R_1/R_2 ratio is 0.6 for the **[Ln.L^1(H$_2$O)]** complexes, except for Yb(III). For a model system, this value is considered reasonable, but higher ratios have been reported for some other related CF_3-containing complexes and **[Tm.DOTMA]**$^-$.[8,24] The remarkably low value for Yb(III) can be attributed to the fast interconversion between the isomeric species in solution.

In 2009, Kuprov developed an iterative global minimisation algorithm allowing the fitting of experimental nuclear relaxation rates, measured at different fields.[25] The advantage of this is to enable the estimation of several useful parameters in the following SBM equation that are difficult to measure empirically *i.e.* μ_{eff}, T_{1e} and τ_r:[3–5]

$$R_1 = \frac{2}{15}\left(\frac{\mu_0}{4\pi}\right)^2 \frac{\gamma_N^2 \mu_{eff}^2}{r^6}\left[\frac{7\tau_{r+e}}{1+\omega_e^2\tau_{r+e}^2} + \frac{3\tau_{r+e}}{1+\omega_N^2\tau_{r+e}^2}\right] + \frac{2}{5}\left(\frac{\mu_0}{4\pi}\right)\frac{\omega_N^2\mu_{eff}^4}{(3kT)^2 r^6}\frac{3\tau_r}{1+\omega_N^2\tau_r^2} \quad (6)$$

where μ_0 is the vacuum permeability, γ_N is the gyromagnetic ratio of the nucleus, μ_{eff} is the effective magnetic moment, r is the electron-nuclear distance, τ_r is the rotational correlation time and ω_N is the nuclear Larmor frequency.

The algorithm uses a Levenberg-Marquardt minimisation technique, and allows individual parameters to be 'fixed' to a specified value. By fixing a parameter, and thereby eliminating it from the estimation process, the minimisation procedure is greatly simplified, but means that reliable values must be used. For example, the temperature is always a fixed value in this work (295 K) because it can be controlled and monitored accurately when acquiring an R_1 measurement. The data can be fitted for each lanthanide(III) complex individually (single resonance fitting) or on a global level with

a common resonance across an isostructural series (global fitting), *e.g.* the *tert*-butyl resonance in this work.

Using global minimisation methods for the complexes ***9-14*** simultaneously, the variation of experimental R_1 data with field has been used to estimate the distance between the lanthanide(III) ion and the *tert*-butyl reporter group, *r*.[26] Using fixed literature values of μ_{eff},[27] fitted data sets for each complex were allowed to converge to well-defined minima with an average r = 6.65±0.14 Å for the **[Ln.L^{1}(H$_2$O)]** series (*Table 2.2 and Figure 2.10*). This correlates well with the predicted Dy(III)-^{1}H reporter group distance range, proposed in *Section 1.2.2.2*, where simulations estimated *r* to be between 6 and 7 Å in order to achieve R_1 values of the order of 100 to 200 s^{-1}.

Table 2.2 Calculated values for *r* (Å) obtained through fitting of experimental R_1 values at 6 different magnetic fields[a] for **[Ln.L^{1}(H$_2$O)]** using a fixed value of μ_{eff}[b] (BM) (D$_2$O, 295 K).

[Ln.L^{1}(H$_2$O)]	**μ_{eff}/ BM**	***r*/ Å**
Tb	9.8	6.63±0.01
Dy	10.3	6.59±0.03
Ho	10.4	6.80±0.02
Er	9.4	6.68±0.01
Tm	7.6	6.35±0.02
Yb	4.3	6.34±0.01
	Average	**6.65**±0.14

(a) The fields are 1.0 T, 4.7 T, 9.4 T, 11.7 T, 14.1, 16.4 T; (b) μ_{eff} was fixed to literature values.[27]

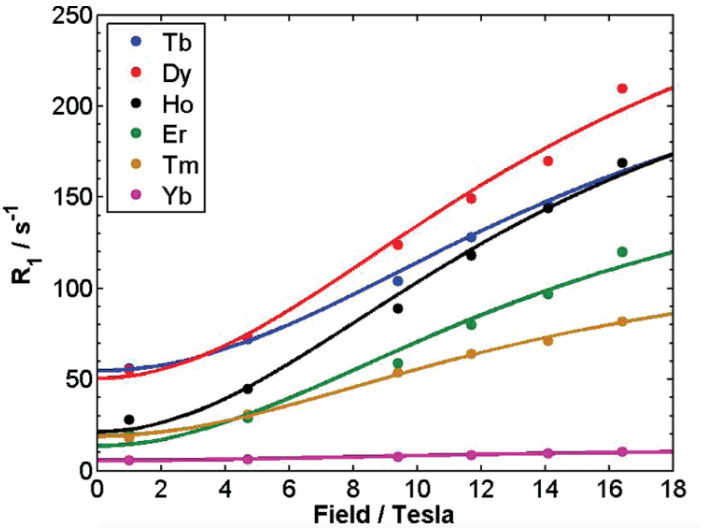

Figure 2.10 ^{1}H NMR relaxation rates, R_1/ s^{-1}, for the *tert*-butyl resonance on **[Ln.L^{1}(H$_2$O)]** as a function of magnetic field, showing the fits (*lines*) to the experimental data points (*circles*) (295 K, D_2O).

The distance between the lanthanide(III) ion and the protons of the *tert*-butyl reporter group was further verified by calculating optimised geometries using *ab initio* and DFT methods without symmetry constraints, based on the yttrium analogue of a published X-ray crystal structure (*Figure 2.11*), by Dr. Mark Fox.[7,28] A mean *r* of 6.62 Å was obtained, once again agreeing with the estimations proposed in *Section 1.2.2.2* for optimising the relaxation rates.

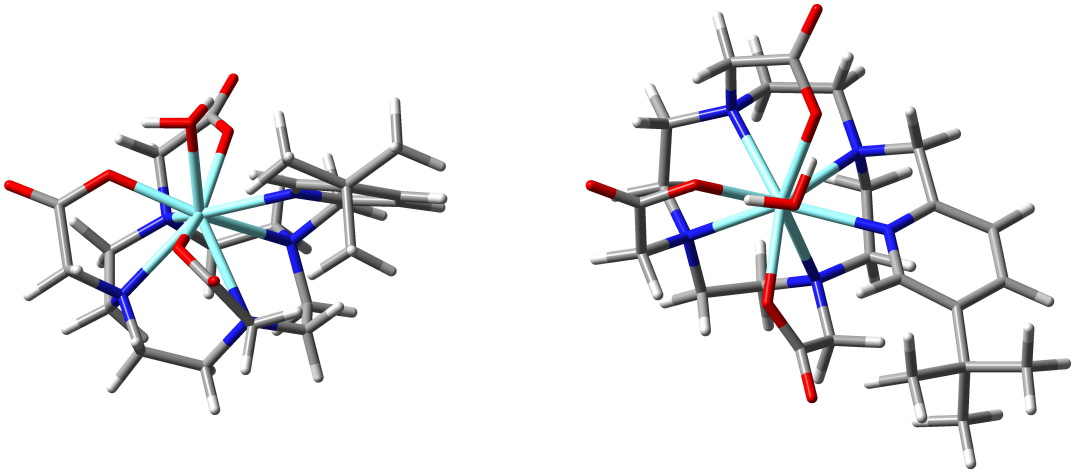

Figure 2.11 DFT optimised structure of **[Y.L^{1}(H$_2$O)]**; *left*, view in the plane of the pyridine ring; *right*, view looking on top of the pyridine ring.[28]

This relaxation behaviour analysis, further reinforces that the Dy(III) complex is a good ^{1}H PARASHIFT probe candidate from the **[Ln.L^{1}(H$_2$O)]** series, by fulfilling the criteria set out in *Section 2.1*. It possesses the required relaxation characteristics, with an R_1 of

the order of 100 to 200 s^{-1} at 7 T, and an R_1/R_2 ratio of 0.6, in addition to its favourable *tert*-butyl chemical shift, over 20 ppm away from the diamagnetic signals *in vivo*. However, while these results are encouraging from a model system point-of-view, it is clear that further sensitivity improvements are required before *in vivo* protocols can be considered. Firstly, the observed R_1 is at the lower end of the 100 to 200 s^{-1} range at 7 T, and the R_1/R_2 ratio is lower than for related examples. It is also proposed that the shift enhancement can be improved upon, given that the further away the reporter resonance is from the water and the fat signals, the better the sensitivity. By shortening the acquisition time, bigger bandwidths can be selected, *i.e.* 20 kHz rather than the 10 kHz demonstrated here. Also, due to its neutral charge it is thought that it will clear rapidly *via* the kidneys much like many of its ^{1}H PARASHIFT predecessors.[29–31]

2.3 Increasing the Signal Intensity: The Bis-carboxylate Parent System

Before *in vivo* studies can be contemplated, improvements to the **[Ln.L^{1}(H$_2$O)]** series are necessary, with both relaxation rate enhancements and signal intensity gains sought after. However, care must be taken to ensure minimal structural modification occurs so that many of the favourable characteristics from the model **[Ln.L^{1}(H$_2$O)]** series are retained. The design of the C_2-symmetric complex, **[Ln.L^{2}(H$_2$O)]$^{+}$** (*Figure 2.0*), was proposed to address these issues. First of all, it is predicted that the *tert*-butyl groups will be equivalent by C_2-symmetry, resulting in a single 18 proton reporter resonance. The structural similarities between the proposed system and **[Ln.L^{1}(H$_2$O)]** has two advantages: the shift and relaxation behaviour will be comparable, and the synthetic route only requires minor modification. The resulting mono-cationic character of the **[Ln.L^{2}(H$_2$O)]$^{+}$** series will undoubtedly have affects on the clearance rate and the biodistribution profile *in vivo*. Despite exchanging a negatively charged hard oxygen donor for a less strongly coordinating pyridyl nitrogen donor, the overall stability of the **[Ln.L^{2}(H$_2$O)]$^{+}$** series is expected to be comparable to the **[Ln.L^{1}(H$_2$O)]** series, as reported in literature.[32]

2.3.1 Synthesis and characterisation

The bis-substituted ligand framework was achieved using a series of protection and alkylation steps (*Scheme 2.2*). Firstly, selective trans-protection of cyclen was achieved under pH control using benzyl chloroformate, to afford compound ***15***, which was *N*-alkylated in the 4- and 10- positions using *tert*-butyl bromoacetate, to give the tetra-substituted macrocycle ***16***. The benzyl protecting groups were removed under high-

pressure hydrogenation over a $Pd(OH)_2/C$ catalyst, to afford the desired bis-substituted ligand framework ***17***, as reported in the literature.[33]

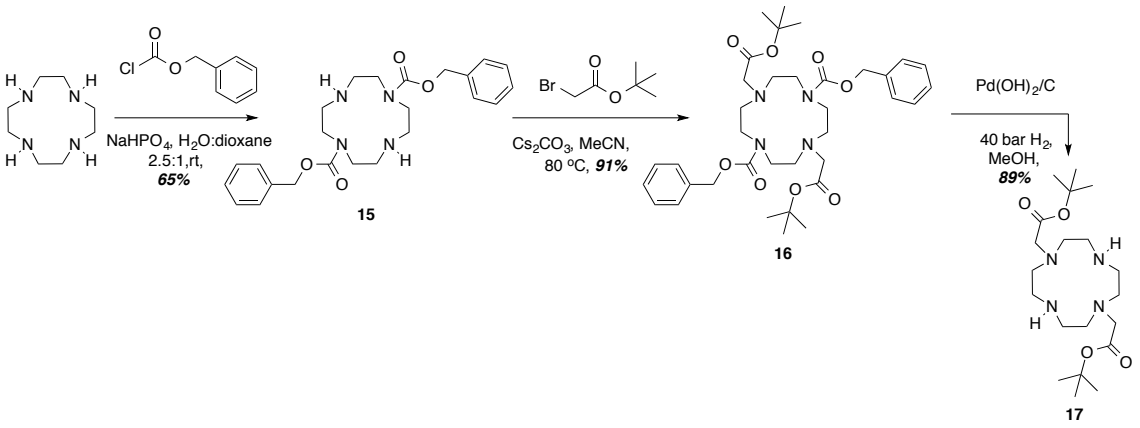

Scheme 2.2 General procedure for the synthesis of the bis-substituted ligand framework, ***17***.

Di-alkylation of the two free amine sites on ***17*** was undertaken, *Scheme 2.3*, using 2.5 equivalents of the previously synthesised mesylate precursor, ***5***. The desired tetra-alkylated ligand, ***18***, was separated from the tri-substituted ligand by silica gel column chromatography, albeit in modest yield. The ligand ***18*** was then deprotected using 6 M HCl to generate the acid salt of the deprotected ligand. Trifluoroacetic acid, used previously, is the obvious choice for the removal of *tert*-butyl protecting groups. However, concentrated HCl was favoured for the treatment of ***18***, since previous unpublished work showed that chloride salts are better tolerated *in vivo*. Complexation of the resulting ligand was achieved with the appropriate hydrated lanthanide(III) chloride, in an aqueous solution maintained at pH 5.5. Preparative reverse-phase HPLC purification yielded the desired series of complex, $\mathbf{[Ln.L^2(H_2O)]^+}$, where Ln = Eu to Yb (***19-26***).

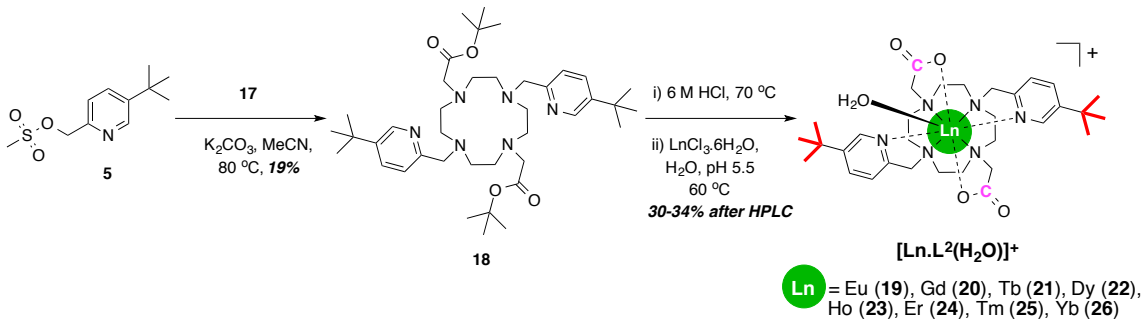

Scheme 2.3 General procedures for the synthesis of the C_2-symmetric parent ^{1}H PARASHIFT probes, $\mathbf{[Ln.L^2(H_2O)]^+}$, ***19-26***.

The purity of complexes ***19-26*** was assessed by analytical reverse-phase HPLC. For this series of complexes, the retention times ranged between 3.6 and 4.8 min. These markedly shorter retention times, compared to the **[Ln.L^{1}(H$_2$O)]** series (*ca.* 8.3 to 8.9 min), reflect an enhancement in the hydrophilicity due to the now cationic nature of the complexes. Again, the identity of the desired complexes was confirmed by high-resolution mass spectrometry, with each complex displaying a characteristic isotope pattern in agreement with the simulated isotope pattern.

The q value for the **[Ln.L^{2}(H$_2$O)]$^{+}$** series was estimated by measuring the radiative lifetimes of the Tb(III) and Eu(III) emissive excited states in H_2O and D_2O (*Table 2.3*) and by determining the relaxivity of the Gd(III) complex using *equation 3*. Both calculations indicated that the complexes in the **[Ln.L^{2}(H$_2$O)]$^{+}$** series possess one bound water molecule (r_{1p} = 5.8±0.02 mM^{-1} s^{-1}).

Table 2.3 Experimentally determined radiative rate constants, k, and derived values of q (±20%) for **[Eu.L^{2}(H$_2$O)]$^{+}$** and **[Tb.L^{2}(H$_2$O)]$^{+}$** (295 K, pH 7.0).

[Ln.L^{2}(H$_2$O)]$^{+}$	k_{H_2O}/ ms^{-1}	k_{D_2O}/ ms^{-1}	q
Eu	1.59	0.34	1.2
Tb	0.55	0.35	0.7

2.3.2 ^{1}H NMR studies: shift and relaxation behaviour

The chemical shift behaviour of the *tert*-butyl reporter group on each complex was analysed by ^{1}H NMR spectroscopy (*Figure 2.12*). Although the shifts appear comparable to those previously observed for the **[Ln.L^{1}(H$_2$O)]** series, closer inspection reveals that they are not quite as large. For example, the Tm(III) and Er(III) *tert*-butyl resonances occur 4 ppm closer to the water signal, at +6.2 ppm and +3.4 ppm, respectively. In three of the complexes, the resonance still possesses the required shift outside of the diamagnetic range, with the Dy(III) complex once again displaying the largest shift. Nevertheless, this resonance is also shifted closer to the water signal at -17.9 ppm, but still in an area of zero background signal *in vivo*.

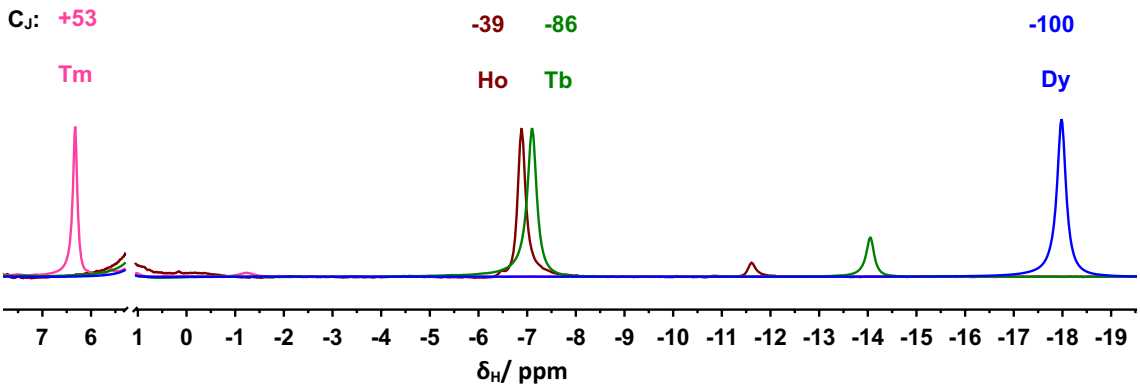

Figure 2.12 Superimposed ^{1}H NMR spectra of C_2-symmetric parent complexes, **[Ln.L^{2}(H$_2$O)]$^{+}$**, highlighting the shift in the *tert*-butyl reporter resonance for Ln = Tm, Ho, Tb and Dy (D_2O, 9.4 T, 295 K), with respect to the corresponding Bleaney coefficients (C_J). The solvent water peak and Er spectrum are omitted for clarity (Er *tert*-butyl is at +3.4 ppm).

In each case, one major isomer was observed which accounted for >90% of the observed signal intensity; an improvement on the **[Ln.L^{1}(H$_2$O)]** series (*ca.* >80%). Recent literature has demonstrated that a structurally similar Yb(III) complex bearing two pyridine carboxylate units exists as a TSAP in the solid-state, with slightly distorted C_2 symmetry.[32] Such information is consistent with the hypothesis that the isomers of **[Dy.L^{2}(H$_2$O)]$^{+}$** are SAP and **[Tm.L^{2}(H$_2$O)]$^{+}$** are TSAP, owing to the change in ligand framework conformation as it accommodates the smaller lanthanide(III) ion, as the series is traversed.

The chemical shift magnitude of the *tert*-butyl group was assessed in complexes ***21-25*** in terms of the Bleaney coefficients (*Figure 2.13*). Once again, the shifts showed a reasonable agreement with the relative ordering predicted by the Bleaney coefficients but failed to fit to a linear trend, with the Tb(III) and Ho(III) complexes displaying unexpectedly similar shifts.

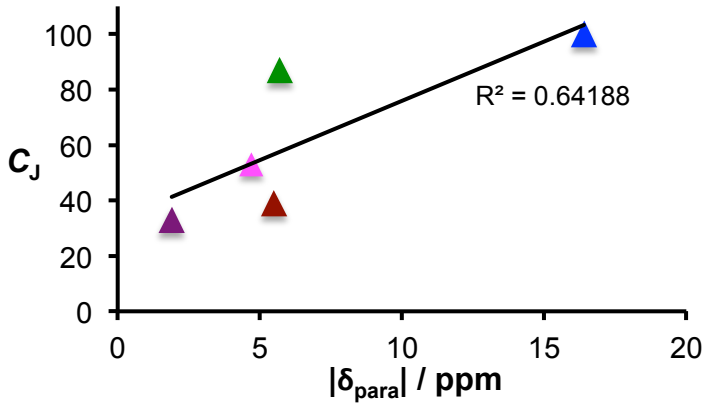

Figure 2.13 Relationship between the magnitude of the paramagnetic shift, $|\delta_{para}|$, of the *tert*-butyl reporter resonance for **[Ln.L^2(H$_2$O)]$^+$** and the Bleaney coefficients for each lanthanide(III) ion. *N.B.* All signs are positive for clarity, the $|\delta_{para}|$ is estimated by assuming the diamagnetic complex has a shift of 1.5 ppm and the line shown is a line of best-fit to the data.

Analysis of the $\Delta J = 1$ manifold in the Eu(III) emission spectrum of **[Eu.L^2(H$_2$O)]$^+$** gave a B_0^2 value equal to -360 cm^{-1} (*Figure 2.14*), suggesting that the crystal field splitting is smaller for the **[Ln.L^2(H$_2$O)]$^+$** series, compared with the **[Ln.L^1(H$_2$O)]** series (*ca.* -500 cm^{-1}). This is somewhat consistent with the decrease in the *tert*-butyl shift magnitude for the **[Ln.L^2(H$_2$O)]$^+$** series, relative to the **[Ln.L^1(H$_2$O)]** series.

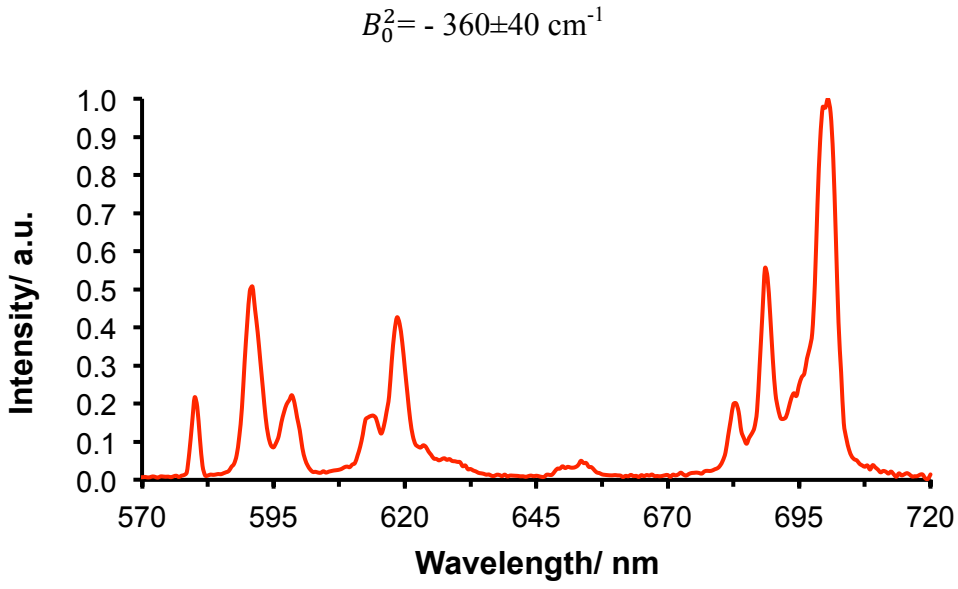

Figure 2.14 Emission spectrum of **[Eu.L^2(H$_2$O)]$^+$** (D$_2$O, 295 K, λ_{exc}= 270 nm), analysis of the $\Delta J = 1$ manifold at 590-595 nm allows the crystal field splitting parameter, B_0^2, to be estimated.

The relaxation behaviour was analysed by measuring the relaxation rates of the major *tert*-butyl resonances of **[Ln.L^2(H$_2$O)]$^+$** at 6 different field strengths (*Table 2.4*). From

the previous series, only **[Dy.L^{1}(H$_2$O)]** possessed the required R_1 values, of the order of 100 to 200 s^{-1} at 7 T. However, the value was around the lower limit of the desired range and so further R_1 enhancements were sought. It is evident from this data that two complexes from the **[Ln.L^{2}(H$_2$O)]$^{+}$** series exhibit enhanced R_1 values that lie in the middle of the desired range. The Dy(III) and Tb(III) complexes both show a 60% increase compared with their predecessors, with remarkable improvements also apparent in their respective R_1/R_2 ratios. The values achieved for Dy(III) and Tm(III), 0.78 and 0.79 respectively, are the highest reported values for these type of systems, with the previous highest values reported for the isomers of **[Tm.DOTMA]$^{-}$** (R_1/R_2 = 0.75 for the major Me resonance; 0.72 for the minor Me resonance).[1] This marked increase in the R_1/R_2 ratio is indicative of an increase in the structural rigidity of the complex. When there are two coordinated pyridyl functionalities, cooperative carboxylate arm rotation is minimised, hence chemical exchange broadening is suppressed. Such an inference also explains the relative increase in the isomeric ratio.

Table 2.4 Experimental longitudinal relaxation rate data for the major *tert*-butyl resonance of **[Ln.L^{2}(H$_2$O)]$^{+}$** at different magnetic field strengths (D$_2$O, 295 K[a]).

Ln	**R_1/ Hz (± error)**						**R_1/R_2[b] (9.4 T)**
	1.0 T	**4.7 T**	**9.4 T**	**11.7 T**	**14.1 T**	**16.4 T**	
Tb	84 (5)	103 (1)	151 (2)	169 (1)	188 (1)	207 (2)	0.79
Dy	89 (3)	119 (1)	174 (1)	203 (1)	230 (1)	256 (1)	0.78
Ho	30 (2)	56 (1)	102 (2)	138 (2)	156 (1)	177 (4)	0.66
Er	7 (1)	19 (1)	41 (5)	53 (7)	71 (9)	81 (21)	0.40
Tm	10 (1)	21 (1)	40 (1)	51 (1)	59 (1)	68 (1)	0.46
Yb	4.0 (0.5)	4.7 (0.2)	7.1 (0.1)	8.3 (0.2)	9.6 (0.3)	10.5 (0.2)	0.22

(a) Temperature was monitored accurately, calibrating against an ethylene glycol shift thermometer; (b) R_2 values were estimated as ($\pi \times \omega_{1/2}$), for a Lorentzian line fit.

Global fitting of the R_1 data for the **[Ln.L^{2}(H$_2$O)]$^{+}$** complex series (*Figure 2.15*), as before, allowed the average distance between the lanthanide(III) ion and the *tert*-butyl reporter group to be estimated as 6.57±0.05 Å (*Table 2.5*).

Table 2.5 Calculated values for r (Å) obtained through fitting of experimental R_1 values at 6 different magnetic fields[a] for **[Ln.L^2(H$_2$O)]$^+$** using a fixed μ_{eff}[b] (BM) (D_2O, 295 K).

[Ln.L^2(H$_2$O)]$^+$	**μ_{eff}/ BM**	***r*/ Å**
Tb	9.8	6.38±0.02
Dy	10.3	6.36±0.01
Ho	10.4	6.78±0.02
Er	9.4	n.d.
Tm	7.6	6.50±0.02
Yb	4.3	6.28±0.03
	Average	**6.57**±0.05

(a) The fields are 1.0 T, 4.7 T, 9.4 T, 11.7 T, 14.1, 16.4 T; (b) μ_{eff} was fixed to literature values.[27] The data set for Er did not converge to a well-defined minimum.

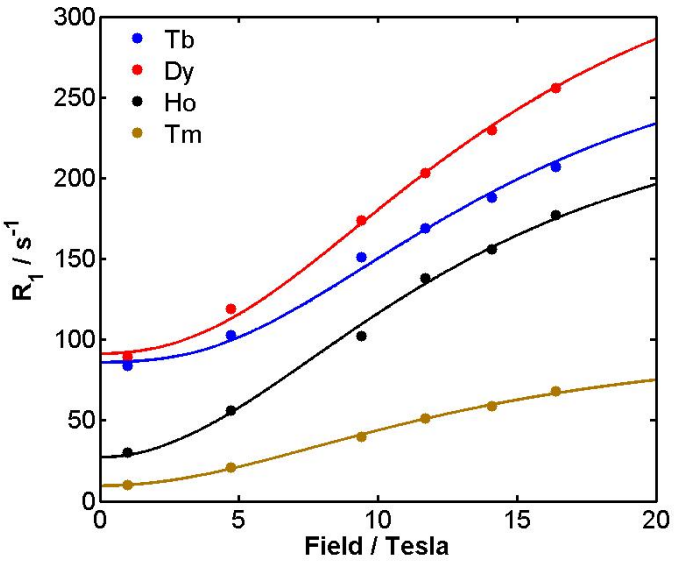

Figure 2.15 ^{1}H NMR relaxation rates, R_1/ s^{-1}, for the *tert*-butyl resonance on **[Ln.L^2(H$_2$O)]$^+$** as a function of magnetic field, showing the fits (*lines*) to the experimental data points (*circles*) (295 K, D_2O). Er was omitted as reliable fitting did not occur.

Both **[Dy.L^1(H$_2$O)]** and **[Dy.L^2(H$_2$O)]$^+$** present very good spectral properties satisfying the key requirements outlined for the design of ^{1}H PARASHIFT probes in *Section 2.1*. Whilst **[Dy.L^1(H$_2$O)]**, possesses the most shifted *tert*-butyl chemical shift, at -20.1 ppm, its R_1 is at the lower limit of the required 100 to 200 s^{-1} range at 7 T. The development of the C_2-symmetric complex, **[Dy.L^2(H$_2$O)]$^+$**, showed a 60% increase in R_1, which offsets the slight reduction in the *tert*-butyl chemical shift at -17.9 ppm. Sufficient signal intensity gains were achieved by doubling the number of nuclei contributing to

the reporter signal and chemical exchange broadening was reduced by increasing the structural rigidity of the complex so that the R_1/R_2 ratio is amongst the highest reported. Such qualities make **[Dy.L^2(H$_2$O)]$^+$** and its congeners an attractive candidate for phantom and *in vivo* MRS studies.

2.3.3 ^{1}H MRS phantom imaging studies

Preliminary phantom imaging studies were carried out at 7 T, using a 2 mM solution of **[Dy.L^2(H$_2$O)]$^+$** in a cut-down 5 mm NMR tube, by Prof. Andrew Blamire at the Newcastle Magnetic Resonance Centre. The NMR tube was placed at 90° to the magnetic field in the bore of a 30 mm birdcage coil, typically used for standard MRI experiments on small mice (≤25 g). Due to its favourable shift and relaxation characteristics, it was proposed that the *tert*-butyl resonance on **[Dy.L^2(H$_2$O)]$^+$** could be observed easily against the background noise. In *Section 2.1*, it was rationalised that a shift < -34 ppm or > +44 ppm is essential, at a 7 T magnetic field, if practicable imaging pulse sequences are to be used to minimise interference from the water signal. In theory, since the *tert*-butyl resonance on **[Dy.L^2(H$_2$O)]$^+$** occurs at -17.9 ppm, a pulse bandwidth of 10 kHz, centred at the *tert*-butyl resonant frequency can be used to selectively excite the *tert*-butyl resonance.[1] The effect of changing the bandwidth on the ^{1}H MRS image of the *tert*-butyl resonance on **[Dy.L^2(H$_2$O)]$^+$** is shown in *Figure 2.16*, where full eradication of the water signal is only demonstrated for 10 kHz. Such a result is expected, when it is considered that the water and *tert*-butyl signals are only 6.7 kHz apart at 7 T.

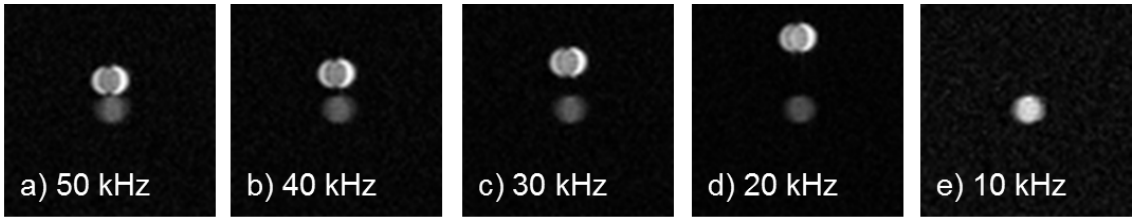

Figure 2.16 Single slice gradient echo 2D scan (axial orientation, 2 mM complex, H_2O) displaying images for the water signal (*top*) and the *tert*-butyl resonance of **[Dy.L^2(H$_2$O)]$^+$** (*bottom*). (*a*-*e*) Variable bandwidths are indicated for each scan.

Whilst this reduced bandwidth method demonstrates the theory, in practice, lower bandwidths result in longer acquisition times. In this case, a 5 mm 2D slice was analysed but it is predicted that problems will arise when applying these sweep widths

to a larger object, *i.e.* a mouse. Before the use of larger bandwidths can be considered, a system needs to be contrived where the *tert*-butyl displays a larger paramagnetic shift.

2.3.4 ^{1}H MRS *in vivo* imaging studies

Proof-of-principle *in vivo* ^{1}H MRS imaging studies were performed by Prof. Andrew Blamire and Dr. Ian Wilson, at the Newcastle Magnetic Resonance Centre, using **[Dy.L^{2}(H$_2$O)]$^{+}$**. Solutions of 0.12 mmol kg^{-1} of **[Dy.L^{2}(H$_2$O)]$^{+}$** were administered to three separate SCID male mice (25 g), bearing HCT-116 tumours (*i.e.* human colorectal carcinoma xenografts). Intravenous administration of **[Dy.L^{2}(H$_2$O)]$^{+}$** *via* the tail vein was 10-14 days post-inoculation to ensure the tumours were about 10 mm in diameter. During the experiment the mice were anaesthetised with oxygen/1-2% isofluorane.

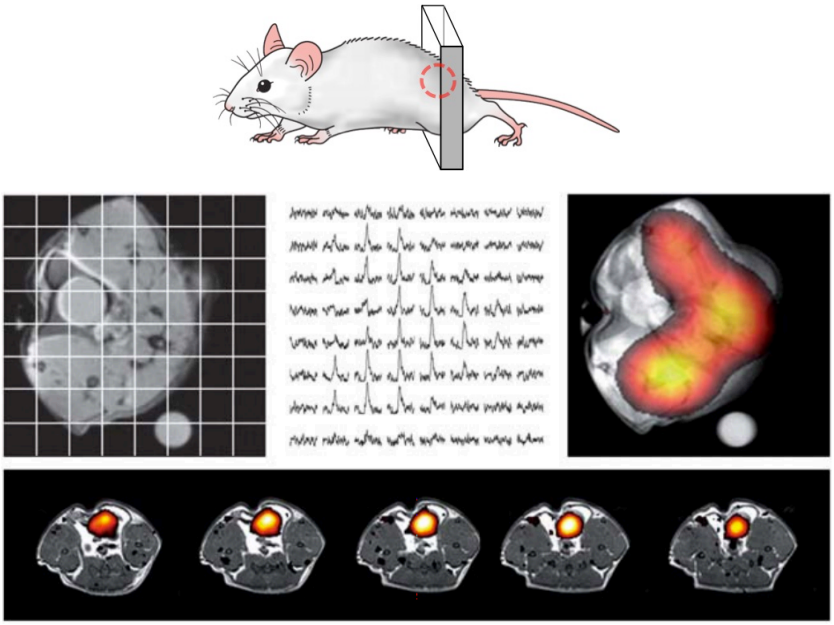

Figure 2.17 *Top left:* spectroscopic imaging grid overlaid onto a representative slice of a structural scan. *Top centre:* localised signal from the *tert*-butyl signal of **[Dy.L^{2}(H$_2$O)]$^{+}$** from each corresponding voxel of the grid 80 min after administration (0.12 mmol/kg complex, 7 T, TR = 104 ms, TE = 1.2 ms, SW = 5 kHz, 64 mm FOV, 8 × 8 matrix, 3 min 34 sec, maximum SNR = 25). *Top right:* Structural scans and colour overlay of spectral peak integrals. *Bottom:* 3D gradient echo ^{1}H MR scan in a different mouse (0.03 mmol/kg complex, 7 T, TR = 10 ms, TE = 4.39 ms, SW = 5 kHz, 5 min 28 sec, maximum SNR = 20).

Strong signals were initially exhibited, but the *tert*-butyl peak was substantially broader than expected *in vivo* with a linewidth around 200 Hz.[1] Localised spectra from across the mice were obtained using a 5 kHz bandwidth, centred upon the -17.9 ppm resonant frequency of interest, to avoid interference from the water protons. An image representation of the distribution of **[Dy.L^{2}(H$_2$O)]$^{+}$** was created by peak integration for

each spatial location and overlaid onto the structural scans (*Figure 2.17)*. In the latter mice, strong localisation of the complex in the muscular tissue was evident, with later accumulation in the bladder. In each case, images were obtained within a relatively short amount of time (<6 min) and the complex was tolerated well.

Despite extremely encouraging preliminary results, the retention of the cationic complex in muscle tissue remains a concern. However, the high sensitivity associated with these complexes has allowed for the acquisition of sufficient signal intensity in a living animal, in under 6 min due to the advantage of having a zero-background signal at the reporter resonant frequency.

2.4 Increasing the Shift: The Phosphinate Parent System

Previous imaging protocols with **[Dy.L^{2}(H$_2$O)]$^{+}$** saw the benefit of using a reduced bandwidth, where the water peak is excluded and the *tert*-butyl peak is imaged selectively. However, in order to increase the bandwidth and reduce imaging acquisition times, a *tert*-butyl shift of < -34 ppm or > +44 ppm is essential at 7 T. Consequently, the tri-phosphinate system, **[Ln.L^{3}]** (*Figure 2.0*), has been designed in accord with literature, whereby substitution of carboxylate for phosphinate arms resulted in large chemical shift enhancements.[8,34] It is predicted that shifts of up to -40 ppm can be achieved for the Dy(III) analogue, and >+40 ppm for Tm(III).

2.4.1 Synthesis and characterisation

The generally accepted methodology for the synthesis of a tri-phosphinate ligand, is shown in *Scheme 2.4*.[8,35,36] First, alkylation of 1,4,7-tris-*tert*-butoxycarbonyl-1,4,7,10-tetraazacyclododecane (tri-BOC) is carried out with the pyridyl arm of interest, where *LG* is the leaving group and *X* is representative of the reporter group. Subsequent removal of the *tert*-butyloxycarbonyl (BOC) protecting groups, with TFA, affords the mono-substituted cyclen compound. Finally, a one-pot synthetic step involving the co-condensation of the secondary amine groups with paraformaldehyde and diethyl methylphosphonite, yields the desired tri-phosphinate ligand, following an Arbusov-type rearrangement.

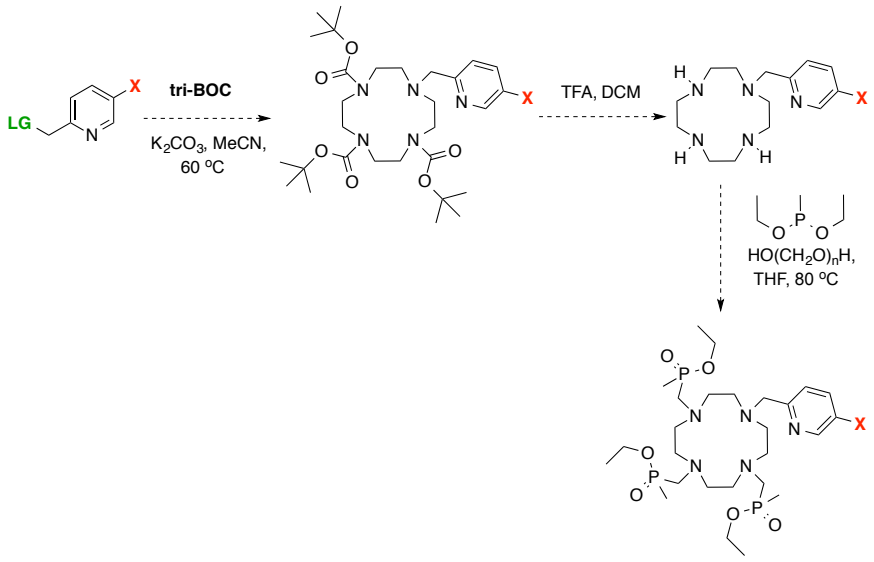

Scheme 2.4 General procedure for the classical synthesis of a tri-phosphinate ligand, where LG = a leaving group *i.e.* Br or OMs, and X = the reporter group *i.e.* CF_3 or ^{t}Bu.

While this synthetic route is widely accepted, the yields for the final step can be rarther low (*ca.* 30-50%). Therefore, it was proposed that in order to produce higher overall yields, a batch of the tri-phosphinate 12-N_4 macrocycle should be made, which can be alkylated with the pyridyl moiety in the penultimate step, preceding deprotection and complexation. This was the case in the syntheses of the **[Ln.L^{1}(H$_2$O)]** and **[Ln.L^{2}(H$_2$O)]$^{+}$** series, where batches of the tri-carboxylate macrocycle, ***1***, and the bis-carboxylate macrocycle, ***17***, were used respectively. This alternative pathway is advantageous because the poorest yielding step is early in the synthetic path, and occurs with a compound that is easily derived from common starting materials. In addition, such an idea allows for alkylation of the free amine site with a variety of different substituents and presents a more efficient synthetic route, rather than repeating *Scheme 2.4* for each different complex.

The synthetic route for the formation of the tri-phosphinate 12-N_4 macrocycle, ***31***, is described in *Scheme 2.5* and employs familiar protecting group chemistry. To begin, the protection of three cyclen amine sites was achieved using 3.1 equivalents of benzyl chloroformate and triethylamine, to afford the carbamate ***27***. The remaining amine site was alkylated, using di-*tert*-butyl dicarbonate, to give the tetra-substituted macrocycle ***28***. Removal of the benzyl protecting groups under high-pressure hydrogenation, with a $Pd(OH)_2$/C catalyst, yielded the mono-BOC protected cyclen compound ***29***. The tri-phosphinate mono-BOC compound, ***30***, was formed by the one-pot co-condensation of

29 with paraformaldehyde and diethyl methylphosphonite. Alumina gel column chromatography was employed for the purification, since previous work showed poor separation of the crude material using silica.

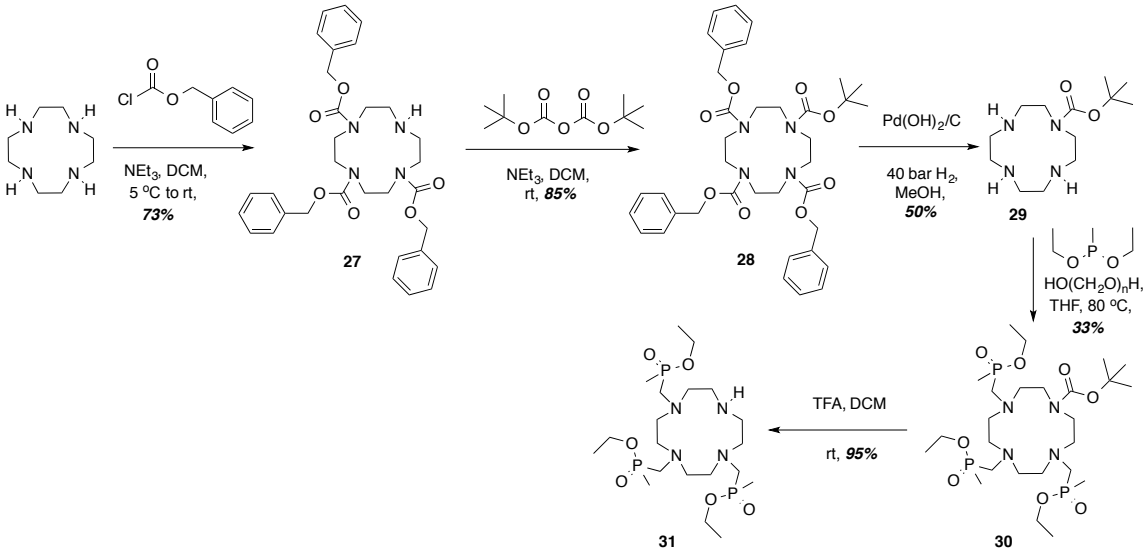

Scheme 2.5 General procedure for the synthesis of the tris-phosphinate ligand framework, ***31***.

The resulting ^{31}P NMR spectrum showed that ***30*** existed as a mixture of stereoisomers in solution, differing in configuration at each phosphorus stereocentre (*Figure 2.18*). Finally, the BOC group was removed using trifluoroacetic acid, to give the desired tri-phosphinate ligand framework, ***31***, after aqueous basic work up.

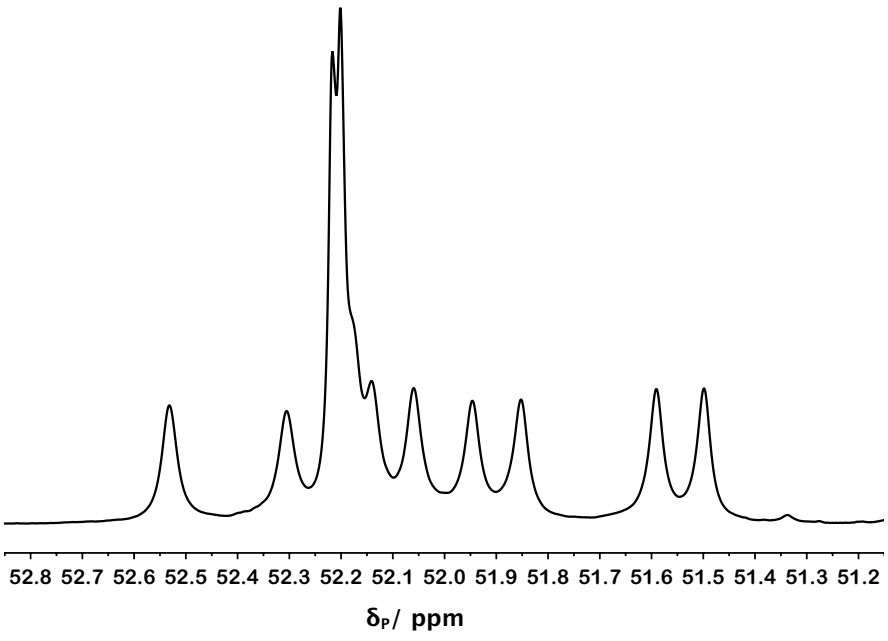

Figure 2.18 ^{31}P NMR spectrum of ***30***, highlighting the presence of stereoisomers ($CDCl_3$, 295 K, 16.4 T).

The remaining secondary amine position on ***31*** was alkylated with the mesylate, ***5*** *(Scheme 2.6)*. Once again, alumina gel column chromatography was used to purify the crude mixture, allowing isolation of the tetra-substituted ligand, ***32***. The phosphinate esters were cleaved under acidic conditions to give the acid salt of the free ligand, and metal complexation was carried out in aqueous solution at pH 5.5, using the appropriate hydrated lanthanide(III) chloride. Preparative reverse-phase HPLC purification yielded the desired series of complex, **[Ln.L^{3}]**, where Ln = Eu to Yb (***33-40***).

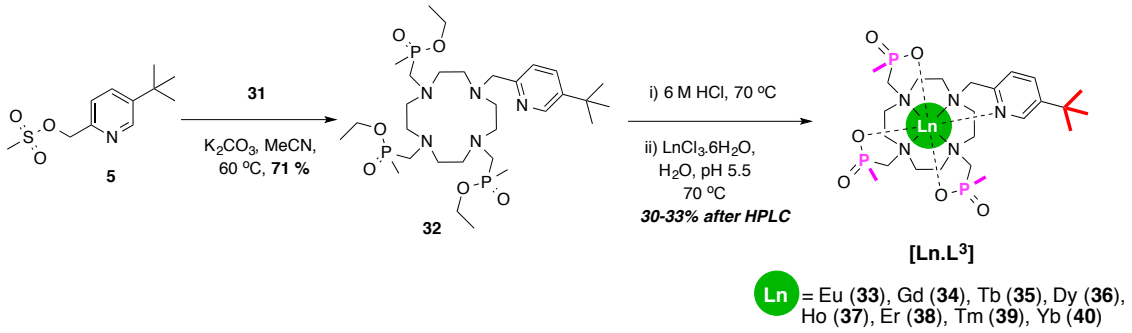

Scheme 2.6 General procedures for the synthesis of the PMe_3 parent ^{1}H PARASHIFT probes, **[Ln.L^{3}]**, ***33-40***.

As for the previous series, the purity of complexes ***33-40*** was evaluated by analytical reverse-phase HPLC (*Figure 2.19* shows **[Er.L^{3}]**). The observed retention times ranged between 8.6 and 10.2 min and so are comparable to the **[Ln.L^{1}(H$_2$O)]** series (*ca.* 8.3 to 8.9 min). Such an observation is consistent with the neutral nature and the structural similarity of the complexes in each series. Again, the identity of the desired complexes was confirmed by high-resolution mass spectrometry, with each complex displaying the expected characteristic isotope pattern.

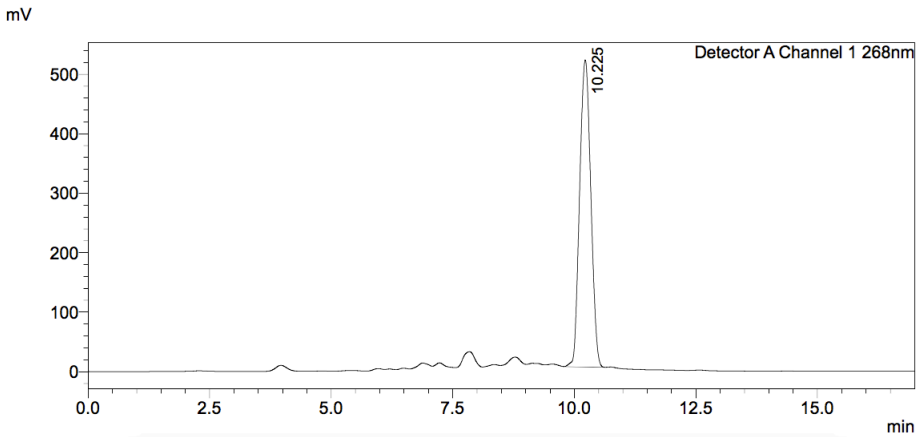

Figure 2.19 Observed analytical reverse-phase HPLC UV chromatogram of **[Er.L^{3}]** (λ= 268 nm, 10-100% MeOH+0.1% formic acid in H_2O+0.1% formic acid over 10 min, t_R=10.2 min).

The hydration state, *q*, for the **[Ln.L^{3}]** series was estimated by measuring both the radiative lifetimes of the Tb(III) and Eu(III) emissive excited states in H_2O and D_2O (*Table 2.6*) and by determining the relaxivity of the Gd(III) complex using *equation 3*. In this case, both calculations suggested that the complexes in the **[Ln.L^{3}]** series do not possess a bound water molecule, *i.e.* they are $q = 0$ with a coordination number of 8 (r_{1p} = 1.5±0.04 mM^{-1} s^{-1}). Such an inference is plausible when the steric bulk of the PMe chelating arms are considered, and is consistent with the behaviour of related tri-phosphinate pyridyl-based systems.[8]

Table 2.6 Experimentally determined radiative rate constants, *k*, and derived values of *q* (±20%) for **[Eu.L^{3}]** and **[Tb.L^{3}]** (295 K, pH 7.0).

[Ln.L^{3}]	k_{H_2O}/ **ms^{-1}**	k_{D_2O}/ **ms^{-1}**	***q***
Eu	0.57	0.48	0
Tb	0.32	0.28	0

2.4.2 ^{1}H NMR studies: shift behaviour

The chemical shift behaviour of the *tert*-butyl reporter group on each complex was analysed by ^{1}H NMR spectroscopy (*Figure 2.20*). A large increase in shift for the **[Ln.L^{3}]** series is clearly evident, with all six *tert*-butyl resonances now possessing the required shifts, far from the diamagnetic range. For this system, the Tb(III) and Tm(III) *tert*-butyl resonances show the largest improvements on their tri-carboxylate analogues (60 ppm) and are the most shifted species with opposite senses, at -77.3 ppm and +67.2 ppm, respectively. The Dy(III) *tert*-butyl was predicted to be the most shifted from its predecessors, and resonates an additional 50 ppm away from the corresponding C_3 parent complex at -75.1 ppm. Consider lastly the cases of Ho(III) and Er(III), each can now be considered as attractive candidates for this work, given their shift enhancements of 30 ppm with respect to their tri-carboxylate analogues (-31.9 ppm and +38.3 ppm, respectively).

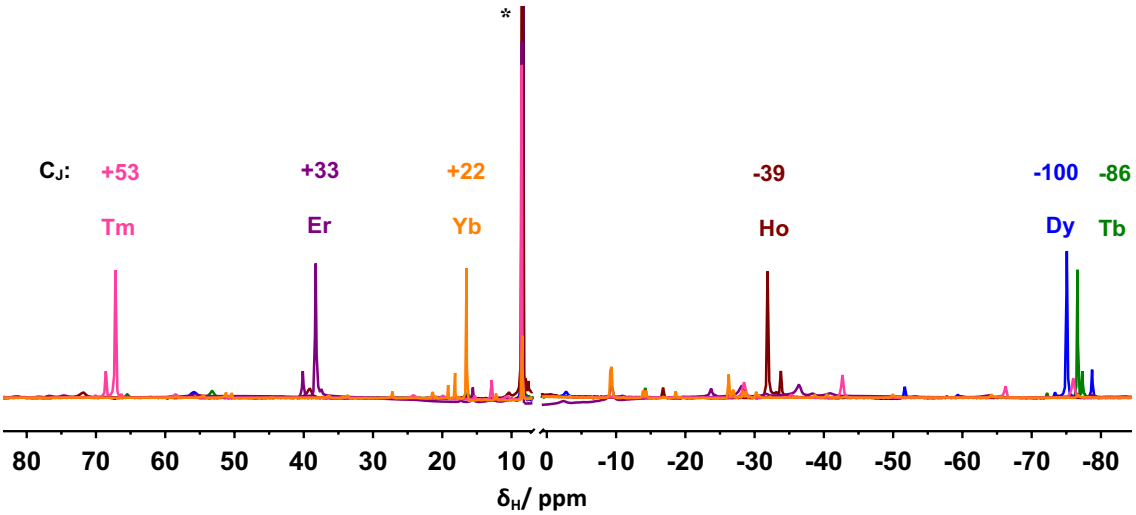

Figure 2.20 Superimposed ^{1}H NMR spectra of PMe_3 parent complexes, **[Ln.L^3]**, highlighting the shift in the *tert*-butyl reporter resonance for Ln = Tm, Er, Yb, Ho, Tb and Dy (D_2O, 9.4 T, 295 K), with respect to the corresponding Bleaney coefficients (C_J). The solvent water peak is omitted for clarity and * represents residual formate from HPLC purification and neutralisation.

For the phosphinate complexes, the number of species in solution can be complicated due to the differing configurations at each phosphorus centre, a phenomenon demonstrated earlier for the diamagnetic molecule ***30*** *(Figure 2.18)*. However, it has been established that mono-amide tri-phosphinate 12-N_4-based lanthanide(III) complexes give rise to two favourable low energy isomers where the chirality at each phosphorus stereocentre is consistent *e.g. RRR* or *SSS*.[37,38] For the pyridyl systems reported here, additional thermodynamically stable configurations are not possible due to the locked configuration of the bound pyridine. As a result, each complex in the **[Ln.L^3]** series exists as one major isomer in solution, accounting for approximately 85% of the observed signal intensity. This observation marks a slight improvement on the **[Ln.L^1(H$_2$O)]** series (*ca.* >80%) whilst remaining comparable to the **[Ln.L^2(H$_2$O)]$^+$** series (>90%).

The magnitude of the paramagnetic shift of the *tert*-butyl group for complexes ***35-40*** did not correlate well to the Bleaney coefficients (*Figure 2.21*). However, as demonstrated before, the shifts do not fit to a linear trend, with the Er(III), Tm(III) and Tb(III) complexes showing the largest deviations.

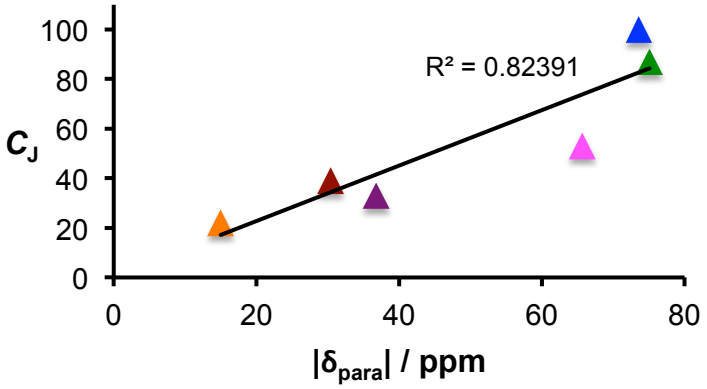

Figure 2.21 Relationship between the magnitude of the paramagnetic shift, $|\delta_{para}|$, of the *tert*-butyl reporter resonance for **[Ln.L^3]** and the Bleaney coefficients for each lanthanide(III) ion. *N.B.* All signs are positive for clarity, the $|\delta_{para}|$ is estimated by assuming the diamagnetic complex has a shift of 1.5 ppm and the line shown is a line of best-fit to the data.

Analysis of the $\Delta J = 1$ manifold in the Eu(III) emission spectrum of **[Eu.L^3]** gave the crystal field splitting parameter, B_0^2, to be -590 cm^{-1} (*Figure 2.22*). An increase in the crystal field splitting for the **[Ln.L^3]** complex series is consistent with the fact that the *tert*-butyl shift magnitude has increased relative to the **[Ln.L^1(H$_2$O)]** and **[Ln.L^2(H$_2$O)]$^+$** series.

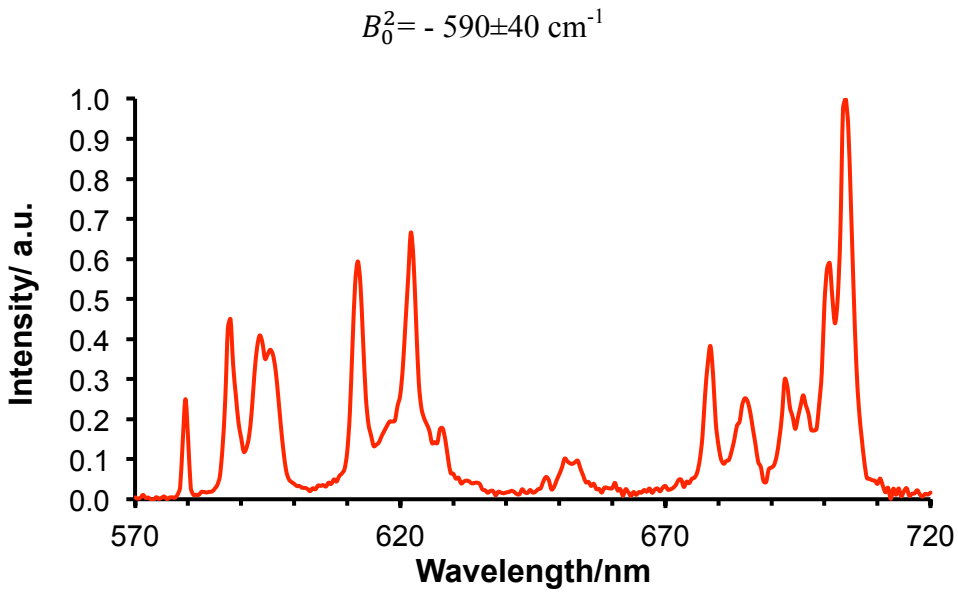

Figure 2.22 Emission spectrum of **[Eu.L^3]** (D_2O, 295 K, λ_{exc}= 270 nm), analysis of the $\Delta J = 1$ manifold at 590-595 nm allows the crystal field splitting parameter, B_0^2, to be estimated.

The sharp well defined ^{1}H NMR spectrum of **[Yb.L^{3}]** was fully assigned (*Figure 2.23*), with the aid of relaxation rate data and by comparison with structurally equivalent systems.

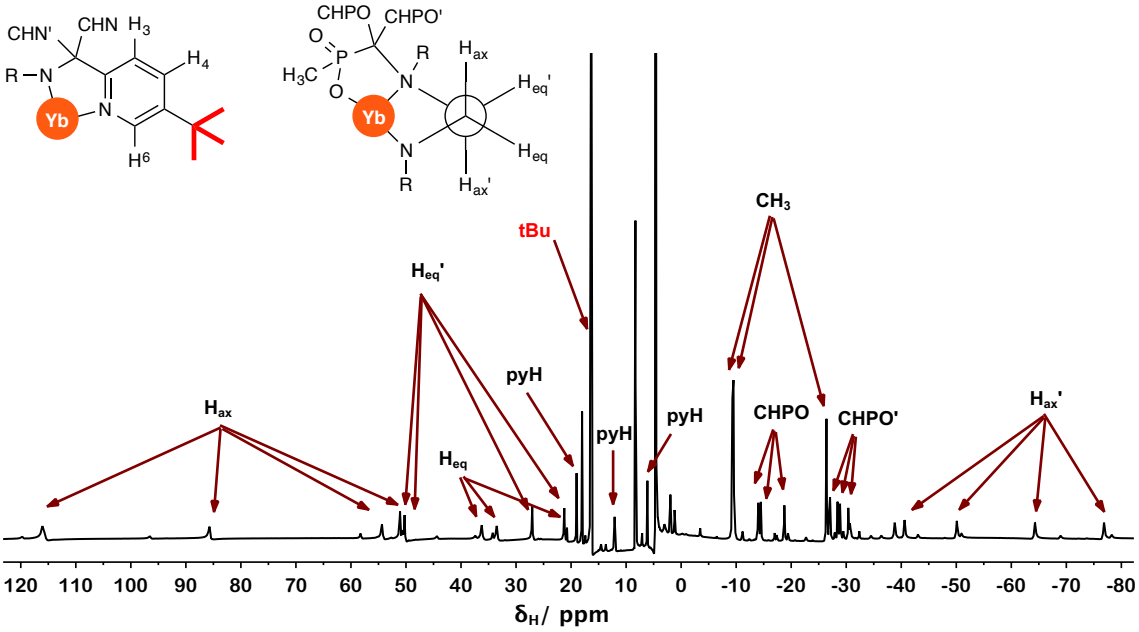

Figure 2.23 Annotated ^{1}H NMR spectrum of **[Yb.L^{3}]** (D_2O, 9.4 T, 295 K). The unassigned resonances are due to the minor isomer.

2.4.3 ^{1}H NMR studies: relaxation behaviour

The relaxation behaviour of the major *tert*-butyl resonances of the **[Ln.L^{3}]** series was assessed at 6 different fields (*Table 2.7*). A decrease in the observed relaxation rates was observed for all the complexes in the **[Ln.L^{3}]** series, except in the case of Er(III), which showed the highest longitudinal relaxation rate across all the fields measured, with a 70% enhancement relative to the tri-carboxylate system. Remarkable also, is the high longitudinal relaxation rate of the Er(III) complex at low field whereas the other complexes show a steeper field dependence. To add to this, only the Er(III) complex possesses the required R_1 value of the order of 100 to 200 s^{-1} at 7 T, with the Dy(III) and Tb(III) complexes each showing a marked decrease in their respective relaxation rates, relative to the tri-carboxylate system. The calculated R_1/R_2 ratios across the series are comparable to those previously observed.[1,8,39] The relatively bulky phosphinate substituents enhance the structural rigidity of the complex by hindering cooperative arm rotation. Global fitting of the experimental R_1 data sets for the **[Ln.L^{3}]** complex series, allowed the average distance between the lanthanide(III) ion and the *tert*-butyl reporter group to be estimated with an average *r* of 6.61±0.07 Å.

Table 2.7 Longitudinal relaxation rate (R_1) data for the major *tert*-butyl resonance of **[Ln.L^3]** at different magnetic field strengths (D_2O, 295 K[a]).

Ln	**R_1/ Hz (± error)**						**R_1/R_2[b] (9.4 T)**
	1.0 T	**4.7 T**	**9.4 T**	**11.7 T**	**14.1 T**	**16.4 T**	
Tb	35 (2)	53 (2)	81 (2)	91 (1)	102 (1)	113 (1)	0.71
Dy	40 (2)	59 (1)	96 (1)	114 (1)	132 (1)	150 (1)	0.59
Ho	35 (1)	61 (2)	100 (1)	127 (1)	147 (1)	166 (1)	0.57
Er	77 (2)	88 (2)	120 (2)	135 (1)	152 (1)	169 (1)	0.71
Tm	18 (2)	55 (1)	97 (1)	115 (1)	129 (1)	142 (1)	0.50
Yb	11.1 (0.1)	10.7 (0.1)	11.4 (0.7)	11.6 (0.6)	12.0 (0.1)	12.4 (0.3)	0.39

(a) Temperature was monitored accurately, calibrating against an ethylene glycol shift thermometer; (b) R_2 values were estimated as ($\pi\omega_{1/2}$), for a Lorentzian line fit.

Such unprecedented relaxation behaviour has been reported for a related tri-phosphinate Er(III) complex with q = 0 and a coordination number of 8 (*Figure 2.24*), suggesting that these tri-phosphinate 12-N_4-based systems show unique behaviour in their Er(III) complexes.[25,28] In contrast, relaxation analyses of the 9 coordinate tri- and bis-carboxylate systems (q = 1) showed that only the Dy(III) and/or Tb(III) complexes possess the required R_1 values of the order of 100 to 200 s^{-1} at 7 T, with the highest relaxation rates observed with the Dy(III) C_2-symmetric parent system. Therefore, it is clear that Er(III) tri-phosphinate complexes, and Dy(III) and/or Tb(III) tri- and bis-carboxylate complexes appear to be the best candidates for use as PARASHIFT probes, in the field range 1.5 to 7.0 T, based on the critical balance between the shift and relaxation behaviour, presented in *Section 2.1*.

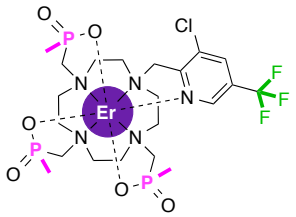

Figure 2.24 Structure of a related tri-phosphinate Er(III) complex, showing analogous relaxation rate behaviour to **[Er.L^3]**.

Overall, the **[Ln.L^{3}]** series demonstrates the desired enhancements in shift behaviour, with shifts of >60 ppm from the water signal achieved in the (Tb(III), Dy(III) and Tm(III) complexes. Such a shift magnitude allows larger bandwidths of 20 kHz to be used in imaging, so that shorter repetition rates and faster data acquisition can occur. The previously overlooked later lanthanide(III) ions, Er(III) and Ho(III) show interesting shift behaviour in this system, with *tert*-butyl groups resonating 30 ppm away from the water signal but remain just inside the desired goal posts of < -34 ppm or > +44 ppm and so are less suitable for imaging with a 20 kHz bandwidth.

The relaxation behaviour presents a few surprises, however. Firstly, both **[Dy.L^{3}]** and **[Tb.L^{3}]** display lower relaxation rates than the tri-carboxylate systems across all the fields measured. Conversely, increases in relaxation rates were observed for Ho(III), Tm(III), Yb(III) and in particular Er(III), which shows a 70% increase across all fields and was the only candidate from the **[Ln.L^{3}]** series with the required relaxation rates of 100 to 200 s^{-1} at 7 T. It is clear that there are stark differences between the shift and relaxation behaviour of the **[Ln.L^{1}(H$_2$O)]** and **[Ln.L^{3}]** systems and a more detailed analysis of this behaviour was carried out.

2.5 Comparing the [Ln.L^{1}(H$_2$O)] and [Ln.L^{3}] Parent Complexes

2.5.1 Shift Behaviour

Comparison of the *tert*-butyl shift behaviour in the two series of complexes (*i.e.* tri-carboxylate *vs.* tri-phosphinate) reveals an increase of over 50 ppm for the tri-phosphinate complexes of Tb(III), Dy(III) and Tm(III) and 30 ppm for Er (III) and Ho (III) (*Table 2.8*). Such large shift differences cannot simply be attributed to a change in the ligand crystal field, as defined by B_0^2 (-590 *vs.* -500 cm^{-1}), or to any significant structural change in these relatively rigid systems.

Table 2.8 ^{1}H NMR *tert*-butyl shift data for the **[Ln.L^{1}(H$_2$O)]** and **[Ln.L^{3}]** complex series' (D_2O, 295 K, 9.4 T).

Lanthanide(III)	**δ_H/ ppm**	
	[Ln.L^{1}(H$_2$O)]	**[Ln.L^{3}]**
Tb	-11.1	-76.6
Dy	-20.1	-75.1
Ho	-7.2	-31.9
Er	+7.0	+38.3
Tm	+10.5	+67.2
Yb	+6.3	+18.1

One of the assumptions of Bleaney's theory concerns the treatment of the *f* electron distribution, detailed on *page 15* in *Section 1.2.1.1*. It is assumed that the unpaired *f* electrons can be treated as a point dipole on the nucleus, but this argument neglects to represent the overall spatial distribution of the 4*f* electron cloud for these anisotropic lanthanide(III) complexes. Recently, Kuprov put forward a new distributed model that better represents the *f* electron density probability functions. However, this is yet to find wide-scale application since it requires a description of the electron probability density.[40] However, a more intuitive approach has been adopted by Rinehart and Long, who simulated the shape variation of the quadrupole moments of the 4*f* electron cloud using the angular dependence of the 4*f* orbitals.[41] The variation in the 4*f* electron density cloud is evident from oblate (where m_l is highest) for Tb(III), Dy(III) and Ho(III), to prolate for Er(III), Tm(III) and Yb(III) (where m_l is lowest) (*Figure 2.25*). Such a variation across the later lanthanide(III) ions correlates with the differing sense of shift incorporated in the Bleaney coefficients, C_J. Note the curious case of Er(III) and Pm(III), which appear almost isotropic in this model, potentially explaining the observation of small paramagnetic shifts in many Er(III) complexes.

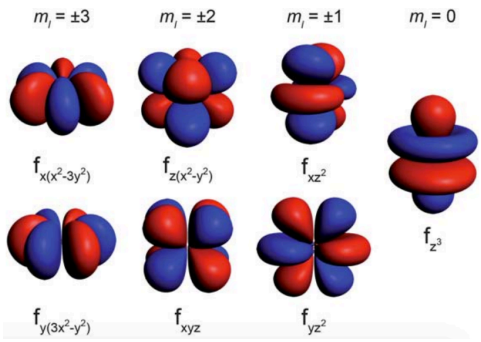

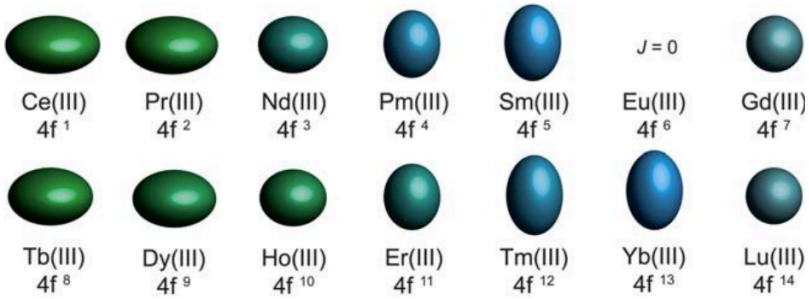

Figure 2.25 Representations of the shape of the *4f* orbitals from the highest magnitude m_l (most oblate on the left) to the lowest magnitude m_l (most prolate on the right) (*bottom*) and the quadrupole approximations of the 4*f* electron cloud for the lanthanide(III) ions (*top*), based on the total angular momentum, *J*, the Stevens coefficient and the 4*f* orbital radii.[41]

Bleaney additionally assumed that the principal axis of magnetisation, defined by the energetically favoured direction of the spontaneous magnetisations, is the same for each lanthanide(III) ion in a complex series. The generalisation that the position of this principal (or easy) axis does not change as the lanthanide(III) ion varies across an isostructural series of complexes is not valid, as demonstrated by Sessoli *et al*.[42] Their work shows the change in the position of the principal axis of magnetisation in the C_4 symmetric **[Ln.DOTA(H$_2$O)]$^-$** series, as the later lanthanide(III) ions are traversed (*Figure 2.26*). In the case of Dy(III), it moves by 90° according to whether or not there is an axially bound water molecule.[43] Such a finding is of particular interest when considering the $q = 0$ and $q = 1$ complexes discussed here. The axis rotates by 90° from Tb(III) to Yb(III) such that for the oblate ions, it is perpendicular to the C_4 axis, and as the ions become more prolate, alignment with the C_4 axis occurs. Again, the most intriguing case is Er(III), which shows a significant discrepancy between experimental data and calculated simulations.

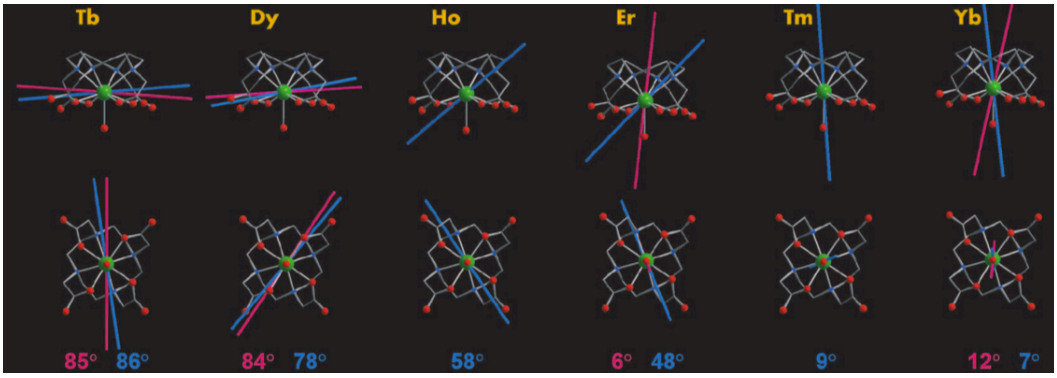

Figure 2.26 The variation in the experimental (*pink*) and calculated (*blue*) easy axis of magnetisation across the **[Ln.DOTA(H$_2$O)]$^-$** series (2 K), shown perpendicular (*top*) and parallel (*bottom*) to the C_4 symmetry axis.[42]

Overall, these findings indicate that the lanthanide(III) ions possess different 4*f* electron distributions depending on the coordination ligand field. Hence, the oblate ions are most likely to show the largest anisotropy when the ligand electron density is mainly above and below the *xy* plane in a 'sandwich' type interaction, and ligands with predominantly equatorial distributed ligand electron density are most likely to show the largest anisotropy for the prolate ions, so as to minimise the repulsive charge between the ligand and the *f* electron cloud.[41,44] As a result, the magnetic moments for the lanthanide(III) ions may vary as a function of their coordination environment, especially in complexes where the ligand field splitting is significantly larger than k_BT. This aspect will be analysed in more detail in *Section 2.5.2*.

Another key issue relates to the anisotropy of the individual m_J states. The separation between the m_J states is a function of ligand geometry and symmetry, and the Boltzmann population depends on their energy separation with respect to k_BT. Consider Tb(III) with a 'sandwich' type ligand: the m_J = ±6 state has oblate electron density, whereas the remaining m_J = 0, ±1, ±2, ±3, ±4 and ±5 states are predominantly prolate in form. Such behaviour leads to a large separation between the ground ±6 state and the higher lying m_J states, and so determines the relative population and overall magnetic anisotropy, at a given temperature. In order to further investigate the paramagnetic NMR shift of the **[Ln.L^{1}(H$_2$O)]** and **[Ln.L^{3}]** systems, analysis of the magnetic anisotropy must consider the population-weighted contribution of the ground and lowest excited m_J states of the lanthanide(III) ion. One possible means of probing these complex issues is to look at the emission profile of relevant **[Ln.L^{1}(H$_2$O)]** and **[Ln.L^{3}]** complexes by optical spectroscopy, in order to interrogate the electronic ground state manifold.

2.5.1.1 Emission Spectra Studies

Lanthanide(III) ion optical emission behaviour can be very sensitive to single ligand variations and can offer information towards elucidating the differing contributions from the m_J states of the electronic ground state to the size and magnitude of the magnetic anisotropy.[45,46] The complexes of Dy(III) and Tb(III) have been investigated here. In each case, the energy gap between the emissive state and the highest lying electronic energy level of the ground state manifold correspond to emission in the visible region of the spectrum. The usefulness of investigating the Eu(III) spectrum,

particularly the energy gap in the $\Delta J = 1$ manifold, has been illustrated previously for all three systems.

The pyridyl group in **[Ln.L^{1}(H$_2$O)]** and **[Ln.L^{3}]** acts as an antenna to aid sensitisation of lanthanide(III) luminescence. Following excitation of the pyridine π to π* transition at 270 nm, intramolecular energy transfer populates the lowest manifold of the excited state of the lanthanide(III) ion ($^{4}F_{9/2}$ for Dy(III), $^{5}D_{4}$ for Tb(III)). For Dy(III), the emissive excited state is relatively long-lived, with lifetimes of the order of 10 μs. Emission spectra of **[Dy.L^{1}(H$_2$O)]** and **[Dy.L^{3}]** were recorded at 295 K in D_2O. As the temperature was decreased from 295 to 80 K, a MeOH/EtOH (1:4) frozen glass containing each complex was examined. In each case, the main observed transitions occur to the $^{6}H_{15/2}$ and $^{6}H_{13/2}$ multiplets of the ground state manifold, centred at 480 and 580 nm respectively (*Figure 2.27*).

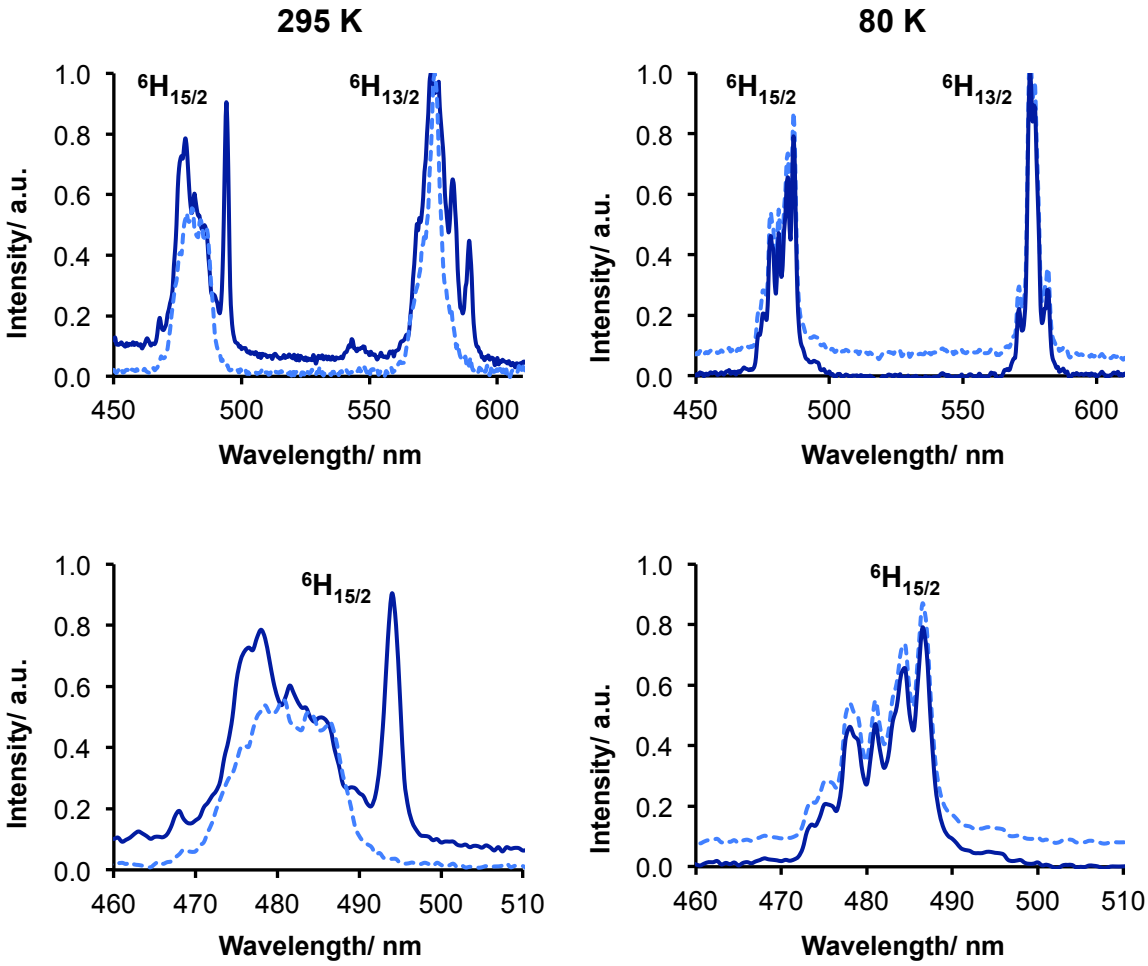

Figure 2.27 (*Left*) Solution emission spectra for **[Dy.L^{1}(H$_2$O)]** (*dash*) and **[Dy.L^{3}]** (*solid*) (D_2O, 295 K, λ_{exc} = 270 nm). (*Right*) **[Dy.L^{1}(H$_2$O)]** (*dash*) and **[Dy.L^{3}]** (*solid*) in a frozen EtOH/MeOH glass (4:1) (80 K, λ_{exc} = 270 nm). (*Bottom*) Expansion of the $^{6}H_{15/2}$ manifolds of **[Dy.L^{1}(H$_2$O)]** and **[Dy.L^{3}]**.

Significant differences were observed between the tri-carboxylate and tri-phosphinate systems at 295 K. The appearance of additional strong transitions in the $^{6}H_{15/2}$ and $^{6}H_{13/2}$ manifolds for the tri-phosphinate system, were observed at lower energy. At first, it was thought to be associated with an increase in the crystal field, previously demonstrated by ^{1}H NMR shift and Eu(III) spectral analyses. However, comparative analysis of the spectral profile at 80 K (where k_BT = 56 cm^{-1}) and 295 K (where k_BT = 204 cm^{-1}) strongly suggested that the additional observed bands for **[Dy.L^{3}]** at 460, 469, 494, 582.5 and 589 nm are 'hot bands' (*Table 2.9*). These typically occur at higher energy, however, as they are associated with transitions from a higher energy component of the $^{4}F_{9/2}$ excited state manifold. Recent Dy(III) emission spectral analyses of 8 or 9 coordinate complexes have shown that the lowest two levels of the $^{4}F_{9/2}$ manifold are separated by about 40 to 60 cm^{-1}.[43,47,48] In the case of **[Dy.L^{1}(H$_2$O)]**, variable temperature emission did not resolve the hot bands so well.

Table 2.9 Energies of transitions observed for **[Dy.L^{1}(H$_2$O)]** and **[Dy.L^{3}]** in solution (D_2O, 295 K).[a,b]

	$^{4}F_{9/2}$ - $^{6}H_{15/2}$ energy gap/ cm^{-1}	**$^{4}F_{9/2}$ - $^{6}H_{13/2}$ energy gap/ cm^{-1}**
[Dy.L^{1}(H$_2$O)]	20,555 20,611 20,812 20,899 21,008 21,097	17,180 17,345 17,390 17,482 **17,575** (w)
[Dy.L^{3}]	**20,242** (s) 20,408 20,620 20,768 20,920 20,986 **21,368** (w) **21,739** (w)	**16,978** (s) **17,167** (s) 17,331 17,422 17,559

(a) Bands in **bold** were absent or of much reduced intensity in a MeOH/EtOH (1:4) frozen glass at 80 K; (b) w = weak, s = strong.

Similarly, following excitation at 270 nm, the emission spectra of **[Tb.L^{1}(H$_2$O)]** and **[Tb.L^{3}]** were recorded in D_2O at 295 K, and in a MeOH/EtOH (1:4) frozen glass at 80 K (*Figure 2.28*). The lifetimes of the Tb(III) emissive states are much longer-lived, falling into the ms range (τ_{D_2O} = 2.5 for **[Tb.L^{1}(H$_2$O)]** and 3.6 ms for **[Tb.L^{3}]**). In the Tb(III) complexes, no evidence of hot bands was found.

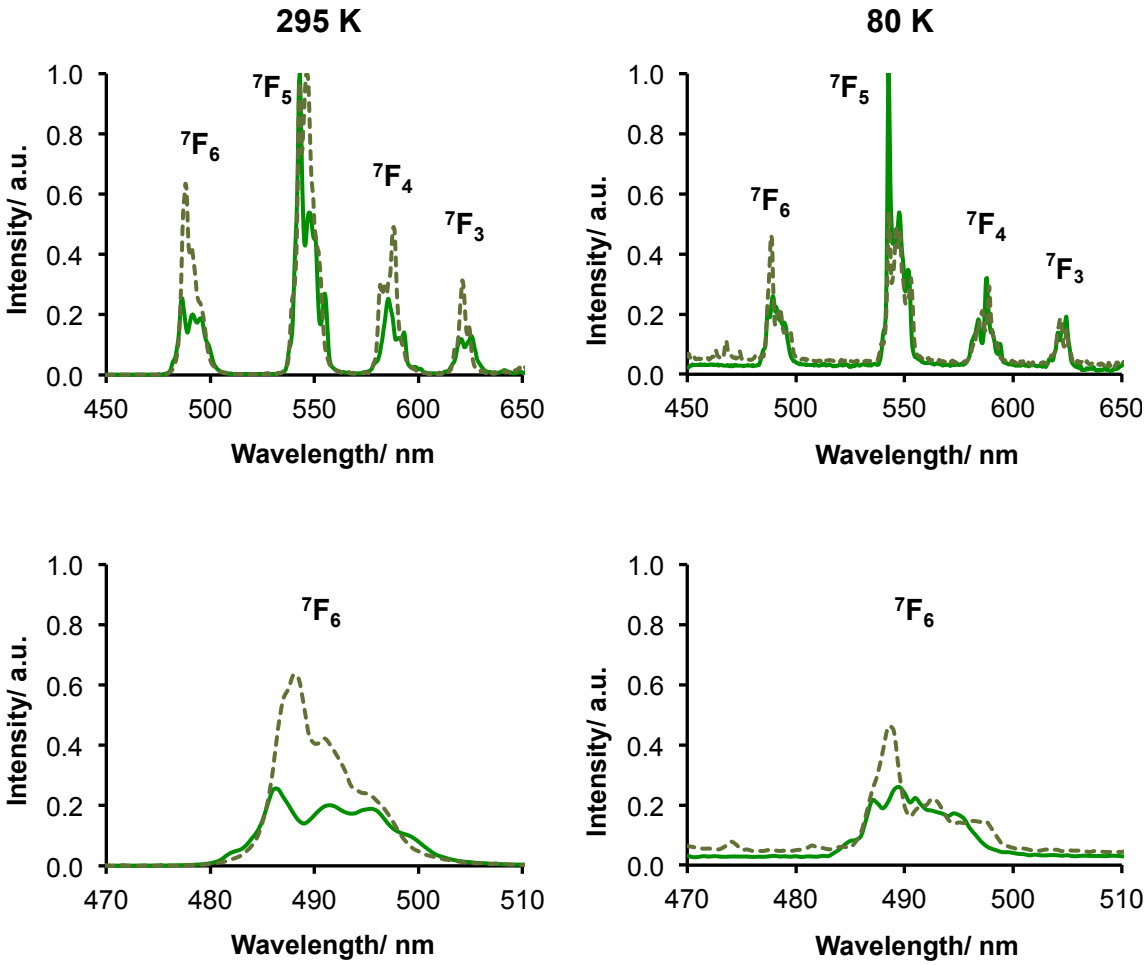

Figure 2.28 (*Left*) Partial solution emission spectra for **[Tb.L^{1}(H$_2$O)]** (*dash*) and **[Tb.L^{3}]** (*solid*) (D_2O, 295K, λ_{exc} 270 nm). (*Right*) **[Tb.L^{1}(H$_2$O)]** (*dash*) and **[Tb.L^{3}]** (*solid*) in a frozen EtOH/MeOH glass (4:1) (80 K, λ_{exc} = 270 nm). (*Bottom*) Expansion of the $^{7}F_6$ manifolds of **[Tb.L^{1}(H$_2$O)]** and **[Tb.L^{3}]**.

The information gained from the emission studies sheds some light on the nature of the relative energies of the ground state multiplets for the Dy(III) and Tb(III) complexes of **L^{1}** and **L^{3}**. However, the scarcity of literature regarding Dy(III) emission and the relation to the anisotropy of the magnetic susceptibility, lends itself to further studies. A handful of investigations into the emissive properties of Er(III) and Tm(III) complexes have been reported, which could be useful here, however the former requires powerful 1064 nm laser excitation,[49] and the latter complexes typically give rise to very weak

emission, attributed to quenching of the Tm(III) excited state by C-H oscillators.[50] Nevertheless, acquiring a library of emission spectra is useful, and offers a comparative analysis; the examples detailed here do not indicate stark differences in the ligand field.

2.5.2 Comparative Analysis of Relaxation Behaviour

Consider last, the longitudinal relaxation rate behaviour of the *tert*-butyl reporter group in each series of complexes. The dependence of R_1 on $(\mu_{\text{eff}})^4$ in the Curie term (the second term) dominates at high field, especially for lanthanide(III) ions possessing large values of μ_{eff}.

$$R_1 = \frac{2}{15}\left(\frac{\mu_0}{4\pi}\right)^2 \frac{\gamma_N^2 \mu_{eff}^2}{r^6}\left[\frac{7\tau_{r+e}}{1+\omega_e^2\tau_{r+e}^2} + \frac{3\tau_{r+e}}{1+\omega_N^2\tau_{r+e}^2}\right] + \frac{2}{5}\left(\frac{\mu_0}{4\pi}\right)\frac{\omega_N^2\mu_{eff}^4}{(3kT)^2 r^6}\frac{3\tau_r}{1+\omega_N^2\tau_r^2} \quad (6)$$

For systems which follow the assumptions of this point dipole model, the relaxation rates should follow the sequence of the μ_{eff} values at high field strengths, *i.e.* [Dy(III), Ho(III)] > Tb(III) > Er(III) > Tm(III) > Yb(III). The experimental data showed that for the 8 coordinate **[Ln.L^3]** series, the Er(III) complex relaxed significantly faster than the Dy(III), Ho(III) and Tb(III) analogues (*Figure 2.29*), whereas in the 9 coordinate **[Ln.L^1(H$_2$O)]** series, the longitudinal relaxation rates followed the order Dy(III) > [Tb(III), Ho(III)] > Er(III) > Tm(III) > Yb(III). Most surprising, is that **[Er.L^3]** has a longitudinal relaxation rate up to 90% higher than the analogous Dy(III) complex at 1.0 T, and **[Tm.L^3]** displays a faster relaxation rate than the corresponding Tb(III) complex between 4.7 and 16.4 T. Field dependent behaviour like this, is unprecedented, and suggests that the assumptions of the BRW model that is used here are not valid, or that values for the magnetic moments of the complexed or bound lanthanide(III) ions differ significantly from their free-ion values.

In BRW theory, the dipolar interaction between the lanthanide(III) ion and the nucleus of interest is considered a point dipole interaction, therefore treating the magnetic susceptibility of the lanthanide(III) ion as a scalar parameter, lacking directionality. In addition, the anisotropy of the static ligand field of a lanthanide(III) complex can certainly affect the degree of anisotropy found in the magnetic susceptibility tensor, neither of which is accounted for in *equation 6*. In the past, the anisotropy of the magnetic susceptibility tensor has been unequivocally considered, leading to the modification of *equation 6* to account for the directionality.[51,52] For such approaches to

be relevant, information concerning the magnetic susceptibility is required, but with this information difficult to obtain, this adaptation is uncited in terms of application.

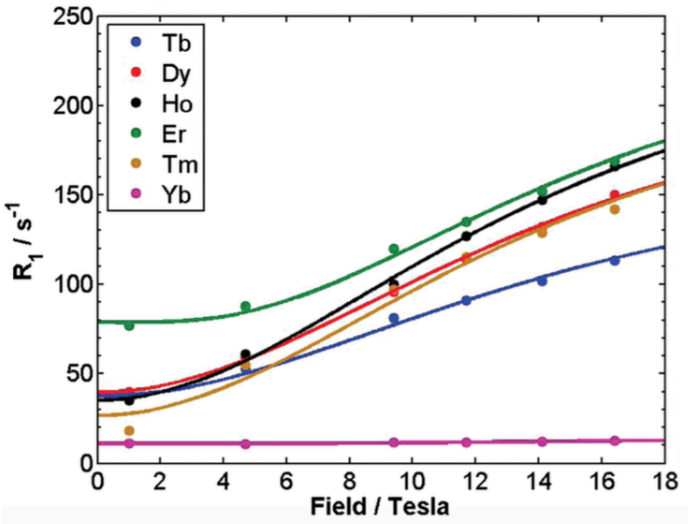

Figure 2.29 ^{1}H NMR relaxation rates, R_1/ s^{-1}, for the *tert*-butyl resonance on **[Ln.L^{3}]** as a function of magnetic field, showing the fits (*lines*) to the experimental data points (*circles*) (295 K, D_2O).

The latter deduction prompted investigations into the magnetic susceptibility of the lanthanide(III) ions in the **[Ln.L^{1}(H$_2$O)]** and **[Ln.L^{3}]** complex series. Dr. Nicola Rogers at Durham University applied the same iterative minimisation fitting method that was used to estimate the distance between the *tert*-butyl reporter group and the lanthanide(III) ion, holding r at 6.6 Å and τ_r at 260 ps, allowing variation of μ_{eff} and T_{1e}.

Table 2.10 Estimated best fit values of μ_{eff} for the **[Ln.L^{1}(H$_2$O)]** and **[Ln.L^{3}]** complex series' (D_2O, 295 K, r = 6.6 Å and τ_r = 260 ps) and free-ion values from the literature[27].

Lanthanide(III)	**μ_{eff}/ BM**		
	Free[27]	**[Ln.L^{1}(H$_2$O)]**	**[Ln.L^{3}]**
Tb	9.8	9.68(02)	8.81(03)
Dy	10.3	10.22(02)	9.47(02)
Ho	10.4	9.82(02)	9.77(02)
Er	9.4	8.95(01)	9.70(02)
Tm	7.6	8.12(03)	9.51(01)
Yb	4.3	4.44(08)	4.57(09)

The magnetic moments for the **[Ln.L^{3}]** series follow the unfamiliar sequence Ho(III) > Er(III) > Tm(III) > Dy(III) > Tb(III) (*Table 2.10*). The largest difference *vs.* the free-ion

value is observed for Tm(III), showing a 24% enhancement. In fact, all the lanthanide(III) ions showed up to 11% variations relative to the free-ion values, except Yb(III) which was within 5%. Notably, the magnetic moments for the **[Ln.L^{1}(H$_2$O)]** series follow the a more plausible order predicted by the free-ion values: Dy(III) > Ho(III) > Tb(III) > Er(III) > Tm(III). Therefore, it can be surmised that the fast relaxation rates of the Tm(III) and Er(III) tri-phosphinate complexes can be attributed, in part, to the discrepancies between the magnetic susceptibilities of the lanthanide(III) ions and the directional dependence on their magnetic susceptibility anisotropy, within each system.

Examples of lanthanide(III) complexes with large crystal fields are seldom studied in detail, but Hölsä has reported a significant magnetic moment variation using SQUID magnetometry, where the room temperature magnetic moments of the LnOBr series (B_0^2 -1200 for Tb to -1350 for Yb) are systematically lower than the free-ion values.[53]

At low field (1.0 T), the order of the measured relaxation rates echoes the sequence of the T_{1e} values, in line with the disappearance of the Curie relaxation contribution (*equation 6*). Even though values for T_{1e} typically fall between 0.1 and 1 ps, the size and order of T_{1e} can vary dramatically, since it is thought to be determined by the transient ligand field and the nature of the lanthanide(III) ion. Therefore, important information can also be gained by investigating the electronic relaxation times, T_{1e}, of the lanthanide(III) ions in the **[Ln.L^{1}(H$_2$O)]** and **[Ln.L^{3}]** complexes.

Table 2.11 Estimated best fit values of T_{1e} for the **[Ln.L^{1}(H$_2$O)]** and **[Ln.L^{3}]** complex series' (D_2O, 295 K, r = 6.6 Å and τ_r = 260 ps).

Lanthanide(III)	**T_{1e}/ ps**	
	[Ln.L^{1}(H$_2$O)]	**[Ln.L^{3}]**
Tb	0.59(02)	0.49(02)
Dy	0.49(02)	0.45(02)
Ho	0.22(02)	0.37(02)
Er	0.17(01)	0.85(01)
Tm	0.29(02)	0.30(01)
Yb	0.29(03)	0.53(02)

For Dy(III), Tb(III) and Tm(III), the differences between the **[Ln.L^{1}(H$_2$O)]** and **[Ln.L^{3}]** series are negligible (≤0.05 ps), whereas dramatic increases are observed for Er(III) (+0.63 ps) and Ho(III) (+0.23 ps) (*Table 2.11*). As *equation 6* suggests, the order of the measured relaxation rates is primarly determined by T_{1e} at low field, hence the remarkably fast relaxation rate of the Er(III) tri-phosphinate complex, in particular, can be rationalised.

The diminishing impact of the Curie relaxation term can be demonstrated by variable temperature ^{1}H NMR studies at different field strengths. The resonant frequency of every nucleus on a paramagnetic lanthanide(III) complex has a T^{-2} dependence in the Curie term of *equation 5*. As expected, the study at high field (11.7 T) revealed the expected dependence of the longitudinal relaxation rate with $1/T^2$ for **[Dy.L^{3}]** (*Figure 2.31)*. In contrast, no significant variation was observed at low field (1.0 T), in accord with the absence of a significant Curie contribution at this field, where the dipolar term dominates.

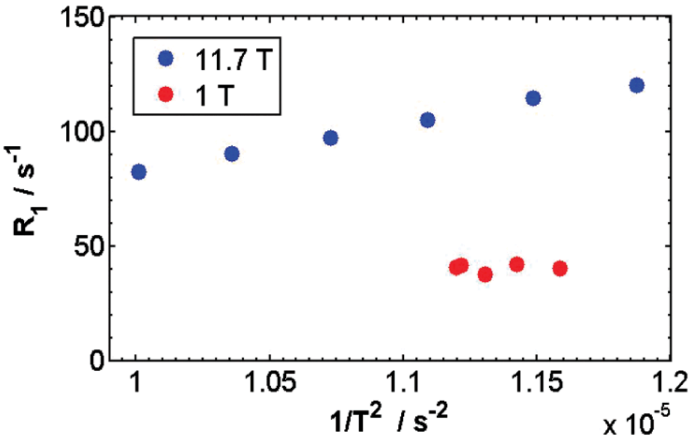

Figure 2.31 ^{1}H NMR relaxation rates, R_1, for the *tert*-butyl resonance on **[Dy.L^{3}]** as a function of $1/T^2$, at 11.7 T (*blue*) and 1.0 T (*red*) (D_2O).

Application of BRW theory here suggests that for both series of complexes, the order of the magnetic moments and the estimated electronic relaxation times were anomalous, explaining the unusually fast relaxation properties of **[Er.L^{3}]** and **[Tm.L^{3}]** compared to **[Dy.L^{3}]** and **[Ho.L^{3}]**. Clearly, the anisotropy of the magnetic susceptibility tensor in the 8 coordinate tri-phosphinate systems, which lack an axial donor, needs to be considered, prompting independent variable temperature electron paramagnetic resonance (EPR) and superconducting quantum interference device (SQUID) magnetometry studies.

2.5.2.1 EPR Studies

EPR spectroscopy provides direct evidence of the low-energy electronic and magnetic structure of paramagnetic species. Lanthanide(III) ions possess first order orbital angular momentum and strong spin-orbit coupling, resulting in total angular momentum states (*i.e.* $J = L + S$). Therefore, the interaction between a lanthanide(III) ion's magnetic moment and its environment is very strong such that the spin-lattice relaxation, T_{1e}, is very fast. This contrasts classical 'spin-only' compounds with orbitally non-degenerate ground states (Cu(II), Gd(III), *etc.*), where orbitally degenerate states are only mixed in *via* high-energy perturbations, resulting in a weaker spin-lattice interaction and therefore slower T_{1e} times. Owing to their fast electronic relaxation times, T_{1e}, lanthanide(III) ions have very weak and broad EPR spectra, such that acquisition must occur at below 10 K in order to observe a signal. At these temperatures k_BT is equal to 5 – 7 cm^{-1}, meaning that only the *very* lowest energy states possess any thermodynamic population. Coupled with the microwave energy in EPR being on the order of a few cm^{-1} at the most, this results in only these lowest states being interrogated.

In these low-symmetry lanthanide(III) systems, the lowest state(s) will either be a Kramers' doublet, pseudo-doublet (near double degeneracy) or singlet, whose characteristics are entirely determined by the environment. The EPR selection rule is $\Delta m_J = \pm 1$ (just like $\Delta m_S = \pm 1$), so that there must be states within the microwave quantum of energy with m_J compositions providing this ±1 difference. For Kramers' ions, the ground doublet must therefore be pure $m_J = \pm ½$ or a mixed doublet; the latter is much more likely in systems of low symmetry. For non-Kramers' ions, there must be a pseudo-doublet ground state with some component of $\Delta m_J = \pm 1$ in order to observe a spectrum.

EPR spectra were measured by Dr. Nicholas Chilton at the EPSRC EPR National Facility at the University of Manchester on desalted samples of the tri-carboxylate, **[Ln.L^{1}(H$_2$O)]**, and tri-phosphinate, **[Ln.L^{3}]**, complexes of Tb(III), Dy(III), Er(III) and Tm(III) at 5 K. The data was collected at Q-band (~34 GHz), both on solid-state and frozen glass (80% water, 20% glycerol, ~ 1 mM) samples. The complexes of Tb(III) and Er(III) were EPR active, whilst the complexes of Dy(III) and Tm(III) were EPR silent. The frozen glass spectra possess a large signal at ~ 12000 G due to impurities in

the glass capillaries and the smaller signal in all spectra at a similar field is due to an impurity in the cavity.

The EPR spectra were similar in the solid and frozen glass for both **[Tb.L^{1}(H$_2$O)]** and **[Tb.L^{3}]** (*Figure 2.32*). The absorption-like feature at low field can most likely be attributed to the large g_z component of a strongly axial pseudo-doublet (Tb(III) is non-Kramers'). The stabilisation of an axial pseudo-doublet can be rationalised on electrostatic grounds,[54] where two *trans*- anionic pendant arms form a stronger axial potential than the single anionic pendant arm *trans* to the pyridine arm. The perpendicular components of the pseudo-doublet (*i.e.* g_x and g_y) are not observed because the sample is weak and the signals are too broad. In solution, the spectra gain slightly more structure due to the hyperfine splitting with the $I = 3/2$ nuclear spin of the isotope, ^{159}Tb (100%).

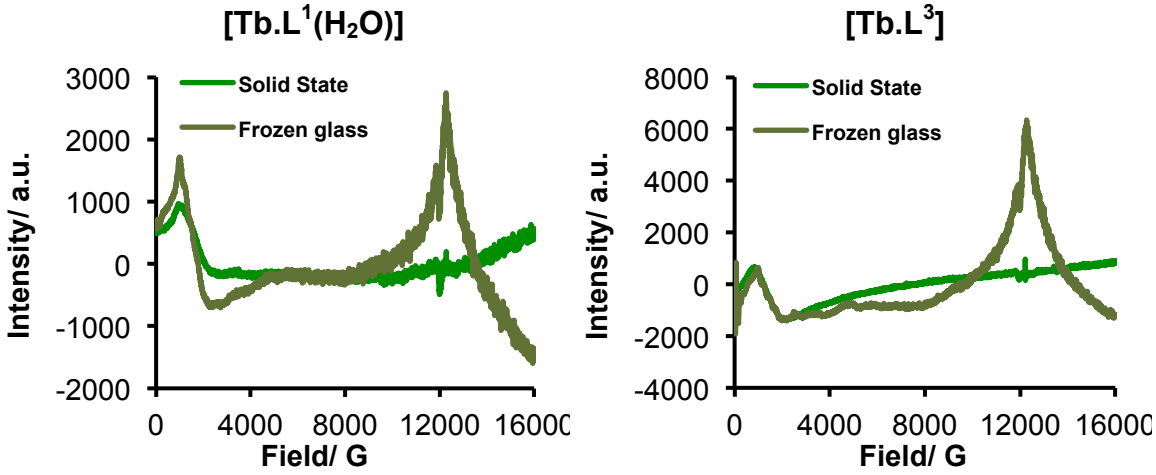

Figure 2.32 Q-band EPR spectra of **[Tb.L^{1}(H$_2$O)]** (*left*) and **[Tb.L^{3}]** (*right*), recorded in the solid-state and in a frozen glass (80% water, 20% glycerol) at 5 K. The large signal at 12000 G is attributed to an impurity in the glass capillary and the small signal at the same field is due to a cavity impurity.

The spectra for **[Er.L^{3}]** appear to be very similar in both the solid and frozen states, displaying two resonances from the ground Kramers' doublet (*Figure 2.33, right*). The low-field feature is attributed to a high g_z value, however the feature at 7000 – 8000 G is yet to be assigned to either a purely axial $g_x = g_y$ signal or only one of these components. In the latter case, the remaining feature may occur at higher field and/or be much broader and is possibly not observed. Such behaviour could relate to the bigger T_{1e} value found for Er(III) in the tri-phosphinate complex, in *Section 2.5.2*. The EPR spectrum for **[Er.L^{1}(H$_2$O)]** in the solid-state is very striking, clearly showing three

transitions corresponding to g_x, g_y and g_z (*Figure 2.33, left*). When recorded as a frozen glass, the spectral profile changes dramatically, apparently indicating that the high field resonances have collapsed down and the g_z feature has moved up in field. Such a marked change between the solid and frozen state spectra implies a significant change in the molecule, resulting in a much more isotropic ground Kramers' doublet, and can be tentatively rationalised by a change in hydration of the complex. In the frozen glass, the sample almost certainly exists as the hydrated species **[Er.L^{1}(H$_2$O)]**. However, it is possible that the complex might not possess bound water in the solid-state, giving rise to stark differences in the EPR spectra of the two samples. An inference such as this is consistent with the spectra obtained for the q = 0 **[Er.L^{3}]** complex, where there is no observed difference between the solid and frozen states. In contrast, both Tb(III) complexes showed similar solid and frozen state EPR spectra, accounted for by their rather hygroscopic and 'sticky' nature in the solid-state.

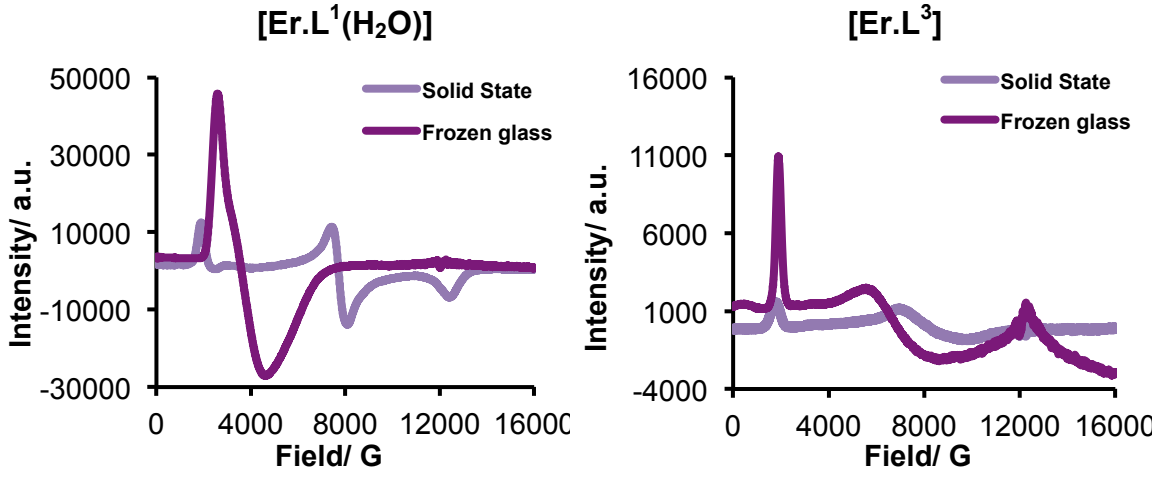

Figure 2.33 Q-band EPR spectra of **[Er.L^{1}(H$_2$O)]** (*left*) and **[Er.L^{3}]** (*right*), recorded in the solid-state and in a frozen glass (80% water, 20% glycerol) at 5 K. The large signal at 12000 G is attributed to an impurity in the glass capillary and the small signal at the same field is due to a cavity impurity.

In these systems, the difference between Er(III) and Dy(III) is remarkable. Both are Kramers' ions but the Er(III) analogues have gorgeous spectra whilst the Dy(III) analogues are EPR silent. This behaviour occurs because, in the same environment, the ground states must have very different m_J compositions, owing to the different nature of the pure m_J states between the two ions. In fact, such an observation makes sense: in the same axial potential (as evidenced for Tb(III)), Dy(III) has a nearly-pure large $|m_J|$ state and Er(III) has a very mixed state.

The non-Kramers' ion Tm(III) appears to have a singlet ground state (see later, *Section 2.5.2.2*) and an EPR spectrum was not observed. In the case of Tb(III), the pseudo-doublet ground state stabilised by the axial potential must possess some $\Delta m_J = \pm 1$ character components. Thus, information about the mixing in Tb(III) compared to Dy(III) can be gleaned, which most likely relates to the low symmetry perturbations affecting the non-Kramers' Tb(III) compared to the Kramers' Dy(III) and reflects the latter's tendency to display Single Molecule Magnetic (SMM) behaviour.[55]

2.5.2.2 Magnetic Susceptibility Studies

Magnetic susceptibility measurements were collected by Dr. Nicholas Chilton at the University of Manchester on the tri-carboxylate, **[Ln.L^{1}(H$_2$O)]**, and tri-phosphinate, **[Ln.L^{3}]**, complexes of Tb(III), Dy(III), Er(III) and Tm(III) at 0.5 T.

The magnetisation profiles for the Tb(III), Dy(III) (shown in *Figure 2.34, left*) and Er(III) samples are consistent with well isolated and anisotropic ground-state doublets (pseudo-doublet in the case of the Tb(III)). The data for both Tm(III) samples exhibit overlapping magnetisation isotherms at 2 and 4 K (*Figure 2.34, right*), indicating an isolated singlet state that has some degree of magnetic character. This singlet state is not a traditional singlet state; instead it is highly anisotropic with a magnetic field dependence (hence non-zero magnetisation). This behaviour explains the lack of an EPR signal for the Tm(III) complexes in *Section 2.5.2.1*, since there is no state within the microwave energy (~ 1 cm^{-1} at Q-band).

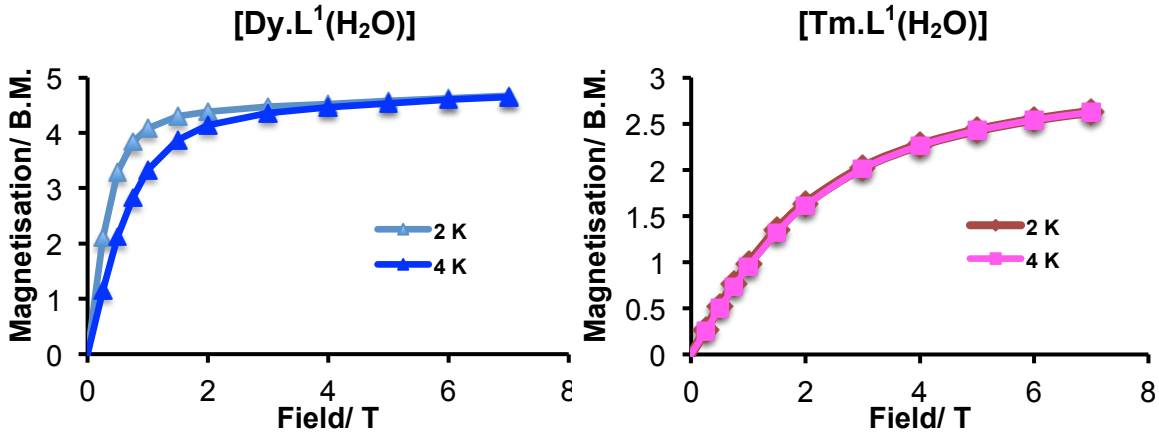

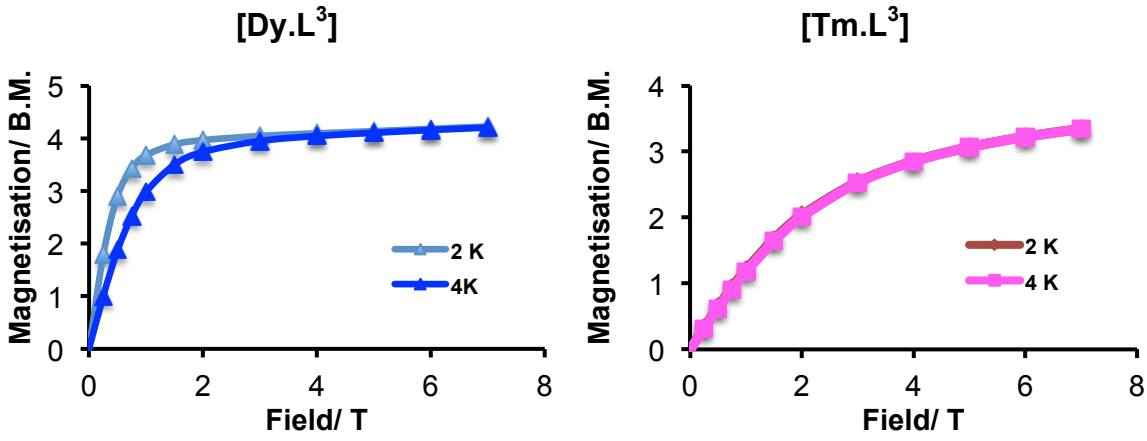

Figure 2.34 The magnetisation of selected **[Ln.L^{1}(H$_2$O)] and [Ln.L^{3}]** complexes as a function of magnetic field strength, measured at 2 and 4 K. (Top, *left*) **[Dy.L^{1}(H$_2$O)]**, (top, *right*) **[Tm.L^{1}(H$_2$O)]**, (bottom, *left*) **[Dy.L^{3}]**; (bottom, *right*) **[Tm.L^{3}].**

In general, the magnetic susceptibility, χT, decreases as a function of decreasing temperature for all four samples, owing to the depopulation of the crystal field states (*Figure 2.35*). Such a profile gives an indication of the splitting of the lowest spin-orbit manifold but cannot provide unequivocal evidence on the energy or m_J composition of the states, in the absence of further more-detailed investigations.

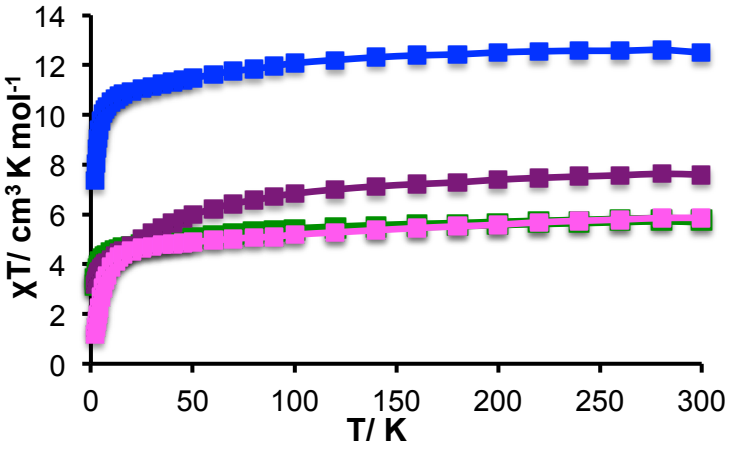

Figure 2.35 The magnetic susceptibility, χT, of the **[Ln.L^{1}(H$_2$O)]** complexes as a function of temperature, where Ln = Tb (green), Dy (blue), Er (purple) and Tm (pink), measured in a 0.5 T field.

However, the experimental magnetic susceptibility values were systematically lower than the theoretical values (*Table 2.12*). Such errors can be attributed to the small amount of sample analysed (< 10 mg) and the presence of diamagnetic impurities (up to ~ 30% sodium formate from HPLC purification), resulting in a small paramagnetic signal comparable to the diamagnetic contribution. A situation such as this means that the diamagnetic impurities cannot accurately be corrected for, and as a result, the

measurements are not entirely representative of the complexes studied here. The situation was exacerbated by the hygroscopic nature of the samples, such that variable water amounts were present long after [Ln(III)] had been calculated on each sample by ICP-MS and BMS methods. However, a general trend has been established where the Dy(III) and Tb(III) tri-carboxylate room temperature average magnetic moments are greater than the analogous tri-phosphinate complexes, and the Er(III) and Tm(III) tri-phosphinate values are greater than the analogous tri-carboxylate complexes, echoing the behaviour observed whilst interrogating μ_{eff} and T_{1e} in *Section 2.5.2*. For example, the values of the magnetic moments suggested for **[Dy.L^{1}(H$_2$O)]** and **[Dy.L^{3}]** from this analysis, of 10 and 9.5 BM respectively, echo the trends observed earlier in the ^{1}H NMR data. Clearly, in the future, the samples must be sealed, after the thorough removal of the diamagnetic impurities has been carried out and/or corrected for, before reliable data can be obtained.

Table 2.12 Theoretical and experimental χT values for the **[Ln.L^{1}(H$_2$O)]** complexes.

Lanthanide(III) ion	**Ground state term**	***g***	**Theoretical χT value**	**Experimental χT value**
Tb	$^{7}F_6$	3/2	11.82	5.75
Dy	$^{6}H_{15/2}$	4/3	14.17	12.50
Er	$^{4}I_{15/2}$	6/5	11.48	7.59
Tm	$^{3}H_6$	7/6	7.15	5.86

2.6 Conclusions

The feasibility of using lanthanide(III) based paramagnetic, *i.e.* PARASHIFT, probes for ^{1}H MRS studies, in which a reporter resonance is highly shifted from the diamagnetic region, has been of interest over the last two decades, as shown by the examples highlighted in *Section 1.3*. However, whilst some promising *in vivo* studies have been reported, limitations regarding signal intensity are continually cited and as a result, high doses and long acquisition times are used. Such limitations pose significant drawbacks to this inherently more sensitive imaging technique, which takes advantage of imaging where there is a zero-background signal *in vivo*, and has left progress in the field somewhat behind that of heteronuclear (*i.e.* ^{19}F) imaging.

The work detailed here goes some way to bridging that gap, focusing on the design, synthesis and application of a novel class of ^{1}H PARASHIFT probes, with the criteria

outlined at the end of *Chapter 1* of fundamental significance. Three parent systems have been derived, in which a reporting *tert*-butyl resonance is incorporated about 6.5 Å from a lanthanide(III) ion in a kinetically stable macrocyclic complex (*Figure 2.36*). At such a distance, the *tert*-butyl reporter is shifted to a ^{1}H NMR window that is well removed from the diamagnetic range, allowing its selective observation. Additionally, prudent selection of the lanthanide(III) ion, in accord with magnetic field strength, leads to R_1 values of the order of 100 to 200 s^{-1}, permitting faster data acquisition per unit time in spectroscopy and imaging protocols; a concept not fully optimised in the literature examples. Furthermore, by selecting a *tert*-butyl group, the number of magnetically equivalent nuclei comprising the reporter resonance is maximised.

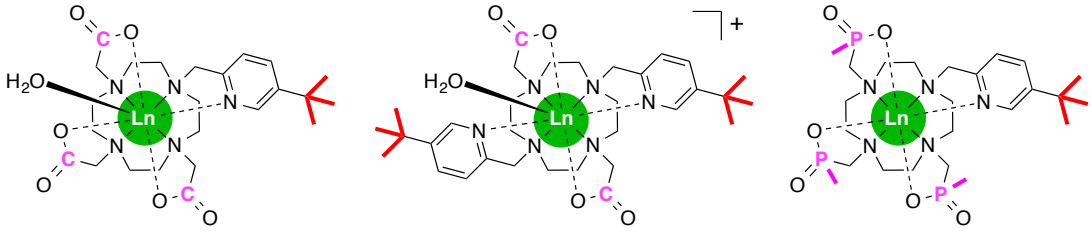

Figure 2.36 The ^{1}H PARASHIFT probes detailed in this Chapter: the model system, **[Ln.L^{1}(H$_2$O)]** (*left*); the C_2-symmetric system, **[Ln.L^{2}(H$_2$O)]$^{+}$** (*middle*) and the phosphinate system, **[Ln.L^{3}]** (*right*).

The Dy(III) complex proved to be the most attractive candidate from the proof-of-principle tri-carboxylate series, **[Ln.L^{1}(H$_2$O)]** (*Figure 2.36*), possessing a *tert*-butyl chemical shift of -20.1 ppm, with an R_1 value of about 100 Hz at 7 T. However, the R_1/R_2 ratio was moderate (0.6 at 9.4 T) and so further enhancements were sought, in order to achieve an R_1/R_2 ratio close to unity and further enhance the sensitivity in MRS protocols.

An enhancement in signal intensity was observed for the C_2-symmetric bis-carboxylate series, **[Ln.L^{2}(H$_2$O)]$^{+}$** (*Figure 2.36*), bearing two equivalent *tert*-butyl reporter groups. The case of Dy(III) once again presented the most attractive candidate for *in vivo* studies, displaying a 60% increase in the R_1 value (150 Hz at 7 T) and a significant increase in the R_1/R_2 ratio (0.8 at 9.4 T). This enhanced sensitivity permitted strong ^{1}H MRS images to be obtained following the injection of solutions of **[Dy.L^{2}(H$_2$O)]$^{+}$** into live mice, showing strong localisation of the complex in the muscular tissue, followed by clearance to the bladder. In each study, the signal for the *tert*-butyl reporter was acquired, without water interference, within a few minutes (<6 min), at a well-tolerated dose (0.12 mmol kg^{-1}) that is of the same order as commercially administered Gd(III)-

based contrast agents. However, in order to further reduce acquisition times, a spectral bandwidth of more than 20 kHz was desired, requiring shifts of over 10 kHz from the water and fat signals *in vivo*.

Remarkable *tert*-butyl chemical shifts of up to ±70 ppm were achieved for the tri-phosphinate series, **[Ln.L^{3}]** (*Figure 2.36*), exhibiting shift enhancements of up to 60 ppm compared to the tri-carboxylate series, in the cases of Tb(III) and Tm(III). Analysis of the relaxation rate behaviour presented a few surprises, however. Only the Er(III) complex showed the required R_1 value at 7 T, and the Tm(III) complex possessed an 80% increase in R_1 relative to its tri-carboxylate analogue. Meanwhile, both the Tb(III) and Dy(III) complexes displayed systematically lower R_1 values in comparison to their tri-carboxylate equivalents.

Such unprecedented behaviour prompted further investigations into the comparative shift and relaxation behaviour of the **[Ln.L^{1}(H$_2$O)]** and **[Ln.L^{3}]** series, where the scope and limitations of current theories that address magnetic susceptibility and its anisotropy in lanthanide(III) complexes were assessed using optical spectroscopy, EPR spectroscopy and SQUID magnetometry. One of the approximations that does not hold up in many lanthanide(III) systems is whether J is a good quantum number in the Landé and Van Vleck approximations, most generally used to treat paramagnetism, and the assumption that J-mixing does not occur. With the 'goodness' of J far from certain, the Bleaney coefficients, C_J, in Bleaney's theory that are derived from J, and μ_{eff} in paramagnetic relaxation theory that is derived from the Landé factor, are rendered inadequate. Whilst these two theories underpin the analysis of paramagnetic induced shifts and paramagnetic relaxation, respectively, clearly a challenge is presented to build a better approach towards predicting the behaviour of lanthanide(III) complexes such as those reported herein, through modern computational methods.

With promising results presented thus far, the basic framework from which future PARASHIFT probes can be derived has been established. The next step for this work is to address the idea of responsiveness, where the relative chemical shift of the reporter resonance is indicative of a stimulus in the local environment of the probe.

2.7 References

1. P. Harvey, A. M. Blamire, I. Wilson, K.-L. N. A. Finney, A. M. Funk, P. K. Senanayake and D. Parker, *Chem. Sci.*, 2013, **4**, 4251–4258.
2. B. Bleaney, *J. Magn. Reson.*, 1972, **8**, 91–100.
3. N. Bloembergen, *J. Chem. Phys.*, 1957, **27**, 572–573.
4. I. Soloman, *Phys. Rev.*, 1955, **99**, 559–565.
5. M. R. Goldman, *J. Magn. Reson.*, 2001, **149**, 160–187.
6. A. G. Redfield, *IBM Journal of Research and Development*, 1957, **1**, 19–31.
7. S. Aime, A. S. Batsanov, M. Botta, J. A. K. Howard, M. P. Lowe and D. Parker, *New J. Chem.*, 1999, 669–670.
8. K. H. Chalmers, M. Botta and D. Parker, *Dalton Trans.*, 2011, **40**, 904–913.
9. O. Reany, T. Gunnlaugsson and D. Parker, *J. Chem. Soc., Perkin Trans. 2*, 2000, 1819–1831.
10. T. W. Bell, L. Y. Hu and S. V. Patel, *J. Org. Chem.*, 1987, **52**, 3847–3850.
11. P. Harvey, Durham University, 2013.
12. A. Beeby, I. M. Clarkson, R. S. Dickens, S. Faulkner, D. Parker, L. Royle, A. S. de Sousa, J. A. G. Williams and M. Woods, *J. Am. Chem. Soc., Perkin Trans. 2*, 1999, 493–504.
13. J.-C. G. Bunzli and C. Piquet, *Chem. Soc. Rev.*, 2005, **34**, 1048–1077.
14. A. E. Merbach and E. Toth, *The chemistry of contrast agents in medicinal magnetic resonance imaging*, Wiley, New York, Chichester, 2001.
15. P. Caravan, J. J. Ellison, T. J. McMurry and R. B. Lauffer, *Chem. Rev.*, 1999, **99**, 2293–2352.
16. V. S. Mironov, Y. G. Galyametdinov, A. Ceulemans, C. Görller-Walrand and K. Binnemans, *Chem. Phys. Lett.*, 2001, **345**, 132–140.
17. V. S. Mironov, Y. G. Galyametdinov, A. Ceulemans, C. Görller-Walrand and K. Binnemans, *J. Chem. Phys.*, 2002, **116**, 4673–4685.
18. R. D. Shannon, *Acta Crystallogr. Sect. A*, 1976, **32**, 751–767.
19. J. B. Gruber, R. P. Leavitt, C. A. Morrison and N. C. Chang, *J. Chem. Phys.*, 1985, **82**, 5373–5378.
20. K. Binnemans and C. Görller-Walrand, *C. Chem. Phys. Lett.*, 1995, **245**, 75–78.
21. A. M. Funk, Durham University, 2014.
22. D. Parker, R. S. Dickens, H. Puschmann, C. Crossland and J. A. K. Howard, *Chem. Rev.*, 2002, **102**, 1977–2010.
23. J. W. Walton, L. D. Bari, D. Parker, G. Pescitelli, H. Puschmann and D. S. Yufit, *Chem. Comm.*, 2011, **47**, 12289–12291.
24. S. Aime, M. Botta, Z. Garda, B. E. Kucera, G. Tireso, V. G. Young and M. Woods, *Inorg. Chem.*, 2011, **50**, 7955–7965.
25. P. Harvey, I. Kuprov and D. Parker, *Eur. J. Inorg. Chem.*, 2012, **12**, 2015–2022.
26. A. M. Funk, P. H. Fries, P. Harvey, A. M. Kenwright and D. Parker, *J. Phys. Chem. A*, 2013, **117**, 905–917.
27. H. Gysling and M. Tsutsui, *Adv. Organomet. Chem.*, 1971, **9**, 361–395.
28. A. M. Funk, P. Harvey, K.-L. N. A. Finney, M. A. Fox, A. M. Kenwright, N. J. Rogers, P. K. Senanayake and D. Parker, *Phys. Chem. Chem. Phys.*, 2015, **17**, 16507–16511.
29. T. Frenzel, K. Roth, S. Kossler, B. Raduchel, H. Bauer, J. Platzek and H.-J. Weinmann, *Magn. Reson. Med.*, 1996, **35**, 364–369.
30. K. Roth, G. Bartholomae, H. Bauer, T. Frenzel, S. Kossler, J. Platzek, B. Raduchel and H.-J. Weinmann, *Angew. Chem. Int. Ed. Engl.*, 1996, **35**, 655–657.

31. S. K. Pakin, S. K. Hekmatyar, P. Hopewell, A. Babsky and N. Bansal, *NMR Biomed.*, 2006, **19**, 116–124.
32. A. Rodríguez-Rodríguez, Z. Garda, E. Ruscsák, D. Esteban-Gómez, A. de Blas, T. Rodríguez-Blas, L. M. P. Lima, M. Beyler, R. Tripier, G. Tircsó and C. Platas-Iglesias, *Dalton Trans.*, 2015, **44**, 5017–5031.
33. Z. Kovacs and A. D. Sherry, *Synthesis-Stuttgart*, 1997, 759–763.
34. K. H. Chalmers, A. M. Kenwright, D. Parker and A. M. Blamire, *Magn. Reson. Med.*, 2011, **66**, 931–936.
35. P. K. Pulukoddy, T. J. Norman, D. Parker, L. Royle and C. J. Broan, *J. Am. Chem. Soc., Perkin Trans. 2*, 1993, **2**, 605–620.
36. E. Cole, C. J. Broan, K. J. Jankowski, P. K. Pulukoddy, D. Parker, A. T. Millican, N. R. A. Beeley, K. Millar and B. A. Boyce, *Synthesis*, 1992, 63–68.
37. S. Aime, M. Botta, D. Parker and J. A. G. Williams, *J. Chem. Soc., Dalton Trans.*, 1995, 2259–2266.
38. D. Parker and J. A. G. Williams, *J. Chem. Soc., Dalton Trans.*, 1996, 3613–3628.
39. K. H. Chalmers, E. De Luca, N. H. M. Hogg, A. M. Kenwright, I. Kuprov, D. Parker, M. Botta, I. Wilson and A. M. Blamire, *Chem. Eur. J.*, 2010, **16**, 134–148.
40. G. T. P. Charnock and I. Kuprov, *Phys. Chem. Chem. Phys.*, 2014, 20184–20189.
41. J. D. Rinehart and J. R. Long, *Chem. Sci.*, 2011, **2**, 2078–2085.
42. M.-E. Boulon, G. Cucinotta, J. Luzon, C. Degl'Innocenti, M. Perfetti, K. Bernot, G. Calvez, A. Caneschi and R. Sessoli, *Angew. Chem. Int. Ed.*, 2013, **52**, 350–354.
43. G. Cucinotta, M. Perfetti, J. Luzon, M. Etienne, P.-E. Car, A. Caneschi, G. Calvez, K. Bernot and R. Sessoli, *Angew. Chem. Int. Ed.*, 2012, **51**, 1606–1610.
44. J. Luzon and R. Sessoli, *Dalton Trans.*, 2012, **41**, 13556–13567.
45. R. S. Dickens, D. Parker, J. I. Bruce and D. J. Tozer, *J. Chem. Soc., Dalton Trans.*, 2003, 1264–1271.
46. O. A. Blackburn, N. F. Chilton, K. Keller, C. E. Tait, W. K. Myers, E. J. McInnes, A. M. Kenwright, P. D. Beer, C. R. Timmel and S. Faulkner, *Angew. Chem. Int. Ed. Engl.*, 2015, **54**, 10783–10786.
47. S. Shintoyo, K. Murakami, T. Fujinami, N. Matsumoto, N. Mochida, T. Ishida, Y. Sunatsuki, M. Watanabe, M. Tsuchimoto, J. Mrozinski, C. Coletti and N. Re, *Inorg. Chem.*, 2014, **53**, 10359–10369.
48. J. Long, V. Remi, R. A. S. FerreIra, L. D. Carlos, F. A. A. Paz, Y. Guari and J. Larionova, *Chem. Comm.*, 2012, **48**, 9974–9976.
49. M. Ren, S.-S. Bao, R. A. S. Ferreira, L.-M. Zheng and L. D. Carlos, *Chem. Comm.*, 2014, **50**, 7621–7624.
50. O. A. Blackburn, M. Tropiano, J. Sorensen, J. Thom, A. Beeby, L. M. Bushby, D. Parker, L. S. Natrajan and S. Faulkner, *Phys. Chem. Chem. Phys.*, 2012, **14**, 13378–13384.
51. I. Bertini, C. Luchinat and G. Parigi, *Prog. Nucl. Magn. Reson. Spectrosc.*, 2002, **40**, 249–273.
52. A. J. Vega and D. Fiat, *Mol. Phys.*, 1976, **31**, 347–355.
53. J. Hölsä, M. Lastusaari, J. Niittykoski and R. S. Puche, *Phys. Chem. Chem. Phys.*, 2002, **4**, 3091–3098.
54. N. F. Chilton, D. Collison, E. J. L. McInnes, R. E. P. Winpenny and A. Soncini, *Nature Commun.*, 2013, **4**, 2551.
55. D. N. Woodruff, R. E. P. Winpenny and R. A. Layfield, *Chem. Rev.*, 2013, **113**, 5110–5148.

Chapter Three: Development of pH Responsive ^{1}H PARASHIFT Probes

3.1 Introduction

As introduced in *Chapter 1*, ^{1}H magnetic resonance spectroscopic imaging studies are limited due to the strong water and fat signals *in vivo*. Following the recent successes in ^{19}F MRI, novel ^{1}H paramagnetic lanthanide(III)-based probes were developed, and described in *Chapter 2*. In such systems, judicious placement of a *tert*-butyl reporter group within 6 to 7 Å of a paramagnetic lanthanide(III) centre has two benefits for MRS imaging protocols. First of all, the chemical shift of the reporter group is enhanced *via* the pseudocontact shift mechanism (see *Section 1.2.1.1, page 15*), leading to observed shifts >60 ppm away from the water signal. Such a shift magnitude is necessary, if bandwidths around 20 kHz are to be used in imaging sequences (*i.e.* δ_H < -34 ppm or > +44 ppm). Secondly, the relaxation behaviour of the *tert*-butyl reporter nuclei has been optimised so that the longitudinal relaxation rate, R_1, is in the 100 to 200 s^{-1} range at 7 T, and chemical exchange broadening processes are limited such that R_1/R_2 is close to unity; permitting fast data acquisition. Such success opens up many possibilities for new imaging experiments to be developed, and with this in mind the next step is to adapt the systems in *Chapter 2* to incorporate responsiveness towards a biologically relevant marker. The responsiveness of a probe is defined as its ability to measure fluctuations in the concentration of a biologically relevant species, such as H^+ (pH) or Ca^{2+} (pM^{n+}), by means of an interpretable experimental read-out.

Of course, the concept of responsive probe behaviour has been demonstrated before, in the field of MRI. In *Section 1.1.1*, the excellence of using the contrast of an MR image to detect even subtle changes in anatomy and function was described. However, the reliability of making diagnoses from the image contrast information alone is poor.[1] For example, in the diagnosis of breast cancer, MRI is far superior to X-radiography in its ability to detect tumours, but it cannot readily distinguish between malignant and cancerous tissue, lending itself to misdiagnoses and needless false-positive results.[2] Also, changes that are detectable by MRI are often only present in the mid- to late-stages of disease development, and detection of these, in some cases, can be too late.[1] In an effort to overcome these limitations and recognising the possibility of probing

physiological environments non-invasively, a vast amount of work has gone into the development of responsive Gd(III)-based MRI contrast agents, where relaxivity changes as a function of an environmental factor in the area in which they localise. Since the relaxivity is concentration dependent (see *equation 3* in *Section 2.2.2*), and therefore complicated to quantify *in vivo*, the majority of the literature reports *in vitro* examples, with very few being translated to *in vivo* studies.[3]

When deciding how to make a system responsive, the parameter under investigation merits careful selection. Perhaps the most straightforward and understood parameter is that of pH; a particular interest in biological systems, where fluctuations can be associated with various pathologies such as stroke, infection and renal failure. A technique with which pH changes can be monitored is highly sought after in cancer diagnosis in particular, with malignant tissue often found to be more acidic due to reduced bicarbonate levels, poor perfusion rates or increased lactic acid secretion.[4,5]

Early techniques for measuring pH included the use of microelectrodes, however due to their destructive and invasive nature, alternative methods have been sought.[6] Before the advent of ^{19}F NMR, ^{31}P MRS studies became the obvious choice due to its 100 % abundance, I = ½, large chemical shift range and the prevalent nature of ^{31}P in many biological metabolites at mM levels; these are detailed in *Section 1.1.2*. However, the limited sensitivity associated with ^{31}P MRS permitted only one example to be applied *in vivo*, presenting measurements from large tissue volumes only and non-discrete pH values for isolated spatial locations.[7]

In light of these limitations, the use of paramagnetic lanthanide(III)-based probes has been investigated, where changes in pH can be signalled by a change in the relative chemical shift of the probe's reporter resonance. As a result of the close proximity (4.5-7.5 Å) of the reporter nuclei to a lanthanide(III) centre, the chemical shift non-equivalence is magnified such that small structural and/or conformational changes afforded by the protonation/deprotonation events result in amplified chemical shift differences between the acid and base forms. This experimental read-out is concentration independent, negating the major problem of calibration that is hindering the translation of responsive Gd(III) contrast agents to *in vivo* protocols.

It was briefly discussed in *Section 1.1.2*, how ^{19}F MRI has been a focus of interest over the last 30 years, and in particular the more recent development of fluorinated paramagnetic lanthanide(III) probes.[8–14] Research in Durham over the last decade has led to the development of novel fluorinated paramagnetic lanthanide(III) complexes with interesting pH responsive ^{19}F chemical shift behaviour. The first example describes a fluorinated Ho(III) complex, where pH sensitivity arises due to the on-off ligation of a sulphonamide moiety, as shown in *Figure 3.0*.[9] The ^{19}F chemical shift separation between the two forms is 40 ppm but chemical exchange between the acid and base forms is slow on the NMR timescale, such that the relative ratios of the two peaks vary with pH. The pK_a of this ratiometric process was found to differ in 0.1 M NaCl solution (5.71) and mouse serum or urine (6.92), due to the presence of competitive hydrogen carbonate binding that shifts the equilibrium in favour of the acid form in the latter.

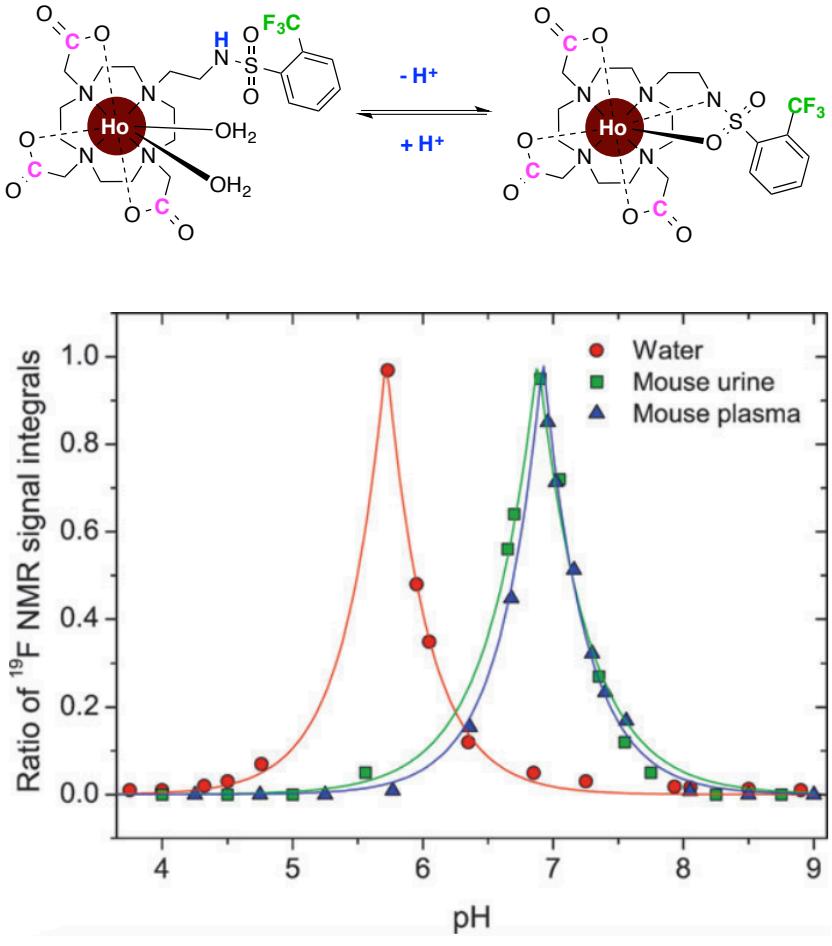

Figure 3.0 (*Top)* Schematic representation of the pH sensitive mode of operation of the sulphonamide moiety on the complex. (*Bottom*) The pH dependence of the ^{19}F chemical shift for the Ho(III) sulphonamide complex in water, mouse urine and mouse plasma.[9]

In the second example, a fluorinated Ho(III) complex with a different pH sensitive coordinated moiety was described, displaying pH sensitivity through the protonation/deprotonation behaviour of an amide nitrogen (*Figure 3.1)*.[9,10] The most promising results were achieved for the *ortho*-cyano bearing system. Unlike the previous example, this system exhibited fast exchange between the acid and base forms on the NMR timescale, so that a time-averaged signal was observed, varying in shift as a function of pH, with a pK_a of 7.1 (*Figure 3.1*). Due to the restricted rotation about the aryl C-N bond, this system exists as two major isomers in solution. Such an occurrence is of benefit ratiometrically, provided that each isomer exhibits large chemical shift non-equivalence and a different pH-dependent chemical shift. As a result, a ratiometric approach was used to calculate the pH, by measuring the shift separation between the two isomers (~$\Delta\delta_F$ = 14 ppm).

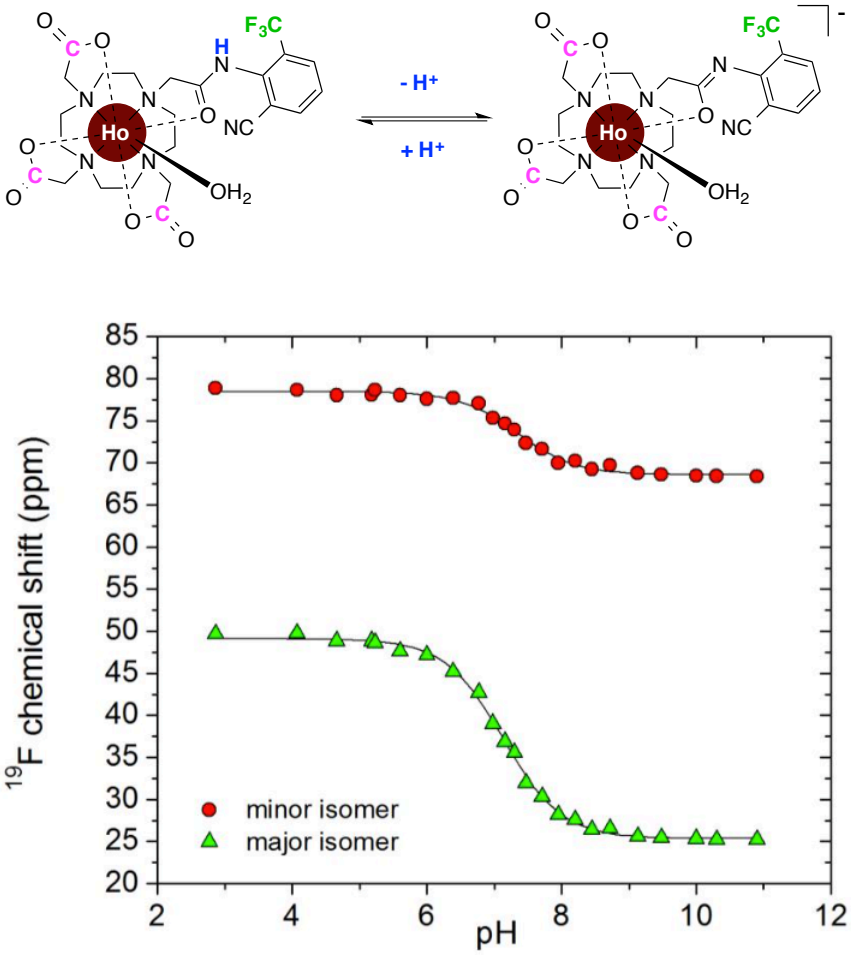

Figure 3.1 (*Top)* Schematic representation of the protonation/deprotonation behaviour of the amide nitrogen on the complex. (*Bottom*) The variation in the ^{19}F chemical shift for the two isomers of the Ho(III) *ortho*-cyano amide complex.[10]

In both examples, the ratiometric approach alleviates the requirement for calibrating the chemical shift: in the second case the pH was measured using the pH dependent chemical shift separation, and in the previous example it relies upon measuring the pH dependent ratio of two signals. Ideally, the number of isomeric species in solution should be minimised so that one signal dominates, and is a key consideration when designing future systems. Also, it is far easier to monitor a shift difference than a relative ratio change in MRS imaging protocols, and so fast exchange on the NMR timescale is favoured. Nevertheless, the works detailed above do possess favourable characteristics, such as pK_a values around 7, and functionality in the physiological range (pH 5.5-7.5).

However, the use of ^{19}F MRI is far from trivial in commercially available ^{1}H operating systems, thus leading to the development of ^{1}H paramagnetic lanthanide(III) (PARASHIFT) probes, such as those described in this thesis. Amongst the ^{1}H PARASHIFT probes highlighted in *Section 1.3*, the Yb(III) and Tm(III) complexes of DOTP were shown to possess pH sensitive chemical shifts (*pages 27 and 29-30*).[15,16] However, neither of these studies appreciated properly the need for a ^{1}H reporter group with a high equivalent spin density, the importance of lanthanide(III) ion selection, or the benefits of paramagnetic longitudinal relaxation enhancement in terms of increasing sensitivity in MRS imaging experiments.

In an effort to address these issues, more recent work in Durham has seen the development of a pH responsive ^{1}H PARASHIFT probe, in close relation to the systems outlined within *Chapter 2*. The complex possesses a *tert*-butyl reporter group, situated 6 to 7 Å away from a paramagnetic lanthanide(III) centre (*Figure 3.2*).[17] Additionally, Dy(III) has been selected in order to achieve the desired enhancements in R_1 (140±8 s^{-1} at 4.7 T, 185±10 s^{-1} at 9.4 T). The pH sensitive mode of operation relies on the previously observed concept of the reversible ligation of a *trans*- sulphonamide moiety. At high pH, the sulphonamide moiety is deprotonated and binds to the lanthanide(III) centre through the nitrogen atom, further stabilised by additional ligation through the sulphur oxygen atom. At pH 8, the *tert*-butyl reporter group resonates at -58.9 ppm (*Figure 3.2*).[18] As the pH lowers, protonation occurs so that sulphonamide coordination can no longer occur and a solvent water molecule binds instead to complete the coordination sphere, a theory confirmed by measuring the radiative lifetimes of the corresponding Tb(III) complex in D_2O and H_2O. At pH 4, the *tert*-butyl reporter

resonance cannot be observed. Such an observation is thought to arise due to the severity of the line-broadening associated with an increased rate of chemical exchange when the sulphonamide functionality is unbound. As a result, in order for pH changes to be measured, an internal standard is required so that relative signal intensity changes can be compared, thereby offering little improvement on the first fluorinated Ho(III) complex.

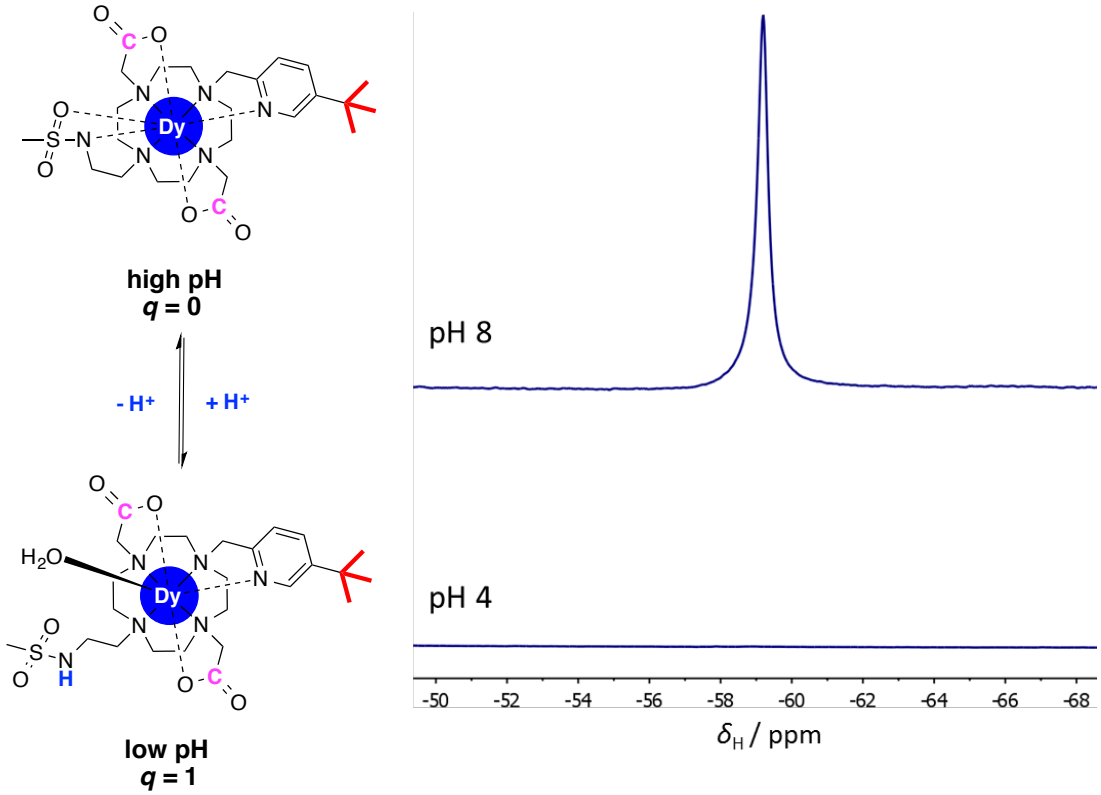

Figure 3.2 (*Left)* Schematic representation of the pH functionality of the sulphonamide moiety on the complex. (*Right*) ^{1}H NMR spectra for the Dy(III) complex at high and low pH values, indicating the 'loss of signal' at low pH (D_2O, 9.4 T, 298 K).[18]

The above analysis of current pH responsive PARASHIFT probes validates the need for the research outlined in the remainder of this Chapter and indicates that ideal probe characteristics include:

- An acid dissociation constant, pK_a, of the sensing functionality around pH 6.5 to 7.
- An operating window in the physiological range (pH 5.5-7.5).
- Sensitivity such that small pH changes translate to observable changes in the chemical shift.
- The existence of one predominant isomer in solution.

- Fast chemical exchange on the NMR timescale, so that a time-averaged signal is observed.
- Protonation/deprotonation events that are not associated with severe line-broadening.

The design of the novel pH responsive ^{1}H PARASHIFT probes detailed herein are generalised in *Figure 3.3*. The design features are in keeping with the complexes described in *Chapter 2*, since the criteria governing their design still applies to this work. Minimal modifications were sought in order to retain as many of the favourable MR properties as possible. The most notable change arises through the incorporation of an acid/base sensitive functionality in the 4-position of the *tert*-butylpyridyl moiety. It is suggested that, due to its close proximity, any change occurring upon the protonation and/or deprotonation of this functional group will have an effect on the *tert*-butyl chemical shift. This effect is of course amplified, due to the close proximity (6.5 Å) of the *tert*-butyl reporter to the lanthanide(III) ion, that a relatively large shift change was foreseen. Additionally, it was thought that because the change is occurring locally on the pyridyl moiety, line-broadening would be minimised, thereby eliminating problems associated with several of the previous examples.

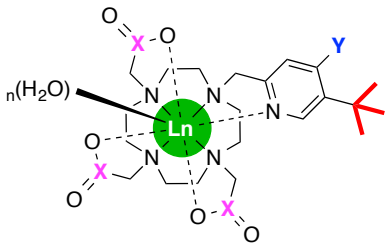

Figure 3.3 The key design features of suggested pH responsive ^{1}H PARASHIFT probes, where X = C or PMe, Y = an acid/base functionality; and n = the number of water molecules (typically 1 when X = C, and 0 when X = PMe).

3.2 First Generation System: A Dimethylamine Substituent

The first system to be designed incorporated a dimethylamine substituent in the 4-position of the *tert*-butylpyridyl moiety, **[Ln.L^{4}(H$_2$O)]** (*Figure 3.4*). It is envisaged that steric inhibition of resonance, created by the *ortho*- *tert*-butyl group, might suppress lone pair conjugation into the pyridine ring. In the absence of the *tert*-butyl group, a *para*-dimethylamine substituent is strongly conjugated, so that protonation at the nitrogen is inhibited and the pK_a <3.[19] Despite the favourable shift enhancements

achieved with phosphinate pendent arms, carboxylate pendent arms were selected for relative ease of synthesis.

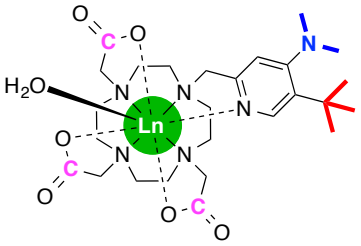

Figure 3.4 The design of the dimethylamine-bearing ^{1}H PARASHIFT probe, **[Ln.L^{4}(H$_2$O)]**.

3.2.1 Complex synthesis and characterisation

The *N*-oxide, ***3***, was prepared as described previously.[17] The desired ring substitution was effected by nitration, using a concentrated mixture of H_2SO_4 and HNO_3, to give the *para*-nitro *N*-oxide, ***41*** (*Scheme 3.0*). The reaction was monitored by thin-layer chromotography and mass spectrometric analysis. Reduction of the nitro- group under low-pressure hydrogenation conditions afforded the amino product, ***42***. However, attempted alkylation with methyl iodide, under both harsh basic and typical S_N2 conditions, did not lead to the desired dimethylamine product. Indeed, only a trace amount of mono-alkylated product was observed by mass spectrometry, suggesting the nitrogen lone pair was still conjugated efficiently, lowering the amine nucleophilicity.

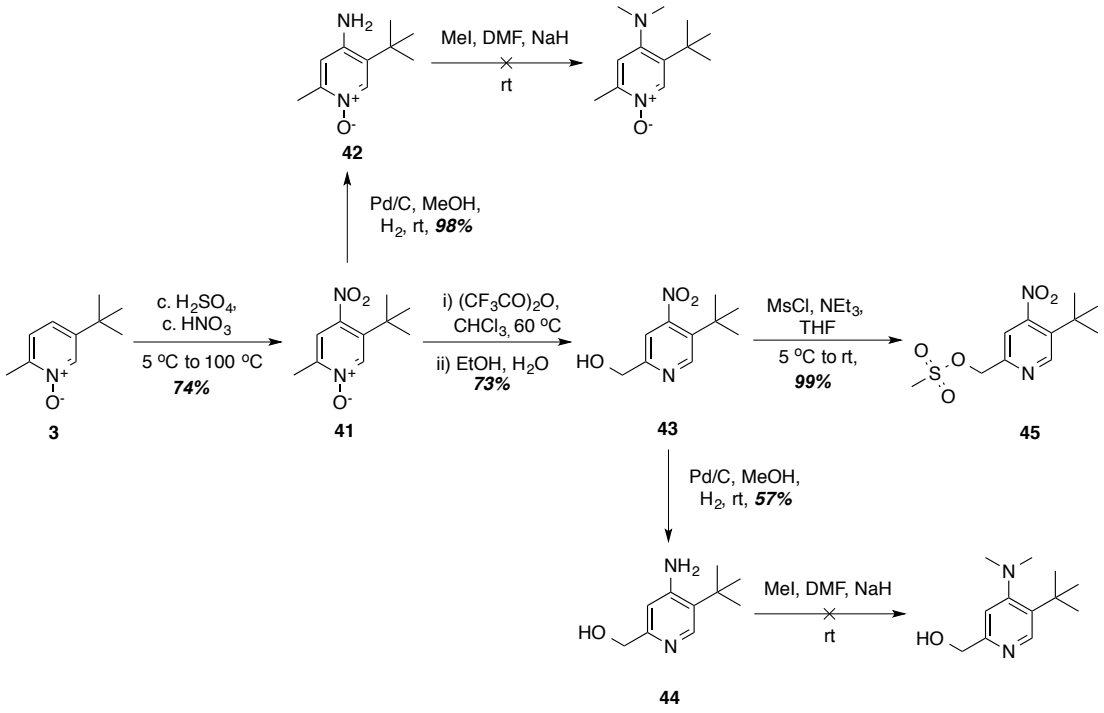

Scheme 3.0 General procedures for the synthesis of the mesylate ***45***.

A similar process was subsequently attempted, opting instead to rearrange the *N*-oxide species prior to reduction and alkylation (*Scheme 3.0*). Accordingly, in the presence of trifluoroacetic anhydride, an intramolecular rearrangement transformed ***41***, to the trifluoroacetate ester intermediate, as characterised by ^{19}F and ^{1}H NMR spectroscopy. The ester was hydrolysed in a 1:1 mixture of ethanol and water to reveal the desired alcohol, ***43***. Nonetheless, following nitro- group reduction, alkylation of the amine species, ***44***, failed to occur again. Such limitations again suggested that the nucleophilicity of the amine is dramatically decreased due to conjugation of the lone pair density into the pyridine ring.

Finally, a reaction pathway involving displacement of the reactive nitro- group on the complex was considered. In this route, the amine species, ***44***, was reacted with methane sulphonyl chloride to gain the mesylate, ***45***, in a near quantitative yield. The mesylate, ***45***, was used without delay to achieve *N*-alkylation of the previously synthesised tri-carboxylate 12-N_4-based macrocycle, ***1*** *(Scheme 3.1)*. Purification of the fully alkylated ligand, ***46***, was achieved using silica gel column chromatography. After the *tert*-butyl ester protecting groups had been removed using trifluoroacetic acid, complexation with Dy(III)Cl_3.6H_2O in aqueous solution, at pH 5.5, gave the intermediate complex, ***47***. The complex ***47*** was characterised by ^{1}H NMR spectroscopy and high-resolution mass spectrometry.

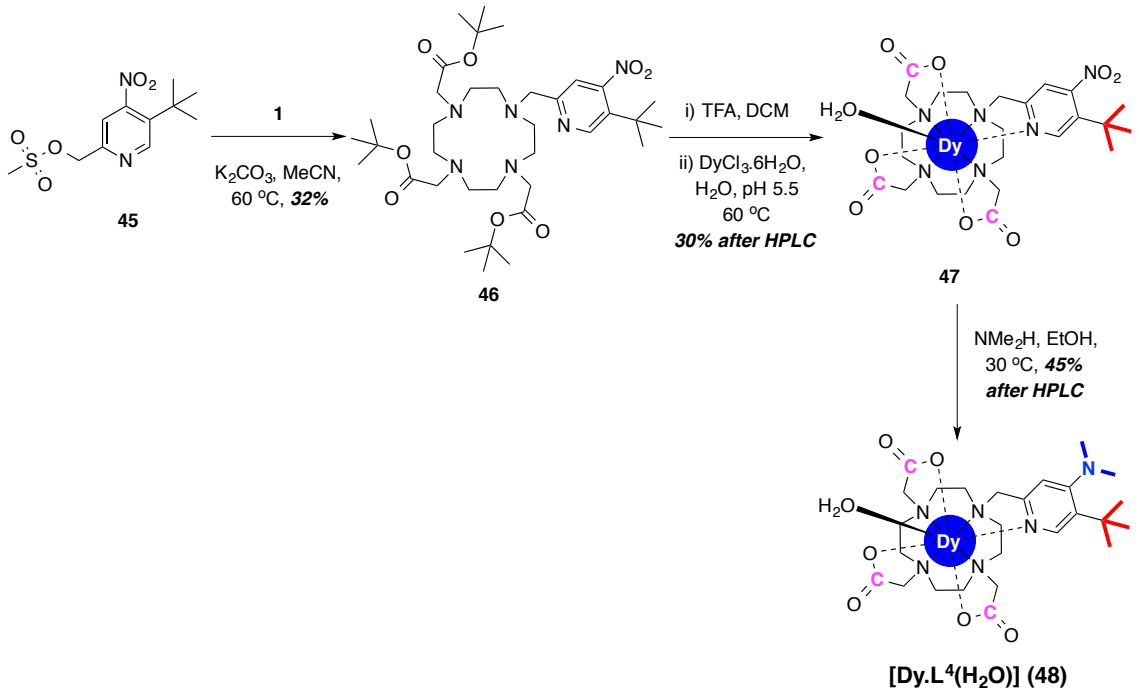

Scheme 3.1 General procedures for the synthesis of **[Ln.L^{4}(H_2O)]**.

In order to transform the *para*-nitro derivative into the desired dimethylamino-compound, a substitution reaction was performed using a solution of dimethylamine in ethanol. This reaction was inspired by previous work in the group, which demonstrated the reactivity of a related 4-nitro-pyridyl 12-N_4-based paramagnetic lanthanide(III) complex towards nucleophilic displacement.[20] It is thought that the enhanced reactivity in the 4-position is brought about by charge transfer to the lanthanide(III) centre, which acts as an 'electron sink' and increases the electrophilicity of the *para*-pyridyl carbon. Following purification of the crude mixture by reverse-phase preparative HPLC (t_R = 5.8 min), **[Dy.L^4(H$_2$O)]** was successfully isolated.

However, the molecular masses of ***47*** and **[Dy.L^4(H$_2$O)]** only differ by 2 mass units, so characterisation by mass spectrometry was uncertain. Other conventional methods such as TLC and reverse-phase analytical HPLC provided ambiguous information, seemingly showing the same retention behaviour as ***47***. In the end, UV absorption spectroscopy and IR spectroscopy were used to confirm the desired identity of **[Dy.L^4(H$_2$O)]**. UV absorption spectral measurements were undertaken for both ***47*** and **[Dy.L^4(H$_2$O)]** (*Figure 3.5*). The values of λ_{max} differ slightly: for ***47***, λ_{max} is 278 nm, whereas for **[Dy.L^4(H$_2$O)]** λ_{max} occurs at 270 nm. Since the observed profile corresponds to the π to π^* transition of the pyridine ring, it was concluded that the substituents were different. This conclusion was also consistent with the absence of the N-O stretching bands at 1540 and 1360 cm^{-1} in the IR spectrum for **[Dy.L^4(H$_2$O)]**.

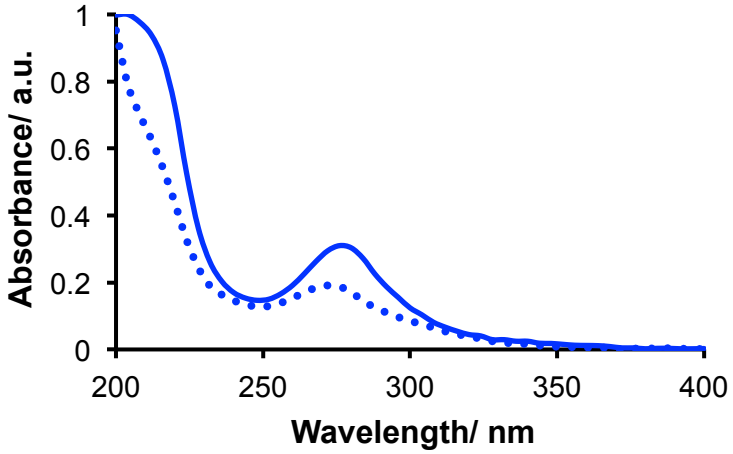

Figure 3.5 Overlaid absorption spectra for ***47*** (*line*) and **[Dy.L^4(H$_2$O)]** (*dash*) (H$_2$O, 295 K, pH 6).

3.2.2 ^{1}H NMR studies: shift and relaxation behaviour

The shift behaviour of the *tert*-butyl reporter groups in complexes ***47*** and **[Dy.L^{4}(H$_2$O)]** was analysed using ^{1}H NMR spectroscopy (*Figure 3.6*). In each case, the *tert*-butyl group was shifted a further 10 ppm compared to the related tri- and bis-carboxylate complexes, **[Dy.L^{1}(H$_2$O)]** and **[Dy.L^{2}(H$_2$O)]$^{+}$** (reported in *Chapter 2*), and resonated at -28.1 ppm and -28.4 respectively.

The ^{1}H NMR spectrum of **[Dy.L^{4}(H$_2$O)]** revealed additional well-shifted resonances at -8.1 and -19.3 ppm, corresponding to the methyl groups on the nitrogen atom (*Figure 3.6*). Integration confirmed this assignment and an investigation into their relaxation rates supported this hypothesis. Interestingly, the diastereotopic methyl groups resonate more than 10 ppm apart due to amplification of the chemical shift non-equivalence induced by the paramagnetic Dy(III) ion. Depending on the geometry adopted by **[Dy.L^{4}(H$_2$O)]**, it can be imagined that each methyl group will be orientated differently, assuming that they do not adopt a conformation purely in the plane of the pyridine ring, as drawn. One methyl group will be arranged so that it is closer to the Dy(III) ion, displaying a greater shift and experiencing a greater enhancement in R_1 (162±3 s^{-1} at 9.4 T), as defined by the pseudocontact shift[21] and SBM[22–24] equations, respectively, with the other showing contrasting behaviour (a slower R_1 value of 57±2 s^{-1} at 9.4 T).

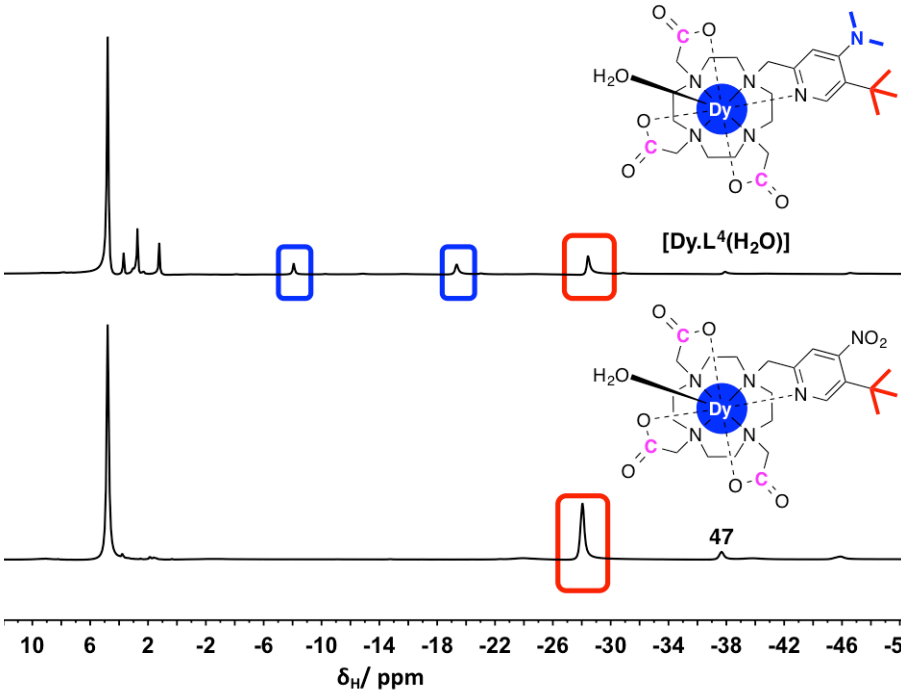

Figure 3.6 Stacked ^{1}H NMR spectra of **[Dy.L^{4}(H$_2$O)]** (*top)* and complex ***47*** (*bottom*), highlighting the major *tert*-butyl and methyl resonances (D$_2$O, pH 6, 295 K, 9.4 T).

The relaxation behaviour of the *tert*-butyl resonances was examined at 6 different field strengths for both ***47*** (Y = NO_2) and **[Dy.L^4(H$_2$O)]** (Y = $N(CH_3)_2$). Rate data are shown in comparison to **[Dy.L^1(H$_2$O)]** (Y = H), *Table 3.0*. An increase in R_1 was observed for the *para*-substituted complexes, relative to the unsubstituted tri-carboxylate complex. When Y = NO_2, the *para*-substituent is strongly electron withdrawing, whereas an $N(CH_3)_2$ normally presents strong electron donating character *vide supra*. Despite this, such a difference appears to have little effect on the observed R_1 values. As a result of selecting Dy(III), the R_1 values are of the required 100 to 200 s^{-1} order at 7 T and the R_1/R_2 ratios are comparable to those previously achieved.[17]

Table 3.0 Experimental longitudinal relaxation rate data for the major *tert*-butyl resonance of ***47*** (Y = NO_2) and **[Dy.L^4(H$_2$O)]** (Y = $N(CH_3)_2$) at different magnetic field strengths (D_2O, 295 K[a]); **[Dy.L^1(H$_2$O)]** (Y = H) is shown for comparison.

Y substituent	**R_1/ s^{-1} (± error)**						**R_1/R_2[b] (9.4 T)**
	1.0 T	**4.7 T**	**9.4 T**	**11.7 T**	**14.1 T**	**16.4 T**	
H	55 (2)	73 (1)	124 (1)	149 (1)	170 (1)	210 (2)	0.56
NO_2	59 (3)	88 (2)	149 (1)	175 (1)	199 (1)	224 (1)	0.46
$N(CH_3)_2$	52 (4)	83 (1)	144 (2)	168 (1)	198 (1)	223 (1)	0.60

(a) Temperature was monitored accurately, calibrating against an ethylene glycol shift thermometer; (b) R_2 values were estimated as ($\pi \times \omega_{1/2}$), for a Lorentzian line fit.

Assuming classical BRW theory, iterative minimisation methods were carried out by Dr. Nicola Rogers to estimate values for μ_{eff}, T_{1e} and τ_R by holding the distance between Dy(III) and the *tert*-butyl group, *r*, at 6.6 Å (*Table 3.1*). Earlier fitting simulations found that this average distance agreed well with the distance estimated using DFT calculations, that were, in turn, based on a closely related X-ray crystal structure.[25]

Table 3.1 Estimated best fit values of μ_{eff}, T_{1e} and τ_R for ***47*** (Y = NO_2) and **[Dy.L^4(H$_2$O)]** (Y = $N(CH_3)_2$) (D_2O, 295 K and *r* = 6.6 Å). **[Dy.L^1(H$_2$O)]** (Y = H) is shown for comparison.

Y substituent	**μ_{eff}/ BM**	**T_{1e}/ ps**	**τ_R/ ps**
H	10.32 (2)	0.52 (2)	196 (3)
NO_2	10.57 (3)	0.52 (3)	285 (3)
$N(CH_3)_2$	10.55 (4)	0.47 (3)	267 (4)

For each complex, the values for μ_{eff} fell within ±5% of the literature value of 10.4 BM.[26] Estimated values for T_{1e} converged uniformly to 0.46 (±0.06) ps, corroborating the similarity of the observed R_1 values at 1.0 T for each of the three complexes, and in accord with the vanishing Curie term at low field. A small increase in τ_R for the *para*-substituted systems is consistent with the complex occupying a slightly larger molecular volume.

3.2.3 pH Responsive chemical shift behaviour

An investigation was carried out to examine the pH dependence of the chemical shift of the *tert*-butyl resonance. A pH titration was performed with a sample of **[Dy.L^4(H$_2$O)]** in D_2O. The pH was raised using NaOD and lowered using DCl. Each time, the pH within the NMR tube was accurately measured using a pH meter, which was pre-calibrated using standard buffer solutions. The operating temperature of the NMR spectrometer was recorded accurately, calibrating against a standard ethylene glycol shift thermometer, to ensure that shift was down to pH variations only (recall the sensitive T^{-2} dependence, *page 13*). The ^{1}H NMR spectrum was acquired at different pD values, ranging from 2.2 to 9.9, where pD = pH + 0.41 (*Figure 3.7*).

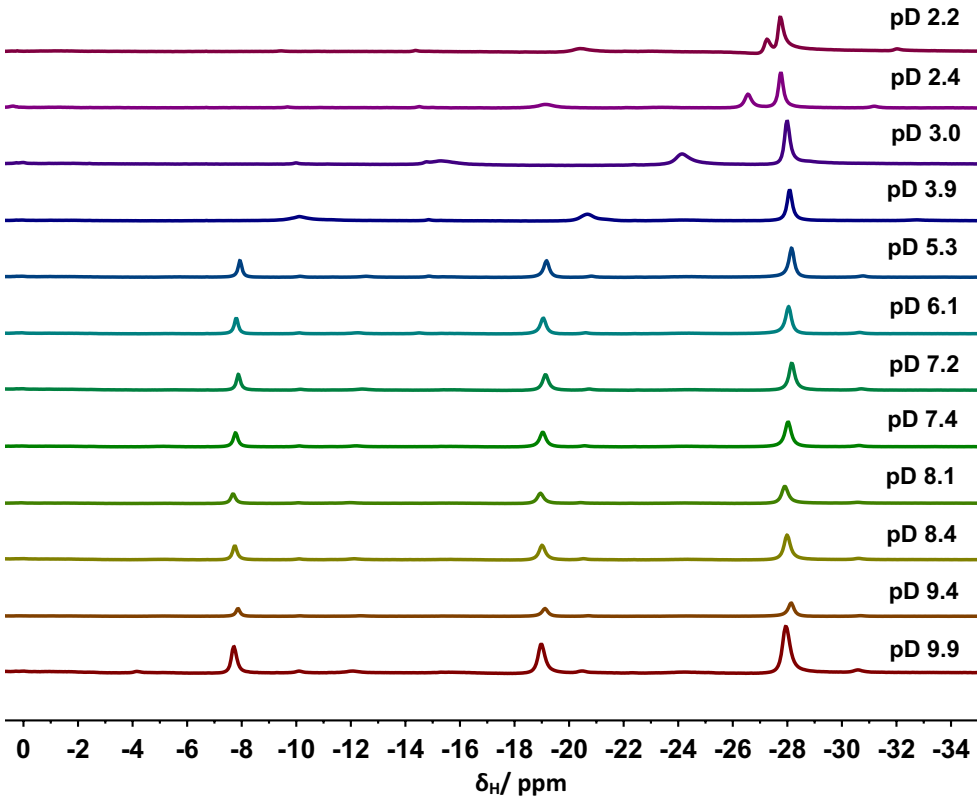

Figure 3.7 Stacked ^{1}H NMR spectra showing the behaviour of the methyl groups and the *tert*-butyl resonance on **[Dy.L^4(H$_2$O)]** as a function of pD, where pD = pH + 0.41 (D_2O, 295 K, 9.4 T).

There was no observable shift in the *tert*-butyl resonance of **[Dy.L^{4}(H$_2$O)]** over the 5-10 pD range. However, upon lowering the pD to 3.9, substantial shifts in the methyl resonances became apparent; shifting further still as the pD was lowered to 2.2. By plotting the change in the chemical shifts of the three resonances as a function of pH, it is evident that about the pK_a, shifts of around 5 ppm/pH unit are observed (*Figure 3.8*). Such shifts suggest that protonation is occurring, albeit at a much lower pH value than had been surmised if steric inhibition of lone pair conjugation was operative. During the synthetic route (*Scheme 3.0*), it became clear that it was difficult to alkylate the pyridyl-amine group citing its poor nucleophilicity due to lone pair conjugation. This phenomenon must also be occurring here, amplified by the presence of the 'electron sink' that is the coordinated Dy(III) ion. Another suggested explanation cites the steric hindrance associated with the bulky *tert*-butyl group, leading to less effective solvation of the protonated amine. The apparent broadening of the observed resonance is ascribed to the dynamic exchange processes associated with nitogen protonation. Such behaviour is not desirable, *Section 3.1*, as it can result in signal intensity loss in MRS imaging protocols.

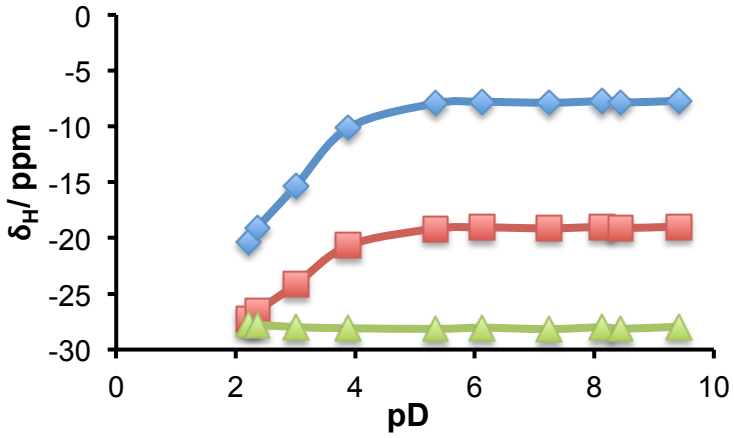

Figure 3.8 Plot showing the change in chemical shifts, δ_H, for NMe^{1} (*blue*), NMe^{2} (*red*) and the *tert*-butyl resonance (*green*) in **[Dy.L^{4}(H$_2$O)]** as a function of pD, where pD = pH + 0.41 (D$_2$O, 295 K, 9.4 T).

Nonetheless, some positive features were established in this work. Firstly, chemical exchange was fast on the NMR timescale, manifesting in a time-averaged signal, which shifted as a function of pH. Secondly, the *para*-substituted complex **[Dy.L^{4}(H$_2$O)]** clearly existed as one dominant isomer in solution, identifiable by the major *tert*-butyl reporter resonance. Finally, a sensitivity of 5 ppm/pH unit was estimated that is of comparable size to the published **[Yb.DOTP]$^{5-}$** example.[15] Sadly, however, the pH shift

sensitivity manifested itself within the methyl signals rather than the *tert*-butyl, which is of paramount importance for the sensitivity of these probes. Notwithstanding the favourable relaxation rate characteristics at 7 T, it is clear that the pK_a associated with this *para*-substituent is unsuitable.

3.3 First Generation System: An Acetamide Substituent

The next system to be considered had an acetamide substituent in the 4-position of the *tert*-butylpyridyl moiety, **[Ln.L^5(H$_2$O)]** (*Figure 3.9*). An acetamide substituent has a pK_a around 15.[27] It was therefore reasoned that **[Ln.L^5(H$_2$O)]** could possess a more desirable pK_a value. In the *para*-substituted complex, it was envisaged that the conjugate base, arising from deprotonation would be stabilised through delocalisation of the negative charge into the coordinated pyridyl moiety. A related effect has been observed in structurally related 4-amide derivative of quinoline containing ligands.[28]

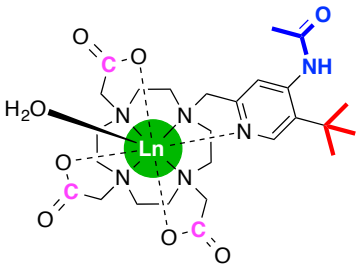

Figure 3.9 The design of the acetamide-bearing ^{1}H PARASHIFT probe, **[Ln.L^5(H$_2$O)]**.

3.3.1 Complex synthesis and characterisation

The synthesis of the acetamide pyridyl precursor, ***52***, began with the previously synthesised amino-alcohol compound, ***44*** (*Scheme 3.2*).

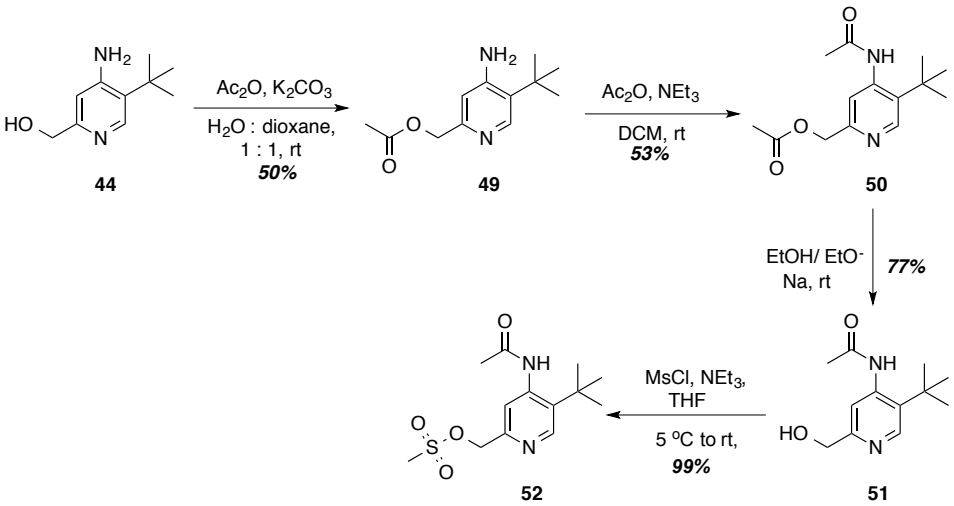

Scheme 3.2 General procedure for the synthesis of the mesylate ***52***.

In the presence of acetic anhydride, it was hypothesised that acetylation would occur on both the amine and alcohol groups. However, due to the poor organic solubility of ***44***, mildly basic conditions were employed, in a water-dioxane mixed solvent. Under these conditions, selective acetylation of the alcohol occured, with the formation of compound ***49*** confirmed by heteronuclear multiple-bond correlation spectroscopy, HMBC (*Figure 3.10*).

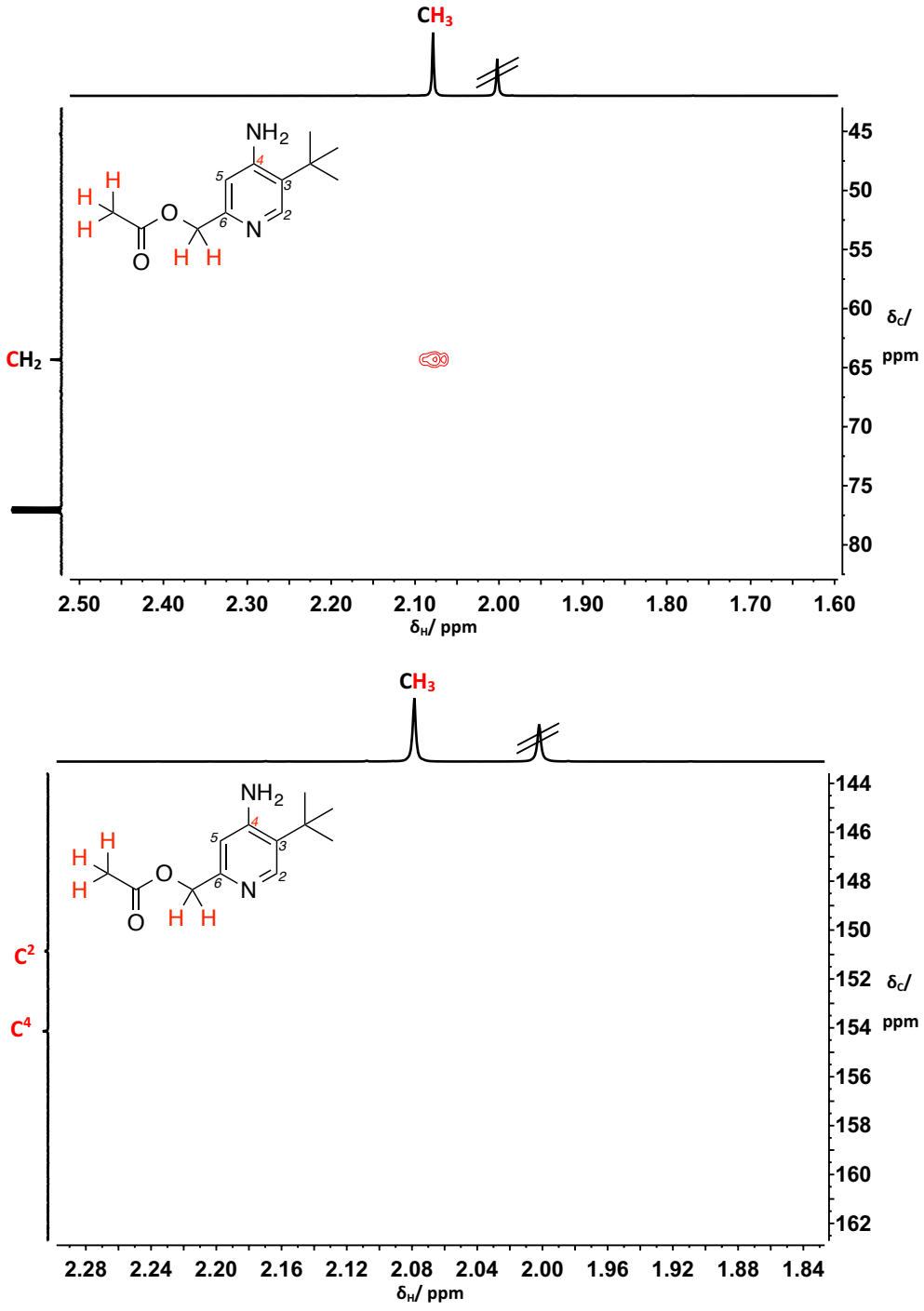

Figure 3.10 HMBC spectra showing the correlation between the acetyl CH_3 and the aryl CH_2 (*top*) and the lack of correlation between the pyridyl C^4 and the acetyl CH_3 (*bottom*) to prove the identity of ***49***. Excess acetic anhydride is crossed out.

Such poor amine reactivity should have been anticipated, however, following the poor nucleophility of the amino- species, ***42*** and ***44***. An organic base and solvent allowed the amine on ***49*** to be successfully acetylated in the subsequent step, however. The acetate ester on ***50*** was cleaved selectively in good yield, using sodium ethoxide in ethanol, to give the desired alcohol ***51***, monitored by TLC and ^{1}H NMR spectroscopy. Afterwards, reaction with methane sulfonyl chloride, in the presence of triethylamine, afforded the mesylate ***52***.

Immediate use of the mesylate ***52*** in an alkylation reaction with the previously synthesised tri-carboxylate 12-N_4-based macrocycle, ***1***, yielded the tetra-substituted ligand, ***53***, following purification by silica gel column chromatography (*Scheme 3.3*). Quantitative removal of the *tert*-butyl esters using trifluoroacetic acid followed by complexation in aqueous solution, with Dy(III) chloride, gave the desired complex, which was purified by reverse-phase preparative HPLC (t_R = 5.7 min).

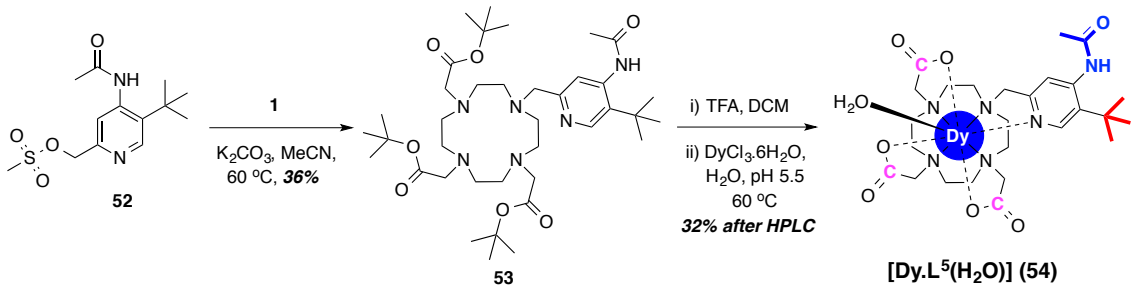

Scheme 3.3 General procedure for the synthesis of the acetamide complex, **[Dy.L^5(H$_2$O)]**.

3.3.2 ^{1}H NMR studies: shift and relaxation behaviour

Analysis by ^{1}H NMR spectroscopy revealed the shift of the major *tert*-butyl resonance at -23.3 ppm for **[Dy.L^5(H$_2$O)]** (*Figure 3.11*), with the acetamido- methyl resonating at -7.7 ppm, in the major isomer. Not surprisingly, such a shift magnitude is comparable to that previously displayed within this work for structurally related tri-carboxylate based systems, but remains significantly less than that observed for the tri-phosphinate analogues (*ca.* -75 ppm for Dy(III)).

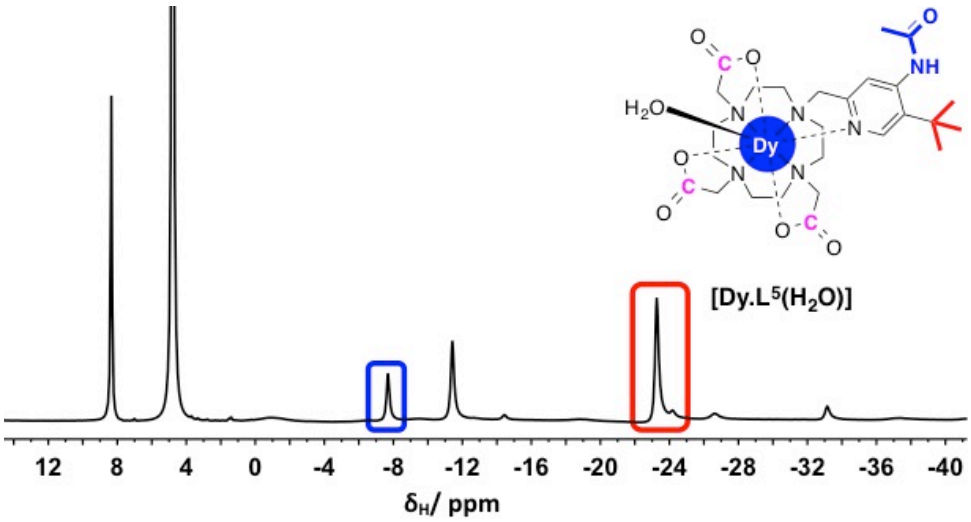

Figure 3.11 ^{1}H NMR spectrum of **[Dy.L^{5}(H$_2$O)]**, highlighting the major *tert*-butyl and methyl resonances (D$_2$O, pD 7, 295 K, 9.4 T).

Examination of the relaxation behaviour of the major *tert*-butyl resonance on **[Dy.L^{5}(H$_2$O)]** revealed a similar R_1 value to the aforementioned *para*-substituted complexes (*Table 3.2*). Typically, as can be predicted for a Dy(III) tri-carboxylate based 12-N$_4$ complex, **[Dy.L^{5}(H$_2$O)]** exhibits an R_1 value in the desired 100 to 200 s^{-1} range at 7 T and an R_1/R_2 ratio that is comparable to those reported.[17]

Table 3.2 Experimental longitudinal relaxation rate data for the major *tert*-butyl resonance of **[Dy.L^{5}(H$_2$O)]** (Y = NHCOCH$_3$) at different magnetic field strengths (D$_2$O, 295 K[a]). **[Dy.L^{1}(H$_2$O)]** (Y = H), ***47*** (Y = NO$_2$) and **[Dy.L^{4}(H$_2$O)]** (Y = N(CH$_3$)$_2$) are shown for comparison.

Y substituent	**R_1/ s^{-1} (± error)**						**R_1/R_2[b] (9.4 T)**
	1.0 T	**4.7 T**	**9.4 T**	**11.7 T**	**14.1 T**	**16.4 T**	
H	55 (2)	73 (1)	124 (1)	149 (1)	170 (1)	210 (2)	0.56
NO$_2$	59 (3)	88 (2)	149 (1)	175 (1)	199 (1)	224 (1)	0.46
N(CH$_3$)$_2$	52 (4)	83 (1)	144 (2)	168 (1)	198 (1)	223 (1)	0.60
NHCOCH$_3$	53 (5)	85 (1)	152 (2)	180 (1)	210 (1)	241 (1)	0.61

(a) Temperature was monitored accurately, calibrating against an ethylene glycol shift thermometer; (b) R_2 values were estimated as ($\pi \times \omega_{1/2}$), for a Lorentzian line fit.

3.3.3 pH Responsive chemical shift behaviour

A ^{1}H NMR spectroscopy pH titration was carried out with **[Dy.L^{5}(H$_2$O)]**, over the pD range 2.5 to 11.5. The chemical shift of the major *tert*-butyl and methyl resonances was recorded at 8 different pD values, along with values for the transverse relaxation rates, R_2, which were estimated from the individual linewidths (at half-height), using a $\pi \times \omega_{1/2}$ relationship in a Lorentzian fit (*Figure 3.12*).

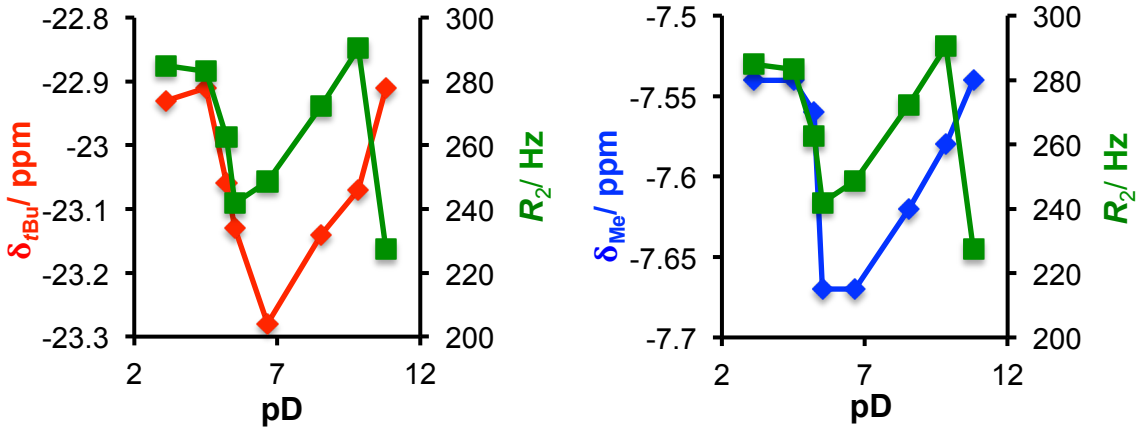

Figure 3.12 Variations of the shift of the major *tert*-butyl resonance (*left*, red), the major methyl resonance (*right*, blue), and the corresponding changes in R_2 (*both*, green) as a function of pD (D_2O, 295 K, 9.4 T).

A negligible shift in the *tert*-butyl resonance was observed over the pD range shown, with minimal fluctuations also apparent in R_2. There appears to be a small, reversible shift change over the pH range 5-9, where R_2 also increases reversibly. Such behaviour is mirrored by the shift of the methyl resonance and suggests that the pK_a of the acetamide substituent could be around 6.5. Whilst this pK_a is highly desirable, a larger shift change is required for use in MRS imaging protocols, since the total shift change of 0.4 ppm is equal to 120 Hz at 7 T, and may therefore be difficult to calibrate accurately.

Given the minimal structural modifications in the 4-position of the *tert*-butyl pyridyl moiety, both **[Dy.L^{4}(H$_2$O)]** and **[Dy.L^{5}(H$_2$O)]** showed similar shift and relaxation properties to the parent tri- and bis-carboxylate complexes (**[Dy.L^{1}(H$_2$O)]** and **[Dy.L^{2}(H$_2$O)]$^{+}$**), detailed in *Chapter 2*. However, the desired pH sensitivity of the *tert*-butyl signal was not achieved through introduction of a dimethylamine or acetamide substituent. In the former case, the pK_a was much too low (< 3), with only the methyl groups shifting as a function of pH (5 ppm/pH unit). In the latter example, the pK_a was

optimised, but the *tert*-butyl resonance did not shift with sufficient magnitude, as a function of pH. Such shift behaviour could be attributed to the magnitude of the shift in these carboxylate complexes; the overall shift is markedly lower than for the related tri-phosphinate system, **[Dy.L^{3}]** (*ca.* δ_H ^{t}Bu = -75 ppm). If Bleaney's theory for the pseudocontact shift of a paramagnetic lanthanide(III) based system is considered, *page 13*, it might be surmised that in order to achieve a larger shift magnitude with respect to pH, the overall shift of the resonance must be greater. As a result, the second generation system detailed in the remainder of this Chapter will focus on enhancing the shift.

3.4 Second Generation System: A Phosphonate Substituent

The design of **[Ln.L^{6}]** incorporates a phosphonate group in the 4-position of the *tert*-butylpyridyl moiety (*Figure 3.13*). The early work on ^{31}P MRS, detailed in *Section 1.1.2*, inspired the selection of this substituent. In each case, the ^{31}P NMR signal shifted as a function of pH, with a pK_a around 7.[29–31] In order to increase the shift magnitude of the *tert*-butyl reporter group, phosphinate arms have been incorporated. At physiological pH, it is expected to exist as the anionic species shown, such that the observable pK_a corresponds to the formation of a dianionic species.

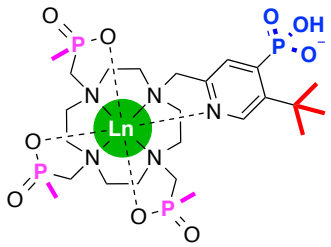

Figure 3.13 The design of the phosphonate-bearing ^{1}H PARASHIFT probe, **[Ln.L^{6}]**.

3.4.1 Complex synthesis and characterisation

A synthetic approach was devised to place the phosphonate group in the desired 4-position, based on a method by Redmore, whereby substitution of a phosphonate group occurred in the sterically hindered 4-position of a positively charged *N*-pyridinium salt.[32] In this work, a bulky triphenylcarbenium ion was used to block the 2- and 6-positions, facilitating selective substitution in the 4-position, albeit in a poor yield (28%). Interestingly, in this procedure the phosphite was sodiated *in situ* to enhance its nucleophilicity. Based on this precedent, alkylation of the oxygen on the previously synthesised *N*-oxide, ***3***, was achieved using dimethylsulfate to give the *N*-pyridinium

ion, ***55*** (*Scheme 3.4)*. Reaction between ***55*** and sodiated-diethylphosphite in neat diethylphosphite gave the pyridyl-phosphonate species, ***56***, observable by low-resolution mass spectrometry, which was then isolated using silica gel column chromatography, albeit in poor yield.

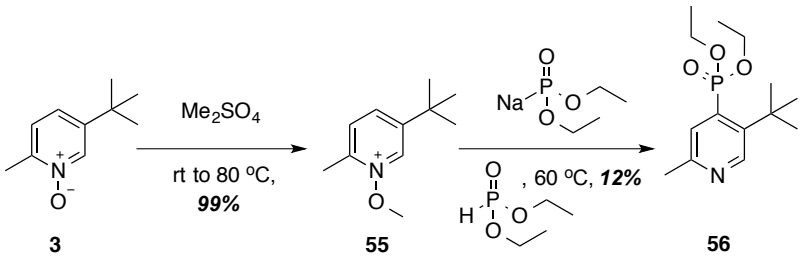

Scheme 3.4 General procedure for the synthesis of the phosphonate labeled *tert*-butylpyridyl moiety, ***56***.

Characterisation of ***56*** by HRMS showed the correct mass for the desired pyridyl-phosphonate species (calcd for $[C_{14}H_{25}NO_3P]^+$ 286.1572, found 286.1574) but the resulting ^{1}H NMR spectrum showed an unexpected splitting pattern in the two aromatic protons (*Figure 3.14*). The most shifted proton is split into a triplet (with J = 8 Hz) and the least shifted proton exists as a doublet of doublets (with J = 3 and 8 Hz).

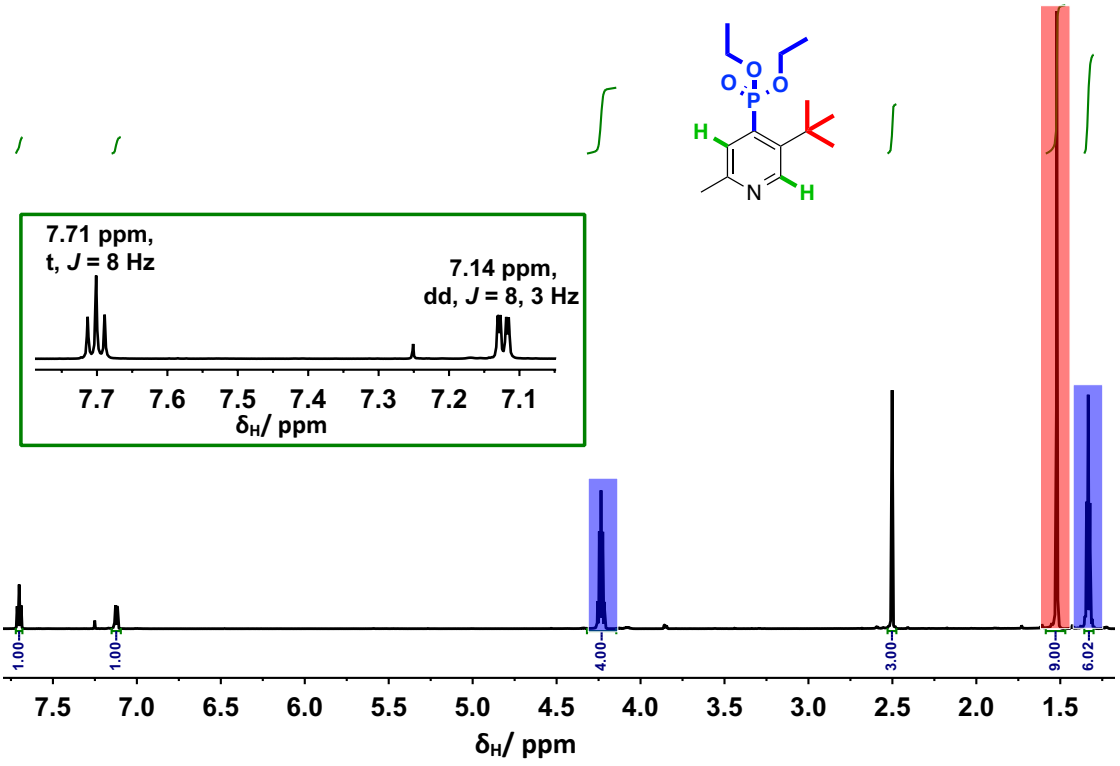

Figure 3.14 ^{1}H NMR spectrum of the pyridyl-phosphonate ***56***, showing expansion of the aromatic protons ($CDCl_3$, 295 K, 16.4 T).

Two constitutional isomers can be proposed as products of the reaction, following substitution at either the 2- or 4-positions (*Figure 3.15*). However, it can be argued that substitution in the 2-position on ***55*** should be disfavoured due to the steric hindrance offered by the neighbouring *tert*-butyl and methoxy substituents. In contrast, nucleophilic substitution in the 4-position appears to be less hindered.

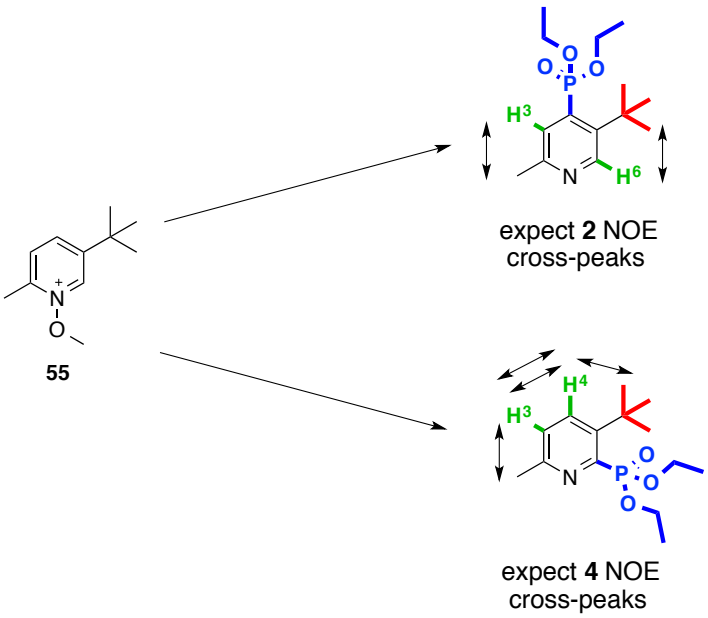

Figure 3.15 Schematic representation of the two possible isomers of the phosphonate labeled *tert*-butylpyridyl moiety, ***56***.

Out of the two-dimensional ^{1}H NMR techniques available, Nuclear Overhauser Effect spectroscopy (NOESY) was selected since it offered the most appropriate information for the characterisation of ***56***. In an NOE spectrum, the cross-peaks are representative of spatially close nuclei, rather than those that are through bond-coupled. As a result, the desired 4- substituted product would show 2 NOE cross-peaks, illustrating the spatial proximity between H^3 and the methyl group, and H^6 and the *tert*-butyl group (*Figure 3.16)*. In the case of the undesired 2- substituted product, 4 NOE cross-peaks would be seen and is the case upon expansion of the NOE spectrum in *Figure 3.16*. It is highly probable that the desired isomer was also formed in the reaction, but was not isolated. The appearance of a triplet in the ^{1}H NMR spectrum, corresponding to H^4, can be attributed to the similarity of the $^{3}J_{HH}$ and $^{4}J_{HP}$ coupling constants (8 Hz), which effectively masks a doublet of doublets.

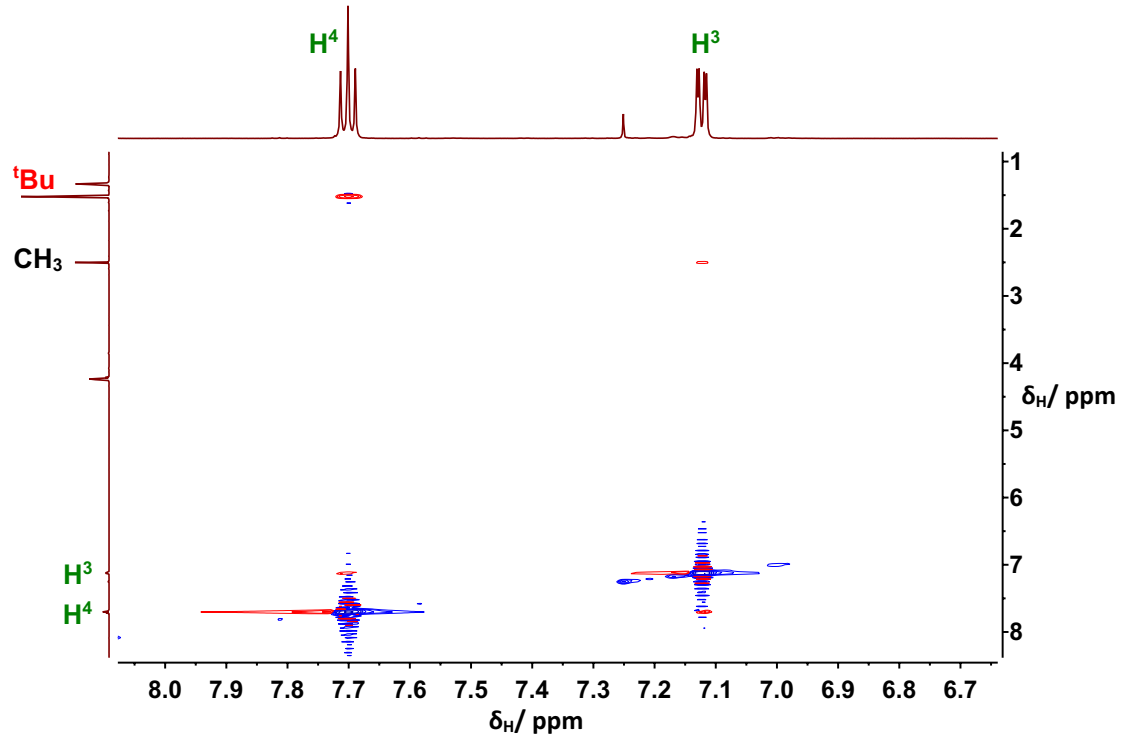

Figure 3.16 ^{1}H NMR 2D NOE spectrum of the pyridyl-phosphonate species, confirming the identity of ***56*** as the 2- substituted product by the revealed 4 red cross-peaks ($CDCl_3$, 295 K, 16.4 T).

Subsequently, a different synthetic route was proposed, utilising palladium-catalysed cross coupling procedures (*Scheme 3.5*). First, the removal of the *N*-oxide on the previously synthesised nitro-derivative, ***41***, was effected using phosphorus tribromide, to give ***57***, after purification on silica gel. Introduction of a bromine atom in the 4-position was furnished in neat acetyl bromide to afford ***58***. The coupling between ***58*** and diethylphosphite was then attempted using two different palladium catalysts. In neither case was reaction to the desired 4- substituted product observed. A possible explanation could be that oxidative addition of the carbon-bromine bond is sterically hindered due to the proximal *tert*-butyl group.

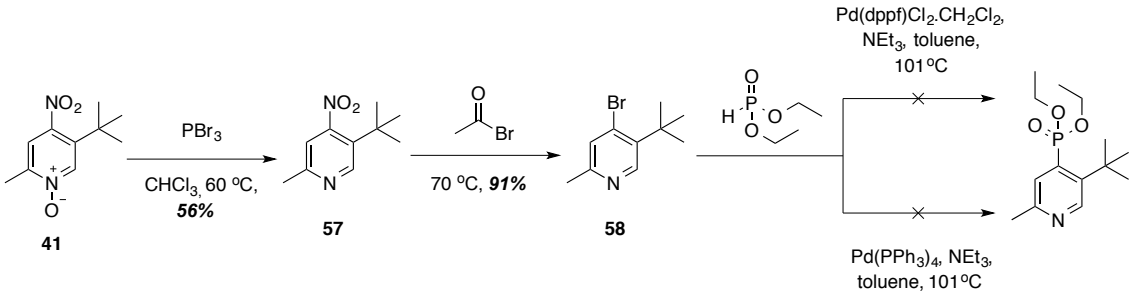

Scheme 3.5 General procedure for the proposed introduction of the phosphonate group by palladium-catalysed cross coupling methods.

In an effort to further weaken the carbon-halogen bond and encourage cross coupling to occur, a route was undertaken, using iodine in the 4-position (*Scheme 3.6*). Diazotisation of the aromatic amine ***42*** was achieved using nitrous acid, which was generated *in situ* using sodium nitrate and fluoroboric acid. Preparation of the halide was completed using potassium iodide, giving ***59*** in moderate yield, following purification by silica gel column chromotography. A [3,3]-sigmatropic rearrangement occurred in acetic anhydride to afford the acetate ester, ***60***. However, as before, the coupling between ***60*** and diethylphosphite yielded no product in the presence of the palladium catalysts used previously.

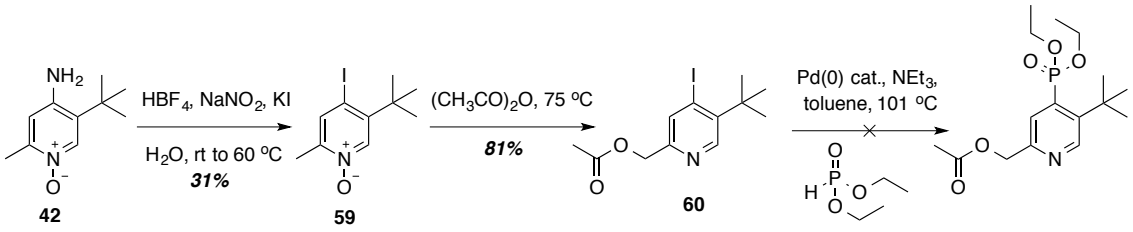

Scheme 3.6 General revised procedure for the proposed introduction of the phosphonate group by palladium-catalysed cross coupling reactions.

A palladium catalysed Arbusov reaction has been reported between triethyl phosphite and a variety of aryl iodides.[33,34] Upon heating $Pd(dba)_2$ and triethyl phosphite to 120 °C, $Pd\{P(OEt)_3\}_4$ formed *in situ* and facilitated the formation of the desired 4-phosphonate species, ***61***, which was isolated on silica gel in a reasonable yield (*Scheme 3.7*).

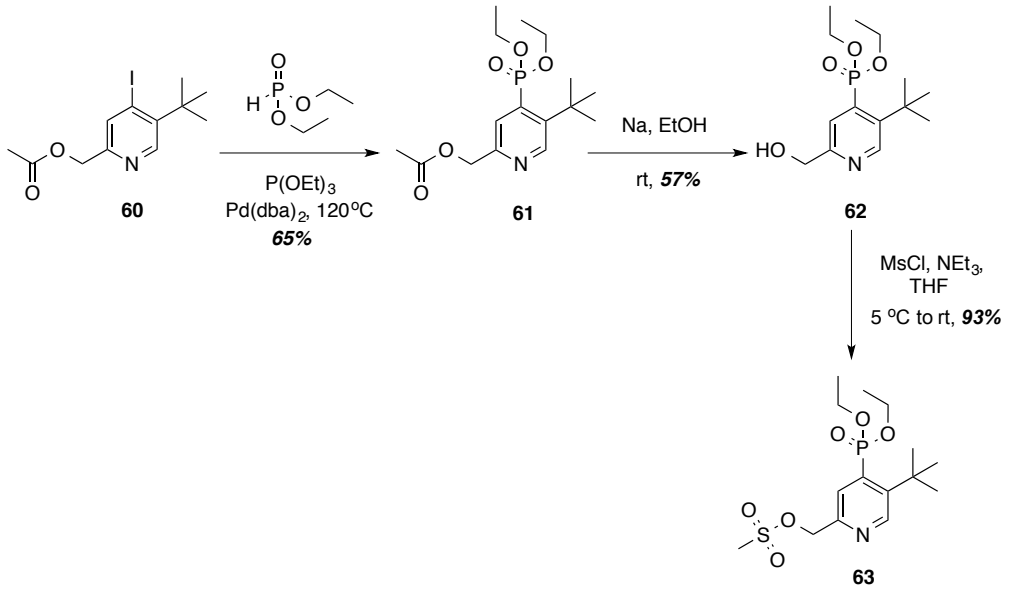

Scheme 3.7 General procedure for the synthesis of the mesylate ***63***.

The aromatic protons, H^6 and H^3, resonated as doublets in the ^{1}H NMR spectrum, with coupling constants of 8 ($^{4}J_{HP}$) and 16 Hz ($^{3}J_{HP}$), respectively. Treatment of ***61*** with freshly prepared sodium ethoxide, effected acetate ester cleavage to give ***62***. Mesylation of ***62*** under standard conditions afforded the mesylate, ***63***, in excellent yield.

Alkylation of the previously synthesised tri-phosphinate 12-N_4-based macrocycle, ***31***, was undertaken with freshly prepared mesylate, ***63*** (*Scheme 3.8*). Reaction completion was monitored by TLC, after which purification using alumina gel column chromatography yielded the tetra-substituted ligand, ***64***. The removal of both the phosphinate and phosphonate esters using 6 M hydrochloric acid was monitored by LRMS and ^{1}H NMR spectroscopy. Following complexation with the appropriate hydrated lanthanide(III) chloride, and isolation by reverse-phase preparative HPLC, the **[Ln.L^6]** series of complexes was prepared, with Ln = Eu, Gd, Tb, Dy, Er and Tm (***65-70***).

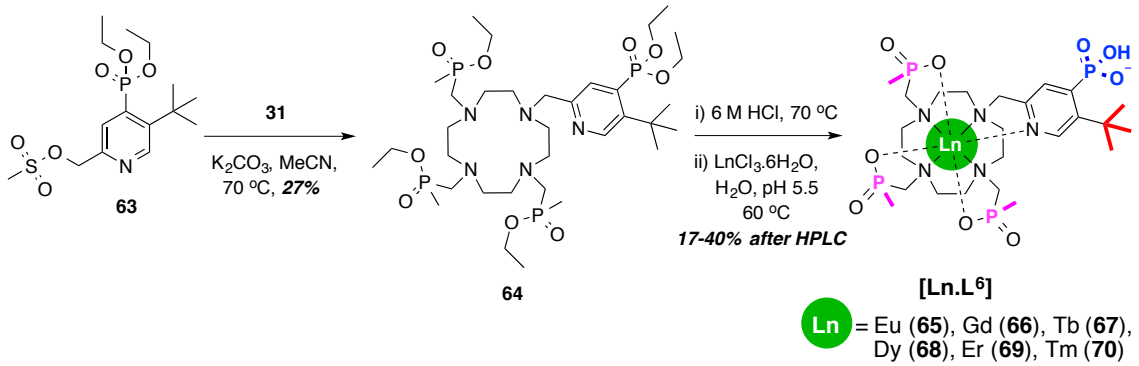

Scheme 3.8 General procedures for the synthesis of the phosphonate-bearing ^{1}H PARASHIFT probes, **[Ln.L^6]**, ***65-70***.

The identity and purity of each complex were established by high-resolution mass spectrometry and analytical reverse-phase HPLC (t_R ranged between 6.8 and 7.3 min). The metal hydration number, q, was assessed at pH 7 by measuring the radiative lifetime of the Eu(III) and Tb(III) excited state, k, in both D_2O and H_2O, as described in *Section 2.2.2*. In the case of **[Tb.L^6]**, values of 0.31 and 0.26 ms^{-1} were recorded experimentally for k_{H_2O} and k_{D_2O} respectively, giving a q value of 0. The experimentally determined values for **[Eu.L^6]** were 1.32 and 0.82 ms^{-1} with a q value of 0.3.

It is expected that such tri-phosphinate complexes will not possess a bound water molecule, due to the steric bulk associated with the PMe chelating arms, and is consistent with each of the **[Ln.L^{3}]** systems discussed in *Section 2.4.1* and related tri-phosphinate based systems.[11] The relaxivity, r_{1p}, of 2.0±0.05 mM^{-1} s^{-1}, obtained for **[Gd.L^{6}]** is consistent with the absense of an inner-sphere water molecule, corresponding well to the value obtained with **[Gd.L^{3}]** (r_{1p} = 1.5±0.04 mM^{-1} s^{-1}). The small increase for the *para*-substituted system is also consistent with an increase in the rotational correlation time, τ_R.

3.4.2 ^{1}H NMR studies: shift and relaxation behaviour

The chemical shifts ascribed to the *tert*-butyl reporter resonance of the **[Ln.L^{6}]** complexes were greater than anticipated, as shown (*Figure 3.17)* for the Tm(III), Er(III), Dy(III) and Tb(III) analogues. Increases of 5 ppm were observed for each lanthanide(III) ion relative to the unsubstituted tri-phosphinate **[Ln.L^{3}]** systems, detailed in *Section 2.4*, and are therefore the most shifted examples of this class. The Tb(III) analogue has the most shifted resonance, despite a Bleaney coefficient lower than Dy(III) (-86 *vs.* -100 respectively). In the Er(III) complex, the *tert*-butyl group resonated at +42.5 ppm, and the major isomer contributed to ≥83% of the total signal in each case.

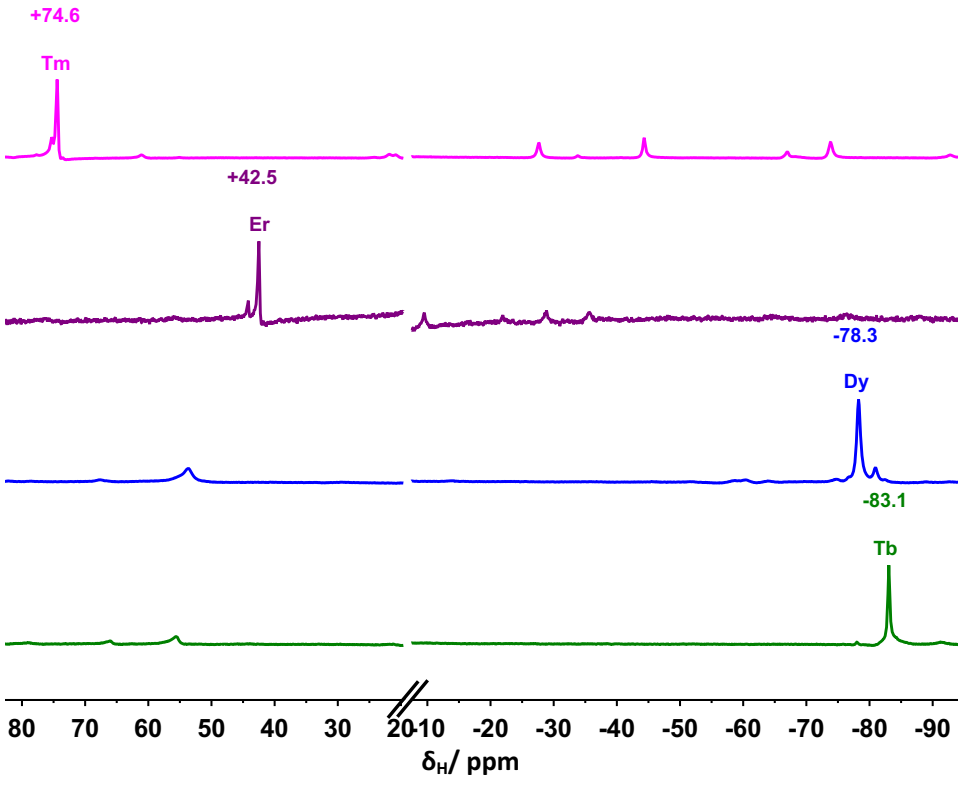

Figure 3.17 Stacked ^{1}H NMR spectra of the **[Ln.L^{6}]** complexes, highlighting the shift (in ppm) of the *tert*-butyl reporter resonance for Ln = Tm, Er, Tb and Dy (D_2O, 9.4 T, 295 K, pD 7.4).

In each case, longitudinal relaxation rate data for the major *tert*-butyl resonances in the **[Ln.L^6]** series were measured at 6 magnetic fields and showed an increase relative to the unsubstituted tri-phosphinate **[Ln.L^3]** complexes (*Table 3.3*). As anticipated from previous investigations,[13,25] the Er(III) analogue displayed the highest R_1 across all the fields. In fact, the previously established R_1 trend where Er(III) > Tm(III) > Dy(III) > Tb(III) is exhibited for this series of complexes also, further exemplifying the earlier finding that Er(III) and Tm(III) tri-phosphinate-based complexes show markedly higher relaxation rates than their Dy(III) and Tb(III) equivalents. Furthermore, in this *para*-substituted system, all four of the complexes that were assessed possess the required R_1 values in the 100 to 200 s^{-1} range at 7 T.

Table 3.3 Longitudinal relaxation rate data for the major *tert*-butyl resonance of **[Ln.L^6]** at different magnetic field strengths (D_2O, pD 7.4, 295 K[a]).

Ln	**R_1/ Hz (± error)**						**R_1/R_2[b] (9.4 T)**
	1.0 T	**4.7 T**	**9.4 T**	**11.7 T**	**14.1 T**	**16.4 T**	
Tb	42 (3)	73 (1)	122 (2)	134 (1)	150 (1)	164 (1)	---
Dy	54 (5)	88 (3)	156 (1)	179 (1)	195 (1)	218 (1)	0.50[c]
Er	92 (10)	117 (7)	173 (3)	198 (3)	214 (7)	239 (8)	---
Tm	25 (4)	99 (5)	139 (1)	160 (1)	179 (1)	190 (1)	---

(a) Temperature was monitored accurately, calibrating against an ethylene glycol shift thermometer; (b) R_2 values were estimated as ($\pi\omega_{1/2}$), for a Lorentzian line fit; (c) measured at pH = 9, at pH 7.1 (*i.e.* the pK_a, at 295 K) T_2^* increases by a factor of 3, see *Section 3.4.3* for more information.

The degree of deviation of the R_1 values from these of the parent, unsubstituted complex was more pronounced with increasing field strength, such that in the case of Dy(III), a 45% R_1 improvement is evident at 16.4 T (for Y = H, R_1 = 150 s^{-1} at 16.4 T). Such increases in R_1 at high field are associated with increases in the Curie contribution to relaxation, and the dominance of the $(\mu_{eff})^4$ term. Estimated values of μ_{eff}, obtained by iterative minimisation methods, demonstrated disparities between **[Dy.L^3]** and **[Dy.L^6]**. In the former case, the μ_{eff} value of 9.47 deviated by more than -5% from the free ion value of 10.4, whereas in the latter, the μ_{eff} value of 10.65 fell within the classical range.[26] Values for τ_R were also estimated for **[Dy.L^3]** and **[Dy.L^6]**, displaying a 38% increase upon inclusion of an anionic *para*-substituent (for Y = H, τ_R = 249 ps; for Y =

PO_3H, τ_R = 345 ps). The increase in relaxivity that was conveyed in *Section 3.4.1* reflects such behaviour and is consistent with the larger apparent molecular volume occupied by the more strongly hydrated anionic **[Dy.L^6]** complex.

Strikingly high R_1 values at clinically relevant field strengths (1.0 to 7.0 T), coupled with a favourable chemical shift, make **[Er.L^6]** an attractive candidate for MRS imaging protocols. In this particular system, the case of Tm(III) can also now be considered of interest, given that it fulfills the required enhancements in R_1 at 7 T.

The achievement of the required R_1 values for the Er(III), Tm(III), Dy(III) and Tb(III) *para*-substituted **[Ln.L^6]** complexes provided encouragement for MRS applications, given that the previously detailed series presented only one attractive candidate for any further investigation. This new series of complexes, through optimisation of both shift and relaxation characteristics, presents the opportunity for using more than one probe in MRS imaging protocols. Investigations into the pH responsive *tert*-butyl chemical shift behaviour were clearly warranted, to assess the utility of these systems as pH probes.

3.4.3 Responsive chemical shift behaviour of [Dy.L^6]

An initial ^{1}H NMR study of **[Dy.L^6]** in D_2O showed reversible pH dependent *tert*-butyl chemical shift behaviour, over the 4.4 to 9.4 pD range. At high pD, the signal resonated at -77.2 ppm, and as the pD decreased the signal shifted to -79.1 ppm (*Figure 3.18*). This culminated in a total shift change, $\Delta\delta_H$ ^{t}Bu, of 1.9 ppm between the protonated and deprotonated forms shown in *Figure 3.19*, corresponding to 570 Hz at 7 T. Such a shift magnitude is 2.5% of the overall observed shift and might explain why the shift difference is greater for this tri-phosphinate system compared to the tri-carboxylate acetamide system, **[Dy.L^5(H$_2$O)]**. Here, the total change is also 2% of the overall shift but the markedly smaller shift (δ_H ^{t}Bu = 23.3 ppm) results in a smaller total change of 0.4 ppm. The shift increase can be linked to the change in solvation around the *tert*-butyl group as the neighbouring phosphonate group becomes more negatively charged, *i.e.* at the pK_a where it changes from mono-anionic to di-anionic.

By plotting the change in the *tert*-butyl chemical shift as a function of pD and fitting the resulting curve, the pK_a of this process was measured to be 7.11±0.05. With the physiological pH window being the range within which it functions, and high sensitivity around the pK_a, the complex, **[Dy.L^6]** was the subject of further studies.

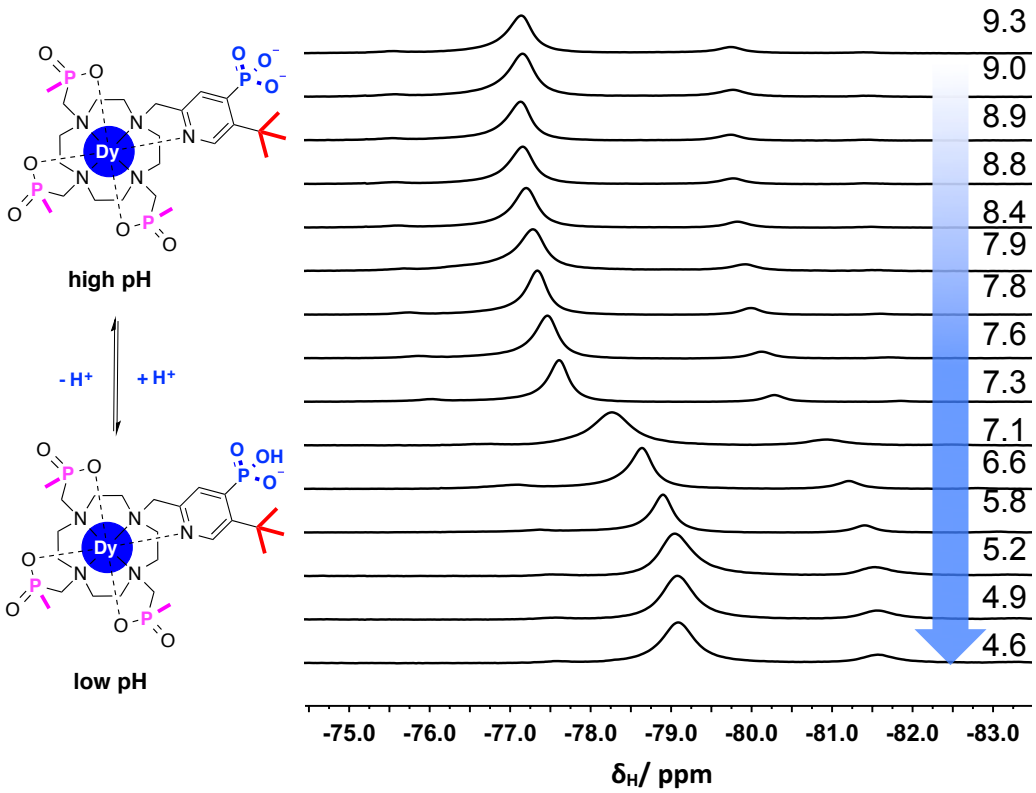

Figure 3.18 The shift in the major *tert*-butyl resonance of **[Dy.L^{6}]** as a function of pD (D_2O, 11.7 T, 295 K) and the corresponding pH equilibrium.

The effect on the transverse relaxation rates, R_2, also needs to be noted, since the criteria detailed in *Section 3.1* clearly set out the need to minimise chemical exchange broadening. It is evident (*Figure 3.18*), that the most broad spectral peak occurs around pD 7.1, when the *tert*-butyl chemical shift is at -78.3 ppm. By estimating the full-width half-height of the spectral peak at the two limiting pD values, 4.4 and 9.4, T_2^* was found to increase by a factor of 3 about the pK_a. However, such behaviour is not thought to have major sensitivity implications when applied to MRS imaging protocols.

Further investigations with **[Dy.L^{6}]** were undertaken in order to establish the pH responsive chemical shift behaviour in aqueous solutions. As a result, studies were carried out in a 0.1 M NaCl solution in H_2O and a 50:50 mixture of murine plasma and H_2O, as a control as *in vivo* work was now envisaged. The shifts differed slightly depending on the medium, with the data recorded in D_2O being shifted to slightly lower frequency (*Figure 3.19*). When locking an NMR instrument to a standard reference solution, a deuterated solvent is typically used. For the experiments run in H_2O, the D_2O lock was present inside an insertable lock tube. In the case of the experiment ran in neat D_2O, the slight upfield shifting of the resonances can be ascribed to the paramagnetic

induced shift effects exerted by the dissolved Dy(III) complex. Nonetheless, the overall profile was similar for the three data sets. The fitted curve for the murine plasma H_2O mix data revealed a sharp region around the pK_a. This is slightly misleading but can be rationalised in part by the buffering that occurs in the aqueous plasma medium and explains why there are no experimental data points between 6.5 and 7.0. The reduction in the pK_a at an ionic strength of >0.05 accords with simple Debye-Hückel theory.

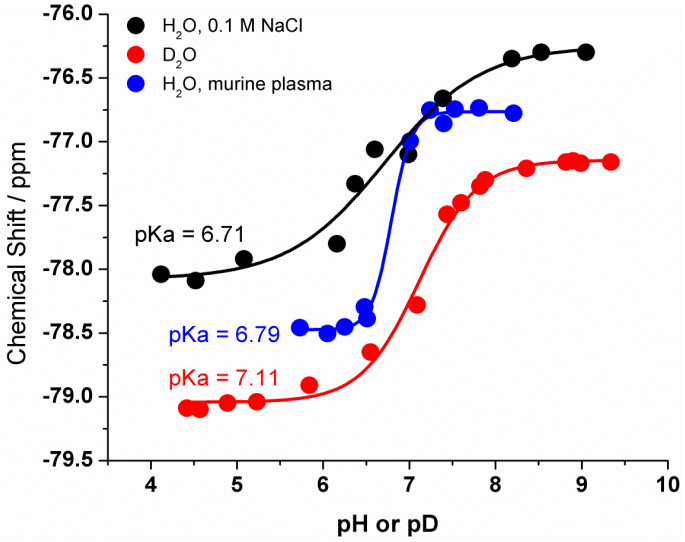

Figure 3.19 The shift in the major *tert*-butyl resonance of **[Dy.L^6]** as a function of pH or pD in a 0.1 M NaCl solution in H_2O (*black*), D_2O (*red*) and a 50:50 mixture of murine plasma and H_2O (*blue*) (11.7 T, 295 K).

The temperature variation of chemical shifts for paramagnetic lanthanide(III) complexes was demonstrated in *Section 1.3*, with several of the ^{1}H PARASHIFT probes reported, offering scope for use in temperature sensing applications. Recalling, the T^{-2} dependence for the pseudocontact shift of nuclei within paramagnetic lanthanide(III) complexes (*equation 1*):

$$\Delta_p = \frac{C_J \mu_B{}^2}{60(kT)^2}\left[\frac{(3\cos^2\theta - 1)}{r^3}B_0^2 + \frac{(sin^2\theta\ \cos 2\varphi)}{r^3}B_2^2\right] \qquad (1)$$

Variations in temperature must be accounted for with *in vivo* protocols. Accordingly, the temperature sensitivity of the *tert*-butyl chemical shift on **[Dy.L^6]** was analysed from 290 to 315 K. Two solutions of **[Dy.L^6]** in D_2O, at pD values either side of the pK_a, and a solution of **[Dy.L^6]** in a 50:50 murine plasma: H_2O mix at pH 7.1 were prepared. The chemical shift of the *tert*-butyl resonance was recorded at 6 temperatures, with each temperature checked by using an ethylene glycol shift thermometer. Each

data set displayed a linear dependence with respect to T (R^2 = 1.00 for the lines of best-fit shown in *Figure 3.20*), shifting 0.41±0.10 ppm/K^{-1} in D_2O and 0.43±0.10 ppm/K^{-1} in murine plasma: H_2O.

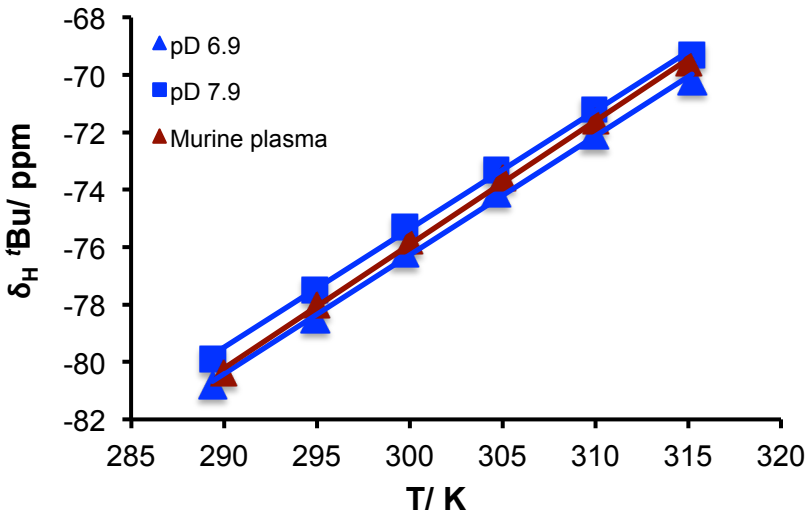

Figure 3.20 Variation in the chemical shift of the major *tert*-butyl resonance of **[Dy.L^6]** as a function of T: pD 6.9 (blue triangles), gradient = 0.414, R^2 = 0.998; pD 7.9 (blue squares), gradient = 0.414, R^2 = 0.998; and in a 50:50 murine plasma: H_2O mix at pH 7.1 (red triangles), gradient = 0.431, R^2 = 0.999 (11.7 T).

The collection of such data for **[Dy.L^6]** allows a 3D volumetric plot to be constructed, depicting the *tert*-butyl chemical shift behaviour in terms of pH and temperature (*Figure 3.21*). Ideally, prior to *in vivo* work, the majority of this plot should be filled in order to ascertain the responsive behaviour of the *tert*-butyl signal in more detail. Thorough work such as this has been demonstrated by Hyder *et al.*, who built up volumetric plots for the pH and temperature sensitivity for four ^{1}H resonances of **[Tm.DOTP]$^{5-}$**.[16] Rather than run consecutive pH titrations at the remaining 5 temperatures, it was decided that more telling information could be gained from phantom imaging studies in a 7 T MRI machine. This work will be discussed in *Section 3.4.5*. Such methodology also allows the feasibility of the chemical shift read-out protocol to be tested and refined prior to *in vivo* studies.

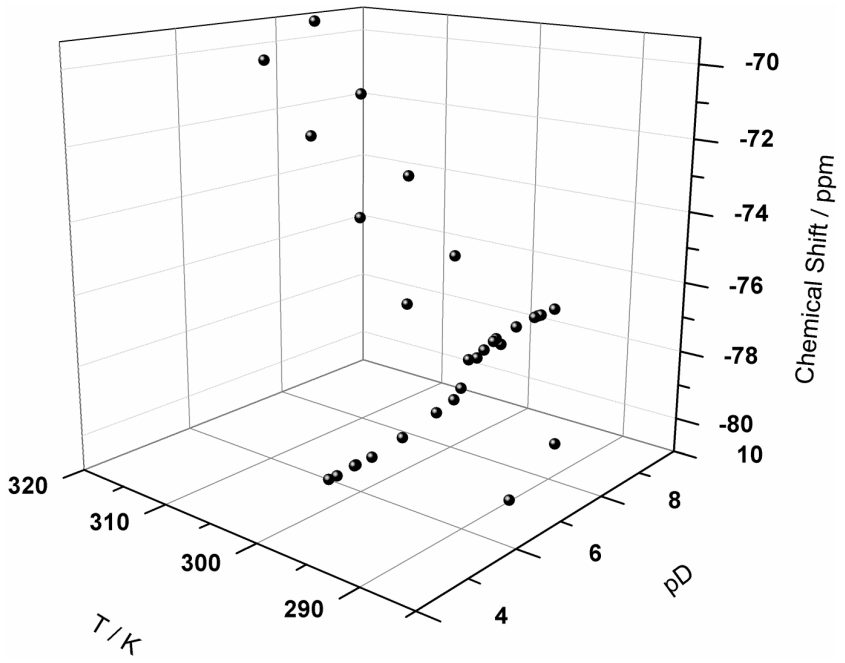

Figure 3.21 3D volumetric plot showing the dependence of the major *tert*-butyl chemical shift of **[Dy.L^{6}]** on the T and pD (D_2O, 11.7 T).

The effect of temperature on the longitudinal relaxation rate, R_1, of the *tert*-butyl resonance of **[Dy.L^{6}]** was also assessed, given the T^{-2} dependence in the Curie term of the following equation:

$$R_1 = \frac{2}{15}\left(\frac{\mu_0}{4\pi}\right)^2 \frac{\gamma_N^2 \mu_{eff}^2}{r^6}\left[\frac{7\tau_{r+e}}{1+\omega_e^2\tau_{r+e}^2} + \frac{3\tau_{r+e}}{1+\omega_N^2\tau_{r+e}^2}\right] + \frac{2}{5}\left(\frac{\mu_0}{4\pi}\right)\frac{\omega_N^2\mu_{eff}^4}{(3kT)^2 r^6}\frac{3\tau_r}{1+\omega_N^2\tau_r^2} \quad (2)$$

The variations in the R_1 of the *tert*-butyl chemical shift on **[Dy.L^{6}]** were measured for the three solutions described above, at 6 temperatures in the 290 to 315 K range. The linearity between R_1 and T^{-2} is evident in *Figure 3.22,* where $R^2 = 0.98$ for the lines of best-fit shown. The data in murine plasma: H_2O displays a slightly steeper gradient compared to the solutions in D_2O, but is less linear. These slight perturbations in R_1 could be accredited to interactions with plasma proteins; but this is not too much of a concern for *in vivo* applications, since the perturbation is negligible.

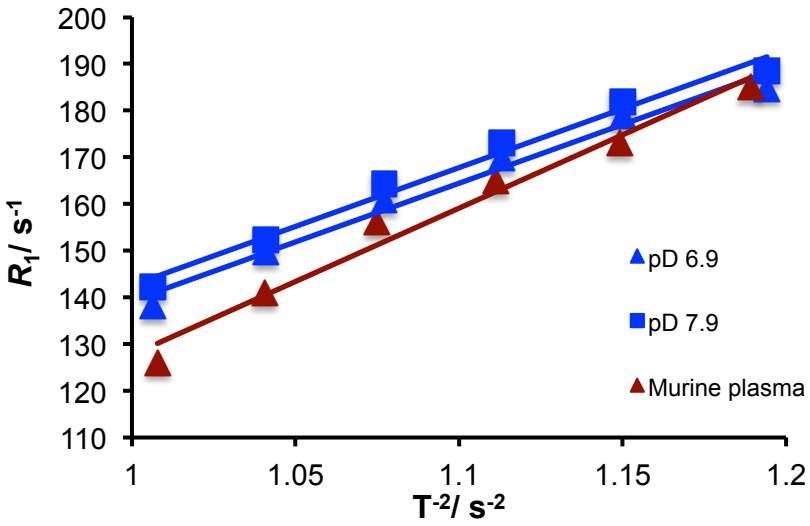

Figure 3.22 Variation in the longitudinal relaxation rate, R_1, of the major *tert*-butyl resonance of **[Dy.L^6]** as a function of T^{-2}: pD 6.9 (blue triangles), gradient = 252, R^2 = 0.984; pD 7.9 (blue squares), gradient = 252, R^2 = 0.980; and in a 50:50 murine plasma: H_2O mix at pH 7.1 (red triangles), y = 314, R^2 = 0.977 (11.7 T).

3.4.4 Responsive chemical shift behaviour of [Tb.L^6], [Er.L^6] and [Tm.L^6]

Due to the favourable shift and relaxation characteristics that were established in *Section 3.4.2*, the chemical shift behaviour of the **[Tb.L^6]**, **[Er.L^6]** and **[Tm.L^6]** complexes were assessed in D_2O. The *tert*-butyl resonance on each complex exhibited pH responsive chemical shift behaviour, as shown in *Figure 3.23*. The total shift change between the acid and base forms of each complex differed slightly. For example, **[Er.L^6]** showed a total shift change of 0.7 ppm, which is half the 1.4 ppm difference found for **[Tb.L^6]**. The overall shift magnitude of the *tert*-butyl resonance of **[Er.L^6]** is half of that for **[Tb.L^6]**, at least in part explaining the observed trend. Since there is no obvious trend with lanthanide(III) ion size or geometry, the pK_a values are proposed to be the same, within the experimental error of ±0.05.

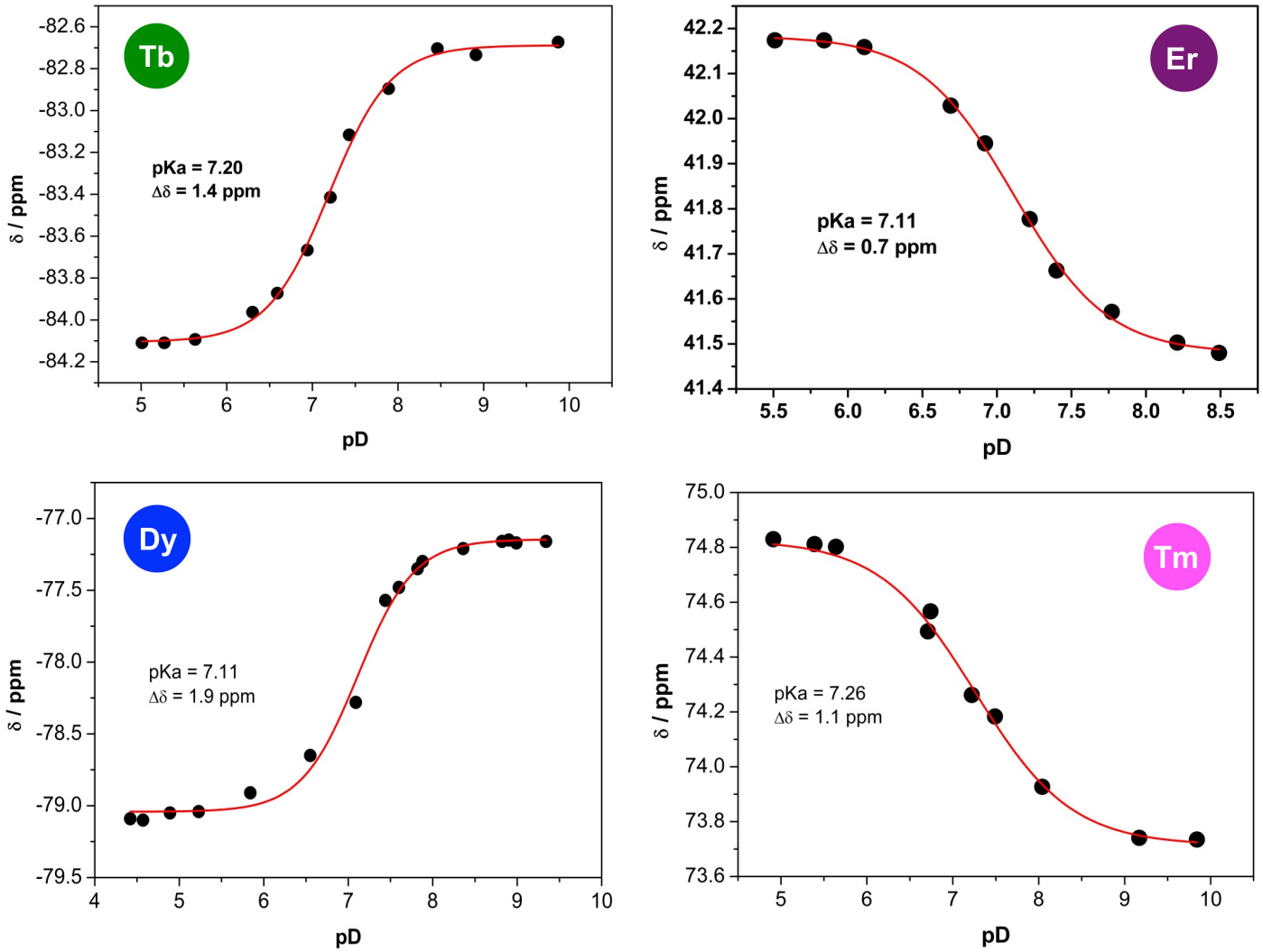

Figure 3.23 The shift in the major *tert*-butyl resonance of **[Ln.L^6]** (Ln = Tb, Dy, Er and Tm) as a function of pD (D_2O, 11.7 T, 295 K).

The linearity of the temperature dependence of the *tert*-butyl resonance for each complex also scaled with the magnitude of the overall *tert*-butyl chemical shift. As shown in *Table 3.4*, the largest temperature coefficient is evident for the most shifted **[Tb.L^{6}]** species, and the smallest for the least shifted species, **[Er.L^{6}]**.

Table 3.4 Comparison of the total shift and temperature sensitivities for the major *tert*-butyl resonance of the **[Ln.L^{6}]** complexes (all D_2O, ~pD 7.4, 11.7 T).

[Ln.L^{6}]	δ_H ^{t}Bu/ ppm	ΔT/ ppm K^{-1}
Tb	-83.1	0.52
Dy	-78.3	0.41
Tm	+74.6	0.44
Er	+42.5	0.24

Prior to the commencement of ^{1}H MRS imaging studies, a control experiment to monitor the change in relaxivity as a function of pH was undertaken with a solution of **[Gd.L^{6}]** (0.5 mM, H_2O). Over the measured pH range of 4 to 9, no significant change was observed in the relaxivity. This is an expected result, given that the coordination number of the metal is not being affected during the deprotonation/protonation process.

3.4.5 ^{1}H MRS phantom imaging studies with [Tm.L^{6}] and [Dy.L^{6}]

Following the *in vitro* analyses of the complexes described in *Sections 3.4.3 and 3.4.4*, and the shift and relaxation successes in *Sections 3.4.*2, Dr. Dara O'Hogain carried out phantom imaging studies at the Newcastle Magnetic Resonance Centre at 300 MHz (7 T). These were undertaken first to assess the feasibility of imaging at such remote spectral frequencies, and second to ascertain whether the shift changes can be observed by imaging methods.

Five equimolar solutions of **[Tm.L^{6}]** were prepared in buffered aqueous solution (0.1 M MOPS), at a range of pH values, inside cut-down 5 mm NMR tubes. The five NMR tubes were placed within a Teflon spacer, as shown in *Figure 3.25 (left)*, with an NMR tube containing deionised water only, occupying the central position. Use of the ^{1}H MRI inactive Teflon spacer ensured that there would be no image interference. Subsequently, the experimental array was placed inside the bore of a 30 mm birdcage coil, typically used for murine imaging. First, an image corresponding to the H_2O protons was obtained by imaging at the H_2O offset (*Figure 3.25, middle*) and second, by

setting the offset to the resonant frequency of **[Tm.L^{6}]** at pH 7 (*Figure 3.25, right*). As a result of using a well-removed offset, an image corresponding to the *tert*-butyl reporter resonance was acquired, separately from the endogenous water signal.

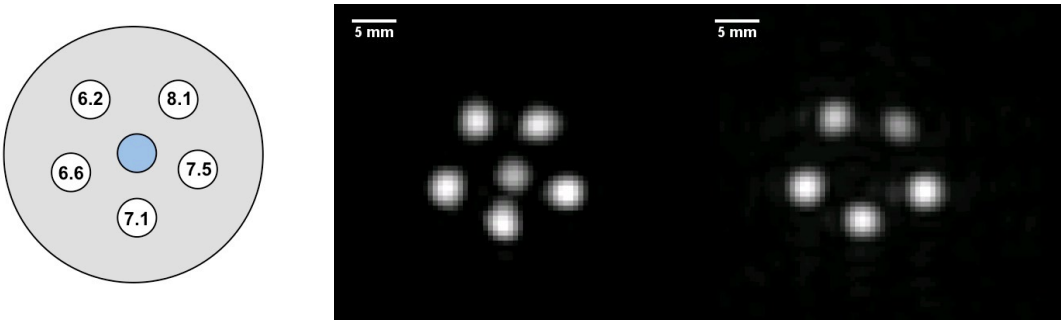

Figure 3.25 (*Left*) Illustration of experimental array, in a Teflon holder, using 5 equimolar solutions of buffered **[Tm.L^{6}]** at different pH values shown and with de-ionised H_2O in the centre (0.1 M MOPS, 1.2 mM, H_2O). (*Middle*) Phantom image at the H_2O offset (-641.4 Hz, intensity scale 0-4000 a.u.). (*Right*) Phantom image at the **[Tm.L^{6}]** *tert*-butyl offset (19103 Hz, intensity scale 0-0.1 a.u.), both: TR = 23.6 ms; TE= 1.2 ms; nt = 4 (H_2O), 80 (*tert*-butyl); SW = 6000 Hz; spectral points 128; spectral width 128; Matrix 16 x 16; FOV 40 x 40; slice thickness 8 mm; T = 303 K).

The feasibility of spectral analysis from the CSI data was demonstrated for the five phantoms of **[Tm.L^{6}]**, with *Figure 3.26* showing the frequency of the *tert*-butyl signal observed in each tube. With a total shift of 144 Hz at 7 T (0.48 ppm) between pH 6.2 and 8.1, the data obtained was in good agreement with the results from the *in vitro* studies.

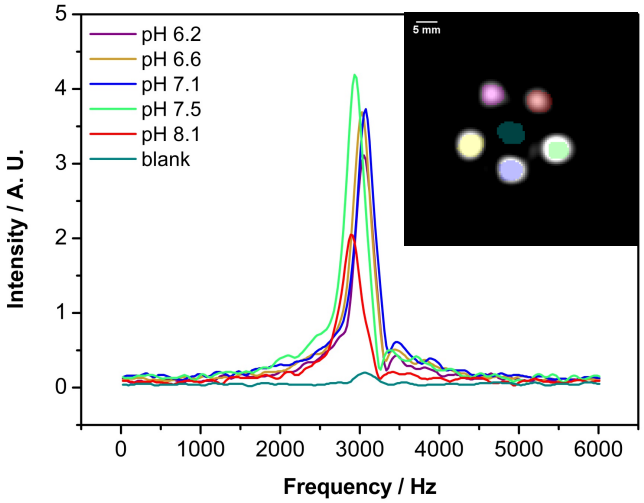

Figure 3.26 Spectral analysis from CSI image of **[Tm.L^{6}]**, showing the frequency detected for each ROI peak for: pH 6.2 (purple), 3037 Hz; 6.6 (yellow); 7.1 (blue); 7.5 (green); and 8.1 (red), 2893 Hz. Total shift = 144 Hz, 0.48 ppm, offset frequency = -27432 Hz, TR = 23.5, TE = 1.2, nt = 30, slice thickness = 8 mm, 128 spectral points, 6010 spectral width, T = 310 K.

The temperature of the five solutions of **[Tm.L^{6}]** was varied using an externally controlled heated airflow around the Teflon spacer array and was monitored by positioning a thermometer in the middle of the array. The PARASHIFT images were acquired 5 min after setting the temperature so as to minimise any chemical shift fluctuations. The plot in *Figure 3.27* shows the temperature dependent *tert*-butyl chemical shift behaviour of the five solutions. Such linear dependencies are in agreement with the data obtained on a spectral NMR instrument (11.7 T) for **[Tm.L^{6}]**, and pH 7, reporting *tert*-butyl chemical shift temperature dependencies of 0.44±0.02 ppm/K.

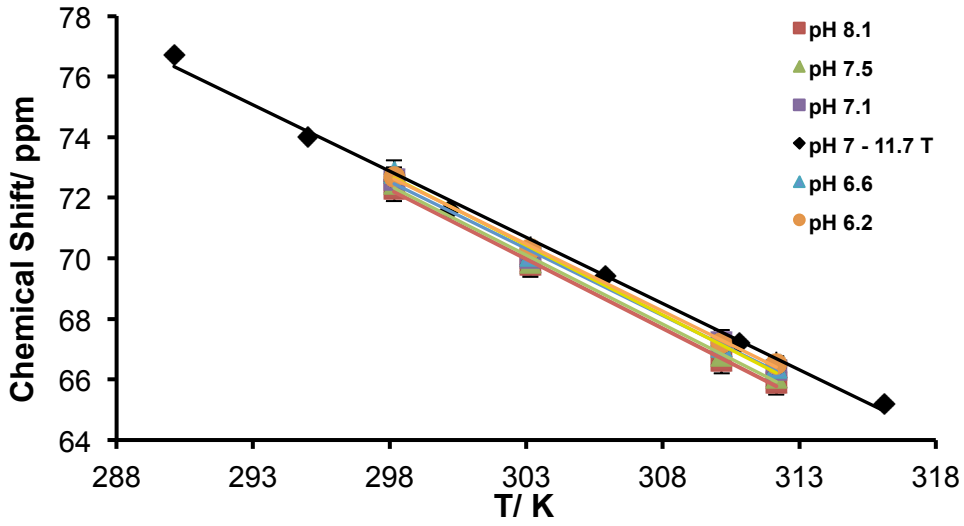

Figure 3.27 Variation in the chemical shift of the major *tert*-butyl resonance of five different pH solutions of **[Tm.L^{6}]** as a function of T (7 T): pH 6.2 (orange), gradient = 0.44; pH 6.6 (blue), gradient = 0.46; pH 7 *in vitro* (black), gradient = 0.44; pH 7.1 (purple), gradient = 0.44; pH 7.5 (green), gradient = 0.46; and pH 8.1 (red), gradient = 0.46. All lines of best-fit have $R^2 = 0.998$.

Next, two fresh solutions of **[Tm.L^{6}]** were prepared in MOPS buffered water, at the extreme pH values of 6.1 and 8.1, so that the shift difference was optimised. A CSI image was acquired of the two phantoms at the *tert*-butyl offset. This image was then processed using the spectral data, gaiting signal intensity at the offset 20227 Hz for pH 6.1 (*Figure 3.28, left*) and 20383 Hz for pH 8.1 (*Figure 3.28, right*). As a result, the applicability of selectively imaging two differently shifted *tert*-butyl resonant frequencies has been demonstrated (*Figure 3.28)*. Clearly, a difference of 144 Hz (*ca.* 0.48 ppm) is not a problem for CSI protocols, and offers much promise for *in vivo* studies.

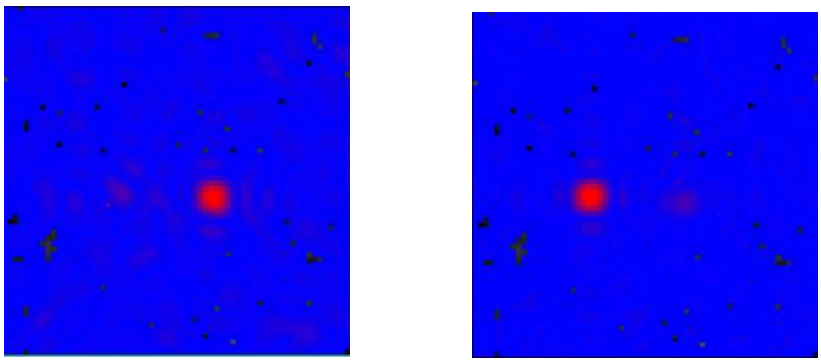

Figure 3.28 CSI image of **[Tm.L^{6}]** phantoms at offset frequency = 20383 Hz, TR = 19.8, TE = 12.4, nt= 40, slice thickness = 10 mm. At pH 6.1 (*left*), pixel intensity showing intensity at a frequency offset of 20227 Hz, and at pH 8.1 (*right*), pixel intensity showing signal intensity at frequency offset of 20383 Hz. (Images use thresholding to reduce noise).

Analogous phantom imaging experiments were repeated with a spacer unit comprising four equimolar solutions of **[Dy.L^{6}]** and de-ionised water (*Figure 3.29, left*). As before, the benefits of using a well-shifted *tert*-butyl reporter signal enabled the acquisition of an image corresponding to the *tert*-butyl signal intensity only, independent of the solvent water.

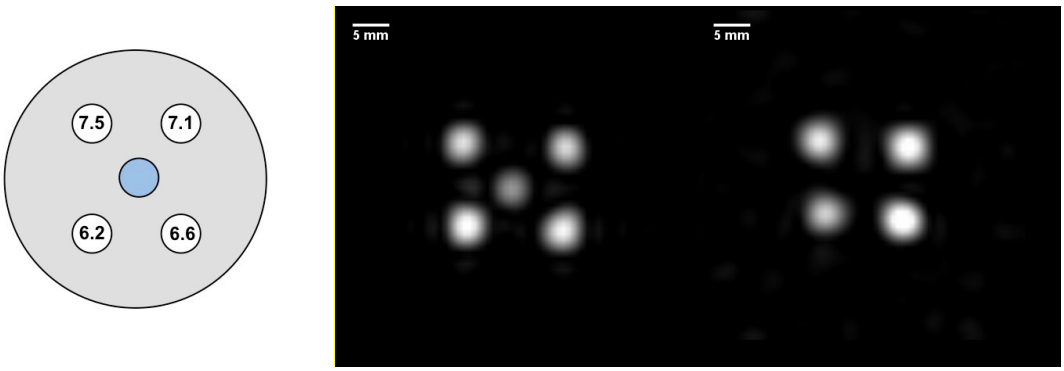

Figure 3.29 (*Left*) Illustration of experimental array, in a Teflon holder, using 4 equimolar solutions of buffered **[Dy.L^{6}]** at different pH values shown and with de-ionised H_2O in the centre (MOPS, 1.2 mM, H_2O). (*Middle*) Phantom image at the H_2O offset (-2839 Hz, intensity scale 0-4000 a.u.). (*Right*) Phantom image at the **[Dy.L^{6}]** *tert*-butyl offset (-27432 Hz, intensity scale 0-0.1 a.u.), both: TR = 17.2 ms; TE= 0.7 ms; nt = 4 (H_2O), 30 (*tert*-butyl); SW = 6000 Hz; spectral points 128; spectral width 8013; Matrix 16 x 16; FOV 40 x 40; slice thickness 60 mm; T = 296 K).

The feasibility of spectral analysis from the CSI data was demonstrated for each phantom of **[Dy.L^{6}]**, with *Figure 3.30* showing the frequency of the *tert*-butyl signal observed in each tube. With a total shift of 318 Hz at 7 T (1.06 ppm) between pH 6.2 and 7.5, the data obtained was in good agreement with the results from the *in vitro*

studies, where the total pH dependent shift for **[Dy.L^{6}]** is greater than the total shift for **[Tm.L^{6}]** (1.06 ppm *vs.* 0.48 ppm here). The difference in the size of the shift change here is somewhat surprising, but is very useful as it distinguishes each from the concomitant temperature dependent behaviour.

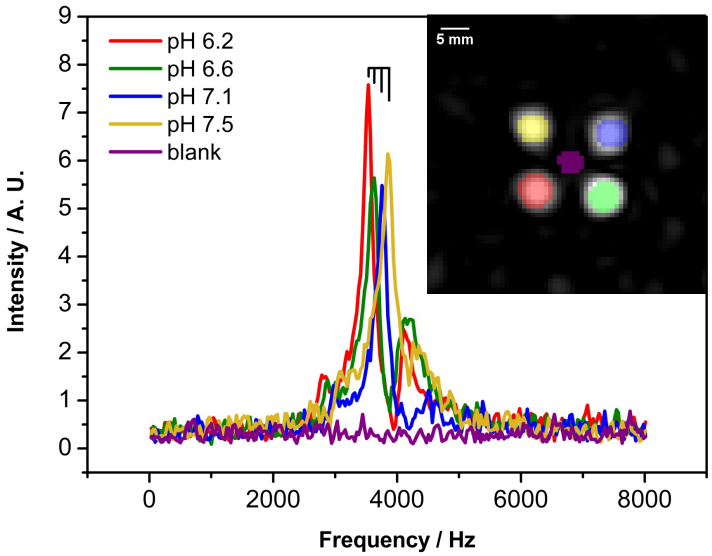

Figure 3.30 Spectral analysis from the CSI image of **[Dy.L^{6}]**, showing the frequency detected for each ROI peak for: pH 6.2 (red), 3543 Hz; 6.6 (green), 3644; 7.1 (blue), 3773 Hz; and 7.5 (yellow), 3861. Total shift = 318 Hz, 1.06 ppm; offset frequency = -27432 Hz, TR = 17.2, TE = 0.7, nt = 30, slice thickness = 60 mm, 128 spectral points, 8013 spectral width, T = 296 K.

3.4.6 ^{1}H MRS *in vivo* imaging studies with [Gd.L^{6}] and [Dy.L^{6}]

In order to establish the biodistribution and clearance profile of the **[Ln.L^{6}]** complexes, preliminary *in vivo* imaging studies focused on using **[Gd.L^{6}]** so that it could be viewed by standard dynamic contrast enhanced ^{1}H MRI protocols. Solutions containing 5 mM **[Gd.L^{6}]** were prepared in saline, and administered to separate anaesthetised mice by intravenous injection *via* the tail vein. The dose administered was calculated to be 0.04 mmol/kg, for a 25 g mouse.

The presence of contrast in the kidney and skeletal muscle first, and the bladder later, arising from **[Gd.L^{6}]**, was observed (*Figure 3.31*). Such a result indicates that the addition of an anionic *para*-substituent facilitates *slightly* slower clearance, affording biodistribution in tissue, and supports well the observation made for an increasing τ_R. A slower rate of clearance, favouring the biliary route, has been recently reported for a structurally related *para*-substituted anionic lanthanide(III) complex.[35] It also marks a *slight* improvement on the outcome of the imaging experiment with the di-carboxylate

parent complex, **[Gd.L^{2}(H$_2$O)]**, which was found to clear more rapidly *via* the kidneys. However, with the SNR increasing in the bladder 30 min after injection, the clearance rate of **[Gd.L^{6}]** is still faster than is ideally required for this work, and so further complex retention is sought.

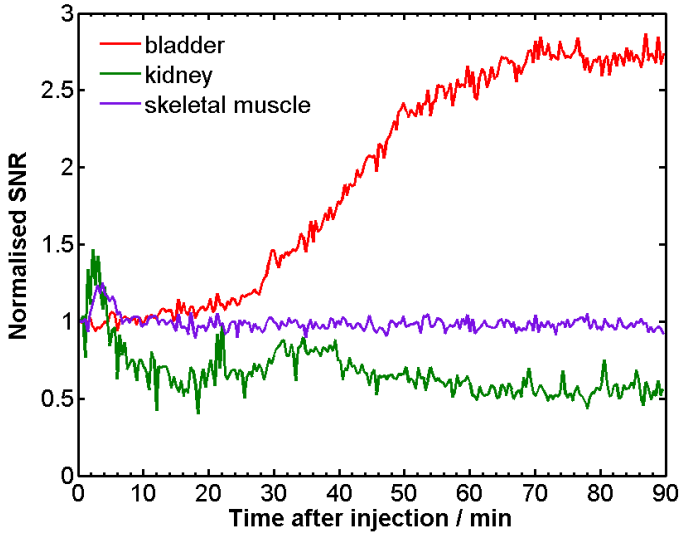

Figure 3.31 A plot of the normalised SNR from the gradient echo multi slice scan of **[Gd.L^{6}]** in the bladder (red), kidney (green) and skeletal muscle (purple) as a function of time after injection for mouse 1. Data was acquired as a gradient echo multi-slice scan, without gaiting, and with the following parameters; TR = 175.54 ms; TE = 4.89 ms; FOV 32 x 32; Matrix 128x128; 18 slices. The total acquisition time = 22.5 s. The mouse was injected with 200 μL of 5 mM **[Gd.L^{6}]** (*i.e.* a 0.04 mmol/kg dose) at time 0 min.

An analogous biodistribution study was undertaken with a 12.5 mM solution of **[Dy.L^{6}]**, injecting a dose of 0.1 mmol/kg. The ^{1}H PARASHIFT scans acquired at the *tert*-butyl offset of **[Dy.L^{6}]** are shown as two slices through the mouse in *Figure 3.32 (top)*, in which the first slice includes the kidneys, and the second slice includes the bladder. Signal intensity corresponding to the *tert*-butyl reporter resonance of **[Dy.L^{6}]** can be seen 4 min after injection, in each kidney, and in the bladder, 10 min after injection. The relative concentration of the *tert*-butyl signal as a function of time after injection shows rapid clearance through the kidneys, with later accumulation in the bladder (*Figure 3.32, bottom*).

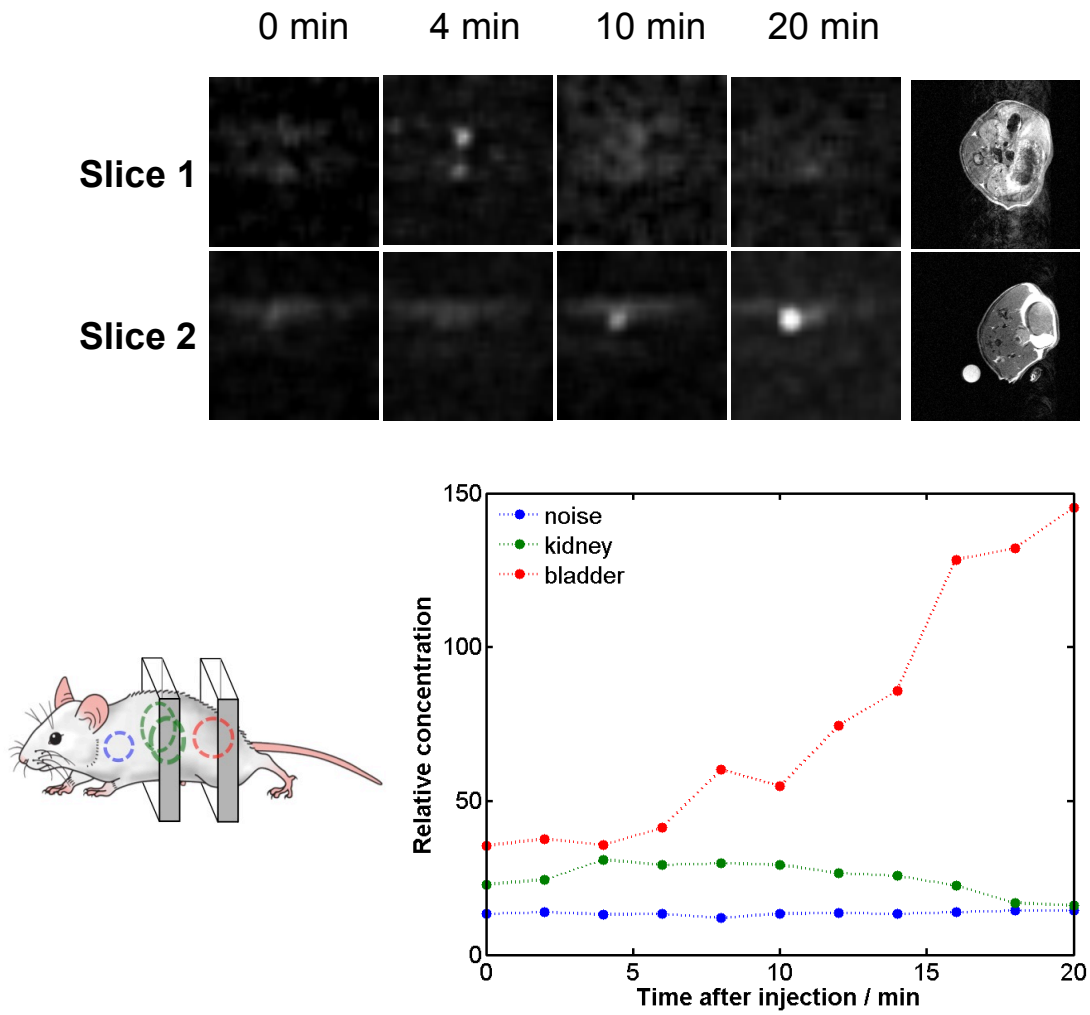

Figure 3.32 (*Top*) The corresponding ^{1}H PARASHIFT scans of two slices through the mouse, injected with 200 µL of 10 mM **[Dy.L^{6}]** at time 0 min, at the time intervals shown. *Slice 1* includes the kidneys, and *slice 2* includes the bladder. *Furthest right* are the standard structural scans (TR = 7.69 ms; TE = 0.73 ms; FOV 32 x 32; Matrix 16x16; 8 mm slices; sweepwidth 20 kHz; duration 63 s. The total acquisition time = 22.5 s). (*Bottom*) A plot of the relative concentration of **[Dy.L^{6}]** in the bladder (red) and kidney (green) as a function of time after injection of a 200 µL of 10 mM **[Dy.L^{6}]** at time 0 min.

Overall, the pH dependence of the *tert*-butyl chemical shift of the **[Ln.L^{6}]** complexes has allowed chemical shift differences of 144 Hz to be observed in MRS protocols, with high sensitivity and confidence. However, despite such behaviour, it is clear that the retention of the **[Ln.L^{6}]** complexes is a concern if *in vivo* pH mapping is to be realised. Of course, the clearance rates of these complexes are species-dependent, and will be slower and differ in the relative proportion of renal/biliary clearance routes for mice *vs.* rats/rabbits/humans.

3.5 Conclusions

The utility of pH responsive PARASHIFT probes has been described in *Section 1.3* (^{1}H) and *Section 3.1* (^{19}F). However, the former cases did not satisfy the requirements for increasing sensitivity in MRS imaging experiments, whilst the latter cases used the less readily observed ^{19}F reporter nucleus. Such drawbacks led to the development of closely related ^{1}H PARASHIFT systems, but extreme line-broadening associated with the pH dependent reversible ligation of a sulphonamide moiety led to significant signal intensity losses, and rendered it unsuitable for *in vivo* applications.

The work described allowed such limitations to be alleviated by fulfilling a new set of criteria (*pages 100-101*). As a result, three systems have been derived, in which minimal structural modifications on the parent systems from *Chapter 2* have occurred in the 4- position of the pyridyl moiety (*i.e. para-* to the coordinated nitrogen atom), such that changes to the favourable shift and relaxation characteristics are minimised.

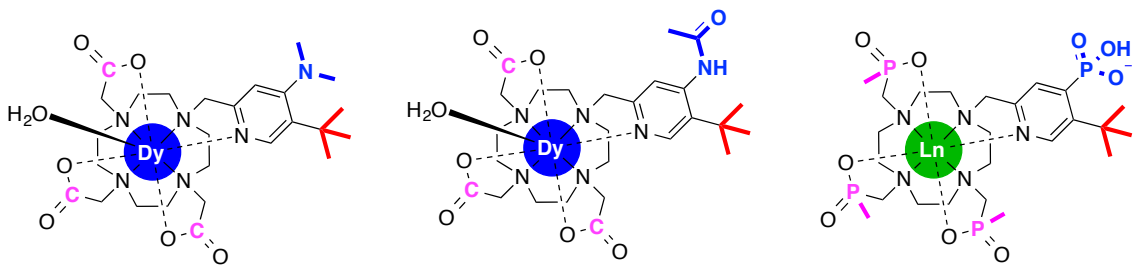

[Dy.L^{4}(H$_2$O)] **[Dy.L^{5}(H$_2$O)]** **[Ln.L^{6}]**

Figure 3.33 The pH responsive ^{1}H PARASHIFT probes detailed in this Chapter: the dimethylamine system, **[Dy.L^{4}(H$_2$O)]** (*left*); the acetamide system, **[Dy.L^{5}(H$_2$O)]** (*middle*) and the phosphonate system, **[Ln.L^{6}]** (*right*).

The dimethylamine substituted complex, **[Dy.L^{4}(H$_2$O)]** (*Figure 3.33*), possessed one major *tert*-butyl resonance at -28.4 ppm, showing a 10 ppm enhancement when compared to the unsubstituted tri-carboxylate analogue, **[Dy.L^{1}(H$_2$O)]** (δ_H = -20.1 ppm). Upon *para-* substitution, R_1 increases of up to 16% are achieved across all measured field strengths. However, there was no observable shift in the *tert*-butyl reporter resonance over the 5-10 pH range. Significant shift dependencies of 5 ppm/pH unit were observed for the diastereotopic methyl groups, at -8.1 and -19.3 ppm, but indicated that the pK_a (<3) of the dimethylamine substituent was too low for physiological purposes.

As expected, the acetamide substituted complex, **[Dy.L^{5}(H$_2$O)]** (*Figure 3.33*), gave rise to one major *tert*-butyl signal at -23.3 ppm, and exhibited the required R_1 enhancements in the 100 to 200 s^{-1} range at 7 T. However, whilst the pK_a was found to be desirable at 6.5, the total *tert*-butyl chemical shift change of 0.4 ppm was deemed to be too difficult to calibrate accurately in MRS imaging protocols.

Tert-butyl chemical shifts up to ±80 ppm were achieved for a phosphonate substituted system, **[Ln.L^{6}]**, marking improvements of 5 ppm when compared to the unsubstituted tri-phosphinate predecessors, **[Ln.L^{3}]**. As has been established for related tri-phosphinate systems, the Er(III) complex showed the highest R_1 across all the fields, with particularly attractive enhancements at clinical field strengths.

The *tert*-butyl resonance on **[Dy.L^{6}]** exhibited the largest total chemical shift change between the acid and base forms (1.9 ppm), and a highly desirable pK_a between 6.7 and 7.1 according to the ionic strength of the medium. Coupled with the enhanced sensitivity of imaging in a well-removed spectral window, such pH responsive chemical shift behaviour permitted the visualisation of the *tert*-butyl signal in both *in vitro* and *in vivo* MRS imaging protocols within a matter of minutes, at a well-tolerated dose, that is the size of clinically accepted contrast agents. However, **[Dy.L^{6}]** appeared to clear rapidly and accumulate in the bladder, mimicking the behaviour observed for **[Dy.L^{2}(H$_2$O)]$^{+}$**.

Clearly, a method needs to be devised to enhance the retention of the complex *in vivo* so that the *tert*-butyl reporter signal can be observed for a longer period of time in MRS imaging procedures, whilst still satisfying the shift and relaxation criteria at the heart of this work. The final Chapter of results and discussion will focus on the concept of substantially increasing the size of the probe, by conjugation of several probes to one polymeric vector.

3.6 References

1. B. Yoo and M. D. Pagel, *Front. Biosci.*, 2008, **13**, 1733–1752.
2. D. A. Bluemke, C. A. Gatsonis, M. H. Chen, G. A. DeAngelis, N. DeBruhl, S. Harms, S. H. Heywang-Kobrunner, N. Hylton, C. K. Kuhl, C. Lehman, E. D. Pisano, P. Causer, S. J. Schnitt, S. F. Smazal, C. B. Stelling, P. T. Weatherall and M. D. Schnall, *J. Amer. Med. Assoc.*, 2004, **292**, 2735–2742.
3. E. Terreno, D. D. Castelli, A. Viale and S. Aime, *Chem. Rev.*, 2010, **110**, 3019–3042.
4. O. Warburg, *On the metabolism of tumours*, Cambridge University Press, Cambridge, 1930.
5. R. A. Gatenby and R. J. Gillies, *Nat. Rev. Cancer*, 2004, **4**, 891–899.
6. J. L. Wike-Hooley, J. Haveman and H. S. Reinhold, *Radiother. Oncol.*, 1984, **2**, 343–366.
7. N. Raghunand, M. I. Altbach, Z. Bhujwalla and R. J. Gillies, in *Proceedings of the ISMRM 5th Annual Meeting, Vancouver*, 1997, p. 1096.
8. P. K. Senanayake, A. M. Kenwright, D. Parker and S. K. van der Hoorn, *Chem. Comm.*, 2007, 2923–2925.
9. A. M. Kenwright, I. Kuprov, E. De Luca, D. Parker, S. U. Pandya, P. K. Senanayake and D. G. Smith, *Chem. Comm.*, 2008, 2514–2516.
10. K. H. Chalmers, E. De Luca, N. H. M. Hogg, A. M. Kenwright, I. Kuprov, D. Parker, M. Botta, I. Wilson and A. M. Blamire, *Chem. Eur. J.*, 2010, **16**, 134–148.
11. K. H. Chalmers, M. Botta and D. Parker, *Dalton Trans.*, 2011, **40**, 904–913.
12. P. Harvey, K. H. Chalmers, E. De Luca, A. Mishra and D. Parker, *Chem. Eur. J.*, 2012, **18**, 8748–8757.
13. P. Harvey, I. Kuprov and D. Parker, *Eur. J. Inorg. Chem.*, 2012, **12**, 2015–2022.
14. E. De Luca, P. Harvey, K. H. Chalmers, A. Mishra, P. K. Senanayake, J. I. Wilson, M. Botta, M. Fekete, A. M. Blamire and D. Parker, *J. Biol. Inorg. Chem.*, 2014, **19**, 215–227.
15. S. Aime, M. Botta, L. Milone and E. Terreno, *Chem. Comm.*, 1996, 1265–1266.
16. D. Coman, H. K. Trubel, R. E. Rycyna and F. Hyder, *NMR Biomed.*, 2009, **22**, 229–239.
17. P. Harvey, A. M. Blamire, I. Wilson, K.-L. N. A. Finney, A. M. Funk, P. K. Senanayake and D. Parker, *Chem. Sci.*, 2013, **4**, 4251–4258.
18. P. Harvey, PhD Thesis, Durham University, 2013.
19. S. Aime, A. S. Batsanov, M. Botta, J. A. K. Howard, M. P. Lowe and D. Parker, *New J. Chem.*, 1999, 669–670.
20. K. L. Gempf, S. J. Butler, A. M. Funk and D. Parker, *Chem. Comm.*, 2013, **49**, 9104–9106.
21. B. Bleaney, *J. Magn. Reson.*, 1972, **8**, 91–100.
22. N. Bloembergen, *J. Chem. Phys.*, 1957, **27**, 572–573.
23. I. Soloman, *Phys. Rev.*, 1955, **99**, 559–565.
24. M. R. Goldman, *J. Magn. Reson.*, 2001, **149**, 160–187.
25. A. M. Funk, P. Harvey, K.-L. N. A. Finney, M. A. Fox, A. M. Kenwright, N. J. Rogers, P. K. Senanayake and D. Parker, *Phys. Chem. Chem. Phys.*, 2015, **17**, 16507–16511.
26. H. Gysling and M. Tsutsui, *Adv. Organomet. Chem.*, 1971, **9**, 361–395.
27. F. G. Bordwell, *Acc. Chem. Res.*, 1988, **21**, 456–463.
28. T. Gunnlaugsson, D. A. McDonaill and D. Parker, *J. Am. Chem. Soc.*, 2001, **123**, 12866–12876.
29. R. B. Moon and J. H. Richards, *J. Biol. Chem.*, 1973, **248**, 7276–7278.

30. M. J. Fisher and P. F. Dillon, *Circulation Res.*, 1987, **60**, 472–477.
31. R. J. Gillies, Z. Liu and Z. Bhujwalla, *Am. J. Physiol., Chem. Physiol. 36*, 1994, **267**, 195–203.
32. D. Redmore, *J. Org. Chem.*, 1976, **41**, 2148–2149.
33. D. Villemin, A. Elbilali, F. Simeon, P.-A. Jaffres, G. Maheut, M. Mosaddak and A. Hakiki, *J. Chem. Research (S)*, 2003, 436–437.
34. T. M. Balthazor and R. C. Grabiak, *J. Org. Chem.*, 1980, 5425–5426.
35. P. K. Senanayake, N. J. Rogers, P. Harvey, K.-L. N. A. Finney, A. M. Funk, J. I. Wilson, R. Maxwell, D. Parker and A. M. Blamire, *Magn. Reson. Med.,* 2016, DOI: 10.1002/mrm.26185.

Chapter Four: A Strategy to Enhance Complex Retention *In Vivo*

4.1 Introduction

As discussed in *Chapter 1*, one of the major problems plaguing any NMR spectroscopy based technique is the inherently low sensitivity. The work discussed in this thesis has set out to alleviate these drawbacks through the use of paramagnetic lanthanide(III)-based complexes, exhibiting sufficient sensitivity gains such that ^{1}H MRS imaging can be carried out *in vivo,* using clinically viable doses with clinically attractive acquisition times. Unfortunately, such approaches have led to fast probe clearance and as a result, the fast accumulation of the reporter signal in the bladder. With temperature and pH maps of the bladder being rather uninteresting, a method using the mouse model available needs to be devised to increase the tissue retention of the complex, such that increases in the local probe signal density can be observed.

One possible means of achieving this is to increase the size of the probe substantially, by covalently linking the lanthanide(III)-based complex to a higher molecular weight adduct (*Figure 4.0*). Originally a method formulated to increase the imaging nuclei density per unit concentration, applications with medium to high molecular weight conjugates have been shown to possess relatively slower rates of clearance from the body.[1–3]

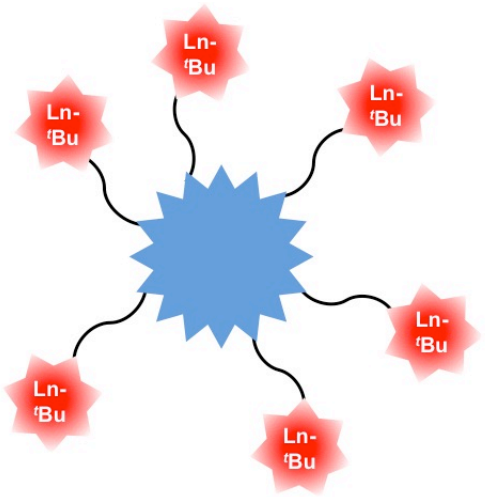

Figure 4.0 Schematic representation of the conjugate principle: where the blue centre represents a high molecular weight adduct, Ln-^{t}Bu the lanthanide(III)-based complex and the black line a covalent bond.

In order to maximise the signal intensity gained through this methodology, it is imperative that the magnetic equivalence of the reporter groups is retained, and that chemical exchange broadening is limited, giving rise to one major signal in solution. Of additional importance are the good biocompatibility characteristics, *i.e.* the low toxicity and good water solubility attained for the PARASHIFT probes detailed in *Chapters 2 and 3*.

A biocompatible vector of particular interest is that of glycol chitosan, a linear polysaccharide derived from chitin, composed of randomly distributed β-(1,4)-linked D-glucosamine and *N*-acetyl-D-glucosamine moieties. Its non-toxicity, biodegradability and good tolerance *in vivo* present crucial characteristics for the applications of this work.[4] In its commercially available form, the mean molecular weight is approximately 195 kD, but a significantly reduced molecular weight polymer (~6.5 kD) can be obtained through acidic digestion of the commercial material with 4 M HCl at 50 °C over a period of 24 h (*Scheme 4.0*).[4–6] This latter compound possesses greatly improved water solubility, and owing to the deacetylation under acidic treatment, yields a material bearing primary amine groups which are amendable for conjugation.

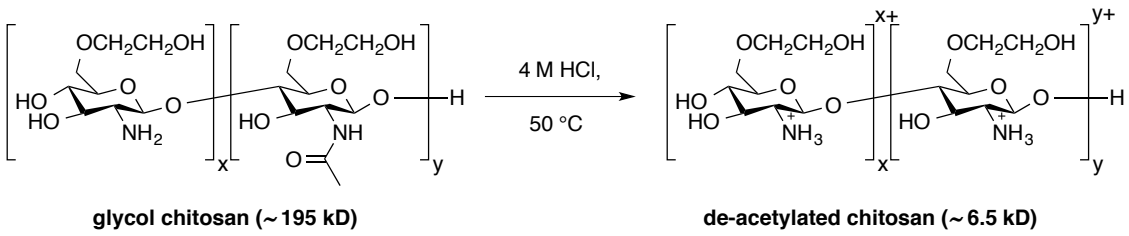

Scheme 4.0 Synthesis of the medium molecular weight deacetylated chitosan from the commercially available glycol chitosan by acidic digestion.

Previous work has demonstrated the preparation of medium molecular weight conjugates by appending paramagnetic lanthanide(III) complexes labeled with a trifluoromethyl reporter group, *via* an amide linkage to the acid digested product (*Figure 4.1*).[7] Characterisation by aqueous gel permeation chromatography (GPC) revealed average molecular weights of 13.8 kD for Gd(III), 14.6 kD for Dy(III) and 16.2 kD for Ho(III), consistent with the addition of 8.5, 9.5 and 13 complexes, respectively. The more promising characteristics were found for the tri-phosphinate Dy(III) complex conjugate (*i.e.* when X = PMe and n = 0, *Figure 4.1*), revealing a ^{19}F signal with one principal (86%) resonance. The independent rotational motion of the

complex with respect to the polymer, meant that the relaxation rates remained largely unaffected, with the conjugate product displaying a decrease in R_2 (440 s^{-1} for free complex *vs.* 367 s^{-1} for the conjugate at 9.4 T) and an increase in the R_1/R_2 ratio (0.42 for free *vs.* 0.50 for conjugate at 9.4 T).

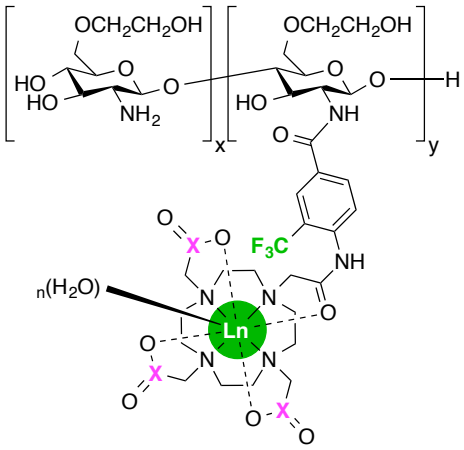

Figure 4.1 The structure of paramagnetic fluorine labeled glycol chitosan conjugates, where Ln = Gd, Dy and Ho, X = C or PMe; and n = the number of water molecules (typically 1 when X = C, and 0 when X = PMe).

Scouting experiments were undertaken to assess the biodistribution of the Gd(III) complex conjugates in nude mice bearing HT29 colorectal tumour xenografts. Doses of the order of 0.017 mmol kg^{-1} led to an almost immediate contrast enhancement (<1 min) in the tumour tissue and bladder by dynamic contrast enhanced ^{1}H MRI (*Figure 4.2*). Over a 10 min acquisition period, rapid and selective uptake of the Gd(III) complex conjugate was observed in the tumour (*Figure 4.2*), owing to an enhanced permeability and retention effect characteristic of such medium molecular weight systems.[8]

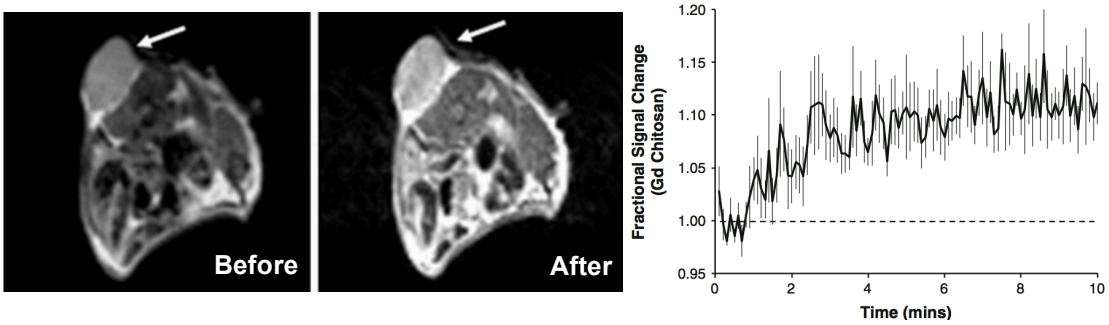

Figure 4.2 (*Left*) T_1-weighted ^{1}H MRI images before and after injection of a 0.017 mmol kg^{-1} dose of a Gd(III) complex conjugate, tumour indicated by an arrow. (*Right*) Temporal profile of the mean signal intensity in the tumour area over a 10 min acquisition window post-Gd(III) administration, where the fluctuations are due to respiratory motion.[7]

4.2 Glycol Chitosan Based System

With this background in mind, a medium molecular weight glycol chitosan conjugate has been designed, conjugated through an amide bond to a paramagnetic lanthanide(III) complex in which a *tert*-butyl reporter group is engineered to be about 6.5 Å from the lanthanide(III) centre (*Figure 4.3*). For this work, a tri-phosphinate-based lanthanide(III) complex has been selected, following the promising shift characteristics achieved in *Section 2.4.2* and the aforementioned work of De Luca *et al.*.[7] Provided that the relaxation behaviour and the magnetic equivalence of the *tert*-butyl reporter resonance are retained in the conjugated species, it is expected that such systems will enhance signal retention *in vivo* in ^{1}H MRS imaging protocols and alleviate some of the clearance problems presented by **[Dy.L^{2}(H$_2$O)]$^{+}$** and **[Dy.L^{6}]** in *Chapters 2 and 3*, respectively.

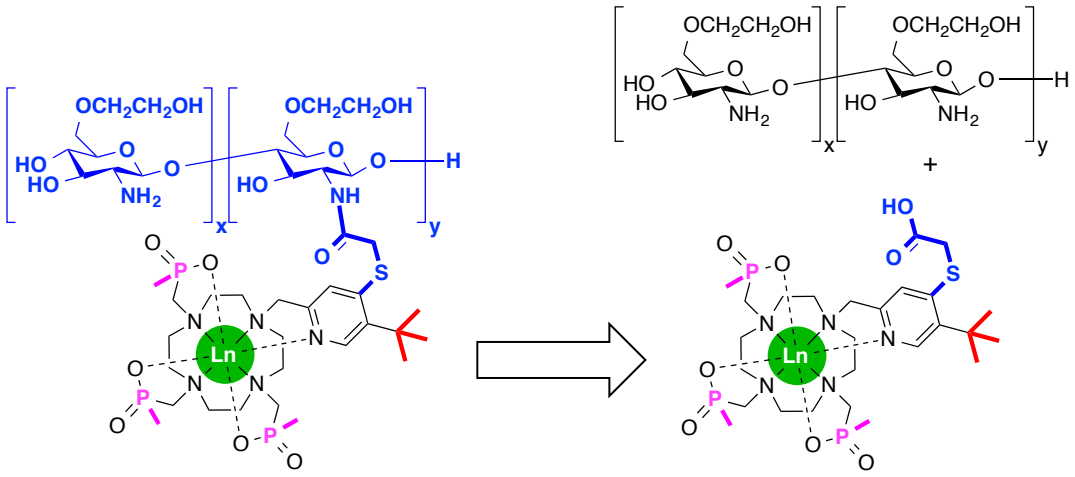

Figure 4.3 The design of a medium molecular weight glycol chitosan conjugate, bearing a *tert*-butyl labeled paramagnetic lanthanide(III) complex (*left*) and the disconnection revealing the target carboxylic acid bearing precursor complex, **[Ln.L^{7}]** (*right*).

4.2.1 The precursor complex, [Ln.L^{7}]

4.2.1.1 Synthesis and characterisation

The synthesis of the precursor complex is detailed in *Scheme 4.1*, beginning with the previously synthesised nitro- alcohol ***43***. Previously alluded to synthetic procedures have shown the ability to replace a nitro- group in the 4-position of a coordinated pyridyl moiety on a paramagnetic lanthanide(III) complex with a sulphur containing compound.[9] In this case, a displacement reaction occurred with ethyl thioglycolate in the presence of sodium hydride, on the diamagnetic substrate ***43*** to achieve the ester ***71***,

following purification by silica gel column chromatography. Formation of the mesylate ***72*** was undertaken using mesyl chloride and triethylamine and proceeded in near quantitative yield.

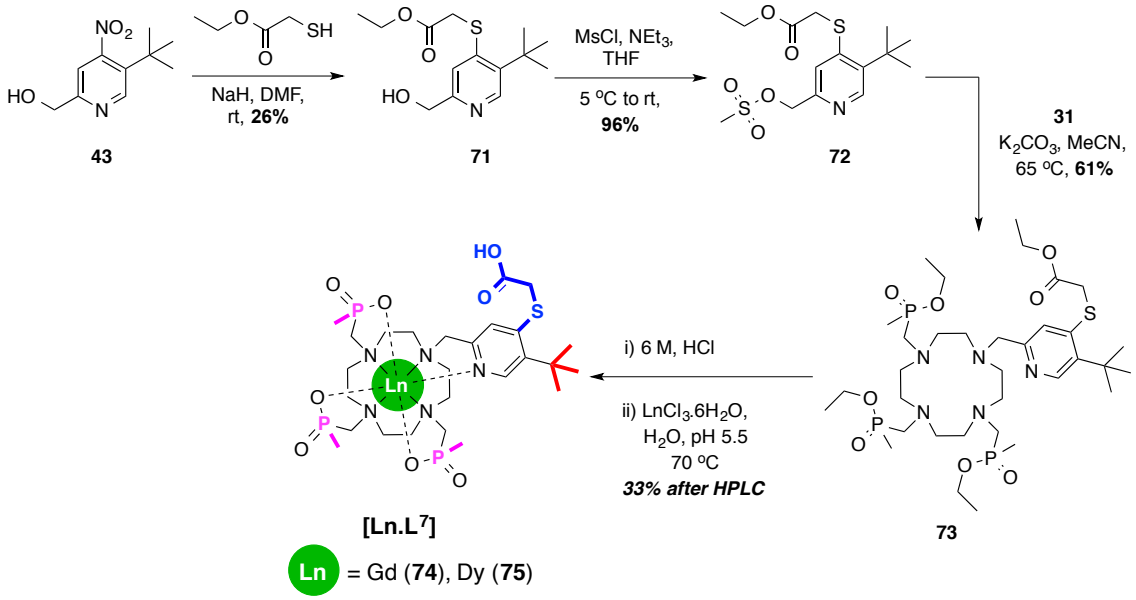

Scheme 4.1 General synthetic procedures for the synthesis of the carboxylic acid bearing precursor complex, **[Ln.L^7]**.

Afterwards, *N*-alkylation of the previously derived tri-phosphinate macrocycle ***31*** was carried out with ***72***, in a small volume of dry acetonitrile to accelerate the reaction towards the tetra-alkylated ligand ***73***. Following isolation by alumina gel column chromatography, the ethyl esters were removed in 6 M hydrochloric acid. Complexation of the corresponding hydrochloride salt of the ligand was achieved by reaction with the hydrated chlorides of Gd(III) and Dy(III), in aqueous solution at pH 5.5. Pure complexes were derived therefrom by reverse-phase preparative HPLC, with high resolution mass spectrometry methods confirming the desired constitution of the complexes in good agreement to the experimentally calculated isotope patterns.

For **[Gd.L^7]**, the relaxivity, r_{1p}, was found to be 1.86±0.05 mM^{-1} s^{-1} (H_2O, 60 MHz, 310 K) and is consistent with the values obtained for the related q = 0 tri-phosphinate systems detailed in *Chapters 2 and 3*. It is expected that a large increase in r_{1p} will accompany the corresponding glycol chitosan conjugate, indicative of the slower molecular tumbling of the overall complex in solution and an increase in the rotational correlation time, τ_r.[8] The literature example described above reports that an r_{1p} value

doubles in magnitude for the glycol chitosan conjugate compared with the free uncoupled tri-carboxylate complex (4.62 *vs.* 11.2 mM^{-1} s^{-1}; H_2O, 60 MHz, 310 K).[7]

4.2.1.2 ^{1}H NMR shift and relaxation behaviour of [Dy.L^7]

The ^{1}H NMR spectrum of **[Dy.L^7]** showed the presence of one major *tert*-butyl signal in solution, indicating the formation of one preferred isomer (85%). The major and minor *tert*-butyl reporter groups resonated at -75.8 and -78.1 ppm, respectively. Such shifts are of comparative magnitude to those reported earlier for the unsubstituted tri-phosphinate **[Dy.L^3]** complex but slightly less than those found for the *para*-substituted **[Dy.L^6]** complex (*ca.* 80 ppm).

The relaxation rate analysis of the major isomer of **[Dy.L^7]** crucially revealed the achievement of the desired R_1 enhancement at clinical field (*Table 4.0*). It is evident that only the *para*-substituted tri-phosphinate systems display the required enhancements, showing 45% improvements compared to their unsubstituted analogues.

Table 4.0 Experimental longitudinal relaxation rate data for the major *tert*-butyl resonance of **[Dy.L^7]** (Y = SCH_2COO^-) at different magnetic field strengths (D_2O, 295 K[a]). **[Dy.L^3]** (Y = H) and **[Dy.L^6]** (Y = PO_3H^-) are shown for comparison.

Y substituent	**R_1/ s^{-1} (± error)**						**R_1/R_2[b] (9.4 T)**
	1.0 T	**4.7 T**	**9.4 T**	**11.7 T**	**14.1 T**	**16.4 T**	
H	40 (2)	59 (1)	96 (1)	114 (1)	132 (1)	150 (2)	0.59
PO_3H^-	54 (5)	88 (3)	156 (1)	179 (1)	195 (1)	218 (1)	0.50
SCH_2COO^-	53 (6)	87 (3)	158 (2)	179 (1)	201 (1)	215 (1)	0.55

(a) Temperature was monitored accurately, calibrating against an ethylene glycol shift thermometer; (b) R_2 values were estimated as ($\pi \times \omega_{1/2}$), for a Lorentzian line fit; (c) measured at pH = 9, at pH 7.1 (*i.e.* the pK_a, at 295 K) T_2^* increases by a factor of 3, see *Section 3.4.3* for more information.

Analogous work has reported the relaxation rate behaviour of the major isomer of a series of *para*-substituted tri-phosphinate Dy(III) complexes across 6 different field strengths (*Figure 4.4*).[10] The degree of deviation of the R_1 values from these of the parent, unsubstituted complex was more pronounced with increasing field strength, such that in the cases of **[Dy.L^6]** (Y= PO_3H^-) and **[Dy.L^7]** (Y = SCH_2COO^-), a 45% R_1 improvement is evident at 16.4 T.

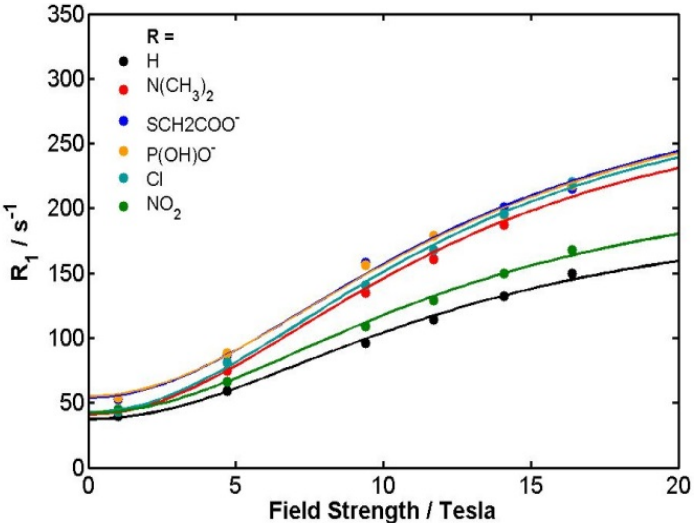

Figure 4.4 ^{1}H NMR relaxation rates, R_1/ s^{-1}, for the *tert*-butyl resonance on **[Dy.L^{3}]** (Y = H), **[Dy.L^{6}]** (Y = PO_3H^-) and **[Dy.L^{7}]** (Y = SCH_2COO^-) as a function of magnetic field, showing the fits (*lines*) to the experimental data points (*circles*) (295 K, D_2O, in the case of **[Dy.L^{6}]** pD 7.4).

Such increases in R_1 at high field are associated with increases in the Curie contribution to relaxation, and the dominance of the $(\mu_{eff})^4$ term. Estimated values of μ_{eff}, obtained by iterative minimisation methods, demonstrated that the value for **[Dy.L^{7}]** fell within ±5% of the classical range (*Table 4.1*).[11] A value for τ_R was also estimated for **[Dy.L^{7}]**, displaying a 38% increase for the inclusion of an anionic *para*-substituent, observed previous. The increases in relaxivity conveyed for both **[Dy.L^{6}]** and **[Dy.L^{7}]** reflect such behaviour and is consistent with the larger apparent molecular volume occupied by the more strongly hydrated anionic complexes. Estimated values for T_{1e} converged uniformly to 0.46 (±0.01) ps, corroborating the similarity of the observed R_1 values at 1.0 T for the three complexes, and in accord with the vanishing Curie term.

Table 4.1 Estimated best fit values of μ_{eff}, T_{1e} and τ_R for **[Dy.L^{7}]** (Y = SCH_2COO^-) (D_2O, 295 K and r = 6.6 Å). **[Dy.L^{3}]** (Y = H) and **[Dy.L^{6}]** (Y = PO_3H^-) are shown for comparison.

Y substituent	μ_{eff}/ BM	T_{1e}/ ps	τ_R/ ps
H	9.47 (3)	0.45 (2)	249 (3)
PO_3H^-	10.65 (6)	0.46 (4)	345 (3)[a]
SCH_2COO^-	10.69 (7)	0.44 (3)	357 (2)[b]

(a) For data fitted with a fixed τ_R = 280 ps, minimisation gave a poorer fit: μ_{eff} = 10.56 B.M. and T_{1e} = 0.51 ps; (b) For data fitted with a fixed τ_R = 280 ps, minimisation gave a poorer fit: μ_{eff} = 10.58 B.M. and T_{1e} = 0.50 ps.

Variable temperature ^{1}H NMR spectroscopy shift studies were undertaken for the major and minor *tert*-butyl resonances of **[Dy.L^{7}]**. A shift change of 0.46 ppm/ K^{-1} was observed for both resonances, owing to the T^{-2} dependence in the Curie term of the pseudocontact shift equation (*Figure 4.5*) and was comparable to the value obtained for the anionic *para*-substituted **[Dy.L^{6}]** complex reported in *Chapter 3* (*ca.* 0.41 ppm/ K^{-1}).

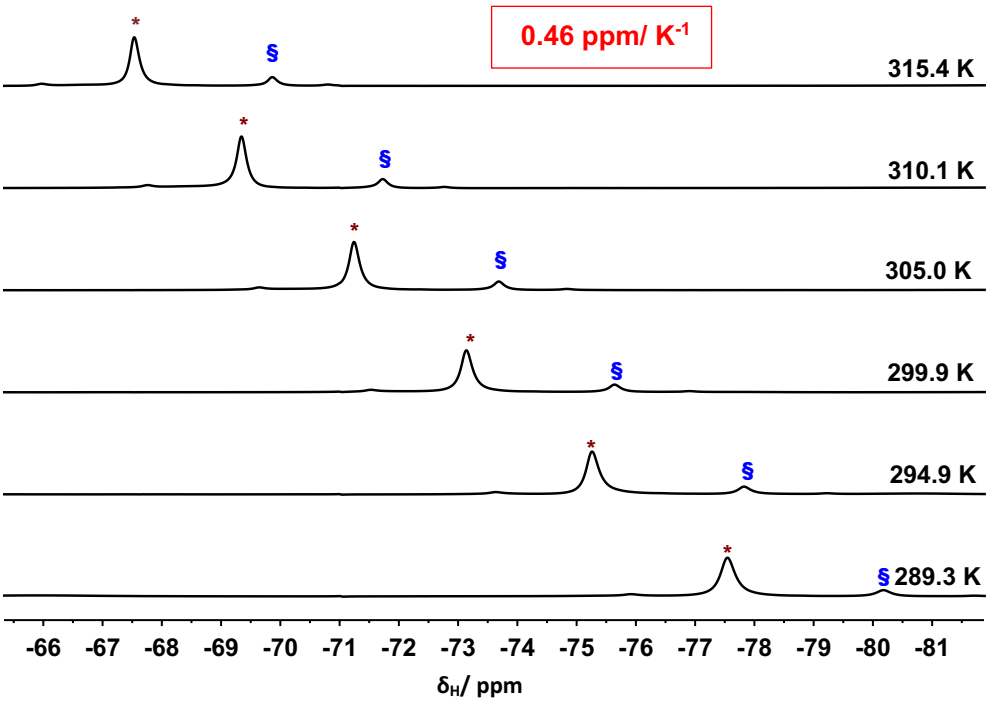

Figure 4.5 Stacked ^{1}H NMR spectra of the major (*) and minor (§) *tert*-butyl resonances of **[Dy.L^{7}]**, showing a change of 0.46 ppm/ K^{-1} as a function of temperature (D_2O, pD 7.4, 11.7 T).

4.2.2 The glycol chitosan conjugate complex, [Dy.L^{7}-chitosan]

4.2.2.1 Synthesis and characterisation

Before coupling reactions were undertaken with **[Ln.L^{7}]**, the residual sodium formate from HPLC purification and neutralisation was removed by passing the complexes through a plug of alumina gel, using 20% methanol in dichloromethane as the carrier solvent, to ensure both complex elution and salt deposition. Following this procedure, the appearance of the complexes changed dramatically from white solids to coloured powders; with the disappearance of sodium formate confirmed by ^{1}H NMR spectroscopy (*Figure 4.6*) and inductively coupled plasma mass spectrometry (ICP-MS).

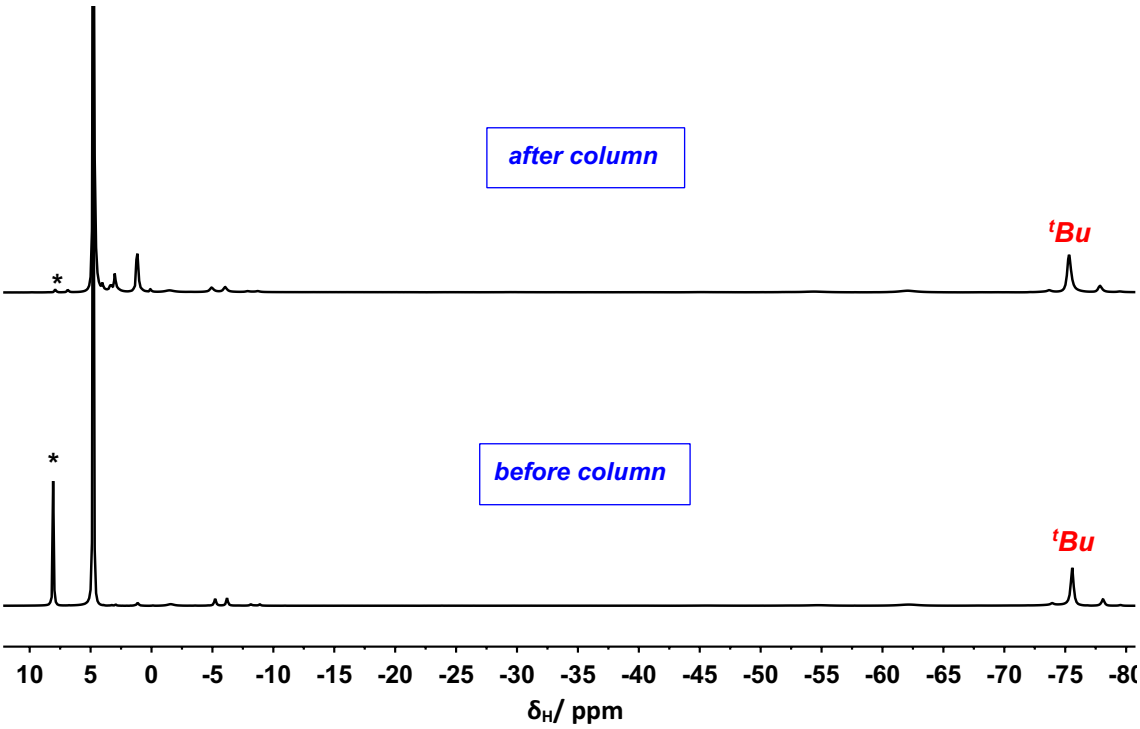

Figure 4.6 Stacked ^{1}H NMR spectra of **[Dy.L^{7}]** showing the disappearance of sodium formate, before (*bottom*) and after (*top*) the desalting procedure (D_2O, 295 K, pD 7.4, 11.7 T).

The synthesis of the desired glycol chitosan conjugate, **[Ln.L^{7}-chitosan]**, was first attempted with **[Dy.L^{7}]**, following literature protocols,[7] and is outlined in *Scheme 4.2*. The carboxylic acid functionality on **[Dy.L^{7}]** was first converted to an active ester, by a reaction with *o*-(benzotriazol-1-yl)-*N,N,N',N'*-tetramethyluronium tetrafluoroborate (TBTU) and *N*-methylmorpholine (NMM) in anhydrous DMF. After stirring for 1 h, allowing sufficient time for the formation of the active ester species, a concentrated aqueous solution of glycol chitosan was added and the resulting mixture was stirred at 40 °C. However, regular mass spectrometry sample analysis showed little evidence of reaction progress, with peaks corresponding to the free complex and the coupling agents evident in each sample.

With the real-time monitoring of reaction progress difficult, after 48 h, the coupling agents were removed by dialysing the reaction mixture against Purite H_2O using commercially available MWCO 0.5 - 1 kD dialysis tubing, for a period of 48 h in which the bulk water was replaced periodically (*i.e.* every 3 h except when overnight). The material was then transferred into MWCO 2 kDa dialysis tubing for a period of 48 h in an effort to exclude the free complex (MW *ca.* 850 g mol^{-1}), evident from earlier mass spectrometry analyses.

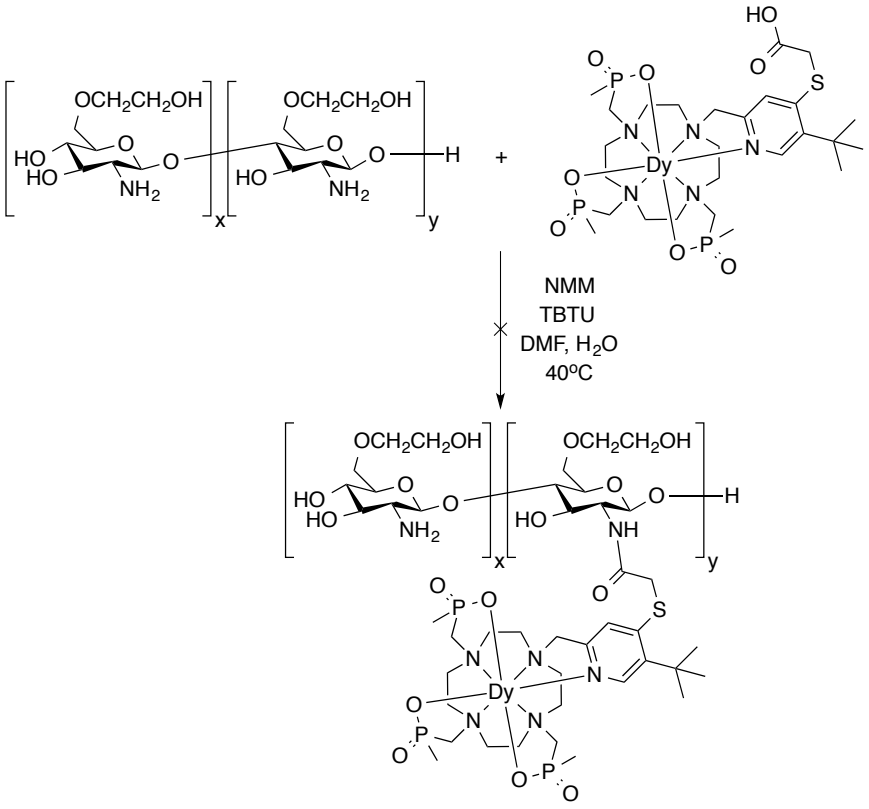

Scheme 4.2 General synthetic procedures for the attempted synthesis of the glycol chitosan conjugate, **[Dy.L^7-chitosan]**.

Following lyophilisation, the material was analysed by ^{1}H NMR, assessing the *tert*-butyl shift and relaxation behaviour in particular. The ^{1}H NMR spectrum showed the presence of one major *tert*-butyl signal in solution, indicating possible equivalence of each complex in the conjugated adduct (~85%). Once again, major and minor isomers were evident, resonating at -75.5 and -78.1 ppm, respectively. However, with the reaction material exhibiting a similar isomeric ratio and shift to the free complex, reverse-phase analytical HPLC was also used to assess the composition of the reaction material. The UV chromatograms for **[Dy.L^7]** and the reaction material looked identical within the 240 and 268 nm detector channels, and indicated that either the reaction had not proceeded to product or that the product was not visible under such conditions. The later inference is not entirely inconceivable, when the poly-disperse nature of the material is considered.

Finally, in order to eliminate one of these possibilities a solid sample was submitted for aqueous GPC analysis at Smithers Rapra. The resulting GPC molecular weight distribution was dominated by a higher molecular weight component with minor lower molecular weight components, implying that reaction to the desired glycol conjugate

species had not occurred. A couple of limiting factors can be at fault here: first, the reaction could be hindered by the proximal steric bulk provided by the *tert*-butyl group, and also, the formation of the active ester species could be reversed back to the carboxylic acid by the addition of solvent water.

4.2.3 The glucosamine conjugate complex, [Dy.L^7-glucosamine]

4.2.3.1 Synthesis and characterisation

The coupling between **[Dy.L^7]** and glucosamine, the monomer unit of glycol chitosan, was tested so that reaction progress could be monitored with more readily available analytical techniques such as mass spectrometry and reverse-phase analytical HPLC, due to its size (*ca.* 1000 g mol^{-1}). The first coupling procedure between **[Dy.L^7]** and glucosamine, obtained by anion exchange of the commercially available hydrochloride salt, utilised the same reaction conditions used previous (*Scheme 4.3*). Similarly, however, reaction progress to the active ester and/ or to the glucosamine conjugate was not evident by MS or HPLC. Previous unpublished work has demonstrated the feasibility of synthesising and isolating the active ester species,[12,13] but subsequent reaction attempts under the same conditions did not yield the active ester species for **[Dy.L^7]**.

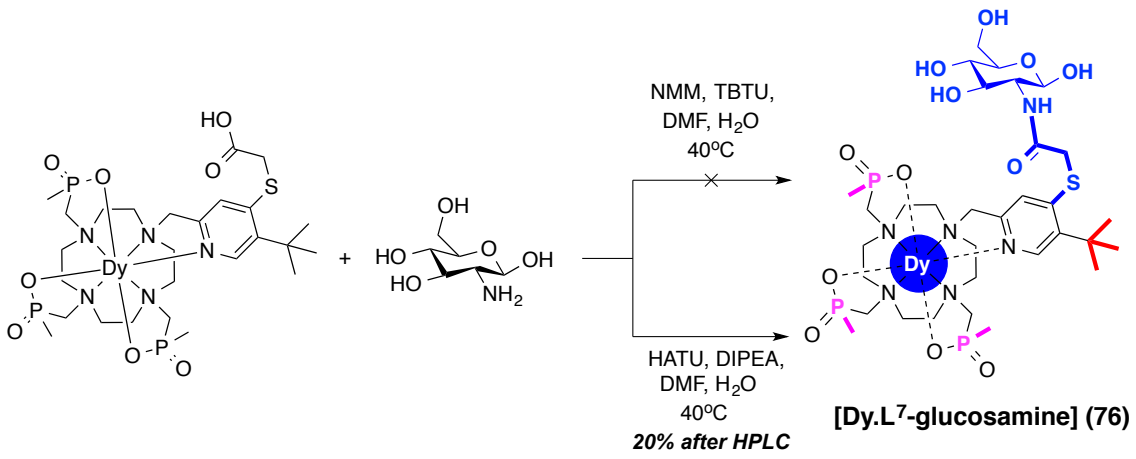

Scheme 4.3 General synthetic procedures for the synthesis of the glucosamine conjugate, **[Dy.L^7-glucosamine],** ***76***.

Instead, a related approach using HATU and *N,N*-diisopropyl ethylamine (DIPEA) was adopted (*Scheme 4.3*). The reaction went to completion, with full consumption of the free complex confirmed by low-resolution mass spectrometry. The crude mixture was precipitated in diethyl ether and triturated with acetonitrile, before being dissolved in

H_2O and purified by reverse-phase preparative HPLC to yield **[Dy.L^7-glucosamine]**, ***76***, as a white solid.

4.2.3.2 ^{1}H NMR shift and relaxation behaviour

The ^{1}H NMR spectrum of **[Dy.L^7-glucosamine]** revealed the presence of an additional isomeric species upon comparison to **[Dy.L^7]** (*Figure 4.7*). This behaviour in solution can attributed to the chiral centre in the 2- position (*) of the glucosamine moiety, giving rise to diastereoisomeric D-Δ and D-Λ complexes in an approximately 1:1 ratio. Clearly, the **[Dy.L^7-glucosamine]** complex is not well suited for ^{1}H MRS imaging, since the complex should exist as one major isomer in solution.

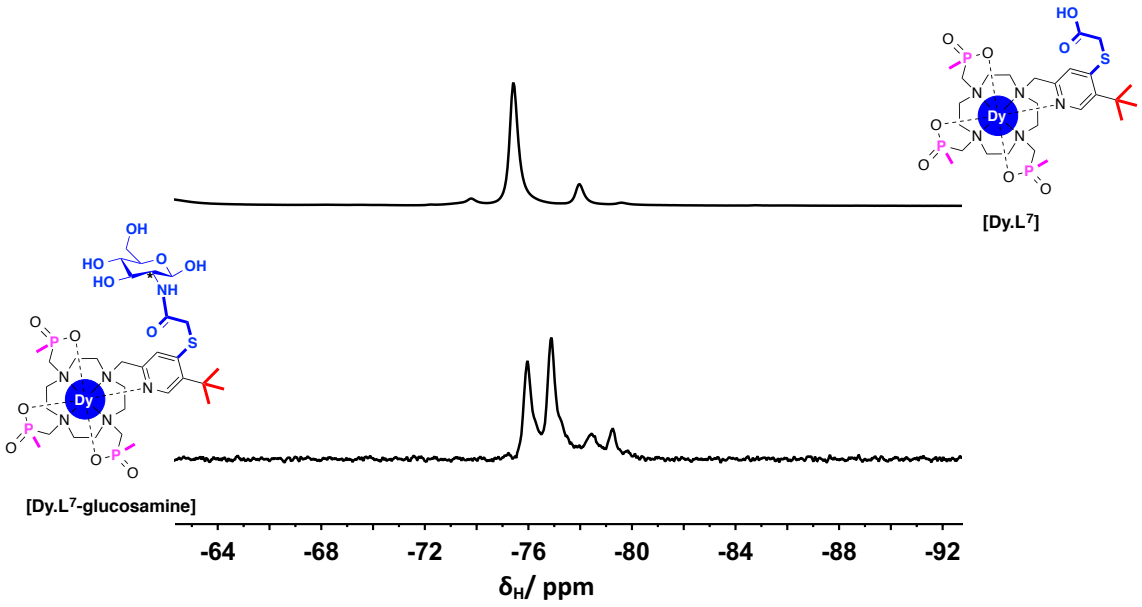

Figure 4.7 Stacked ^{1}H NMR spectra of **[Dy.L^7]** (*top*) and **[Dy.L^7-glucosamine]** (*bottom*) showing the appearance of an additional isomeric species due to chiral centre marked with an * (D_2O, 295 K, pD 7.4, 9.4 T).

Next, assessment of the relaxation rate behaviour indicated that appending a large molecule did not affect the favourable R_1 of the *tert*-butyl reporter group, already obtained for **[Dy.L^7]** (*Table 4.0*). At 9.4 T, the R_1 of the major *tert*-butyl group(s) on **[Dy.L^7-glucosamine]** were 140 Hz, compared to 158 Hz for the *tert*-butyl group on **[Dy.L^7]**. The R_1/R_2 ratio also remained largely affected, giving values of ~0.49 and 0.55, respectively.

4.2.4 The glycol chitosan conjugate complex revisited, [Dy.L^7-chitosan]

4.2.4.1 Synthesis and characterisation

Following the successful reaction between **[Dy.L^7]** and glucosamine under adapted literature conditions, an analogous reaction was undertaken with glycol chitosan (*Scheme 4.4*).

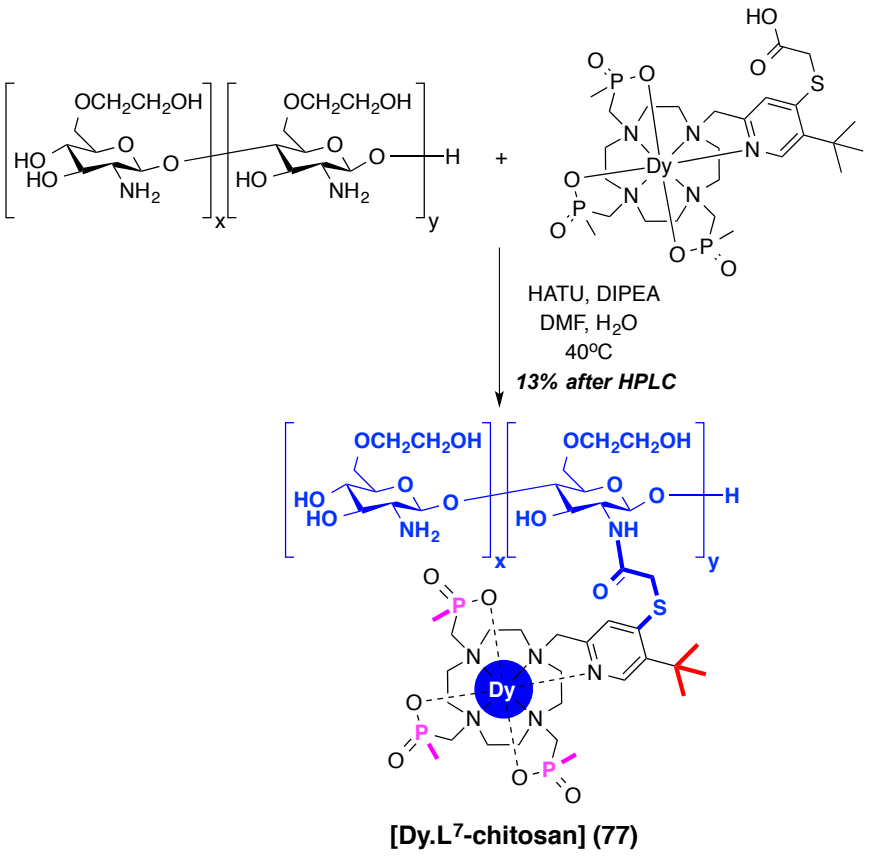

Scheme 4.4 General synthetic procedures for the synthesis of the glycol chitosan conjugate, **[Dy.L^7-chitosan],** *77*.

For the initial characterisation of reaction progress, reverse-phase analytical HPLC was preferred. The comparative UV chromatograms (268 nm) for **[Dy.L^7]** and the reaction mixture are shown in *Figure 4.8*. Indication of reaction completion was afforded by the trace observation of **[Dy.L^7]** in the top chromatogram at t_R = 10.3 min and the marked change in retention time. The reaction mixture chromatogram suggests that the compound is highly water soluble, eluting almost immediately at t_R = 1.7 min, where the solvent is predominantly water (10% MeOH+0.1% formic acid in H_2O+0.1% formic acid) and is consistent with the formation of the highly water soluble glycol chitosan conjugate complex, **[Dy.L^7-chitosan]**.

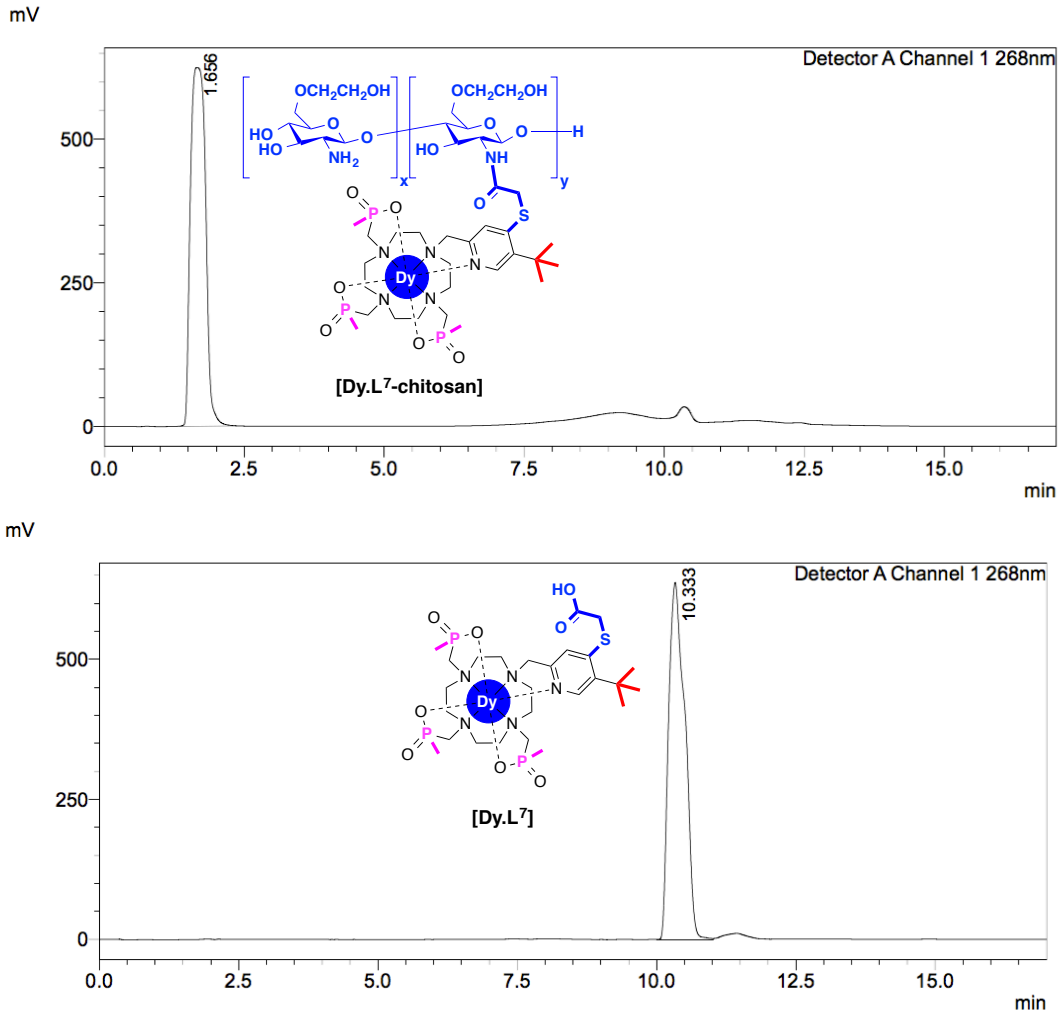

Figure 4.8 Observed analytical reverse-phase HPLC UV chromatograms of **[Dy.L^7-chitosan]** (*top*) and **[Dy.L^7]** (*bottom*) (λ= 268 nm, 10-100% MeOH+0.1% formic acid in H_2O+0.1% formic acid over 10 min, t_R=1.7 and 10.3 min, respectively).

Following the work up of the crude reaction mixture by dialysis, initial ^{1}H NMR studies on the lyophilised solid further confirmed that a reaction had occurred to form **[Dy.L^7-chitosan]**. The complex apparently existed as one major species in solution, evident from the observation of one major *tert*-butyl signal at -75.2 ppm, indicating the magnetic equivalence of the complexes in the conjugated adduct (*Figure 4.9*).

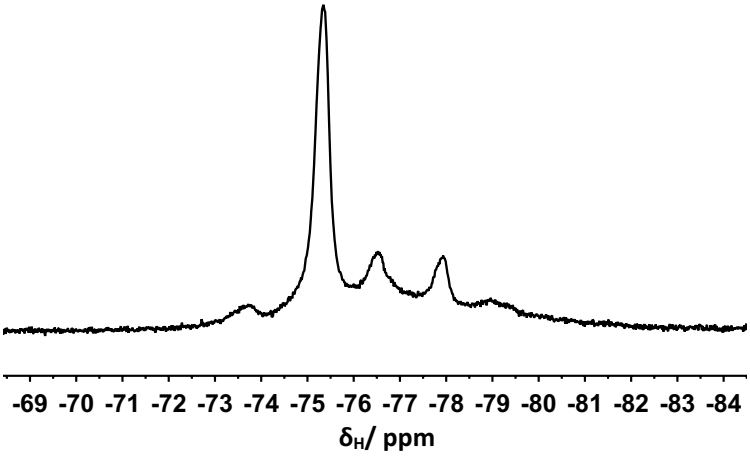

Figure 4.9 ^{1}H NMR spectrum of **[Dy.L^{7}-chitosan]** (D_2O, 295 K, pD 7.4, 9.4 T).

The mean R_1 value of the *tert*-butyl reporter group in **[Dy.L^{7}-chitosan]** was measured and showed the required enhancement of 100 to 200 s^{-1} at 7 T (*Table 4.1*). Upon comparison with the values measured for the **[Dy.L^{7}]** complex, it is evident that the relaxation rate behaviour remains largely unaffected for the higher molecular weight conjugate species. This was proposed to be the case, due to the fast independent motion of the complex with respect to the slow motion of the polymer, in solution.

Table 4.1 Experimental longitudinal relaxation rate data for the major *tert*-butyl resonance of **[Dy.L^{7}]** and **[Dy.L^{7}-chitosan]** (D_2O, 295 K[a]).

Complex	**R_1/ s^{-1} (± error)**						**R_1/R_2[b] (9.4 T)**
	1.0 T	**4.7 T**	**9.4 T**	**11.7 T**	**14.1 T**	**16.4 T**	
[Dy.L^{7}]	53 (6)	87 (3)	158 (2)	179 (1)	201 (1)	215 (1)	0.55
[Dy.L^{7}-chitosan]	n.d.[c]	88 (1)	148 (2)	175 (1)	197 (1)	221 (1)	0.53

(a) Temperature was monitored accurately, calibrating against an ethylene glycol shift thermometer; (b) R_2 values were estimated as ($\pi \times \omega_{1/2}$), for a Lorentzian line fit; (c) The signal was too weak/ broad.

The final characterisation of **[Dy.L^{7}-chitosan]** by aqueous GPC analysis is ongoing but must be carried out before ^{1}H MRS imaging studies can be considered. It is imperative that the complex constitution of the conjugate species is ascertained, so that concentrations can be calculated for forthcoming *in vivo* studies.

4.4 Conclusions

A high molecular weight adduct has been investigated as a potential platform for the conjugation of multiple *tert*-butyl labeled lanthanide(III) based complexes as a strategy to enhance complex retention *in vivo*. The selected platform is a modified, reduced molecular weight (6.5 kD) form of the naturally derived polymer, glycol chitosan.

The precursor complex, **[Ln.L^7]**, was designed and synthesised, bearing a carboxylic acid moiety that offered amide linkage potential to the free amines on the chitosan polymer. Following unsuccessful reaction attempts using a literature coupling procedure,[7] a modified method using HATU was tested for the coupling between **[Dy.L^7]** and glucosamine, the monomer component of chitosan. The formation and isolation of **[Dy.L^7-glucosamine]** gave rise to two diasteroisomeric pairs of complex isomers, evidenced by the appearance of a second set of *tert*-butyl peaks in the ^{1}H NMR spectrum. As a result of **[Dy.L^7-glucosamine]** not forming one predominant isomer in solution, it was not considered for further investigations.

The peptide-coupling reagent, HATU, was subsequently used in the successful coupling between the reduced weight chitosan compound and **[Dy.L^7]** to afford the desired **[Dy.L^7-chitosan]** species, characterised by both reverse-phase analytical HPLC and ^{1}H NMR spectroscopy. The ^{1}H NMR shift and relaxation analyses of **[Dy.L^7-chitosan]** satisfied the criteria for ^{1}H MRS imaging purposes with a shift at -75.2 ppm for its *tert*-butyl reporter signal, comprising ~80% of the signal and a favourable R_1 at 7 T of ~120 s^{-1}. Provided that GPC anaylsis confirms that the identity of **[Dy.L^7-chitosan]**, forthcoming *in vivo* studies are expected to show a slower rate of clearance from the body, with non-specific distribution throughout the tumour and the tissue.[1–3] Due to the advantages of imaging in a spectral region with zero background signal *in vivo* in ^{1}H PARASHIFT protocols, it is expected that the *tert*-butyl reporter group will be imaged selectively using a clinically accepted dose and within a matter of minutes, analogous to the previous examples detailed in this work. The advantage of *tert*-butyl signal retention *in vivo* is so additional anatomical areas can be analysed (*i.e.* not the bladder) in a greater time window for imaging, in which the compound is still expected to clear and accumulate in the bladder so as not to incur any toxicity effects, thereby affording improvements on the previously detailed systems.

4.6 References

1. H. Kobayashi, S. Kawamoto, S.-K. Jo, H. L. Bryant, M. . W. Brechbiel and R. A. Star, *Bioconjugate Chem.*, 2003, **14**, 388–394.
2. G. H. Lee, Y. Chang and T.-J. Kim, *Eur. J. Inorg. Chem.*, 2012, 1924–1933.
3. P. Harvey, I. Kuprov and D. Parker, *Eur. J. Inorg. Chem.*, 2012, **12**, 2015–2022.
4. T. Nam, S. Park, S. Y. Lee, K. Park, K. Choi, I. C. Song, M. H. Han, J. J. Leary, S. K. Yuk, I. C. Kwon, K. Kim and S. Y. Jeong, *Bioconjugate Chem.*, 2010, **21**, 578–582.
5. J. Y. Son, J. S. Jang, Y. W. Cho, H. Chung, R.-W. Park, I. C. Kwon, I.-S. Kim, J. Y. Park, S. B. Seo, C. R. Park and S. Y. Jeong, *J. Control. Release*, 2003, **91**, 135–145.
6. S. J. Lee, H. Koo, D.-E. Lee, S. Min, S. Lee, X. Chen, Y. Choi, J. F. Leary, K. Park, S. Y. Jeong, I. C. Kwon, K. Kim and K. Choi, *Biomaterials*, 2011, **32**, 4021–4029.
7. E. De Luca, P. Harvey, K. H. Chalmers, A. Mishra, P. K. Senanayake, J. I. Wilson, M. Botta, M. Fekete, A. M. Blamire and D. Parker, *J. Biol. Inorg. Chem.*, 2014, **19**, 215–227.
8. P. Caravan, J. J. Ellison, T. J. McMurry and R. B. Lauffer, *Chem. Rev.*, 1999, **99**, 2293–2352.
9. K. L. Gempf, S. J. Butler, A. M. Funk and D. Parker, *Chem. Comm.*, 2013, **49**, 9104–9106.
10. N. J. Rogers, K.-L. N. A. Finney, P. K. Senanayake and D. Parker, *Phys. Chem. Chem. Phys.,* 2016, **18**, 4370-4375.
11. H. Gysling and M. Tsutsui, *Adv. Organomet. Chem.*, 1971, **9**, 361–395.
12. E. De Luca, PhD Thesis, Durham University, 2010.
13. P. Harvey, PhD Thesis, Durham University, 2013.

Chapter Five: Conclusions and Future Work

5.1 General Conclusions

From the outset, the aim of this project has been to design, synthesise and evaluate a novel class of ^{1}H PARASHIFT probes that can be used for *in vivo* ^{1}H magnetic resonance imaging and spectroscopy studies. ^{1}H MRS promises to be a powerful imaging technique, offering non-invasive information without the need to know local probe concentrations, as long as the intense background signal arising from the water and fat signals *in vivo* is negated.

Through the inclusion of a *tert*-butyl reporter group, within 6 to 7 Å of a lanthanide(III) ion, on a kinetically stable macrocylic complex based on 1,4,7,10-tetraazacyclododecane-1,4,7,10-triacetic acid (DO3A) or 1,4,7,10-tetraazacyclododecane-4,10-diacetic acid (DO2A) (*Figure 5.0*), chemical shifts up to 80 ppm away from the water signal have been achieved. By *moving the goal posts* for ^{1}H MRS imaging to a spectral region with zero-background signal *in vivo*, the sensitivity associated with the technique is increased significantly. At this distance, concomitant enhancements in the longitudinal relaxation rate, R_1, of the *tert*-butyl reporter offer further sensitivity gains when the lanthanide(III) ion is selected judiciously, by allowing faster data acquisition, provided that the R_1/R_2 ratio is close to unity.

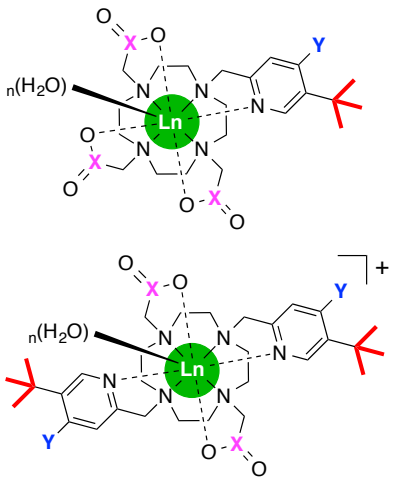

[Ln.L^1(H$_2$O)]: X = C, Y = H, n = 1
[Ln.L^3]: X = PMe, Y = H, n = 0
47: X = C, Y = NO_2, n = 1
[Ln.L^4(H$_2$O)]: X = C, Y = $N(CH_3)_2$, n = 1
[Ln.L^5(H$_2$O)]: X = C, Y = $NHCOCH_3$, n = 1
[Ln.L^6]: X = PMe, Y = PO_3H^-, n = 0
[Ln.L^7]: X = PMe, Y = SCH_2COO^-, n = 0
[Ln.L^7-glucosamine]: X = PMe, Y = SCH_2COO-glucosamine, n = 0
[Ln.L^7-chitosan]: X = PMe, Y = SCH_2COO-chitosan, n = 0

[Ln.L^2(H$_2$O)]$^+$: X = C, Y = H, n = 1

Figure 5.0 The general design of the ^{1}H PARASHIFT probes detailed within this thesis: where X = C (tri-carboxylate) or PMe (tri-phosphinate), Y = H, NO_2, $N(CH_3)_2$, $NHCOCH_3$, PO_3H^- or SCH_2COO^-, and n = the number of coordinated water molecules (typically n = 1 when X = C or n = 0 when X = PMe).

Three series of ^{1}H PARASHIFT complexes, **[Ln.L^1(H$_2$O)]**, **[Ln.L^2(H$_2$O)]$^+$** and **[Ln.L^3]**, were derived and synthesised in *Chapter 2*. The **[Dy.L^2(H$_2$O)]$^+$** complex showed a good balance between shift and relaxation enhancement. Such enhanced sensitivity permitted rapid detection of **[Dy.L^2(H$_2$O)]$^+$** in live mice using ^{1}H MRS, within a few minutes, following the tail vein injection of a 0.1 mmol kg^{-1} dose. However, the largest *tert*-butyl chemical shifts were observed for the Tb(III), Dy(III) and Tm(III) complexes of the tri-phosphinate **[Ln.L^3]** series, resonating at up to ±70 ppm, thus favouring the use of larger imaging bandwidths (*e.g.* 20 kHz) in ^{1}H MRS protocols with a concomitant reduction in acquisition times.

The favourable design features established in the parent systems were carried through to *Chapter 3*, where minimal structural modifications afforded three series of pH responsive ^{1}H PARASHIFT probes, **[Ln.L^4(H$_2$O)]**, **[Ln.L^5(H$_2$O)]** and **[Ln.L^6]**. By far the most promising pH dependent *tert*-butyl chemical shift behaviour was exhibited by the complexes in the **[Ln.L^6]** series, with pK_a values around 7, functionality in the physiological range and a total shift change of 1.9 ppm between the acid and base forms (for Dy(III)). Once again, the enhanced sensitivity allowed the detection of **[Dy.L^6]** and **[Tm.L^6]** in phantom ^{1}H MRS imaging protocols, where the feasibility of pH chemical shift imaging was realised. In preliminary *in vivo* studies, the signal was obtained within a matter of minutes, following the tail vein injection of a 0.1 mmol/kg dose of **[Dy.L^6]**.

Following the rapid *in vivo* clearance of both **[Dy.L^2(H$_2$O)]$^+$** and **[Dy.L^6]**, *Chapter 4* described a strategy for enhancing the retention of the complexes, and hence the *tert*-butyl signal, *in vivo*, through the conjugation of multiple ^{1}H PARASHIFT probes to a large polymeric vector. Two conjugated species were formed following the design and synthesis of a precursor complex, **[Ln.L^7]**, by appending a carboxylic acid functionality in an amide linkage with glucosamine and glycol chitosan to form **[Dy.L^7-glucosamine]** and **[Dy.L^7-chitosan]**, respectively. The **[Dy.L^7-glucosamine]** complex was isolated as two major diastereoisomeric species with separate *tert*-butyl chemical shifts in the ^{1}H NMR spectrum, hence rendering it inappropriate for application here. Conversely, the **[Dy.L^7-chitosan]** complex possessed the required shifted *tert*-butyl and relaxation characteristics, with *tert*-butyl resonance equivalence observed by the appearance of one major ^{1}H NMR signal in solution. Whilst preliminary *in vivo* studies are yet to be carried out, **[Dy.L^7-chitosan]** is expected to show the desired slower rate of clearance from the body.

Surprisingly large R_1 enhancements were observed in the cases of the Er(III) and Tm(III) tri-phosphinate complexes, leading to the conclusion that Er(III) tri-phosphinate complexes, and Dy(III) and/or Tb(III) tri- and bis-carboxylate complexes appear to be the best candidates for use as ^{1}H PARASHIFT probes, in the field range 1.5 to 7.0 T, based on the critical balance defined between shift and relaxation enhancement. Such unprecedented behaviour challenges the theories with which the paramagnetic shift and relaxation of these lanthanide(III) based complexes are currently modeled. However, whilst the limitations and inadequacies of the current theories have been alluded to and, in part, evaluated here, more work is required to pave a way towards formulating a better model for predicting their behaviour and with it, developing a toolkit for the design of future ^{1}H PARASHIFT probes.

5.2 Short-term Future Work

5.2.1 EPR and SQUID Analysis of [Ln.L^1(H$_2$O)] and [Ln.L^3]

At the end of *Chapter 2* (*Sections 2.5.2.1 and 2.5.2.2*), preliminary EPR spectroscopy and SQUID magnetometry results were reported in a comparative study between the tri-carboxylate, **[Ln.L^1(H$_2$O)]**, and the tri-phosphinate parent systems, **[Ln.L^3]**. EPR spectroscopy on solid and frozen samples at 5 K probed the very lowest m_J states, since they are the only ones populated in the Boltzmann distribution. The general results were promising, highlighting that there are significant differences in the m_J composition of the ground states of the lanthanide(III) ions in these complexes. The SQUID magnetometry studies revealed a significant variation from the predicted magnetic moments. However, despite these promising general trends, a more in-depth EPR spectroscopy and SQUID magnetometry treatment is required on larger quantities of sample, where water and other impurities are rigorously excluded, before reliable data is obtained.

5.2.2 Co-injection *In Vivo* Studies with [Dy.L^6] and [Tm.L^6]

In *Chapter 3* (*Section 3.4)*, the pH responsive *tert*-butyl chemical shift behaviour of the ^{1}H PARASHIFT probes, **[Ln.L^6]**, were evaluated *in vitro.* Phantom and preliminary *in vivo* ^{1}H MRS studies with **[Dy.L^6]** and **[Tm.L^6]** demonstrated the feasibility of a non-invasive pH CSI approach. However, future work should seek to consider the possibility of co-injecting **[Dy.L^6]** and **[Tm.L^6]**, where the difference between the *tert*-butyl chemical shifts can be monitored as a function of pH and temperature. The *tert*-butyl

groups on **[Dy.L^6]** and **[Tm.L^6]** exhibit different temperature and pH dependencies, as demonstrated from the *in vitro* analysis. With temperature and pH unknown entities *in vivo*, due to the similar distribution profiles of **[Dy.L^6]** and **[Tm.L^6]**, a potential means of internal calibration is afforded since the local conditions will be the same for each complex. *In vitro* calibration studies can be carried out using the existing data in this thesis. The *tert*-butyl groups of **[Dy.L^6]** and **[Tm.L^6]** resonate 150 ppm apart but can be imaged in ^{1}H MRS imaging protocols, utilising the sequences demonstrated in this work. However, for the method to work, the two spectral windows will need to be viewed alternately and sequentially throughout the duration of the imaging experiment, in order to exclude the background signals. The advantages of using the **[Tb.L^6]** and **[Er.L^6]** complexes should also be considered, since they exhibit the most remarkable shift and relaxation characteristics, respectively.

5.3 Long-term Future Work

5.3.1 Another Strategy for Enhancing Complex Retention *In Vivo*

The strategy devised in *Chapter 4*, for enhancing complex retention *in vivo*, focused on appending multiple *tert*-butyl labeled paramagnetic lanthanide(III) complexes to a medium to high molecular weight vector. Whilst characterisation by GPC analysis and *in vivo* studies are ongoing with **[Dy.L^7-chitosan]**, future work could also focus on the design and synthesis of a lower molecular weight analogue, with the $9N_3$-based framework suggested in *Figure 5.1*. Advantages over a poly-disperse chitosan system include the relatively straightforward, in-house, characterisation of the conjugate, and the ease with which the number of attached complexes can be quantified. Provided that the magnetic equivalence of the *tert*-butyl groups is retained, and the shift and relaxation characteristics satisfy the ^{1}H PARASHIFT probe criteria, it is believed that this system will clear slower from the body, compared with the complexes detailed here.

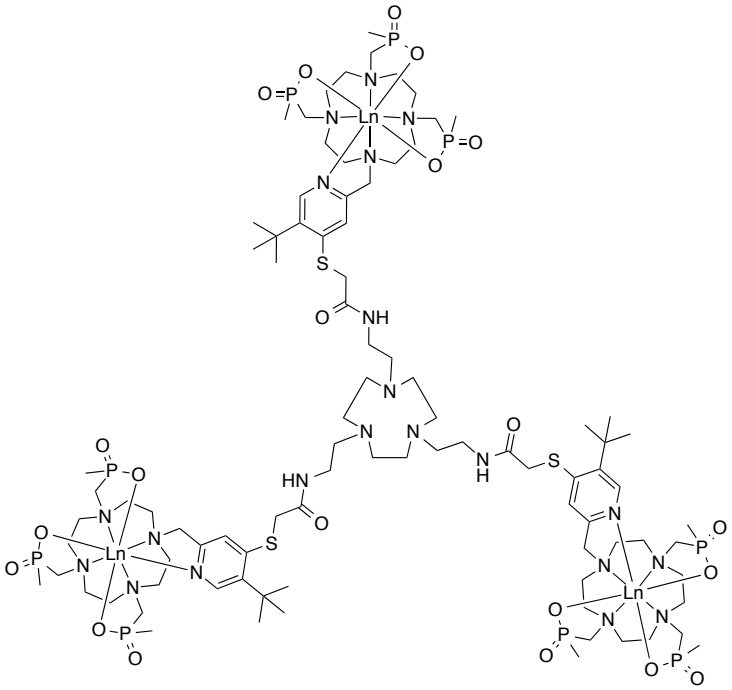

Figure 5.1 Proposed structure of a triazacyclononane, $9N_3$, based conjugate species using **[Ln.L^7]**.

5.3.2 Creating a p[M^{n+}] Responsive ^{1}H PARASHIFT Probe

The final future direction for this work should be in the design, synthesis and evaluation of a ^{1}H PARASHIFT probe capable of sensing changes in metal ion concentration, p[M^{n+}]. In a p[M^{n+}] responsive system, the binding of a metal should induce a chemical shift change in the *tert*-butyl reporter group. As a result, and in accord with the favourable design features of the pH responsive system, **[Ln.L^6]**, a general structure has been proposed in *Figure 5.2*. It is hypothesised that by functionalising the 3- and 4-positions of the pyridyl moiety, in close proximity to the *tert*-butyl reporter group, with chelating arms that display a high affinity for a particular metal ion, in the concentration range at which it is present *in vivo*, the desired shift changes will be observed upon metal binding.

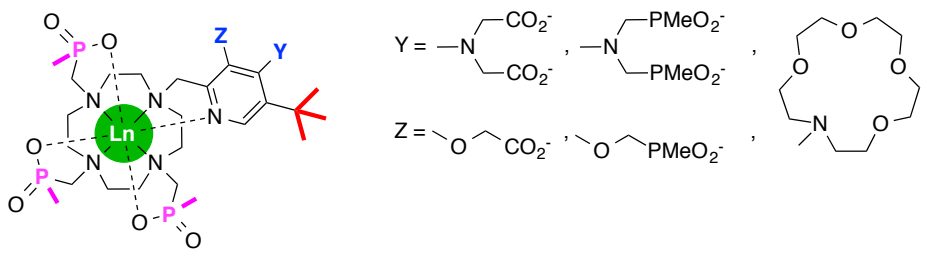

Figure 5.2 Possible design features of a p[M^{n+}] responsive ^{1}H PARASHIFT probe, building on the successes of the work in this thesis.

5.4 Final Thoughts

The birth of human MRI in 1977 is regarded unequivocally and universally as one of the most importance developments in modern day medicine. Despite its worldwide adoption, the technique is extremely limited to only the observation of the water signal in living systems, with the non-invasive detection of relevant small metabolites impossible in a background of 55 M water, and as a complication of the inherent sensitivity issues with any NMR spectroscopy based technique. Nevertheless, it is evident from the work in this thesis that existing modern clinical instrumentation can be used to image the ^{1}H NMR signal of an administered probe selectively. Such ^{1}H PARASHIFT probes offer themselves to a novel imaging modality, called ^{1}H PARASHIFT MRS, in which data acquisition occurs within minutes with doses of the same order as for clinically approved Gd(III) contrast agents, due to enhanced signal sensitivity. This approach may only mark the beginning of a field that can be developed further towards making 'smart' and/ or targeted probes and with it, a new toolkit for non-invasively interrogating the *in vivo* environment.

Chapter Six: Experimental

6.1 Experimental Procedures

6.1.1 General Procedures

All solvents used were laboratory grade and anhydrous solvents, when required, were freshly distilled over the appropriate drying agent. Water was purified by the 'Purite$_{STILL}$plus' system, with a conductivity of ≤ 0.04 μS cm^{-1}. All reagents used were purchased from commercial suppliers and were used without further purification. Reactions requiring anhydrous conditions were carried out using Schlenk line techniques under argon. Where necessary, solvents were degassed using the freeze-thaw cycle method.

Thin layer chromatography was performed on silica plates (Merck Art 5554) or neutral aluminium plates (Merck Art 5550) and visualised under UV irradiation (254 nm), or by staining with either iodine or Dragendorff's reagent (solution of bismuth nitrate and potassium iodide in AcOH and H_2O). Preparative column chromatography was performed using silica gel (Merck Silica Gel 60, 230-400 mesh) or neutral alumina (Merck Aluminium Oxide 90, activity II-III, 70-230 mesh), with the latter pre-soaked in ethyl acetate overnight before use.

Dialysis was performed with Float-A-Lyzer G2 filters MWCO 0.5-1 kD (Spectrum Laboratories, Inc) or modified benzoylated dialysis tubing MWCO 2 kD (Sigma Aldrich). The first type of tubing was washed thoroughly; first with a 50: 50 EtOH: H_2O mix, and then with H_2O, as per manufacturer's advice. The second type of tubing was treated with a 0.3% (w/v) sodium sulfide solution at 70 °C for 1 min, washed with hot water (60 °C) for 2 min, acidified with 0.2% sulfuric acid, and rinsed with hot water, as per the manufacturer's advice. After addition of the material to the tubing, the ends of the tubing were secured (using provided screw tops) and the ensemble submerged in stirring H_2O (*ca.* 800 mL). The bulk H_2O was exchanged 4 times over a 72 h period, to ensure a positive dialysis gradient was maintained. Filtering of the tubing contents and lyophilisation yielded the desired product.

pH measurements were carried out at 295 K using a Jenway 3320 pH meter with a Sigma Aldrich micro-pH combination electrode. Calibration was performed using

commercially available buffer solutions at pH 4.00±0.02, pH 7.00±0.02, and pH 10.00±0.02 (Sigma Aldrich). Diluted aqueous solutions of NaOD and DCl (in D_2O) were used for pD adjustments; NaOH and HCl (in H_2O) for pH adjustments. For measurements in D_2O, the pD is calculated as pD = pH + 0.41, where pH is the meter reading. Protonation constants were measured at 295 K and 500 MHz using diluted solutions of the complex (1 mM) in D_2O, unless otherwise stated. For solutions of H_2O and mouse plasma (diluted 1:1 with Purite water), a coaxial insert containing D_2O was used to lock the NMR instrument. The resulting curves reporting the ^{1}H NMR chemical shift *vs*. pH were fitted by non-linear least squares iterative analysis by Boltzmann using Origin 8.0 software, producing estimates of the pK_a values.

All complex yields are omitted due to the presence of residual sodium formate from reverse-phase HPLC purification and subsequent neutralisation.

6.1.2 Characterisation: NMR Spectroscopy

^{1}H, ^{13}C and ^{31}P NMR spectra were recorded in commercially available deuterated solvents on a Varian Mercury-200 (^{1}H at 199.975, ^{13}C at 50.289, ^{19}F 188.179, ^{31}P 80.985 MHz), Varian Mercury-400 (^{1}H at 399.960, ^{13}C at 100.572, ^{19}F 376.338, ^{31}P at 161.943 MHz), Bruker Avance-400 (^{1}H at 400.052, ^{13}C at 100.603, ^{19}F 376.423, ^{31}P at 161.980 MHz), Varian Inova-500 (^{1}H at 499.722, ^{13}C at 125.671, ^{19}F 470.253, ^{31}P at 202.375 MHz), Appleby VNMRS-600 (^{1}H at 599.832, ^{13}C at 150.828, ^{19}F 564.385, ^{31}P at 242.862 MHz), or Varian VNMRA-700 (^{1}H at 699.731, ^{13}C at 175.948, ^{19}F 658.405, ^{31}P at 283.256 MHz) spectrometer. All chemical shifts are given in ppm and all coupling constants are reported in Hz, to the nearest 0.5. Where required, the operating temperature of the spectrometer was measured with the aid of an internal calibration solution of ethylene glycol. For non-deuterated solutions, a coaxial insert containing D_2O was used to lock the NMR instrument. Measurements at 1.0 T (42.5 MHz ^{1}H) were made on a Magritek Spinsolve spectrometer. The recorded free induction decays were processed using backward linear prediction, optimal exponential weighting, zero-filling, Fourier transform, phasing and baseline correction (by polynomial fitting). The signals were integrated by Lorentzian line fitting.

^{1}H longitudinal relaxation times were measured in dilute D_2O solutions at 295 K using the inversion-recovery technique, on spectrometers operating at fields of 1.0, 4.7, 9.4, 11.7, 14.1 and 16.4 T. Each relaxation time measurement was repeated three times to

reduce experimental error. The number of transients used in the measurements was determined by the signal-to-noise ratio of the sample. The signal was fully recovered during the inversion-recovery sequence to minimise the experimental error. Fitting errors were determined by calculating the standard deviation of a set of relaxation times.

Relaxation rate data was fitted by Dr. Nicola Rogers at Durham University, using a modified algorithm originally provided by Dr. Ilya Kuprov at the University of Southampton. The algorithm uses the SBM equations to fit the measured relaxation rate data using the Matlab internal Levenberg-Marquardt minimisation of the non-linear squares error function and the results were analysed iteratively. Some parameters were used globally in the series, and others used for each lanthanide individually. Magnetic moments for each lanthanide(III) were taken from the literature.

Concentrations of the lanthanide(III) complexes were calculated using the bulk magnetic susceptibility (BMS) method, using 1% ^{t}BuOH/ H_2O solutions of the complexes, with a coaxial insert containing the same solution without the complex added.

Water proton T_1 measurements were recorded on a Bruker Minispec mq60 (60 MHz, 310 K), and are reported as the mean value of three measurements. The relaxivities, r_{1p}, of the compounds were calculated as the slope of the function shown in *equation 1*.[1]

$$\frac{1}{T_{1,obs}} = \frac{1}{T_{1,d}} + r_{1p}[Gd(III)] \quad (1)$$

where $T_{1,obs}$ is the measured T_1, $T_{1,d}$ is the diamagnetic contribution of the solvent (calculated to be 4000 ms), and [Gd.L_n] is the concentration in mM of the appropriate Gd(III) complex. The error for each relaxivity value was less than 0.3 mM^{-1} s^{-1}.

Variable temperature NMR spectroscopy was carried out using the Varian VNMRS-500 spectrometer with the assistance of Dr. Nicola Rogers at Durham University, using the ethylene glycol method (mentioned above) to confirm the operating temperature of the spectrometer at each temperature measured. Samples were inserted at 295 K with shift and T_1 measurements made over the range 290-315 K, using the *tert*-butyl chemical shift (T^{-2} shift dependence).

6.1.3 Characterisation: Optical Techniques

All samples for optical analyses were contained in quartz cuvettes with a path length of 1 cm and a polished base. Measurements were recorded at 295 K, unless stated otherwise. Low temperature (80 K) emission spectra were obtained with the assistance of Dr. Lars-Olaf Pålsson.

UV/Vis absorbance spectra were measured on a Perkin Elmer Lambda 900 UV/Vis/NIR spectrometer, using FL Winlab software. Samples were measured relative to a reference of pure solvent contained in a matched cell.

Emission spectra were measured on a ISA Joblin-Yvon Spec Fluorolog-3 luminescent spectrometer, using DataMax v2.20 software. Excitation wavelengths were selected according to the specific measurement of λ_{max}. An integration time of 0.5 s, increment of 0.5 nm, and excitation and emission slit widths of 2.5 and 1.0 nm, respectively, were used throughout unless stated otherwise.

Lifetime measurements were carried out using a Perkin Elmer LS55 luminescence spectrometer. Lanthanide excited state lifetimes were measured by excitation of the sample by a short pulse of light followed by monitoring the integrated intensity of light emitted during a fixed gate time, t_g, after a delay time of t_d. Excitation and emission wavelengths were selected based upon the lanthanide(III) complex. Measurements were made for at least 30 delay times over a period of three or more lifetimes. A gate time of 0.1 ms was used and the excitation and emission slits were both set to 6 nm. The obtained decay curves were fitted to *equation 2*.

$$I = A_0 + A_1 e^{-kt} \qquad (2)$$

where I is the intensity at time t after the excitation pulse; A_0 is the intensity after decay is completed; A_1 is the pre-exponential factor and k is the rate constant for decay of the excited state. The excited state lifetime, τ, is the inverse of the rate constant, k.

The inner sphere hydration number (q) was obtained by measuring the excited state lifetime in H_2O and D_2O, following D_2O exchange, of a Eu(III) and/or Tb(III) complex (*vide infra*). The q value was calculated using *equations 3* and *4*:[2]

$$q_{Eu} = 1.2\left(k_{H_2O} - k_{D_2O} - 0.25 - 0.075n\right) \quad (3)$$

$$q_{Tb} = 5.0\left(k_{H_2O} - k_{D_2O} - 0.06 - 0.010n\right) \quad (4)$$

where k_{H_2O} and k_{D_2O} are the rate constants for the depopulation of the lanthanide(III) emissive excited state in each solvent (derived as the reciprocals of the luminescence lifetimes of the complex in each solvent, τ_{H_2O} and τ_{H_2O}, respectively, and n is the number of proximate carbonyl-bound amide groups.

6.1.4 Characterisation: Other Techniques

Low resolution electrospray mass spectra were obtained on a TQD mass spectrometer, operating in positive or negative ion mode, equipped with an Acquity UPLC, an electrospray ion source and an Acquity photodiode array detector (Waters Ltd, UK). High-resolution electrospray mass spectra were recorded on a LCT Premier XE mass spectrometer or a QTOF Premier mass spectrometer, both equipped with an Acquity UPLC, a lock-mass electrospray ion source and an Acquity photodiode array detector (Waters Ltd, UK).

Dr. Nicholas Chilton at the University of Manchester collected EPR spectra and SQUID data. Q-band (~34 GHz) EPR spectra were measured with a Bruker EMX spectrometer (EPSRC EPR National Facility) fitted with a CF935 cryostat connected to an Oxford Intelligent Temperature Controller, on both solid-state and frozen glass samples (80% water, 20% glycerol, ~1 mM) at 5 K. Magnetic measurements were obtained using a Quantum Design MPMS-XL7 SQUID magnetometer on powder samples contained in gelatin capsules at the centre of a drinking straw. The data were corrected for the diamagnetism of the straw and capsule as well as that of the sample.

Gel permeation chromatography (GPC) was undertaken at Smithers Rapra UK, using a Viscotek Model 301 TDA instrument with associated pump, autosampler, and refractive index detector (with differential pressure and light scattering). Agilent PLaquagel-OH Guard plus 2 x PLaquagel-OH Mixed-M, 30 cm, 8 μm columns were used with an eluent composed of 0.5 M $NaNO_3$, 0.01 M NaH_2PO_4 at pH 2 at a flow rate of 1.0 mL/min at 30°C. The GPC system was calibrated using Pullulan polysaccharides and the data analysed using Malvern/Viscotek 'OmniSec' software.

Melting points were recorded using a Gallenkamp (Sanyo) apparatus and are uncorrected.

6.1.5 HPLC Analysis

Reverse phase HPLC was performed at 295 K using a Shimadzu system consisting of a Degassing Unit (DGU-20A_{5R}), a Prominence Preparative Liquid Chromotograph (LC-20AP), a Prominence UV/Vis Detector (SPD-20A) and a Communications Bus Module (CBM-20A). An XBridge C18 19 x 100 mm, 5 μm column was used to purify the complexes on a preparative scale (flow rate 17 mL/min) and a Shimadzu ShimPack VP-ODS column, 4.6 x 150 mm, 5 μm (flow rate 2 mL/min) was used for analytical scale purifications. A gradient elution with a solvent system composed of H_2O + 0.1% HCOOH/ MeOH + 0.1% HCOOH was performed for a total run time of 17 min. The separation details are reported below (*Table 6.0*). Fraction collection was performed manually.

Table 6.0 Preparative procedure: flow rate = 17 mL/min; Solvent A = H_2O+0.1% formic acid; Solvent B = MeOH+0.1% formic acid.

Time (min)	Solvent A (%)	Solvent B (%)
0	90	10
3	90	10
13	0	100
16	0	100
17	90	10

6.1.6 Imaging Studies

Imaging studies were carried out by Prof. Andrew Blamire, Dr. Ian Wilson and Dr. Dara O'Hogain at the Newcastle Magnetic Resonance Centre, using a 7 T (300 MHz) Varian Unity Inova microimaging/ pre-clinical system equipped with broadband capability and actively shielded gradients. *In vitro* experiments were performed with a 30 mm i.d. birdcage volume coil (Rapid Biomedical), and *in vivo* experiments were performed with a 39 mm i.d. birdcage volume coil. The coils were used for both signal excitation and reception.

For phantom studies, dilute aqueous samples were placed in cut-down NMR tubes and positioned on the axis of the coil. For *in vivo* studies, mice were anaesthetised with an oxygen/1-2% isofluorane mixture. Complexes were administered intravenously as saline solutions *via* the tail vein, with the doses quoted calculated by BMS and ICP-OES. Sequence parameters differ and are as quoted.

6.2 Synthetic Procedures

1. 1,4,7-Tris(*tert*-butoxycarbonylmethyl)-1,4,7,10-tetraazacyclododecane[3]

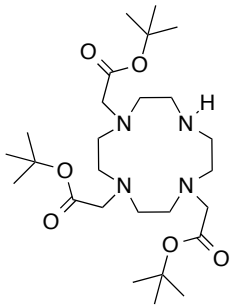

Tert-butyl bromoacetate (11.5 mL, 78.3 mmol) was added to a stirred solution of 1,4,7,10-tetraazacyclododecane (5.0 g, 29.0 mmol) and $NaHCO_3$ (6.50 g, 78.3 mmol) in anhydrous MeCN (190 mL) and the resulting mixture stirred at rt for 18 h under argon. The reaction mixture was filtered and the solvent removed under reduced pressure. The resulting white residue was dissolved in a minimal amount of toluene, with heating, and upon cooling a white solid precipitated out of solution (6.7 g, 45%). R_f (10% MeOH/CH_2Cl_2) = 0.29; m.p. 184-185 °C (lit. m.p. 183-184 °C); ^{1}H NMR (400 MHz, $CDCl_3$) δ 10.03 (br s, 1H, NH), 3.37 (s, 4H, CH_2), 3.29 (s, 2H, CH_2), 3.04-3.15 (br m, 4H, cyclen CH_2), 2.78-2.98 (br m, 12H, cyclen CH_2), 1.46 (s, 18H, $C(CH_3)_3$), 1.45 (s, 9H, $C(CH_3)_3$); ^{13}C NMR (101 MHz, $CDCl_3$) δ 169.5 (CO), 168.7 (CO), 80.9 ($\underline{C}(CH_3)_3$), 80.7 ($\underline{C}(CH_3)_3$), 57.2 (CH_2), 50.3 (cyclen CH_2), 48.2 (cyclen CH_2), 46.6 (cyclen CH_2), 27.2 ($C(\underline{C}H_3)_3$), 27.1 ($C(\underline{C}H_3)_3$); ESI-LRMS (+) *m/z* 515.7 $[M+H]^+$; ESI-HRMS (+) calcd for $[C_{26}H_{51}N_4O_6]^+$ 515.3809, found 515.3804.

2. 5-*tert*-Butyl-2-methylpyridine

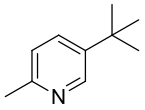

Copper(I) cyanide (20 mg) was added to a solution of anhydrous THF (50 mL) and anhydrous Et_2O (100 mL) and the resulting suspension cooled to -78 ^{o}C. To this was added *tert*-butylmagnesium chloride (58 mL, 2.0 M in Et_2O, 116.2 mmol) and the mixture was stirred at -78 ^{o}C for 20 min under an atmosphere of argon. After this, 5-bromo-2-methylpyridine (10.0 g, 58.1 mmol) was added and the reaction mixture was allowed to warm to rt, where it was stirred for a further 18 h. Upon completion,

NH_4OH (sat. aq. solution, 50 mL) was added dropwise. The mixture was extracted with Et_2O (3 × 200 mL) before the organic layers were combined, dried over $MgSO_4$, and the solvent removed under reduced pressure. This partially volatile yellow liquid was used without further purification (6.0 g, 69%). ^{1}H NMR (400 MHz, $CDCl_3$) δ 8.43 (s, 1H, H^6), 7.44 (dd, ^3J = 8, ^4J = 2, 1H, H^4), 6.95 (d, ^3J = 8, 1H, H^3), 2.38 (s, 3H, CH_3), 1.20 (s, 9H, $C(CH_3)_3$); ^{13}C NMR (101 MHz, $CDCl_3$) δ 154.8 (C^2), 146.1 (C^6), 142.3 (C^5), 132.8 (C^4), 122.1 (C^3), 32.8 ($\underline{C}(CH_3)_3$), 30.6 ($C(\underline{C}H_3)$), 20.4 (CH_3); ESI-LRMS (+) *m/z* 150.1 $[M+H]^+$; ESI-HRMS (+) calcd for $[C_{10}H_{16}N]^+$ 150.1283, found 150.1270.

3. 5-*tert*-Butyl-2-methylpyridin-1-oxide

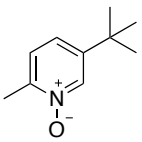

*m*CPBA (8.0 g, 52.3 mmol) was added to a stirred solution of 5-*tert*-butyl-2-methylpyridine (6.0 g, 12.7 mmol) in anhydrous $CHCl_3$ (100 mL). The resulting solution was stirred at rt for 18 h under argon, before being quenched with Na_2SO_4 (sat. aq. solution, 50 mL) and stirred for a further 10 min. The organic layer was extracted and washed with $NaHCO_3$ (sat. aq. solution, 100 mL). The aqueous layer was then extracted with CH_2Cl_2 (3 × 150 mL), the organic layers combined, dried over Na_2SO_4 and the solvent removed under reduced pressure. The resulting yellow oil was purified by silica gel column chromatography, eluting with a gradient starting from 100% CH_2Cl_2 to 2% MeOH/ CH_2Cl_2, to yield a pale yellow liquid (6.0 g, 90%). R_f (10% MeOH/ CH_2Cl_2) = 0.46; ^{1}H NMR (400 MHz, $CDCl_3$) δ 8.26 (d, ^4J = 1, 1H, H^6), 7.11-7.17 (m, 2H, H^3, H^4), 2.44 (s, 3H, CH_3), 1.25 (s, 9H, $C(CH_3)_3$); ^{13}C NMR (101 MHz, $CDCl_3$) δ 146.5 (C^2), 144.8 (C^6), 136.4 (C^5), 124.8 (C^4), 123.0 (C^3), 32.6 ($\underline{C}(CH_3)_3$), 29.6 ($C(\underline{C}H_3)$), 16.4 (CH_3); ESI-LRMS (+) *m/z* 166.1 $[M+H]^+$; ESI-HRMS (+) calcd for $[C_{10}H_{16}NO]^+$ 166.1232, found 166.1223.

4. (5-*tert*-Butylpyridin-2-yl)methanol

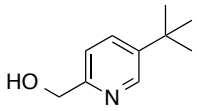

Trifluoroacetic anhydride (22 mL, 156.8 mmol) was added to a solution of 5-*tert*-butyl-2-methylpyridin-1-oxide (5.0 g, 30.3 mmol) in anhydrous $CHCl_3$ (40 mL). The resulting mixture was heated at 60 ^oC for 18 h under an atmosphere of argon. Reaction completion was confirmed by ^1H NMR spectroscopy before the solvent was removed under reduced pressure. The resulting bright yellow oil was stirred in a mixture of EtOH (25 mL) and H_2O (25 mL) for 2 h. The solution was concentrated (*ca.* 10 mL) and extracted with CH_2Cl_2 (3 × 100 mL). The organic layers were combined, dried over $MgSO_4$, and the solvent removed under reduced pressure. The resulting orange oil was purified by silica gel column chromatography, eluting with a gradient starting from 100% CH_2Cl_2 to 5% MeOH/ CH_2Cl_2, to yield a yellow oil (4.0 g, 80%). R_f (10% MeOH/ CH_2Cl_2) = 0.46; ^1H NMR (400 MHz, $CDCl_3$) δ 8.56 (d, ^4J = 2, 1H, H^6), 8.35 (dd, ^3J = 8, ^4J = 2, 1H, H^4), 7.75 (d, ^3J = 8, 1H, H^3), 4.96 (s, 2H, CH_2), 1.30 (s, 9H, $C(CH_3)_3$); ^{13}C NMR (101 MHz, $CDCl_3$) δ 153.8 (C^2), 150.2 (C^6), 144.1 (C^5), 137.8 (C^3), 124.5 (C^4), 61.0 (CH_2), 34.5 ($\underline{C}(CH_3)_3$), 30.3 ($C(\underline{C}H_3)$); ESI-LRMS (+) *m/z* 166.3 $[M+H]^+$; ESI-HRMS (+) calcd for $[C_{10}H_{16}NO]^+$ 166.1232, found 166.1231.

5. (5-*tert*-Butylpyridin-2-yl)methyl methanesulfonate

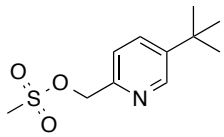

(5-*tert*-Butylpyridin-2-yl)methanol (1.0 g, 6.06 mmol) was dissolved in dry THF (7 mL) and cooled to 5 ^oC. Triethylamine (1.3 mL, 9.08 mmol) and mesyl chloride (0.7 mL, 9.08 mmol) were added dropwise. After addition, the reaction mixture was allowed to warm to rt and stirred for 30 min before the solvent was removed under reduced pressure. The residue was dissolved in brine (10 mL) and extracted with CH_2Cl_2 (2 × 25 mL). The organic layers were combined, dried over $MgSO_4$, and the solvent removed under reduced pressure to yield an orange oil, which was used immediately (1.1 g, 76 %). R_f (10% MeOH/ CH_2Cl_2) = 0.76; ^1H NMR (400 MHz, $CDCl_3$) δ 8.57 (d,

^4J = 2, 1H, H^6), 8.15 (dd, ^3J = 8, ^4J = 2, 1H, H^4), 7.75 (d, ^3J = 8, 1H, H^3), 5.44 (s, 2H, CH_2), 3.07 (s, 3H, SCH_3), 1.24 (s, 9H, $C(CH_3)_3$); ESI-LRMS (+) *m/z* 244.3 $[M+H]^+$; ESI-HRMS (+) calcd for $[C_{11}H_{18}NO_3S]^+$ 244.1007, found 244.1020.

6. *tert*-Butyl-2,2',2''-(10-((5-*tert*-butylpyridin-2-yl)methyl)-1,4,7,10-tetraazacyclododecane-1,4,7-triyl)triacetate

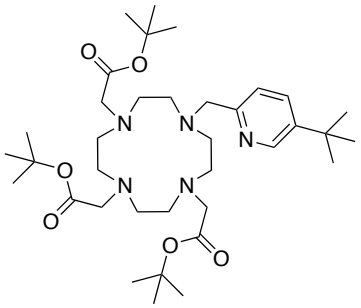

A stirred mixture of 1,4,7-tris(*tert*-butoxycarbonylmethyl)-1,4,7,10-tetraazacyclododecane (2.2 g, 4.19 mmol), (5-*tert*-butylpyridin-2-yl)methyl methanesulfonate (1.1 g, 4.61 mmol), and K_2CO_3 (1.2 g, 8.38 mmol) in anhydrous MeCN (15 mL) was heated at 70 ^oC for 18 h under argon. The reaction mixture was cooled and filtered, before the solvent was removed under reduced pressure. The resulting brown oil was purified by silica gel column chromatography, eluting with a gradient starting from 100% CH_2Cl_2 to 1% MeOH/ CH_2Cl_2 to yield a yellow oil (0.90 g, 30%). R_f (10% MeOH/ CH_2Cl_2) = 0.42; ^1H NMR (400 MHz, $CDCl_3$) δ 8.20 (d, ^4J = 2, 1H, H^6), 7.58 (dd, ^3J = 8, ^4J = 2, 1H, H^4), 7.02 (d, ^3J = 8, 1H, H^3), 3.07 (br m, 12H, NCH_2COO^tBu/cyclen CH_2/NCH_2py), 2.31 (br m, 12H, NCH_2COO^tBu/cyclen CH_2/NCH_2py), 1.42 (s, 9H, py$C(CH_3)_3$), 1.39 (br s, 18H, $COOC(C\underline{H}_3)_3$), 1.21 (s, 9H, $COOC(C\underline{H}_3)_3$); ^{13}C NMR (101 MHz, $CDCl_3$) δ 171.6 ($\underline{C}OO(CH_3)_3$), 154.6 (C^2), 144.8 (C^6), 143.3 (C^5), 132.7 (C^3), 121.0 (C^4), 81.0 ($COO\underline{C}(CH_3)_3$), 80.6 ($COO\underline{C}(CH_3)_3$), 57.3 ($pyCH_2$), 54.3 (cyclen CH_2), 50.3 (cyclen CH_2), 46.5 (cyclen CH_2), 32.3 ($py\underline{C}(CH_3)_3$), 30.0 ($pyC(\underline{C}H_3)_3$), 27.2 ($COOC(\underline{C}H_3)_3$), 26.9 ($COOC(\underline{C}H_3)_3$); ESI-LRMS (+) *m/z* 662.4 $[M+H]^+$; ESI-HRMS (+) calcd for $[C_{36}H_{64}N_5O_6]^+$ 662.4851, found 662.4856.

7. Europium(III) complex of 1,4,7-tris(acetic acid)-10-((5-*tert*-butylpyridin-2-yl)methyl)-1,4,7,10-tetraazacyclododecane, [Eu.L^1(H$_2$O)]

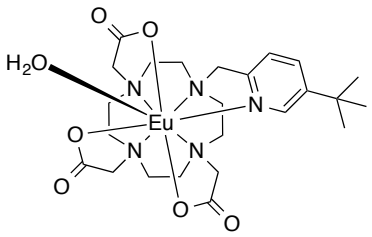

tert-Butyl-2,2',2''-(10-((5-*tert*-butylpyridin-2-yl)methyl)-1,4,7,10-tetraazacyclododecane-1,4,7-triyl)triacetate (100 mg, 0.15 mmol) was dissolved in CH_2Cl_2 (1 mL) and to this was added TFA (1 mL). The resulting mixture was stirred at rt for 18 h. Excess CH_2Cl_2 and TFA were removed under reduced pressure and the resulting yellow residue was repeatedly washed with CH_2Cl_2 (3 x 1 mL). Deprotection was monitored by ESI-LRMS (+) (*m/z* 494.2 $[M+H]^+$; ESI-HRMS (+) calcd for $[C_{24}H_{40}N_5O_6]^+$ 494.2979, found 494.2963) and complete deprotection was confirmed by ^{1}H NMR spectroscopy. The residue was dissolved in H_2O (2 mL) and the pH adjusted to 5.5. To this was added $EuCl_3.6H_2O$ (63 mg, 0.17 mmol) and the resulting mixture was stirred at 70 ^oC for 18 h, before the solvent was removed under reduced pressure. The resulting yellow solid was purified by reverse-phase HPLC (10-100% MeOH in H_2O over 10 min; t_R = 8.9 min) to yield a white solid (30 mg). ^{1}H NMR (400 MHz, D_2O) δ 32.2, 29.7, 29.3, 25.3 (H_{ax}), 13.3, 7.1, 3.7, 3.5 (H_{eq}'), 2.1 ($C(C\underline{H}_3)_3$), 1.4, -3.5, -8.3, -14.7 (H_{eq}), -14.0, -14.2, -17.8, -19.1 (H_{ax}'); ESI-LRMS (+) *m/z* 644.0 $[M+H]^+$; ESI-HRMS (+) calcd for $[C_{24}H_{37}N_5O_6{}^{151}Eu]^+$ 642.1942, found 642.1935.

8. [Gd.L^1(H$_2$O)]

An analogous procedure to that described for the synthesis of **[Eu.L^1(H$_2$O)]** was followed using *tert*-butyl-2,2',2''-(10-((5-*tert*-butylpyridin-2-yl)methyl)-1,4,7,10-tetraazacyclododecane-1,4,7-triyl)triacetate (100 mg, 0.15 mmol) and $GdCl_3.6H_2O$ (63 mg, 0.17 mmol), to yield a white solid (32 mg). t_R = 8.4 min; ESI-LRMS (+) *m/z* 648.9 $[M+H]^+$; ESI-HRMS (+) calcd for $[C_{24}H_{37}N_5O_6{}^{155}Gd]^+$ 646.1970, found 646.1960; r_{1p} = 4.8±0.01 mM^{-1} s^{-1} (H_2O, 60 MHz, 310 K).

9. [Tb.L^1(H$_2$O)]

An analogous procedure to that described for the synthesis of **[Eu.L^1(H$_2$O)]** was followed using *tert*-butyl-2,2',2''-(10-((5-*tert*-butylpyridin-2-yl)methyl)-1,4,7,10-

tetraazacyclododecane-1,4,7-triyl)triacetate (100 mg, 0.15 mmol) and $TbCl_3.6H_2O$ (63 mg, 0.17 mmol), to yield a white solid (30 mg). t_R = 9.3 min; ^{1}H NMR (400 MHz, D_2O) δ -11.1 ($C(C\underline{H}_3)_3$); ESI-LRMS (+) *m/z* 651.1 $[M+H]^+$; ESI-HRMS (+) calcd for $[C_{24}H_{37}N_5O_6{}^{159}Tb]^+$ 650.1997, found 650.1967.

10. [Dy.L^1(H$_2$O)]

An analogous procedure to that described for the synthesis of **[Eu.L^1(H$_2$O)]** was followed using *tert*-butyl-2,2',2''-(10-((5-*tert*-butylpyridin-2-yl)methyl)-1,4,7,10-tetraazacyclododecane-1,4,7-triyl)triacetate (100 mg, 0.15 mmol) and $DyCl_3.6H_2O$ (63 mg, 0.17 mmol), to yield a white solid (30 mg). t_R = 8.9 min; ^{1}H NMR (400 MHz, D_2O) δ -20.1 ($C(C\underline{H}_3)_3$); ESI-LRMS (+) *m/z* 652.3 $[M+H]^+$; ESI-HRMS (+) calcd for $[C_{24}H_{36}N_5O_6Na^{160}Dy]^+$ 673.1815, found 673.1824.

11. [Ho.L^1(H$_2$O)]

An analogous procedure to that described for the synthesis of **[Eu.L^1(H$_2$O)]** was followed using *tert*-butyl-2,2',2''-(10-((5-*tert*-butylpyridin-2-yl)methyl)-1,4,7,10-tetraazacyclododecane-1,4,7-triyl)triacetate (100 mg, 0.15 mmol) and $HoCl_3.6H_2O$ (64 mg, 0.17 mmol), to yield a white solid (32 mg). t_R = 8.3 min; ^{1}H NMR (400 MHz, D_2O) δ -7.2 ($C(C\underline{H}_3)_3$); ESI-LRMS (+) *m/z* 656.0 $[M+H]^+$; ESI-HRMS (+) calcd for $[C_{24}H_{37}N_5O_6{}^{165}Ho]^+$ 656.2047, found 656.2058.

12. [Er.L^1(H$_2$O)]

An analogous procedure to that described for the synthesis of **[Eu.L^1(H$_2$O)]** was followed using *tert*-butyl-2,2',2''-(10-((5-*tert*-butylpyridin-2-yl)methyl)-1,4,7,10-tetraazacyclododecane-1,4,7-triyl)triacetate (100 mg, 0.15 mmol) and $ErCl_3.6H_2O$ (63 mg, 0.17 mmol), to yield a white solid (29 mg). t_R = 8.7 min; ^{1}H NMR (400 MHz, D_2O) δ 7.0 ($C(C\underline{H}_3)_3$); ESI-LRMS (+) *m/z* 657.1 $[M+H]^+$; ESI-HRMS (+) calcd for $[C_{24}H_{37}N_5O_6{}^{166}Er]^+$ 657.2047, found 657.2045.

13. [Tm.L^1(H$_2$O)]

An analogous procedure to that described for the synthesis of **[Eu.L^1(H$_2$O)]** was followed using *tert*-butyl-2,2',2''-(10-((5-*tert*-butylpyridin-2-yl)methyl)-1,4,7,10-tetraazacyclododecane-1,4,7-triyl)triacetate (100 mg, 0.15 mmol) and $TmCl_3.6H_2O$ (63 mg, 0.17 mmol), to yield a white solid (33 mg). t_R = 8.6 min; ^{1}H NMR (400 MHz, D_2O)

δ 10.5 ($C(C\underline{H}_3)_3$); ESI-LRMS (+) *m/z* 661.3 $[M+H]^+$; ESI-HRMS (+) calcd for $[C_{24}H_{36}N_5O_6NaTm]^+$ 682.1906, found 682.1880.

14. [Yb.L^1(H$_2$O)]

An analogous procedure to that described for the synthesis of **[Eu.L^1(H$_2$O)]** was followed using *tert*-butyl-2,2',2''-(10-((5-*tert*-butylpyridin-2-yl)methyl)-1,4,7,10-tetraazacyclododecane-1,4,7-triyl)triacetate (100 mg, 0.15 mmol) and $YbCl_3.6H_2O$ (63 mg, 0.17 mmol), to yield a white solid (28 mg). t_R = 8.4 min; ^{1}H NMR (400 MHz, D_2O) δ 124.0, 115.6, 112.8, 98.0 (H_{ax}), 40.8, 26.6, 20.1, 19.5 (H_{eq}), 15.4, 13.7, 11.3, 7.72 (H_{ax}'), 6.3 ($C(CH_3)_3$), 1.08, -1.41 (pyH), -8.84 (CHCO), -19.8 (CHCO'), -20.5, -47.2 (CHCO), -47.5, -55.9 (CHCO'), -65.9, -67.1, -69.7, -72.3 (H_{eq}'); ESI-LRMS (+) *m/z* 665.0 $[M+H]^+$; ESI-HRMS (+) calcd for $[C_{24}H_{37}N_5O_6{}^{170}Yb]^+$ 661.2092, found 661.2100.

15. 1,4,7,10-Tetraazacyclododecane-1,7-dicarboxylic acid dibenzyl ester[4]

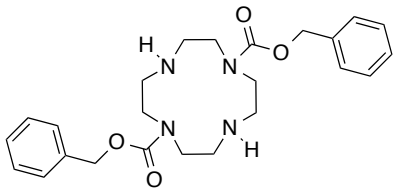

1,4,7,10-Tetraazacyclododecane (3.5 g, 20.3 mmol) was dissolved in a solution of distilled H_2O:dioxane (50:20 mL), followed by addition of Na_2HPO_4 (9.8 g, 69.0 mmol). The pH of the solution was adjusted to 2.5 by careful addition of conc. HCl (aq). Benzyl chloroformate (7.3 mL, 50.8 mmol) in dioxane (10 mL) was added dropwise over a period of 30 min and the solution left to stir for a further 18 h at rt. The solvent was evaporated under reduced pressure and the residue dissolved in H_2O (100 mL), followed by adjustment of the pH to 7 by addition of conc. KOH (aq). The aqueous phase was extracted with Et_2O (2 × 100 mL), followed by CH_2Cl_2 (2 × 100 mL). The organic phases were combined, dried over $MgSO_4$, filtered, and the solvent removed under reduced pressure to give a clear viscous oil. The oil was dissolved in CH_2Cl_2 (10 mL) and cold Et_2O (100 mL) was added, causing a white solid to precipitate (5.80 g, 65%). m.p. 115-117 °C (lit. m.p. 116-117 °C); ^{1}H NMR (400 MHz, $CDCl_3$) δ 7.29–7.42 (m, 10H, Ar), 5.17 (s, 4H, Cbz CH_2), 3.27–4.13 (br m, 8H, cyclen CH_2), 2.76–3.22 (br m, 8H, cyclen CH_2), 1.70 (br s, 2H, NH); ^{13}C NMR (176 MHz,

$CDCl_3$) δ 156.2 (CO), 128.0 (Ar), 128.4 (Ar), 128.5 (Ar), 128.7 (Ar), 135.8 (Ar), 67.8 (Cbz CH_2), 67.9 (Cbz CH_2), 49.0 (cyclen CH_2), 50.5 (cyclen CH_2); ESI-LRMS (+) *m/z* 441.6 $[M+H]^+$; ESI-HRMS (+) calcd for $[C_{24}H_{33}O_4N_4]^+$ 441.2502, found 441.2514.

16. 4,10-Bis-*tert*-butoxycarbonylmethyl-1,4,7,10-tetraazacyclododecane-1,7-dicarboxylic acid dibenzyl ester[5]

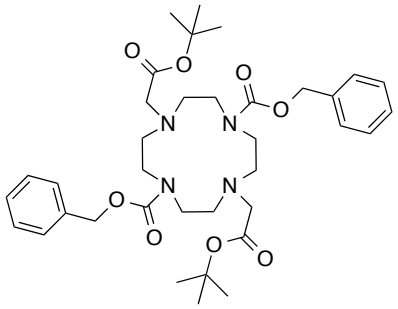

1,4,7,10-Tetraazacyclododecane-1,7-dicarboxylic acid dibenzyl ester (5.8 g, 13.2 mmol) and *tert*-butyl bromoacetate (4.5 mL, 30.4 mmol) were dissolved in anhydrous MeCN (70 mL), followed by the addition of Cs_2CO_3 (12.9 g, 39.6 mmol). The mixture was heated at 80 ^oC for 18 h. The solution was cooled and filtered, before the solvent was removed under reduced pressure. The resulting dark yellow oil was purified by silica gel column chromatography, eluting with a gradient starting from 100% CH_2Cl_2 to 2% MeOH/CH_2Cl_2 to yield a dark yellow oil (8.0 g, 91%). R_f (10% MeOH/CH_2Cl_2) = 0.53; ^1H NMR (400 MHz, $CDCl_3$) δ 7.28-7.38 (10H, m, Ar), 5.12 (4H, s, Cbz CH_2), 3.14-3.51 (12H, cyclen CH_2/CH_2CO), 2.74-2.96 (8H, br s, CH_2 ring), 1.42 (18H, s, $C(CH_3)_3$); ^{13}C NMR ($CDCl_3$, 101 MHz) δ 169.6 (CO), 155.5 (CO), 135.9 (Ar), 127.5 (Ar), 127.0 (Ar), 126.9 (Ar), 80.0 $\underline{C}(CH_3)_3$, 66.0 (CH_2Ar), 55.0 ($\underline{C}H_2CO$), 52.9- 53.7 (br, cyclen CH_2), 45.7- 46.1 (br, cyclen CH_2), 27.2 $C(\underline{C}H_3)_3$; ESI-LRMS (+) *m/z* 669.3 $[M+H]^+$; ESI-HRMS (+) calcd for $[C_{36}H_{53}O_8N_4]^+$ 669.3863, found 669.3868.

17. (7-*tert*-Butoxycarbonylmethyl-1,4,7,10-tetraazacyclododec-1-yl)-acetic acid *tert*-butyl ester[5]

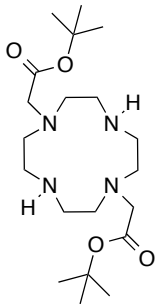

4,10-Bis-*tert*-butoxycarbonylmethyl-1,4,7,10-tetraazacyclododecane-1,7-dicarboxylic acid dibenzyl ester (2.0 g, 2.99 mmol) was dissolved in MeOH (10 mL) to which $Pd(OH)_2/C$ (Pd content 10%, 50 mg) was added. The vessel was then loaded onto a Parr hydrogenator (pressure 40 bar H_2) and the reaction mixture agitated for 3 days. After this time, the catalyst was filtered off and the solvent removed under reduced pressure to yield a yellow oil (1.1 g, 89 %). ^{1}H NMR (400 MHz, $CDCl_3$) δ 3.28 (4H, s, CH_2CO), 2.81 (8H, br m, cyclen CH_2), 2.65 (8H, br m, cyclen CH_2), 1.36 (18H, s, $C(CH_3)_3$); ^{13}C NMR (101 MHz, $CDCl_3$) δ 170.7 (CO), 80.7 ($\underline{C}(CH_3)_3$, 60.1 (CH_2), 45.8, 49.1, 51.1, 56.3 (cyclen CH_2), 27.6 $C(\underline{C}H_3)_3$; ESI-LRMS (+) *m/z* 401.3 $[M+H]^+$; ESI-HRMS (+) calcd for $[C_{20}H_{41}O_4N_4]^+$ 401.3128, found 401.3109.

18. *tert*-Butyl 2,2'-(4,10-bis((5-*tert*-butylpyridin-2-yl)methyl)-1,4,7,10-tetraazacyclododecane-1,7-diyl)diacetate

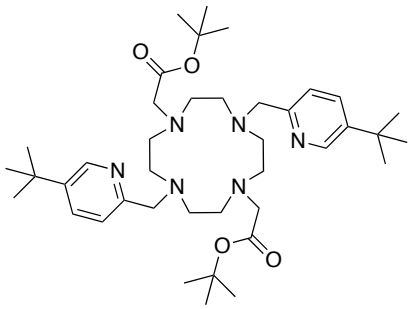

(7-*tert*-Butoxycarbonylmethyl-1,4,7,10-tetraazacyclododec-1-yl)-acetic acid *tert*-butyl ester (0.27 g, 0.67 mmol) was dissolved in anhydrous MeCN (4 mL) and to this was added K_2CO_3 (0.23 g, 1.68 mmol). The resulting mixture was stirred for 10 min under argon before (5-*tert*-butylpyridin-2-yl)methyl methanesulfonate (0.41 mg, 1.68 mmol)

in anhydrous MeCN (1 mL) was added dropwise. The reaction mixture was heated at 60 °C for 18 h under argon. After this time, the solution was allowed to cool to rt and filtered. The resulting orange oil was purified by silica gel column chromatography, eluting with a gradient starting from 100% CH_2Cl_2 to 4% MeOH/ CH_2Cl_2 to yield a sticky brown oil (0.16 g, 13%). R_f (10% MeOH/ CH_2Cl_2) = 0.38; ^{1}H NMR (400 MHz, $CDCl_3$) δ 8.37 (d, ^4J = 2, 2H, H^6), 7.65 (dd, ^3J = 8, ^4J = 2, 2H, H^4), 7.08 (d, ^3J = 8, 2H, H^3), 3.68 (br s, 4H, NCH_2py), 2.76 (br m, 12H, NCH_2COO^tBu/cyclen CH_2), 2.39 (br m, 8H, cyclen CH_2), 1.29 (s, 18H, py$C(CH_3)_3$), 1.26 (s, 18H, $OC(CH_3)_3$); ^{13}C NMR (151 MHz, $CDCl_3$) δ 172.0 ($\underline{C}OOC(CH_3)_3$), 155.1 (C^2), 146.0 (C^6), 144.5 (C^5), 133.7 (C^4), 122.1 (C^3), 81.7 ($COO\underline{C}(CH_3)_3$), 58.1 (pyCH_2), 57.2 ($N\underline{C}H_2CO$), 53.4 (cyclen CH_2), 50.3 (cyclen CH_2), 33.3 (py$\underline{C}(CH_3)_3$), 31.0 (py$C(\underline{C}H_3)_3$), 27.9 ($COOC(\underline{C}H_3)_3$); ESI-LRMS (+) *m/z* 695.3 $[M+H]^+$; ESI-HRMS (+) calcd for $[C_{40}H_{66}N_6O_4]^+$ 695.5224, found 695.5232.

19. Europium(III) complex of 2,2'-(4,10-bis((5-*tert*-butylpyridin-2-yl)methyl)-1,4,7,10-tetraazacyclododecane-1,7-diyl)diacetic acid, $[Eu.L^2(H_2O)]^+$

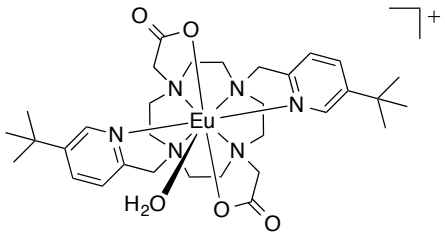

tert-Butyl 2,2'-(4,10-bis((5-*tert*-butylpyridin-2-yl)methyl)-1,4,7,10-tetraazacyclododecane-1,7-diyl)diacetate (17 mg, 0.02 mmol) was dissolved in HCl (6 M, 1 mL) and heated to 90 °C for 18 h. The solvent was removed under reduced pressure and the resulting yellow residue was repeatedly washed with CH_2Cl_2 (3 × 1 mL). Deprotection was monitored by ESI-LRMS (+) (*m/z* 583.3 $[M+H]^+$; ESI-HRMS (+) calcd for $[C_{32}H_{51}N_6O_4]^+$ 583.3972, found 583.3961) and complete deprotection was confirmed by ^{1}H NMR spectroscopy. The residue was dissolved in H_2O (2 mL) and the pH adjusted to 5.5. To this was added $EuCl_3.6H_2O$ (10 mg, 0.03 mmol) and the resulting mixture was stirred at 70 °C for 18 h, before the solvent was removed under reduced pressure. The resulting yellow solid was purified by reverse-phase HPLC (10-100% MeOH in H_2O over 10 min; t_R = 3.6 min) to yield a white solid (5 mg). ^{1}H NMR

(400 MHz, D_2O) δ 1.7 ($C(CH_3)_3$); ESI-LRMS (+) *m/z* 733.1 $[M]^+$; ESI-HRMS (+) calcd for $[C_{32}H_{48}N_6O_4{}^{151}Eu]^+$ 731.2930, found 731.2906.

20. $[Gd.L^2(H_2O)]^+$

An analogous procedure to that described for the synthesis of **$[Eu.L^2(H_2O)]^+$** was followed using *tert*-butyl 2,2'-(4,10-bis((5-*tert*-butylpyridin-2-yl)methyl)-1,4,7,10-tetraazacyclododecane-1,7-diyl)diacetate (17 mg, 0.02 mmol) and $GdCl_3.6H_2O$ (10 mg, 0.03 mmol), to yield a white solid (4 mg). t_R = 3.9 min; ESI-LRMS (+) *m/z* 738.03 $[M]^+$; ESI-HRMS (+) calcd for $[C_{32}H_{48}N_6O_4{}^{154}Gd]^+$ 734.2946, found 734.2938; r_{1p} = 5.8±0.02 $mM^{-1}\,s^{-1}$ (H_2O, 60 MHz, 310 K).

21. $[Tb.L^2(H_2O)]^+$

An analogous procedure to that described for the synthesis of **$[Eu.L^2(H_2O)]^+$** was followed using 2,2'-(4,10-bis((5-*tert*-butylpyridin-2-yl)methyl)-1,4,7,10-tetraazacyclododecane-1,7-diyl)diacetic acid (17 mg, 0.02 mmol) and $TbCl_3.6H_2O$ (10 mg, 0.03 mmol), to yield a white solid (5 mg). t_R = 4.5 min; ^1H NMR (400 MHz, D_2O): δ = -7.2 ($C(CH_3)_3$); ESI-LRMS (+) *m/z* 739.9 $[M]^+$; ESI-HRMS (+) calcd for $[C_{32}H_{48}N_6O_4\,Tb]^+$ 739.2991, found 739.2985

22. $[Dy.L^2(H_2O)]^+$

An analogous procedure to that described for the synthesis of **$[Eu.L^2(H_2O)]^+$** was followed using *tert*-butyl 2,2'-(4,10-bis((5-*tert*-butylpyridin-2-yl)methyl)-1,4,7,10-tetraazacyclododecane-1,7-diyl)diacetate (36 mg, 0.05 mmol) and $DyCl_3.6H_2O$ (24 mg, 0.07 mmol), to yield a white solid (11 mg). t_R = 4.2 min; ^1H NMR (400 MHz, D_2O) δ -17.9 ($C(CH_3)_3$); ESI-LRMS (+) *m/z* 743.7 $[M]^+$; ESI-HRMS (+) calcd for $[C_{32}H_{48}N_6O_4{}^{160}Dy]^+$ 740.2989, found 740.2997.

23. $[Ho.L^2(H_2O)]^+$

An analogous procedure to that described for the synthesis of **$[Eu.L^2(H_2O)]^+$** was followed using *tert*-butyl 2,2'-(4,10-bis((5-*tert*-butylpyridin-2-yl)methyl)-1,4,7,10-tetraazacyclododecane-1,7-diyl)diacetate (17 mg, 0.02 mmol) and $HoCl_3.6H_2O$ (10 mg, 0.03 mmol), to yield a white solid (5 mg). t_R = 3.7 min; ^1H NMR (400 MHz, D_2O) δ -7.0 ($C(CH_3)_3$); ESI-LRMS (+) *m/z* 745.0 $[M]^+$; ESI-HRMS (+) calcd for $[C_{32}H_{48}N_6O_4Ho]^+$ 745.3040, found 745.3055.

24. $[Er.L^2(H_2O)]^+$

An analogous procedure to that described for the synthesis of **$[Eu.L^2(H_2O)]^+$** was followed using *tert*-butyl 2,2'-(4,10-bis((5-*tert*-butylpyridin-2-yl)methyl)-1,4,7,10-tetraazacyclododecane-1,7-diyl)diacetate (17 mg, 0.02 mmol) and $ErCl_3.6H_2O$ (12 mg, 0.02 mmol), to yield a white solid (5 mg). t_R = 4.8 min; ^{1}H NMR (400 MHz, D_2O) δ 3.4 ($C(CH_3)_3$); ESI-LRMS (+) *m/z* 747.9 $[M]^+$; ESI-HRMS (+) calcd for $[C_{32}H_{48}N_6O_4{}^{164}Er]^+$ 744.3029, found 744.3038.

25. $[Tm.L^2(H_2O)]^+$

An analogous procedure to that described for the synthesis of **$[Eu.L^2(H_2O)]^+$** was followed using 2,2'-(4,10-bis((5-*tert*-butylpyridin-2-yl)methyl)-1,4,7,10-tetraazacyclododecane-1,7-diyl)diacetic acid (17 mg, 0.02 mmol) and $TmCl_3.6H_2O$ (10 mg, 0.03 mmol) to give a white solid (5 mg). t_R = 4.4 min; ^{1}H NMR (400 MHz, D_2O): δ 6.2 ($C(CH_3)_3$); ESI-LRMS (+) *m/z* 750.0 $[M]^+$; ESI-HRMS (+) calcd for $[C_{32}H_{48}N_6O_4Tm]^+$ 749.3079, found 749.3100.

26. $[Yb.L^2(H_2O)]^+$

An analogous procedure to that described for the synthesis of **$[Eu.L^2(H_2O)]^+$** was followed using *tert*-butyl 2,2'-(4,10-bis((5-*tert*-butylpyridin-2-yl)methyl)-1,4,7,10-tetraazacyclododecane-1,7-diyl)diacetate (17 mg, 0.02 mmol) and $YbCl_3.6H_2O$ (12 mg, 0.02 mmol), to yield a white solid (5 mg). t_R = 3.9 min; ^{1}H NMR (400 MHz, D_2O) δ 9.1 ($C(CH_3)_3$); ESI-LRMS (+) *m/z* 754.1 $[M]^+$; ESI-HRMS (+) calcd for $[C_{32}H_{48}N_6O_4{}^{170}Yb]^+$ 750.3085, found 750.3049.

27. 1,4,7-Tri-benzyl 1,4,7,10-tetraazacyclododecane 1,4,7-tricarboxylate

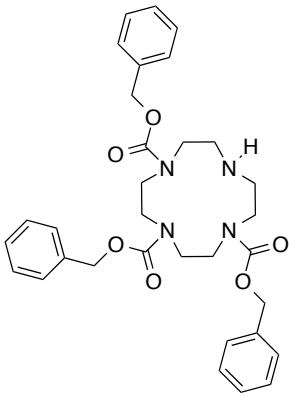

1,4,7,10-Tetraazacyclododecane (2.5 g, 14.5 mmol) was dissolved in dry CH_2Cl_2 (80 mL) and to this was added triethylamine (6.3 mL, 45.0 mmol). The resulting solution was stirred at 5 ^oC for 10 min, before the dropwise addition of a solution of benzyl chloroformate (6.4 mL, 45.0 mmol) in dry CH_2Cl_2 (20 mL). After addition, the solution was stirred at rt for a further 18 h. The solvent was removed under reduced pressure and the resulting pale yellow oil was purified by silica gel column chromatography, eluting with a gradient starting from 100% CH_2Cl_2 to 2% MeOH/ CH_2Cl_2 to yield a colourless oil (6.1 g, 73%). R_f (10% MeOH/ CH_2Cl_2) = 0.54; ^1H NMR (400 MHz, $CDCl_3$) δ 7.22-7.33 (m, 15H, ArH), 5.00-5.06 (m, 6H, CH_2O), 3.63-3.67 (m, 2H, cyclen CH_2), 3.16-3.55 (m, 12H, cyclen CH_2), 2.75-2.92 (m, 2H, cyclen CH_2); ^{13}C NMR (101 MHz, $CDCl_3$) δ 156.1 (CO), 136.4 (Ar), 136.3 (Ar), 128.4 (Ar), 128.3 (Ar), 127.7 (Ar), 127.6 (Ar), 127.4 (Ar), 67.2 (CH_2O), 66.8 (CH_2O), 53.5 (cyclen CH_2), 50.6 (cyclen CH_2), 50.3 (cyclen CH_2), 50.2 (cyclen CH_2), 50.1 (cyclen CH_2), 45.6 (cyclen CH_2); ESI-LRMS (+) *m/z* 575.1 $[M+H]^+$; ESI-HRMS (+) calcd for $[C_{32}H_{39}N_4O_6]^+$ 575.2870, found 575.2867.

28. 1,4,7-Tri-benzyl 10-*tert*-butyl 1,4,7,10-tetraazacyclododecane 1,4,7,10-tetracarboxylate

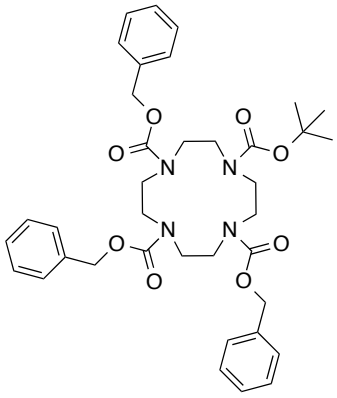

1,4,7-Tri-benzyl 1,4,7,10-tetraazacyclododecane 1,4,7-tricarboxylate (1.3 g, 2.26 mmol) was dissolved in dry CH_2Cl_2 (15 mL) and to this was added triethylamine (0.4 mL, 2.94 mmol). The resulting solution was stirred at rt for 10 min, before the addition of di-*tert*-butyl dicarbonate (0.64 g, 2.94 mmol). The resulting solution was stirred at rt for a further 18 h before the solvent was removed under reduced pressure. The resulting yellow oil was purified by silica gel column chromatography, eluting with a gradient starting from 100% CH_2Cl_2 to 2% MeOH/ CH_2Cl_2 to yield a colourless oil (1.3 g, 85%). R_f (10% MeOH/ CH_2Cl_2) = 0.69; ^1H NMR (400 MHz, $CDCl_3$) δ 7.21-7.34 (m,

15H, ArH), 5.06 (s, 2H, CH_2O), 5.03 (s, 4H, CH_2O), 3.00-3.54 (br m, 16H, cyclen CH_2), 1.36 (s, 9H, $C(CH_3)_3$); ^{13}C NMR (101 MHz, $CDCl_3$) δ 156.8 (CO), 136.4 (Ar), 128.6 (Ar), 128.4 (Ar), 128.3 (Ar), 128.2 (Ar), 82.8 ($\underline{C}(CH_3)_3$), 67.3 (CH_2O), 49.9-50.7 (br, cyclen CH_2), 28.4 ($C(\underline{C}H_3)_3$); ESI-LRMS (+) *m/z* 675.1 $[M+H]^+$; ESI-HRMS (+) calcd for $[C_{37}H_{47}N_4O_8]^+$ 675.3394, found 675.3406.

29. *tert*-Butyl-1,4,7,10-tetraazacyclododecane carboxylate

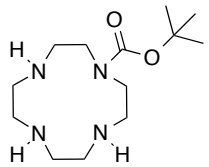

1,4,7-Tri-benzyl 10-*tert*-butyl 1,4,7,10-tetraazacyclododecane 1,4,7,10-tetracarboxylate (1.3 g, 1.93 mmol) was dissolved in MeOH (25 mL) and to this was added $Pd(OH)_2/C$ (~200 mg). The reaction vessel was loaded onto a Parr hydrogenator, where it was subject to agitation for 18 h, under a pressure of 40 bar H_2. The catalyst was filtered through Celite and the solvent was removed under reduced pressure. The resulting solid was washed with a minimum amount of NaOH (aq. solution, 1 mL), and extracted into CH_2Cl_2 (3 × 30 mL), before the organic layers were combined, dried over $MgSO_4$, and the solvent removed under reduced pressure to yield a pale yellow oil (0.52 g, 99%). ^1H NMR (400 MHz, CD_3OD) δ 5.03 (br s, NH), 3.52-3.60 (m, 4H, cyclen CH_2), 3.22-3.27 (m, 4H, cyclen CH_2), 3.10-3.21 (m, 8H, cyclen CH_2), 1.49 (s, 9H, $C(CH_3)_3$); ^{13}C NMR (101 MHz, CD_3OD) δ 157.5 (CO), 82.3 ($\underline{C}(CH_3)_3$), 48.2 (cyclen CH_2), 46.9 (cyclen CH_2), 45.6 (cyclen CH_2), 44.5 (cyclen CH_2), 28.7 ($C(\underline{C}H_3)_3$); ESI-LRMS (+) *m/z* 273.2 $[M+H]^+$; ESI-HRMS (+) calcd for $[C_{13}H_{29}N_4O_2]^+$ 273.2291, found 273.2296.

30. *tert*-Butyl-4,7,10-tri{[ethoxy(methyl)phosphoryl]methyl}-1,4,7,10-tetraazacyclododecane-1-carboxylate

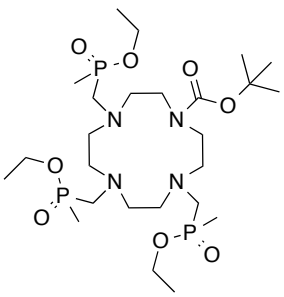

tert-Butyl-1,4,7,10-tetraazacyclododecane carboxylate (0.52 g, 1.91 mmol) and paraformaldehyde (1.15 g, 38.2 mmol) were dissolved in anhydrous THF (30 mL) and the resulting suspension was heated at 80 ^{o}C for 3 h. Diethyl methylphosphonite (1.7 mL, 11.5 mmol) was added and the solution stirred at 80 ^{o}C for a further 18 h. The solution was cooled and filtered, before the solvent was removed under reduced pressure. The residual brown oil was purified by alumina gel column chromatography, eluting with a gradient starting from 100% CH_2Cl_2 to 2% MeOH/ CH_2Cl_2 to yield a yellow oil (0.4 g, 33%). R_f (10% MeOH/ CH_2Cl_2) = 0.76; ^{1}H NMR (400 MHz, $CDCl_3$) δ 3.93 (q, $^3J_{PH}$ = 7, 6H, $POCH_2$), 3.09-3.60 (br m, 6H, PCH_2N), 2.41-3.00 (br m, 16H, cyclen CH_2), 1.33-1.47 (m, 9H, PCH_3), 1.32 (s, 9H, $C(CH_3)_3$), 1.18 (t, $^3J_{PH}$ = 7, 9H, $POCH_2C\underline{H}_3$); ^{31}P NMR (162 MHz, $CDCl_3$) δ 52.53, 52.31, 52.22, 52.20, 52.18, 52.24, 52.06, 51.95, 51.85, 51.85, 51.59, 51.49 (mixture of isomers); ^{13}C NMR (176 MHz, $CDCl_3$) δ 155.5 (CO), 79.5 ($\underline{C}(CH_3)_3$), 59.9-60.1 (m, $POCH_2$), 52.7-55.1 (m, cyclen CH_2), 45.9 (PCH_2N), 45.6 (PCH_2N), 45.5 (PCH_2N), 28.4 ($C(\underline{C}H_3)_3$), 16.6 (t, $^3J_{CP}$ = 6, $POCH_2\underline{C}H_3$), 13.5-13.9 (m, PCH_3); ESI-LRMS (+) *m/z* 633.2 $[M+H]^+$; ESI-HRMS (+) calcd for $[C_{25}H_{56}N_4O_8P_3]^+$ 633.3311, found 633.3312.

31. Ethyl[(4,7-di{[ethoxy(methyl)phosphoryl]methyl}-1,4,7,10-tetraazacyclododecane-1-yl)methyl](methyl)phosphinate

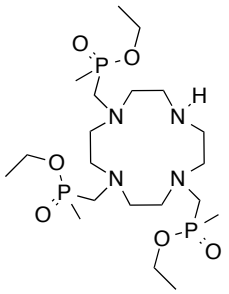

tert-Butyl-4,7,10-tri{[ethoxy(methyl)phosphoryl]methyl}-1,4,7,10-tetraazacyclododecane-1-carboxylate (0.4 g, 0.63 mmol) was dissolved in anhydrous CH_2Cl_2 (2 mL) and to this was added TFA (2 mL). The resulting solution was stirred at rt for 18 h, before the solvent was removed under reduced pressure. The resulting yellow oil was dissolved in a minimal amount of H_2O (3 mL). The pH of the water layer was adjusted to 12 using solid NaOH before being extracted with CH_2Cl_2 (4 × 10 mL). The CH_2Cl_2 layers were combined, dried over $MgSO_4$, and the solvent removed under reduced pressure to yield a yellow oil (0.22 g, 66%). ^{1}H NMR (400 MHz,

$CDCl_3$) δ 3.90-4.08 (m, 6H, $POCH_2$), 2.60-3.32 (br m, 22H, cyclen CH_2, PCH_2N), 1.46 (d, $^2J_{PH}$ = 13, 9H, PCH_3), 1.25 (t, $^3J_{PH}$ = 7, 9H, $POCH_2C\underline{H}_3$); ^{31}P NMR (162 MHz, $CDCl_3$) δ 54.2, 53.8, 53.5, 53.2, 50.4 (mixture of isomers); ^{13}C NMR (101 MHz, $CDCl_3$) δ 60.1-60.6 (m, $POCH_2$), 56.2-56.6 (m, cyclen CH_2), 55.1-55.5 (m, cyclen CH_2), 52.5-53.2 (m, cyclen CH_2), 46.8-47.3 (m, PCH_2N), 16.7 (t, $^3J_{CP}$ = 6, $POCH_2\underline{C}H_3$), 14.2 (t, $^1J_{CP}$ = 12, $P\underline{C}H_3$), 13.3 (t, $^1J_{CP}$ = 12, $P\underline{C}H_3$); ESI-LRMS (+) *m/z* 533.1 $[M+H]^+$; ESI-HRMS (+) calcd for $[C_{20}H_{48}N_4O_6P_3]^+$ 533.2787, found 533.2811.

32. Ethyl ({4-[(5-*tert*-butylpyridin-2-yl)methyl]-7,10-di{[ethoxy(methyl)phosphoryl]methyl}-1,4,7,10-tetraazacyclododecan-1-yl}methyl)(methyl)phosphinate

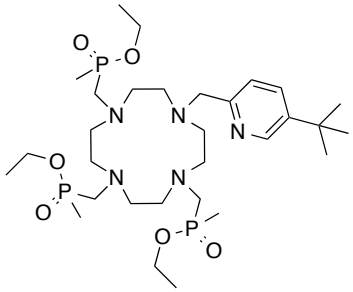

Ethyl[(4,7-di{[ethoxy(methyl)phosphoryl]methyl}-1,4,7,10-tetraazacyclododecane-1-yl)methyl](methyl)phosphinate (0.64 g, 1.20 mmol) was dissolved in anhydrous MeCN (7 mL) and to this was added K_2CO_3 (0.36 g, 2.64 mmol). (5-*tert*-Butylpyridin-2-yl)methyl methanesulfonate (0.32 g, 1.32 mmol) was then added dropwise as a solution in anhydrous MeCN (5 mL). The resulting mixture was heated at 70 ^{o}C for 18 h, under argon. The reaction mixture was cooled and the inorganic salts were removed by centrifugation. The solvent was removed under reduced pressure and the resulting red oil was purified by alumina gel column chromatography, eluting with a gradient starting from 100% CH_2Cl_2 to 1% MeOH/ CH_2Cl_2 to yield an orange oil (0.37 g, 45%). R_f (10% MeOH/ CH_2Cl_2) = 0.70; ^{1}H NMR (400 MHz, $CDCl_3$) δ 8.57 (d, ^4J = 2, 1H, H^6), 7.66 (dd, 8.57, ^3J = 8, ^4J = 2, 1H, H^4), 7.29 (d, ^3J = 8, 1H, H^3), 3.89-4.11 (m, 6H, $POCH_2$), 3.46-3.57 (m, 8H, PCH_2N, $pyCH_2$), 2.63-3.14 (br m, 16H, cyclen CH_2), 2.01 (s, 9H, $C(CH_3)_3$), 1.41-1.60 (m, 9H, PCH_3), 1.21-1.32 (m, 9H, $POCH_2C\underline{H}_3$); ^{31}P NMR (162 MHz, $CDCl_3$) δ 54.0, 53.9, 53.8, 53.6, 53.2, 51.7, 51.6, 51.5 (mixture of isomers); ESI-LRMS (+) *m/z* 680.2 $[M+H]^+$; ESI-HRMS (+) calcd for $[C_{30}H_{61}N_5O_6P_3]^+$ 680.3825, found 680.3824.

33. Europium(III) complex of ({4-[(5-*tert*-butylpyridin-2-yl)methyl]-7,10-di{[hydroxy(methyl)phosphoryl]methyl}-1,4,7,10-tetraazacyclododecan-1-yl}methyl)(methyl)phosphinic acid, [Eu.L^3]

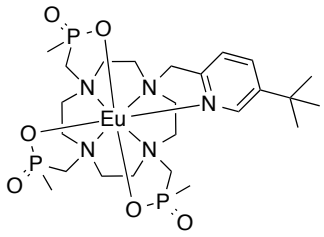

Ethyl ({4-[(5-*tert*-butylpyridin-2-yl)methyl]-7,10-di{[ethoxy(methyl)phosphoryl]methyl}-1,4,7,10-tetraazacyclododecan-1-yl}methyl)(methyl)phosphinate (45 mg, 0.065 mmol) was dissolved in aqueous HCl (6 M, 2 mL) and stirred at 70 ^{o}C for 18 h. Complete ester hydrolysis was confirmed by ^{31}P NMR spectroscopy ((162 MHz, D_2O) δ 37.0, 34.4, 30.6), before the solvent was removed under reduced pressure. The resulting yellow oil was dissolved in H_2O (2 mL). The pH of the solution was adjusted to 5.5 using NaOH and $EuCl_3.6H_2O$ (36 mg, 0.098 mmol) was added. The resulting solution was stirred at 70 ^{o}C for 18 h before the solvent was removed under reduced pressure. The resulting yellow solid was purified by reverse-phase HPLC (10-100% MeOH in H_2O over 10 min; t_R = 8.6 min) to yield a white solid (15 mg). ^{1}H NMR (400 MHz, D_2O) δ 2.9 ($C(CH_3)_3$ major), 1.5 ($C(CH_3)_3$ minor); ESI-LRMS (+) *m/z* 746.4 $[M+H]^+$; ESI-HRMS (+) calcd for $[C_{24}H_{46}N_5O_6P_3{}^{151}Eu]^+$ 745.4931, found 745.4929.

34. [Gd.L^3]

An analogous procedure to that described for **[Eu.L^3]** was followed using ethyl ({4-[(5-*tert*-butylpyridin-2-yl)methyl]-7,10-di{[ethoxy(methyl)phosphoryl]methyl}-1,4,7,10-tetraazacyclododecan-1-yl}methyl)(methyl)phosphinate (45 mg, 0.065 mmol) and $GdCl_3.6H_2O$ (36 mg, 0.098 mmol), to yield a white solid (15 mg). t_R = 9.0 min; ESI-LRMS (+) *m/z* 750.4 $[M+H]^+$; ESI-HRMS (+) calcd for $[C_{24}H_{46}N_5O_6P_3{}^{154}Gd]^+$ 747.1870, found 747.1899; r_{1p} = 1.5±0.04 mM^{-1} s^{-1} (H_2O, 60 MHz, 310 K).

35. [Tb.L^3]

An analogous procedure to that described for **[Eu.L^3]** was followed using ethyl ({4-[(5-*tert*-butylpyridin-2-yl)methyl]-7,10-di{[ethoxy(methyl)phosphoryl]methyl}-1,4,7,10-

tetraazacyclododecan-1-yl}methyl)(methyl)phosphinate (45 mg, 0.065 mmol) and $TbCl_3.6H_2O$ (37 mg, 0.098 mmol), to yield a white solid (16 mg). t_R = 8.6 min; ^1H NMR (400 MHz, D_2O) δ -76.6 ($C(CH_3)_3$ major), -77.3 ($C(CH_3)_3$ minor); ESI-LRMS (+) *m/z* 751.8 $[M+H]^+$; ESI-HRMS (+) calcd for $[C_{24}H_{46}N_5O_6P_3{}^{159}Tb]^+$ 752.1914, found 752.1925.

36. [Dy.L^3]

An analogous procedure to that described for **[Eu.L^3]** was followed using ethyl ({4-[(5-*tert*-butylpyridin-2-yl)methyl]-7,10-di{[ethoxy(methyl)phosphoryl]methyl}-1,4,7,10-tetraazacyclododecan-1-yl}methyl)(methyl)phosphinate (45 mg, 0.065 mmol) and $DyCl_3.6H_2O$ (37 mg, 0.098 mmol), to yield a white solid (16 mg). t_R = 8.7 min; ^1H NMR (400 MHz, D_2O) δ -75.1 ($C(CH_3)_3$ major), -78.7 ($C(CH_3)_3$ minor); ESI-LRMS (+) *m/z* 757.8 $[M+H]^+$; ESI-HRMS (+) calcd for $[C_{24}H_{46}N_5O_6P_3{}^{160}Dy]^+$ 753.1913, found 753.1926.

37. [Ho.L^3]

An analogous procedure to that described for **[Eu.L^3]** was followed using ethyl ({4-[(5-*tert*-butylpyridin-2-yl)methyl]-7,10-di{[ethoxy(methyl)phosphoryl]methyl}-1,4,7,10-tetraazacyclododecan-1-yl}methyl)(methyl)phosphinate (45 mg, 0.065 mmol) and $HoCl_3.6H_2O$ (37 mg, 0.098 mmol), to yield a white solid (15 mg). t_R = 9.6 min; ^1H NMR (400 MHz, D_2O) δ -31.9 ($C(CH_3)_3$ major), -33.8 ($C(CH_3)_3$ minor); ESI-LRMS (+) *m/z* 758.7 $[M+H]^+$; ESI-HRMS (+) calcd for $[C_{24}H_{46}N_5O_6P_3{}^{165}Ho]^+$ 758.1964, found 758.1970.

38. [Er.L^3]

An analogous procedure to that described for **[Eu.L^3]** was followed using ethyl ({4-[(5-*tert*-butylpyridin-2-yl)methyl]-7,10-di{[ethoxy(methyl)phosphoryl]methyl}-1,4,7,10-tetraazacyclododecan-1-yl}methyl)(methyl)phosphinate (45 mg, 0.065 mmol) and $ErCl_3.6H_2O$ (37 mg, 0.098 mmol), to yield a white solid (16 mg). t_R = 10.2 min; ^1H NMR (400 MHz, D_2O) δ 38.3 ($C(CH_3)_3$ major), 40.1 ($C(CH_3)_3$ minor); ESI-LRMS (+) *m/z* 758.9 $[M+H]^+$; ESI-HRMS (+) calcd for $[C_{24}H_{46}N_5O_6P_3{}^{164}Er]^+$ 757.1953, found 757.1962.

39. [Tm.L^3]

An analogous procedure to that described for **[Eu.L^3]** was followed using ethyl ({4-[(5-*tert*-butylpyridin-2-yl)methyl]-7,10-di{[ethoxy(methyl)phosphoryl]methyl}-1,4,7,10-tetraazacyclododecan-1-yl}methyl)(methyl)phosphinate (45 mg, 0.065 mmol) and $TmCl_3.6H_2O$ (38 mg, 0.098 mmol), to yield a white solid (16 mg). t_R = 9.3 min; ^{1}H NMR (400 MHz, D_2O) δ 67.2 ($C(CH_3)_3$ major), 68.6 ($C(CH_3)_3$ minor); ESI-LRMS (+) *m/z* 762.5 $[M+H]^+$; ESI-HRMS (+) calcd for $[C_{24}H_{46}N_5O_6P_3{}^{169}Tm]^+$ 762.2003, found 762.2012.

40. [Yb.L^3]

An analogous procedure to that described for **[Eu.L^3]** was followed using ethyl ({4-[(5-*tert*-butylpyridin-2-yl)methyl]-7,10-di{[ethoxy(methyl)phosphoryl]methyl}-1,4,7,10-tetraazacyclododecan-1-yl}methyl)(methyl)phosphinate (45 mg, 0.065 mmol) and $YbCl_3.6H_2O$ (38 mg, 0.098 mmol), to yield a white solid (15 mg). t_R = 9.0 min; ^{1}H NMR (400 MHz, D_2O) δ 116.1, 85.7, 54.4, 51.1 (H_{ax}), 50.7, 50.3 (H_{eq}'), 36.2, 33.5 (H_{eq}), 21.1 (H_{eq}'), 21.1 (H_{eq}), 19.0 (pyH), 16.5 ($C(CH_3)_3$, 12.1, 6.13 (pyH), -9.13, -9.52 (CH_3), -14.1, -14.5, -18.8 (CHPO), -26.4 (CH_3), -27.1, -28.4, -28.9, -30.4 (CHPO'), -40.6, -50.1, -63.4, -76.8 (H_{ax}'); ESI-LRMS (+) *m/z* 767.9 $[M+H]^+$; ESI-HRMS (+) calcd for $[C_{24}H_{46}N_5O_6P_3{}^{170}Yb]^+$ 763.2009, found 763.2007.

41. 5-*tert*-Butyl-2-methyl-4-nitropyridin-1-oxide

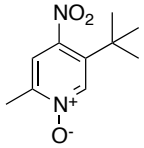

5-*tert*-Butyl-2-methylpyridine 1-oxide (3.20 g, 19.4 mmol) was dissolved in conc. H_2SO_4 (98%, 11.0 mL, 209.5 mmol) and stirred for 10 min at 5 °C. To this was added HNO_3 (70%, 7.0 mL, 161.0 mmol) dropwise and the resulting mixture was heated to 100 °C for 18 h. After this time, the solution was dropped onto ice and stirred for 1 h before the aqueous mixture was extracted with CH_2Cl_2 (3 × 150 mL). The organic layers were combined, dried over $MgSO_4$ and the solvent removed under reduced pressure. The resulting green oil was purified by silica gel column chromatography, eluting with a gradient starting from 100% CH_2Cl_2 to 2% MeOH/ CH_2Cl_2, to yield a bright yellow oil (3.0 g, 74%). R_f (10% MeOH/ CH_2Cl_2) = 0.47; ^{1}H NMR (400 MHz,

$CDCl_3$) δ 8.76 (s, 1H, H^6), 7.58 (s, 1H, H^3), 2.64 (s, 3H, CH_3), 1.35 (s, 9H, $C(CH_3)_3$); ^{13}C NMR (101 MHz, $CDCl_3$) δ 152.5 (C^2), 151.1 (C^5), 142.3 (C^6), 139.3 (C^4), 122.6 (C^3), 35.7 ($\underline{C}(CH_3)_3$), 29.9 ($C(\underline{C}H_3)_3$), 17.5 (CH_3); ESI-LRMS (+) *m/z* 211.1 $[M+H]^+$; ESI-HRMS (+) calcd for $[C_{10}H_{15}N_2O_3]^+$ 211.1083, found 211.1088.

42. 4-Amino-5-*tert*-butyl-2-methylpyridin-1-oxide

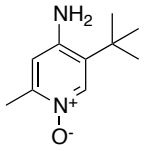

5-*tert*-Butyl-2-methyl-4-nitropyridin-1-oxide (1.9 g, 9.04 mmol) was dissolved in MeOH (50 mL) and Pd/C was added (Pd content 10 %, 190 mg). The vessel was then loaded onto a Parr hydrogenator (pressure 40 bar H_2) and the reaction mixture was agitated for 18 h. After this time, the mixture was filtered before the methanolic solution was evaporated under reduced pressure to yield an orange oil (1.6 g, 98%). R_f (10% MeOH/ CH_2Cl_2) = 0.28; ^1H NMR (400 MHz, CD_3OD) δ 7.95 (s, 1H, H^6), 6.68 (s, 1H, H^3), 3.32 (s, 3H, CH_3), 1.37 (s, 9H, $C(CH_3)_3$); ^{13}C NMR (101 MHz, CD_3OD) δ 152.2 (C^2), 148.0 (C^5), 138.1 (C^6), 129.4 (C^4), 112.2 (C^3), 34.1 ($\underline{C}(CH_3)_3$), 26.8 ($C(\underline{C}H_3)_3$), 16.9 (CH_3); ESI-LRMS (+) *m/z* 181.1 $[M+H]^+$; ESI-HRMS (+) calcd for $[C_{10}H_{17}N_2O]^+$ 181.1341, found 181.1350.

43. (5-*tert*-Butyl-4-nitropyridin-2-yl)methanol

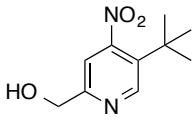

Trifluoroacetic anhydride (20 mL, 143.0 mmol) was added to a solution of 5-*tert*-butyl-2-methyl-4-nitropyridin-1-oxide (3.0 g, 14.3 mmol) in $CHCl_3$ (40 mL). The resulting mixture was heated at 60 ^oC for 18 h under an atmosphere of argon. Reaction completion was confirmed by ^1H NMR spectroscopy before the solvent was removed under reduced pressure. The resulting bright yellow oil was stirred in a mixture of EtOH (20 mL) and H_2O (20 mL) for 2 h. The solution was concentrated (*ca.* 10 mL) and extracted with CH_2Cl_2 (3 × 100 mL), before the organic layers were combined, dried over $MgSO_4$, and the solvent removed under reduced pressure. The resulting yellow oil

was purified by silica gel column chromatography, eluting with a gradient starting from 100% CH_2Cl_2 to 1% MeOH/ CH_2Cl_2 to yield a yellow oil (2.2 g, 73%). R_f (10% MeOH/ CH_2Cl_2) = 0.45; ^{1}H NMR (400 MHz, $CDCl_3$) δ 8.78 (s, 1H, H^6), 7.27 (s, 1H, H^3), 4.79 (s, 2H, CH_2), 4.09 (br s, 1H, OH), 1.40 (s, 9H, $C(CH_3)_3$); ^{13}C NMR (101 MHz, $CDCl_3$) δ 160.1 (C^2), 156.9 (C^5), 150.3 (C^6), 133.7 (C^4), 114.0 (C^3), 63.9 ($\underline{C}H_2$), 34.7 ($\underline{C}(CH_3)_3$), 30.5 ($C(\underline{C}H_3)_3$); ESI-LRMS (+) *m/z* 211.52 $[M+H]^+$; ESI-HRMS (+) calcd for $[C_{10}H_{15}N_2O_3]^+$ 211.1083, found 211.1087.

44. (4-Amino-5-*tert*-butyl-pyridin-2-yl)methanol

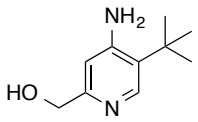

(5-*tert*-Butyl-4-nitropyridin-2-yl)methanol (600 g, 2.90 mmol) was dissolved in MeOH (10 mL) and to this was added Pd/C (0.18 g). The reaction vessel was degassed three times using a vacuum and a H_2 balloon, until a positive pressure of H_2 was obtained. The resulting solution was stirred at rt for 3 h before the reaction mixture was filtered. The resulting yellow oil was dissolved in CH_2Cl_2 (10 mL), before being washed with H_2O (3 × 10 mL). The aqueous layers were combined and the solvent removed under reduced pressure to yield a yellow oil (300 mg, 57 %). ^{1}H NMR (400 MHz, CD_3OD) δ 7.88 (s, 1H, H^6), 6.81 (s, 1H, H^3), 4.64 (s, 2H, CH_2), 1.38 (s, 9H, $C(CH_3)_3$); ^{13}C NMR (101 MHz, CD_3OD) δ 159.9 (C^5), 152.7 (C^2), 137.2 (C^6), 128.6 (C^4), 107.9 (C^3), 60.2 (CH_2), 34.0 ($\underline{C}(CH_3)_3$), 28.4 ($C(\underline{C}H_3)_3$); ESI-LRMS (+) *m/z* 181.9 $[M+H]^+$; ESI-HRMS (+) calcd for $[C_{10}H_{17}N_2O]^+$ 181.1341, found 181.1332.

45. (5-*tert*-Butyl-4-nitropyridin-2-yl)methyl methanesulfonate

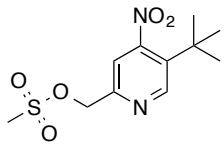

(5-*tert*-Butyl-4-nitropyridin-2-yl)methanol (0.28 g, 1.32 mmol) was dissolved in dry THF (5 mL) and cooled to 5 ^{o}C. Triethylamine (0.46 mL, 3.30 mmol) and mesyl chloride (0.26 mL, 3.30 mmol) were added dropwise. After addition, the reaction mixture was allowed to warm to rt and stirred for 20 min before the solvent was

removed under reduced pressure. The residue was dissolved in brine (15 mL) and extracted with CH_2Cl_2 (3 × 10 mL). The organic layers were combined, dried over $MgSO_4$, and the solvent removed under reduced pressure to yield an orange oil, which was used immediately (0.38 g, 99 %). R_f (10% MeOH/ CH_2Cl_2) = 0.75; ^{1}H NMR (600 MHz, $CDCl_3$) δ 8.77 (s, 1H, H^6), 7.28 (s, 1H, H^3), 5.23 (s, 2H, CH_2), 3.04 (s, 3H, CH_3), 1.32 (s, 9H, $C(CH_3)_3$); ESI-LRMS (+) *m/z* 289.11 $[M+H]^+$; ESI-HRMS (+) calcd for $[C_{11}H_{17}N_2O_5S]^+$ 289.0858, found 289.0854.

46. *tert*-Butyl-2,2',2''-(10-((5-*tert*-butyl-4-nitropyridin-2-yl)methyl)-1,4,7,10-tetraazacyclododecane-1,4,7-triyl)triacetate

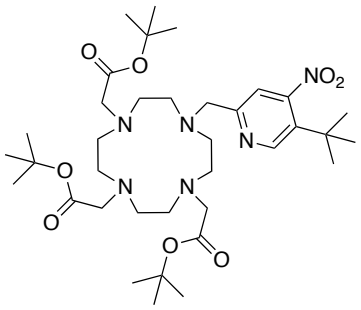

1,4,7-Tris(*tert*-butoxycarbonylmethyl)-1,4,7,10-tetraazacyclododecane (0.61 g, 1.20 mmol) was dissolved in anhydrous MeCN (5 mL) and to this was added K_2CO_3 (0.33 g, 2.40 mmol). (5-*tert*-Butyl-4-nitropyridin-2-yl)methyl methanesulfonate (0.38 g, 1.32 mmol) was added dropwise as a solution in MeCN (5 mL). The resulting mixture was heated at 60 ^{o}C for 18 h, under argon. The reaction mixture was cooled and filtered before the solvent was removed under reduced pressure. The resulting orange oil was purified by silica gel column chromatography, eluting with a gradient starting from 100% CH_2Cl_2 to 3% MeOH/ CH_2Cl_2 to yield a yellow oil (0.3 g, 32%). R_f (10% MeOH/ CH_2Cl_2) = 0.46; ^{1}H NMR (200 MHz, $CDCl_3$) δ 8.49 (s, 1H, H^6), 7.05 (s, 1H, H^3), 3.84 (br m, 4H, NCH_2COO^tBu/cyclen CH_2/NCH_2py), 3.04 (br m, 8H, NCH_2-COO^tBu/cyclen CH_2/NCH_2py), 2.29 (br m, 12H, NCH_2COO^tBu/cyclen CH_2/NCH_2py), 1.45 (s, 18H, $COOC(C\underline{H}_3)_3$), 1.43 (br s, 9H, $pyC(C\underline{H}_3)_3$), 1.21 (s, 9H, $COOC(C\underline{H}_3)_3$); ^{13}C NMR (150 MHz, $CDCl_3$) δ 173.0 ($\underline{C}OO(CH_3)_3$), 169.5 ($\underline{C}OO(CH_3)_3$), 159.6 (C^5), 156.8 (C^2), 150.1 (C^6), 133.2 (C^4), 115.5 (C^3), 82.4 ($py\underline{C}(CH_3)_3$), 82.2 ($COO\underline{C}(CH_3)_3$), 82.1 ($COO\underline{C}(CH_3)_3$), 61.6 (cyclen CH_2), 58.1 ($pyCH_2$), 55.4 (cyclen CH_2), 53.6 (cyclen CH_2), 52.1 (cyclen CH_2), 34.5 ($pyC(\underline{C}H_3)_3$), 30.5 ($COOC(\underline{C}H_3)_3$), 28.2 ($COOC(\underline{C}H_3)_3$);

ESI-LRMS (+) *m/z* 706.99 $[M+H]^+$; ESI-HRMS (+) calcd for $[C_{36}H_{63}N_6O_8]^+$ 707.4707, found 707.4700.

47. Dysprosium(III) complex of 1,4,7-tris(acetic acid)-10-((5-*tert*-butyl-4-nitropyridin-2-yl)methyl)-1,4,7,10-tetraazacyclododecane

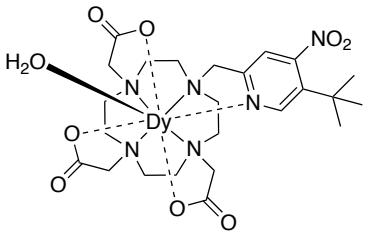

tert-Butyl-2,2',2''-(10-((5-*tert*-butyl-4-nitropyridin-2-yl)methyl)-1,4,7,10-tetraazacyclododecane-1,4,7-triyl)triacetate (17 mg, 0.03 mmol) was dissolved in CH_2Cl_2 (1 mL) and to this was added TFA (1 mL). The resulting mixture was stirred at rt for 18 h, before the solvent was removed under reduced pressure. The resulting yellow residue was repeatedly washed with CH_2Cl_2 (3 × 1 mL). Deprotection was confirmed by ESI-LRMS (+) (*m/z* 530.02 $[M+H]^+$; ESI-HRMS (+) calcd for $[C_{24}H_{39}N_6O_8]^+$ 539.2829, found 539.2841) and ^{1}H NMR spectroscopy. The residue was dissolved in H_2O (2 mL) and the pH adjusted to 5.5. To this was added $DyCl_3.6H_2O$ (16 mg, 0.04 mmol) and the resulting mixture was stirred at 70 ^oC for 18 h, before the solvent was removed under reduced pressure. The resulting white solid was purified by reverse-phase HPLC (10-100% MeOH in H_2O over 10 min; t_R = 5.8 min) to yield an off-white solid (6 mg). ^{1}H NMR (400 MHz, D_2O) δ -28.0 ($C(CH_3)_3$); ESI-LRMS (+) *m/z* 699.5 $[M+H]^+$; ESI-HRMS (+) calcd for $[C_{24}H_{36}N_6O_8{}^{160}Dy]^+$ 696.1847, found 696.1860.

48. Dysprosium(III) complex of 1,4,7-tris(acetic acid)-10-((5-*tert*-butyl-4-dimethylaminopyridin-2-yl)methyl)-1,4,7,10-tetraazacyclododecane, [Dy.L^4(H_2O)]

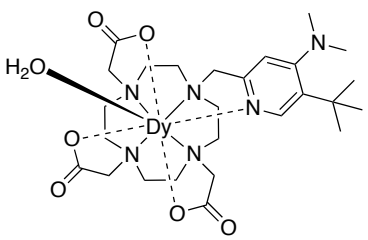

The dysprosium(III) complex of 1,4,7-tris(acetic acid)-10-((5-tert-butyl-4-nitropyridin-2-yl)methyl)-1,4,7,10-tetraazacyclododecane, ***47*** (6.3 mg, 0.001 mmol) was dissolved in dimethylamine (1 mL, 5.6 M in EtOH) and the resulting solution was stirred at 30 ^{o}C for 4 h. The solution was neutralised using acetic acid and the solvent was removed under reduced pressure. The resulting yellow glassy solid was purified by reverse-phase HPLC (10-100% MeOH in H_2O over 10 min; t_R = 5.8 min) to yield a white solid (3 mg). ^{1}H NMR (400 MHz, D_2O) δ -8.1 (NCH_3), -19.3 (NCH_3), -28.4 ($C(CH_3)_3$); ESI-LRMS (+) *m/z* 698.7 $[M+H]^+$; ESI-HRMS (+) calcd for $[C_{26}H_{42}N_6O_6{}^{160}Dy]^+$ 694.2418, found 694.2444.

49. (4-Amino-5-*tert*-butyl-pyridin-2-yl)methyl acetate

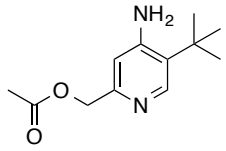

K_2CO_3 (0.55 g, 4.00 mmol) was added to a stirred solution of (4-amino-5-*tert*-butyl-pyridin-2-yl)methanol (0.30 g, 1.67 mmol) in H_2O (3 mL). After 5 min, acetic anhydride (1.56 mL, 16.7 mmol) was added as a solution in dioxane (3 mL) and the resulting mixture was stirred at rt for 30 min. The dioxane was removed under reduced pressure and the aqueous layer extracted with CH_2Cl_2 (3 × 15 mL). The organic layers were combined, dried over $MgSO_4$ and the solvent was removed under reduced pressure. The resulting yellow oil was purified by silica gel column chromatography, eluting with a gradient starting from 100% CH_2Cl_2 to 5% MeOH/ CH_2Cl_2, to yield a yellow oil (0.19 g, 50%). R_f (10% MeOH/ CH_2Cl_2) = 0.18; ^{1}H NMR (700 MHz, $CDCl_3$) δ 8.14 (s, 1H, H^6), 6.67 (s, 1H, H^3), 5.40 (br s, 2H, NH_2), 5.07 (s, 2H, CH_2), 2.09 (s, 3H, CH_3), 1.35 (s, 9H, $C(CH_3)_3$); ^{13}C NMR (176 MHz, $CDCl_3$) δ 170.7 (CO), 154.2 (C^4), 150.9 (C^2), 143.6 (C^6), 127.1 (C^5), 109.5 (C^3), 64.4 (CH_2), 33.1 ($\underline{C}(CH_3)_3$), 28.9 ($C(\underline{C}H_3)_3$), 20.9 (CH_3); ESI-LRMS (+) *m/z* 223.0 $[M+H]^+$; ESI-HRMS (+) calcd for $[C_{12}H_{19}N_2O_2]^+$ 223.1447, found 223.1499.

50. (5-*tert*-Butyl-4-acetamidopyridin-2-yl)methyl acetate

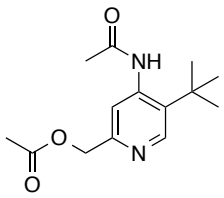

Acetic anhydride (1.1 mL, 11.1 mmol) and triethylamine (0.56 mL, 5.05 mmol) were added to a stirred solution of (4-amino-5-*tert*-butyl-pyridin-2-yl)methyl acetate (0.19 mg, 0.84 mmol) in anhydrous CH_2Cl_2 (3 mL) and the resulting solution stirred at rt for 18 h. The mixture was washed with Na_2CO_3 (sat. aq. solution, 15 mL) and extracted with CH_2Cl_2 (3 × 15 mL). The organic phases were combined, dried over $MgSO_4$ and the solvent removed under reduced pressure. The resulting brown oil was purified by silica gel column chromatography, eluting with a gradient starting from 100% CH_2Cl_2 to 2% MeOH/ CH_2Cl_2, to yield an off-white solid (0.12 mg, 53%). R_f (10% MeOH/ CH_2Cl_2) = 0.53; m.p. 138-140 ^oC; ^1H NMR (700 MHz, $CDCl_3$) δ 8.53 (s, 1H, H^6), 8.06 (br s, 1H, NH), 7.50 (s, 1H, H^3), 5.13 (s, 2H, CH_2), 2.21 (s, 3H, NCOC$\underline{H}_3$), 2.12 (s, 3H, OCOC$\underline{H}_3$), 1.43 (s, 9H, C(C$\underline{H}_3$)$_3$); ^{13}C NMR (176 MHz, $CDCl_3$) δ 170.7 (OCO), 167.9 (NCO), 154.7 (C^2), 148.0 (C^6), 143.7 (C^4), 131.9 (C^5), 115.4 (C^3), 66.5 (CH_2), 33.2 ($\underline{C}(CH_3)_3$), 30.4 (C($\underline{C}H_3$)$_3$), 25.1 (NCO$\underline{C}H_3$), 20.8 (OCO$\underline{C}H_3$); ESI-LRMS (+) *m/z* 265.7 $[M+H]^+$; ESI-HRMS (+) calcd for $[C_{14}H_{21}N_2O_3]^+$ 265.1552, found 265.1546; Anal Calcd (%) for $C_{10}H_{15}INO$: C, 63.62; H, 7.63; N, 10.60, found: C, 63.58; H, 7.69; N, 10.52.

51. *N*-[5-*tert*-Butyl-2-(hydroxymethyl)pyridine-4-yl]acetamide

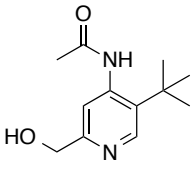

(5-*tert*-Butyl-4-acetamidopyridin-2-yl)methyl acetate (117 mg, 0.44 mmol) was dissolved in anhydrous EtOH (5 mL) and purged with argon for 10 min, before sodium metal (~10 mg) was added. The resulting solution was stirred at rt for 1 h, under an atmosphere of argon. The solvent was removed under reduced pressure and the residue dissolved in CH_2Cl_2 (10 mL). This was washed with H_2O (10 mL), which was

subsequently neutralised. The aqueous layer was washed with CH_2Cl_2 (3 × 10 mL), before the organic layers were combined, dried over $MgSO_4$ and the solvent removed under reduced pressure to yield a colourless oil (75 mg, 77%). ^{1}H NMR (400 MHz, $CDCl_3$) δ 8.50 (s, 1H, H^6), 7.98 (br s, 1H, H^3), 7.50 (br s, 1H, NH), 4.70 (s, 2H, CH_2), 2.23 (s, 3H, CH_3), 1.46 (s, 9H, $C(CH_3)_3$); ^{13}C NMR (151 MHz, $CDCl_3$) δ 168.1 (NCO), 158.5 (C^2), 147.2 (C^6), 143.7 (C^4), 131.6 (C^5), 113.9 (C^3), 64.0 (CH_2), 33.3 ($\underline{C}(CH_3)_3$), 30.6 ($C(\underline{C}H_3)_3$), 25.3 ($NCO\underline{C}H_3$); ESI-LRMS (+) *m/z* 223.6 $[M+H]^+$; ESI-HRMS (+) calcd for $[C_{12}H_{19}N_2O_2]^+$ 223.1447, found 223.1458.

52. (5-*tert*-Butyl-4-acetamidopyridin-2-yl)methyl methanesulfonate

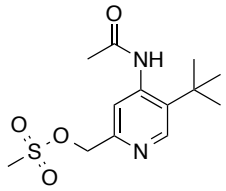

N-[5-*tert*-Butyl-2-(hydroxymethyl)pyridine-4-yl]acetamide (75 mg, 0.34 mmol) was dissolved in dry THF (3 mL) and cooled to 5 ^{o}C. Triethylamine (70 μL, 0.51 mmol) and mesyl chloride (32 μL, 0.41 mmol) were added dropwise. After addition, the reaction mixture was allowed to warm to rt and stirred for 30 min before the solvent was removed under reduced pressure. The residue was dissolved in brine (10 mL) and extracted with CH_2Cl_2 (3 × 10 mL). The organic layers were combined, dried over $MgSO_4$, and the solvent removed under reduced pressure to yield an orange oil, which was used immediately (102 mg, quant.). ^{1}H NMR (400 MHz, $CDCl_3$) δ 8.35 (s, 1H, H^6), 7.60 (s, 1H, H^3), 7.55 (br s, 1H, NH), 5.34 (s, 2H, CH_2), 2.99 (s, SCH_3), 2.21 (s, 3H, CH_3), 1.47 (s, 9H, $C(CH_3)_3$); ESI-LRMS (+) *m/z* 301.0 $[M+H]^+$; ESI-HRMS (+) calcd for $[C_{13}H_{21}N_2O_4S]^+$ 301.1222, found 301.1231.

53. *tert*-Butyl-2-2'-2''-(10-{[4-acetylamino-5-(*tert*-butyl)-2-pyridyl]methyl}-1,4,7,10-tetrazacyclododecane-1,4,7-triacetate

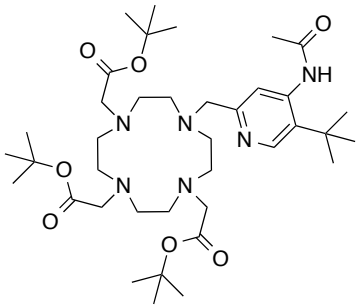

1,4,7-Tris(*tert*-butoxycarbonylmethyl)-1,4,7,10-tetraazacyclododecane (175 mg, 0.34 mmol) was dissolved in anhydrous MeCN (2 mL) and to this was added K_2CO_3 (94 mg, 0.68 mmol). (5-*tert*-Butyl-4-acetamidopyridin-2-yl)methyl methanesulfonate (102 mg, 0.34 mmol) was then added dropwise as a solution in anhydrous MeCN (3 mL). The resulting mixture was heated at 70 ^{o}C for 5 h, under argon. The reaction mixture was cooled and filtered before the solvent was removed under reduced pressure. The resulting yellow oil was purified by silica gel column chromatography, eluting with a gradient starting from 100% CH_2Cl_2 to 1% MeOH/ CH_2Cl_2 to yield a colourless oil (87 mg, 36%). R_f (10% MeOH/ CH_2Cl_2) = 0.45; ^{1}H NMR (400 MHz, $CDCl_3$) δ 8.88 (br s, 1H, NH), 8.18 (s, 1H, H^6), 7.41 (s, 1H, H^3), 3.17-3.91 (br m, 4H, NCH_2COO^tBu/cyclen CH_2/NCH_2py), 2.79-3.13 (br m, 8H, NCH_2COO^tBu/cyclen CH_2/NCH_2py), 2.37-2.77 (br m, 8H, NCH_2COO^tBu/cyclen CH_2/NCH_2py), 2.32 (s, 3H, CH_3), 2.17-2.30 (br m, 4H, NCH_2COO^tBu/cyclen CH_2/NCH_2py), 1.45 (s, 9H, $COOC(C\underline{H}_3)_3$), 1.37 (s, 9H, $pyC(C\underline{H}_3)_3$), 1.35 (br s, 18H, $COOC(C\underline{H}_3)_3$); ^{13}C NMR (176 MHz, $CDCl_3$) δ 172.4 ($\underline{C}OO(CH_3)_3$), 170.1 ($N\underline{C}O$), 156.5 (C^2), 147.6 (C^6), 144.4 (C^5), 136.6 (C^4), 121.1 (C^3), 58.4 ($py\underline{C}H_2$), 56.6, 55.3, 53.5, 50.5 (cyclen CH_2), 33.6 ($py\underline{C}(CH_3)_3$), 30.9 ($COO\underline{C}(CH_3)_3$), 28.0 ($pyC(\underline{C}H_3)_3$), 27.9 ($COOC(\underline{C}H_3)_3$), 24.8 (CH_3); ESI-LRMS (+) *m/z* 719.0 $[M+H]^+$; ESI-HRMS (+) calcd for $[C_{38}H_{67}N_6O_7]^+$ 719.5071, found 719.5052.

54. Dysprosium(III) complex of 1,4,7-tris(acetic acid)-10-{[4-acetylamino-5-(*tert*-butyl)-2-pyridyl]methyl}-1,4,7,10-tetrazacyclododecane, [Dy.L^5(H_2O)]

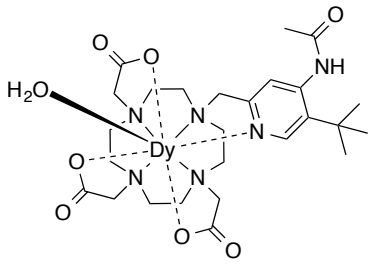

tert-Butyl-2-2'-2''-(10-{[4-acetylamino-5-(*tert*-butyl)-2-pyridyl]methyl}-1,4,7,10-tetrazacyclododecane-1,4,7-triacetate (13 mg, 0.02 mmol) was dissolved in CH_2Cl_2 (1 mL) and to this was added TFA (1 mL). The resulting mixture was stirred at rt for 18 h, before the solvent was removed under reduced pressure. The resulting residue was repeatedly washed with CH_2Cl_2 (3 × 1 mL). Deprotection was monitored by ESI-LRMS (+) (*m/z* 551.0 $[M+H]^+$; ESI-HRMS (+) calcd for $[C_{26}H_{43}N_6O_7]^+$ 551.3193, found 551.3184) and ^{1}H NMR spectroscopy. The residue was dissolved in H_2O (2.5 mL) and the pH adjusted to 5.5. To this was added $DyCl_3.6H_2O$ (9 mg, 0.02 mmol) and the resulting mixture was stirred at 90 ^oC for 18 h. The solvent was removed under reduced pressure and the resulting white solid was purified by reverse-phase HPLC (10-100% MeOH in H_2O over 10 min; t_R = 5.7 min) to yield an off-white solid (5 mg). ^{1}H NMR (400 MHz, D_2O, pD 6.7) δ -7.7 ($COCH_3$, major), -11.4 (($C(CH_3)_3$, minor), -23.3 (($C(CH_3)_3$, major), -33.2 ($COCH_3$, minor); ESI-LRMS (+) *m/z* 711.0 $[M+H]^+$; ESI-HRMS (+) calcd for $[C_{26}H_{40}N_6O_7{}^{160}Dy]^+$ 708.2211, found 708.2197.

55. 1-Methoxy-2-methyl-5-*tert*-butylpyridinium methyl sulfate

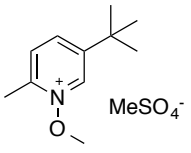

Dimethyl sulfate (2 mL, 17.1 mmol) was added slowly to 5-*tert*-butyl-2-methylpyridin-1-oxide (0.85 g, 5.15 mmol). The solution was heated at 80 °C for 5 h, before being stirred at rt for 18 h. The solvent was removed under reduced pressure to yield a brown oil, which was used without purification (0.92 g, 99%). R_f (10% MeOH/ CH_2Cl_2) = 0.18; ^{1}H NMR (400 MHz, $CDCl_3$) δ 8.71 (d, ^4J = 2, 1H, H^6), 8.36 (dd, ^3J = 8, ^4J = 2, 1H, H^4), 7.94 (d, ^3J = 8, 1H, H^3), 4.41 (s, 3H, OCH_3), 2.83 (s, 3H, CH_3), 1.40 (s, 9H,

$C(C\underline{H}_3)_3$); ^{13}C NMR (101 MHz, $CDCl_3$) δ 152.1 (C^2), 150.5 (C^6), 142.8 (C^5), 137.2 (C^4), 130.4 (C^3), 69.2 (OCH_3), 34.9 ($\underline{C}(CH_3)_3$), 30.2 ($C(\underline{C}H_3)$), 16.8 (CH_3); ESI-LRMS (+) *m/z* 180.5 $[M+H]^+$; ESI-HRMS (+) calcd for $[C_{11}H_{18}NO]^+$ 180.1388, found 180.1390.

56. Diethyl[2-methyl-5-(*tert*-butyl)-6-pyridyl]phosphonate

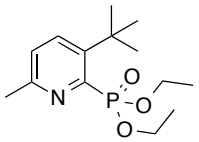

1-Methoxy-2-methyl-5-*tert*-butylpyridinium methyl sulfate (0.92 g, 5.10 mmol) and sodio-diethylphosphite (1.63 g, 10.2 mmol) were dissolved in diethylphosphite (10 mL). The resulting solution was heated at 60 °C for 18 h, before the solvent was removed under reduced pressure. The resulting yellow solid was dissolved in H_2O (50 mL) and extracted with CH_2Cl_2 (3 × 50 mL). The organic layers were dried over $MgSO_4$ and the solvent removed under reduced pressure. The resulting yellow oil was purified by silica gel column chromatography, eluting with a gradient starting from 100% CH_2Cl_2 to 4% MeOH/ CH_2Cl_2 to yield a pale yellow oil (170 mg, 12%). R_f (10 % MeOH/ CH_2Cl_2) = 0.64; ^1H NMR (700 MHz, $CDCl_3$) δ 7.71 (dd, $^3J_{HH}$ = 8, $^4J_{HP}$ = 8, 1H, H^4), 7.14 (dd, $^3J_{HH}$ = 8, $^5J_{HP}$ = 3, 1H, H^3), 4.22-4.26 (m, ^3J = 7, 4H, PCH_2), 2.52 (s, 3H, $pyCH_3$), 1.54 (s, 9H, $C(CH_3)_3$), 1.35 (t, ^3J = 7, 6H, $CH_2C\underline{H}_3$); ^{31}P NMR (162 MHz, $CDCl_3$) δ 11.6-11.9 (m, $^3J_{PH}$ = 7); ^{13}C NMR (176 MHz, $CDCl_3$) δ 154.3 (d, $^3J_{CP}$ = 22, C^2), 149.9 (d, $^1J_{CP}$ = 226, C^6), 148.6 (s, $^2J_{CP}$ = 30, C^5), 135.4 (d, $^3J_{CP}$ = 13, C^4), 124.9 (s, $^4J_{CP}$ = 4, C^3), 62.9 (d, $^3J_{PH}$ = 7, PCH_2), 35.3 ($\underline{C}(CH_3)_3$), 31.6 ($C(\underline{C}H_3)$), 16.4 (d, $^4J_{PH}$ = 7, CH_3); ESI-LRMS (+) *m/z* 286.2 $[M+H]^+$; ESI-HRMS (+) calcd for $[C_{14}H_{25}NO_3P]^+$ 286.1572, found 286.1574.

57. 5-(*tert*-Butyl)-2-methyl-4-nitropyridine

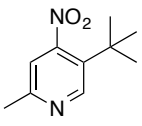

5-*tert*-Butyl-2-methyl-4-nitropyridin-1-oxide (1.9 g, 9.04 mmol) was dissolved in anhydrous $CHCl_3$ (50 mL) and PBr_3 (2.6 mL, 27.1 mmol) was added dropwise. The

mixture was stirred at 60 °C for 18 h under argon, before the solvent was removed under reduced pressure. The resulting brown residue was quenched cautiously using NaOH (aq. 2 M, 50 mL) and the resulting solution was extracted with CH_2Cl_2 (3 × 50 mL). The organic layers were combined, dried over $MgSO_4$ and the solvent removed under reduced pressure. The resulting yellow oil was purified by silica gel column chromatography, eluting with a gradient starting from 100% CH_2Cl_2 to 2% MeOH/ CH_2Cl_2 to yield a yellow oil (0.98 mg, 56%). R_f (10% MeOH/ CH_2Cl_2) = 0.59; ^{1}H NMR (400 MHz, $CDCl_3$) δ 8.74 (s, 1H, H^6), 7.03 (s, 1H, H^3), 2.59 (s, 3H, CH_3), 1.41 (s, 9H, $C(C\underline{H}_3)_3$); ^{13}C NMR (101 MHz, $CDCl_3$) δ 158.3 (C^2), 156.3 (C^5), 150.6 (C^6), 131.6 (C^4), 115.9 (C^3), 34.3 ($\underline{C}(CH_3)_3$), 30.4 ($C(\underline{C}H_3)_3$), 23.6 (CH_3); ESI-LRMS (+) *m/z* 195.5 $[M+H]^+$; ESI-HRMS (+) calcd for $[C_{10}H_{15}N_2O_2]^+$ 195.1134, found 195.1135.

58. 4-Bromo-5-(*tert*-butyl)-2-methylpyridine

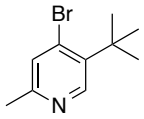

5-(*tert*-Butyl)-2-methyl-4-nitropyridine (300 mg, 1.55 mmol) was dissolved in acetyl bromide (10 mL, 140.0 mmol) and the resulting mixture was stirred at 70 °C for 18 h. The resulting brown solution was cooled and dropped cautiously onto cold MeOH (50 mL). The solvent was removed under reduced pressure and the resulting brown solid was purified by silica gel column chromatography, eluting with a gradient starting from 100% CH_2Cl_2 to 2% MeOH/ CH_2Cl_2 to yield an orange oil (320 mg, 91%). R_f (10 % MeOH/ CH_2Cl_2) = 0.58; ^{1}H NMR (400 MHz, CD_3OD) δ 8.52 (s, 1H, H^6), 8.25 (s, 1H, H^3), 2.70 (s, 3H, CH_3), 1.59 (s, 9H, $C(C\underline{H}_3)_3$); ^{13}C NMR (101 MHz, CD_3OD) δ 153.2 (C^5), 146.6 (C^6), 144.6 (C^2), 141.1 (C^4), 135.6 (C^3), 37.4 ($\underline{C}(CH_3)_3$), 29.0 ($C(\underline{C}H_3)_3$), 18.8 (CH_3); ESI-LRMS (+) *m/z* 228.3 $[M+H]^+$; ESI-HRMS (+) calcd for $[C_{10}H_{15}N^{79}Br]^+$ 228.0388, found 228.0360.

59. 5-*tert*-Butyl-4-iodo-2-methylpyridin-1-oxide

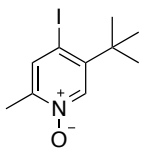

To a cold solution of 4-amino-5-*tert*-butyl-2-methylpyridin-1-oxide (1.6 g, 8.88 mmol) and HBF_4 (2.3 mL, 17.8 mmol) in H_2O (40 mL) was added a dropwise solution of $NaNO_2$ (1.2 g, 17.8 mmol) in H_2O (5 mL). Potassium iodide (2.0 g, 12.4 mmol) was slowly added to the suspension, over several portions. The reaction mixture was allowed to stir at rt for 5 min before being heated at 60 ^oC for 30 min. The mixture was cooled to rt and the pH adjusted to 10 with KOH. The organics were extracted with CH_2Cl_2 (3 × 100 mL) and washed with $NaHCO_3$ (sat. aq. solution, 100 mL) before being dried over $MgSO_4$ and the solvent removed under reduced pressure. The resulting brown oil was purified by silica gel column chromatography, eluting with a gradient starting from 100% CH_2Cl_2 to 2% MeOH/ CH_2Cl_2 to yield an orange solid (0.8 g, 31%). R_f (10 % MeOH/ CH_2Cl_2) = 0.37; m.p. 153-155 ^oC; ^1H NMR (400 MHz, $CDCl_3$) δ 8.23 (s, 1H, H^6), 7.80 (s, 1H, H^3), 2.41 (s, 3H, CH_3), 1.48 (s, 9H, $C(CH_3)_3$); ^{13}C NMR (101 MHz, $CDCl_3$) δ 152.5 (C^2), 146.5 (C^5), 139.8 (C^6), 138.4 (C^4), 122.2 (C^3), 35.9 ($\underline{C}(CH_3)_3$), 29.1 ($C(\underline{C}H_3)_3$), 16.7 (CH_3); ESI-LRMS (+) *m/z* 291.9 $[M+H]^+$; ESI-HRMS (+) calcd for $[C_{10}H_{15}{}^{127}INO]^+$ 292.0198, found 292.0208; Anal Calcd (%) for $C_{10}H_{15}INO$: C, 41.26; H, 4.85; N, 4.81, found: C, 41.11; H, 4.78; N, 4.79.

60. (5-*tert*-Butyl-4-iodopyridin-2-yl)methyl acetate

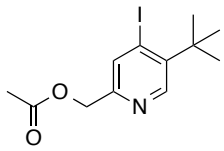

5-*tert*-Butyl-4-iodo-2-methylpyridin-1-oxide (0.8 g, 2.75 mmol) was dissolved in acetic anhydride (10 mL) and the solution was heated to 75 °C for 3 h. The solvent was removed under reduced pressure and the resulting orange oil was purified by silica gel column chromatography, eluting with a gradient starting from 100% CH_2Cl_2 to 2% MeOH/ CH_2Cl_2 to yield an orange oil (0.74 g, 81%). R_f (10 % MeOH/ CH_2Cl_2) = 0.62; ^1H NMR (400 MHz, $CDCl_3$) δ 8.53 (s, 1H, H^6), 7.94 (s, 1H, H^3), 5.11 (s, 2H, CH_2), 2.16 (s, 3H, CH_3), 1.54 (s, 9H, $C(CH_3)_3$); ^{13}C NMR (101 MHz, $CDCl_3$) δ 170.7 (CO), 158.5 (C^2), 147.6 (C^5), 145.0 (C^6), 136.3 (C^4), 107.0 (C^3), 65.5 (CH_2), 35.9 ($\underline{C}(CH_3)_3$), 29.6 ($C(\underline{C}H_3)_3$), 21.0 (CH_3); ESI-LRMS (+) *m/z* 333.8 $[M+H]^+$; ESI-HRMS (+) calcd for $[C_{12}H_{17}{}^{127}INO_2]^+$ 334.0304, found 334.0307.

61. [5-*tert*-Butyl-4-(diethoxyphosphoryl)pyridin-2-yl]methyl acetate

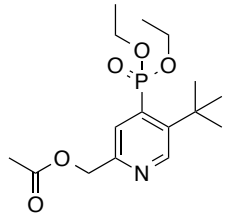

(5-*tert*-Butyl-4-iodopyridin-2-yl)methyl acetate (425 mg, 1.28 mmol) was dissolved in triethylphosphite (10 mL, 58.3 mmol). To this was added $Pd(dba)_2$ (73 mg, 10 mol%, 0.128 mmol) and the resulting solution was heated at 120 ^{o}C for 18 h. The solvent was removed by vacuum distillation and the resulting brown oil was purified by silica gel column chromatography, eluting with a gradient starting from 100% CH_2Cl_2 to 1% MeOH/ CH_2Cl_2, to yield a yellow oil (284 mg, 65%). R_f (10% MeOH/ CH_2Cl_2) = 0.56; ^{1}H NMR (400 MHz, $CDCl_3$) δ 8.84 (d, $^4J_{HP}$ = 8, 1H, H^6), 7.80 (d, $^3J_{HP}$ = 16, 1H, H^3), 5.21 (s, 2H, CH_2), 4.05-4.14 (m, $^3J = 7_{HP}$, 4H, $POCH_2$), 2.16 (s, 3H, $pyCH_3$), 1.58 (s, 9H, $C(CH_3)_3$), 1.31-1.37 (m, $^4J = 7_{HP}$, 6H, $POCH_2C\underline{H}_3$); ^{31}P NMR (162 MHz, $CDCl_3$) δ 16.1-16.5 (m, $^3J_{PH}$ = 7); ^{13}C NMR (101 MHz, $CDCl_3$) δ 170.7 (CO), 153.1 (d, $^3J_{CP}$ = 12, C^6), 149.2 (d, $^3J_{CP}$ = 13, C^2), 147.7 (d, $^2J_{CP}$ = 11, C^5), 136.8 (d, $^1J_{CP}$ = 179, C^4), 126.5 (d, $^2J_{CP}$ = 7, C^3), 66.4 (CH_2O), 63.8 (d, $^2J_{PH}$ = 6, $POCH_2$), 36.0 ($\underline{C}(CH_3)_3$), 31.6 ($C(\underline{C}H_3)$), 21.0 (CH_3), 16.3 (d, $^3J_{PH}$ = 6, $POCH_2\underline{C}H_3$); ESI-LRMS (+) *m/z* 344.2 $[M+H]^+$; ESI-HRMS (+) calcd for $[C_{16}H_{27}NO_5P]^+$ 344.1627, found 344.1628.

62. Diethyl [5-*tert*-butyl-2-(hydroxymethyl)pyridin-4-yl]phosphonate

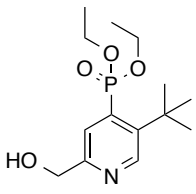

[5-*tert*-Butyl-4-(diethoxyphosphoryl)pyridin-2-yl]methyl acetate (300 mg, 0.87 mmol) was dissolved in anhydrous EtOH (4 mL) and purged with argon for 10 min, before sodium metal (~15 mg) was added. The resulting solution was stirred at rt for 1 h, under an atmosphere of argon. The solvent was removed under reduced pressure and the residue dissolved in CH_2Cl_2 (7 mL). This was washed with H_2O (2 mL), before the aqueous layer was rewashed with CH_2Cl_2 (3 × 7 mL). The organic layers were

combined, dried over $MgSO_4$ and the solvent removed under reduced pressure. The resulting brown oil was purified by silica gel column chromatography, eluting with a gradient starting from 100% CH_2Cl_2 to 2% MeOH/ CH_2Cl_2, to yield a yellow oil (150 mg, 57%). R_f (10% MeOH/ CH_2Cl_2) = 0.48; ^{1}H NMR (400 MHz, $CDCl_3$) δ 8.80 (d, $^4J_{HP}$ = 8, 1H, H^6), 7.79 (d, $^3J_{HP}$ = 15, 1H, H^3), 4.80 (s, 2H, CH_2), 4.07-4.14 (m, $^3J = 7_{HP}$, 4H, $POCH_2$), 2.58 (br s, OH), 1.59 (s, 9H, $C(CH_3)_3$), 1.35 (t, $^4J = 7_{HP}$, 6H, $POCH_2C\underline{H}_3$); ^{31}P NMR (162 MHz, $CDCl_3$) δ 15.8-16.2 (m, $^3J_{PH}$ = 7); ^{13}C NMR (176 MHz, $CDCl_3$) δ 157.3 (d, $^3J_{CP}$ = 11, C^6), 148.1 (d, $^3J_{CP}$ = 13, C^2), 146.7 (d, $^2J_{CP}$ = 11, C^5), 136.5 (d, $^1J_{CP}$ = 179, C^4), 125.3 (d, $^2J_{CP}$ = 7, C^3), 64.2 (CH_2O), 62.7 (d, $^2J_{PH}$ = 6, $POCH_2$), 35.8 (d, $^3J_{CP}$ = 3, $\underline{C}(CH_3)_3$), 31.6 ($C(\underline{C}H_3)$), 16.3 (d, $^3J_{PH}$ = 6, $POCH_2\underline{C}H_3$); ESI-LRMS (+) *m/z* 302.2 $[M+H]^+$; ESI-HRMS (+) calcd for $[C_{14}H_{25}NO_4P]^+$ 302.1521, found 302.1519.

63. [5-*tert*-Butyl-4-(diethoxyphosphoryl)pyridin-2-yl]methyl methane sulfonate

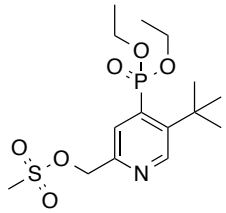

Diethyl [5-*tert*-butyl-2-(hydroxymethyl)pyridin-4-yl]phosphonate (150 mg, 0.50 mmol) was dissolved in anhydrous THF (4 mL) and cooled to 5 ^oC. Triethylamine (140 µL, 1.00 mmol) and mesyl chloride (58 µL, 0.75 mmol) were added dropwise and the resulting solution was stirred at rt for 30 min. The solvent was removed under reduced pressure before the residue was dissolved in brine (5 mL) and extracted with CH_2Cl_2 (3 × 10 mL). The organic layers were combined, dried over $MgSO_4$, and the solvent removed under reduced pressure to yield an orange oil, which was used immediately (176 mg, 93%). R_f (10% MeOH/ CH_2Cl_2) = 0.56; ^{1}H NMR (400 MHz, $CDCl_3$) δ 8.78 (d, $^4J_{HP}$ = 8, 1H, H^6), 7.84 (d, $^3J_{HP}$ = 15, 1H, H^3), 5.26 (s, 2H, CH_2), 4.06-4.16 (m, $^3J_{HP}$ = 6, 4H, $POCH_2$), 3.05 (s, 3H, CH_3), 1.52 (s, 9H, $C(CH_3)_3$), 1.29 (dt, $^3J_{HP}$ = 6, $^4J_{HP}$ = 1, 6H, $POCH_2C\underline{H}_3$); ^{31}P NMR (162 MHz, $CDCl_3$) δ 15.4-15.8 (m, $^3J_{PH}$ = 6); ESI-LRMS (+) *m/z* 380.5 $[M+H]^+$; ESI-HRMS (+) calcd for $[C_{15}H_{27}NO_6PS]^+$ 380.1297, found 380.1308.

64. Diethyl {5-*tert*-butyl-2-[(4,7,10-tri{[ethoxy(methyl)phosphoryl]methyl}-1,4,7,10-tetraazacyclododecan-1-yl)methyl]pyridin-4-yl}phosphonate

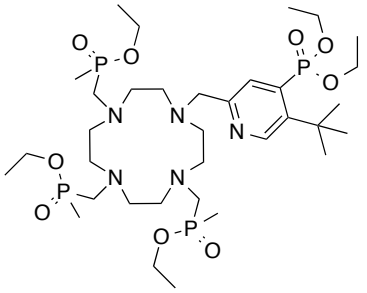

Ethyl[(4,7-di{[ethoxy(methyl)phosphoryl]methyl}-1,4,7,10-tetraazacyclododecane-1-yl)methyl](methyl)phosphinate (540 mg, 1.42 mmol) was dissolved in anhydrous MeCN (5 mL) and to this was added K_2CO_3 (196 mg, 1.42 mmol). [5-*tert*-Butyl-4-(diethoxyphosphoryl)pyridin-2-yl]methyl methane sulfonate (500 mg, 0.94 mmol) was then added dropwise as a solution in anhydrous MeCN (10 mL). The resulting mixture was heated at 70 ^{o}C for 18 h, under argon. The reaction mixture was cooled and the inorganic salts were removed by centrifugation. The solvent was removed under reduced pressure and the resulting red oil was purified by alumina gel column chromatography, eluting with a gradient starting from 100% CH_2Cl_2 to 2% MeOH/ CH_2Cl_2 to yield an orange oil (210 mg, 27%). R_f (10% MeOH/ CH_2Cl_2) = 0.65; ^{1}H NMR (400 MHz, $CDCl_3$) δ 8.73 (d, $^4J_{HP}$ = 8, 1H, H^6), 7.88 (d, $^3J_{HP}$ = 16, 1H, H^3), 4.09-4.16 (m, 4H, $POCH_2$), 3.93-4.05 (m, 6H, $POCH_2$), 3.50-3.74 (m, 8H, NCH_2), 2.53-3.49 (br m, 16H, cyclen CH_2), 1.39-1.54 (m, 18H, $C(CH_3)_3$, PCH_3), 1.20-1.32 (m, 15H, $POCH_2C\underline{H}_3$); ^{31}P NMR (162 MHz, $CDCl_3$) δ 53.5, 52.9, 52.5, 52.4, 52.3, 52.2, 52.0, 51.9, 51.7, 51.5 (NCH_2P, mixture of isomers), 16.6, 15.9, 14.4 (pyP, mixture of isomers); ^{13}C NMR (101 MHz, $CDCl_3$) δ 149.0 (C^2), 136.2 (C^5), 129.5 (C^6), 127.3 (C^4), 111.7 (C^3), 62.5-62.8 (m, $POCH_2$), 59.7-60.3 (m, $POCH_2$), 53.0-55.0 (m, PCH_2N, $pyCH_2$, cyclen CH_2), 36.3 ($\underline{C}(CH_3)_3$), 31.3 ($C(\underline{C}H_3)_3$), 16.6 (d, $^3J_{CP}$ = 6, $POCH_2\underline{C}H_3$), 16.2 (d, $^3J_{CP}$ = 6, $POCH_2\underline{C}H_3$), 13.0-14.9 (m, $P\underline{C}H_3$); ESI-LRMS (+) *m/z* 816.7 $[M+H]^+$; ESI-HRMS (+) calcd for $[C_{34}H_{70}N_5O_9P_4]^+$ 816.4124, found 816.4129.

65. Europium(III) complex of {5-*tert*-butyl-2-[(4,7,10-tri{[hydroxy(methyl)phosphoryl]methyl}-1,4,7,10-tetraazacyclododecan-1-yl)methyl]pyridin-4-yl}phosphonic acid, [Eu.L^6]

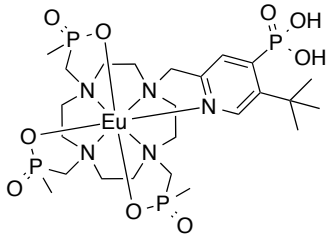

Diethyl {5-*tert*-butyl-2-[(4,7,10-tri{[ethoxy(methyl)phosphoryl]methyl}-1,4,7,10-tetraazacyclododecan-1-yl)methyl]pyridin-4-yl}phosphonate (15 mg, 0.02 mmol) was dissolved in aqueous HCl (6 M, 2 mL) and stirred at 70 ^{o}C for 18 h. Complete ester cleavage was confirmed by ESI-MS (+) (LR: *m/z* 676.6 [M+H]+; HR: *m/z* calcd for $[C_{24}H_{50}N_5O_9P_4]^+$ 676.2559, found 676.2557). The solvent was removed under reduced pressure and the resulting yellow oil was dissolved in H_2O (2 mL). The pH of the solution was adjusted to 5.5 using NaOH and $EuCl_3.6H_2O$ (10 mg, 0.028 mmol) was added. The resulting solution was stirred at 70 ^{o}C for 18 h before the solvent was removed under reduced pressure. The resulting yellow solid was purified by reverse-phase HPLC (10-100% MeOH in H_2O over 10 min; t_R = 7.3 min) to yield a white solid (5 mg). ^{1}H NMR (400 MHz, pD 7.4, $CDCl_3$) δ 3.1 ($C(CH_3)_3$ major), 1.4 ($C(CH_3)_3$ minor); ESI-LRMS (+) *m/z* 825.8 $[M+H]^+$; ESI-HRMS (+) calcd for $[C_{24}H_{47}N_5O_9P_4{}^{151}Eu]^+$ 824.1523, found 824.1549.

66. [Gd.L^6]

An analogous procedure to that described for the synthesis of **[Eu.L^6]** was followed using diethyl {5-*tert*-butyl-2-[(4,7,10-tri{[ethoxy(methyl)phosphoryl]methyl}-1,4,7,10-tetraazacyclododecan-1-yl)methyl]pyridin-4-yl}phosphonate (20 mg, 0.033 mmol) and $GdCl_3.6H_2O$ (14 mg, 0.036 mmol), to yield a white solid (5 mg). t_R = 7.1 min; ESI-LRMS (+) *m/z* 830.4 $[M+H]^+$; ESI-HRMS (+) calcd for $[C_{24}H_{47}N_5O_9P_4{}^{154}Gd]^+$ 827.1533, found 827.1561; r_{1p} = 2.0±0.05 mM^{-1} s^{-1} (H_2O, 60 MHz, 310 K).

67. [Tb.L^6]

An analogous procedure to that described for the synthesis of **[Eu.L^6]** was followed using diethyl {5-*tert*-butyl-2-[(4,7,10-tri{[ethoxy(methyl)phosphoryl]methyl}-1,4,7,10-

tetraazacyclododecan-1-yl)methyl]pyridin-4-yl}phosphonate (20 mg, 0.033 mmol) and $TbCl_3.6H_2O$ (14 mg, 0.037 mmol), to yield a white solid (7 mg). t_R = 7.3; min; ^{1}H NMR (400 MHz, pD 7.4, $CDCl_3$) δ -78.3 ($C(CH_3)_3$ minor), -83.4 ($C(CH_3)_3$ major); ESI-LRMS (+) *m/z* 832.2 $[M+H]^+$; ESI-HRMS (+) calcd for $[C_{24}H_{47}N_5O_9P_4{}^{159}Tb]^+$ 832.1578, found 832.1562.

68. [Dy.L^6]

An analogous procedure to that described for the synthesis of **[Eu.L^6]** was followed using diethyl {5-tert-butyl-2-[(4,7,10-tri{[ethoxy(methyl)phosphoryl]methyl}-1,4,7,10-tetraazacyclododecan-1-yl)methyl]pyridin-4-yl}phosphonate (50 mg, 0.06 mmol) and $DyCl_3.6H_2O$ (10 mg, 0.028 mmol), to yield a white solid (20 mg). t_R = 6.8 min; ^{1}H NMR (400 MHz, pD 7.4, $CDCl_3$) δ -78.3 ($C(CH_3)_3$ major), -81.0 ($C(CH_3)_3$ minor); ^{31}P NMR (162 MHz, $CDCl_3$) δ -38.2 (pyP); ESI-LRMS (+) *m/z* 836.4 $[M+H]^+$; ESI-HRMS (+) calcd for $[C_{24}H_{47}N_5O_9P_4{}^{160}Dy]^+$ 833.1576, found 833.1573.

69. [Er.L^6]

An analogous procedure to that described for the synthesis of **[Eu.L^6]** was followed using diethyl {5-tert-butyl-2-[(4,7,10-tri{[ethoxy(methyl)phosphoryl]methyl}-1,4,7,10-tetraazacyclododecan-1-yl)methyl]pyridin-4-yl}phosphonate (20 mg, 0.033 mmol) and $ErCl_3.6H_2O$ (14 mg, 0.066 mmol), to yield a white solid (9 mg). t_R = 7.0 min; ^{1}H NMR (400 MHz, $CDCl_3$) δ 42.5 ($C(CH_3)_3$ major), 44.2 ($C(CH_3)_3$ minor); ESI-LRMS (+) *m/z* 840.1 $[M+H]^+$; ESI-HRMS (+) calcd for $[C_{24}H_{47}N_5O_9P_4{}^{164}Er]^+$ 837.1616, found 837.1636.

70. [Tm.L^6]

An analogous procedure to that described for the synthesis of **[Eu.L^6]** was followed using diethyl {5-tert-butyl-2-[(4,7,10-tri{[ethoxy(methyl)phosphoryl]methyl}-1,4,7,10-tetraazacyclododecan-1-yl)methyl]pyridin-4-yl}phosphonate (50 mg, 0.06 mmol) and $TmCl_3.6H_2O$ (14 mg, 0.066 mmol), to yield a white solid (20 mg). t_R = 6.9 min; ^{1}H NMR (400 MHz, $CDCl_3$) δ 74.6 ($C(CH_3)_3$ major), 75.5 ($C(CH_3)_3$ minor); ESI-LRMS (+) *m/z* 841.9 $[M+H]^+$; ESI-HRMS (+) calcd for $[C_{24}H_{47}N_5O_9P_4{}^{154}Tm]^+$ 842.1667, found 842.1647.

71. Ethyl 2-{[5-*tert*-butyl-2-(hydroxymethyl)pyridine-4-yl]sulfonyl}acetate[6]

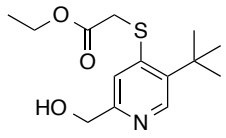

Ethyl thioglycolate (1.4 mL, 12.6 mmol) and NaH (0.3 g, 12.6 mmol) were dissolved in anhydrous DMF (7 mL) and stirred for 10 min at rt. (5-*tert*-Butyl-4-nitropyridin-2-yl)methanol (2.2 g, 10.5 mmol) was added dropwise as a solution in anhydrous DMF (3 mL) and the resulting solution was stirred at rt for 18 h. The solvent was removed under reduced pressure before the resulting red oil was dissolved in H_2O (50 mL) and extracted with ethyl acetate (3 × 70 mL). The organic layers were combined, dried over $MgSO_4$ and the solvent removed under reduced pressure. The resulting orange oil was purified by silica gel column chromatography, eluting with a gradient starting from 100% CH_2Cl_2 to 5% MeOH/ CH_2Cl_2 to yield an orange oil (0.8 g, 26%). R_f (10% MeOH/ CH_2Cl_2) = 0.32; ^{1}H NMR (400 MHz, $CDCl_3$) δ 8.39 (s, 1H, H^6), 7.21 (s, 1H, H^3), 4.68 (s, 2H, OCH_2), 4.18 (q, $^3J_{HH}$ = 7, 2H, $OC\underline{H}_2CH_3$), 3.78 (s, 2H, SCH_2), 1.48 (s, 9H, $C(CH_3)_3$), 1.23 (t, $^3J_{HH}$ = 7, 3H, $CH_2C\underline{H}_3$); ^{13}C NMR (101 MHz, $CDCl_3$) δ 168.5 (CO), 157.5 (C^2), 147.4 (C^5), 145.7 (C^6), 140.5 (C^4), 118.1 (C^3), 64.0 (OCH_2), 61.9 (OCH_2), 53.4 (SCH_2), 35.1 ($\underline{C}(CH_3)_3$), 29.6 ($C(\underline{C}H_3)_3$), 14.0 (CH_3); ESI-LRMS (+) *m/z* 284.9 $[M+H]^+$; ESI-HRMS (+) calcd for $[C_{14}H_{22}NO_3S]^+$ 284.1320, found 284.1330.

72. Ethyl 2-({5-*tert*-butyl-2-[(methanesulfonyloxy)methyl]pyridin-4-yl}sulfanyl)acetate[6]

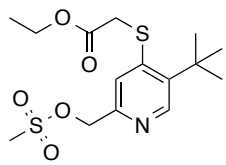

Ethyl 2-{[5-*tert*-butyl-2-(hydroxymethyl)pyridine-4-yl]sulfonyl}acetate (0.14 g, 0.49 mmol) was dissolved in anhydrous THF (4 mL) and cooled to 5 ^{o}C. Triethylamine (90 μL, 0.64 mmol) and mesyl chloride (50 μL, 0.64 mmol) were added dropwise and the resulting solution was stirred at rt for 30 min. The solvent was removed under reduced pressure and the residue dissolved in brine (5 mL) and extracted with CH_2Cl_2 (3 × 15 mL). The organic layers were combined, dried over $MgSO_4$, and the solvent removed

under reduced pressure to yield a red oil, which was used immediately (0.17 g, 96%). R_f (10% MeOH/ CH_2Cl_2) = 0.72; ^{1}H NMR (400 MHz, $CDCl_3$) δ 8.30 (s, 1H, H^6), 7.21 (s, 1H, H^3), 5.08 (s, 2H, OCH_2), 4.02 (q, $^3J_{HH}$ = 7, 2H, $OC\underline{H}_2CH_3$), 3.68 (s, 2H, SCH_2), 2.95 (s, 3H, SCH_3), 1.34 (s, 9H, $C(CH_3)_3$), 1.21 (t, $^3J_{HH}$ = 7, 3H, $CH_2C\underline{H}_3$); ESI-LRMS (+) *m/z* 362.4 $[M+H]^+$; ESI-HRMS (+) calcd for $[C_{15}H_{24}NO_5S_2]^+$ 362.1096, found 362.1114.

73. Ethyl 2-({5-*tert*-butyl-2-[(4,7,10-tri{[ethoxy(methyl)phosphoryl]methyl}-1,4,7,10-tetraazacyclododecan-1-yl)methyl]pyridin-4-yl}sulfanyl)acetate

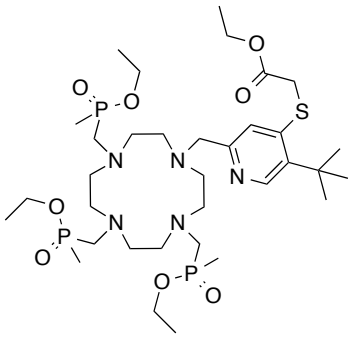

Ethyl[(4,7-di{[ethoxy(methyl)phosphoryl]methyl}-1,4,7,10-tetraazacyclododecane-1-yl)methyl](methyl)phosphinate (220 mg, 0.41 mmol) was dissolved in anhydrous MeCN (4 mL) and to this was added K_2CO_3 (113 mg, 0.82 mmol). Ethyl 2-({5-*tert*-butyl-2-[(methanesulfonyloxy)methyl]pyridin-4-yl}sulfanyl)acetate (170 mg, 0.47 mmol) was then added dropwise as a solution in anhydrous MeCN (4 mL). The resulting mixture was heated at 70 ^oC for 18 h, under argon. The reaction mixture was cooled and the inorganic salts were removed by centrifugation. The solvent was removed under reduced pressure and the resulting red oil was purified by alumina gel column chromatography, eluting with a gradient starting from 100% CH_2Cl_2 to 2% MeOH/ CH_2Cl_2 to yield an orange oil (230 mg, 61%). R_f (10% MeOH/ CH_2Cl_2) = 0.64; ^{1}H NMR (400 MHz, $CDCl_3$) δ 8.45, 8.31 (s, 1H, H^6), 7.34, 7.13 (s, 1H, H^3), 4.05-4.17 (m, 2H, OCH_2), 3.85-4.03 (m, 6H, $POCH_2$), 3.74-3.83 (m, 2H, SCH_2), 2.82-3.17 (m, 8H, PCH_2N, $pyCH_2$), 2.06-2.80 (br m, 16H, cyclen CH_2), 1.41-1.51 (m, 9H, PCH_3), 1.40 (s, 9H, $C(CH_3)_3$), 1.11-1.30 (m, 12H, $POCH_2C\underline{H}_3$, $OCH_2C\underline{H}_3$); ^{31}P NMR (162 MHz, $CDCl_3$) δ 54.0, 53.4, 52.9, 52.7, 52.4, 52.3, 52.2, 52.1, 51.9, 51.7, 51.6, 51.2 (mixture of isomers); ^{13}C NMR (101 MHz, $CDCl_3$) δ 168.6 ($CH_2\underline{C}O$), 155.5 (C^2), 147.3 (C^5), 146.3 (C^6), 140.6 (C^4), 120.3 (C^3), 61.7-61.9 (m, OCH_2), 59.9-60.2 (m, $POCH_2$, SCH_2), 53.6-54.7 (m, PCH_2N, $pyCH_2$), 51.4-52.6 (m, cyclen CH_2), 35.1 ($\underline{C}(CH_3)_3$), 29.6

($C(\underline{C}H_3)_3$), 16.5-16.7 (m, $POCH_2\underline{C}H_3$), 14.1 ($OCH_2\underline{C}H_3$), 12.9-13.9 (m, $P\underline{C}H_3$); ESI-LRMS (+) *m/z* 798.1 $[M+H]^+$; ESI-HRMS (+) calcd for $[C_{34}H_{67}N_5O_8P_3S]^+$ 798.3923, found 798.3939.

74. Gadolinium(III) complex of {[4-({5-*tert*-butyl-4-[(2-ethoxy-2-oxoethyl)sulfanyl]pyridin-2-yl}methyl)-10-{[ethoxy(methyl)phosphoryl]methyl}-7-{[hydroxy(methyl)phosphoryl]methyl}-1,4,7,10-tetraazacyclododecan-1-yl]methyl}(methyl)phosphinic acid, [Gd.L^7]

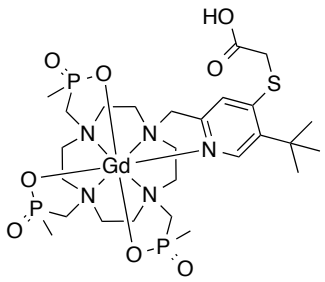

Ethyl 2-({5-*tert*-butyl-2-[(4,7,10-tri{[ethoxy(methyl)phosphoryl]methyl}-1,4,7,10-tetraazacyclododecan-1-yl)methyl]pyridin-4-yl}sulfanyl)acetate (30 mg, 0.044 mmol) was dissolved in aqueous HCl (6 M, 1 mL) and stirred at 70 ^oC for 18 h. Complete ester hydrolysis was confirmed by ESI-MS (+) (LR: *m/z* 686.2 [M+H]+; HR: *m/z* calcd for $[C_{26}H_{51}N_5O_8P_3S]^+$ 686.2671, found 686.2666). The solvent was removed under reduced pressure and the resulting yellow oil was dissolved in H_2O (1 mL). The pH of the solution was adjusted to 5.5 using NaOH and $GdCl_3.6H_2O$ (24 mg, 0.066 mmol) was added. The resulting solution was stirred at 70 ^oC for 18 h before the solvent was removed under reduced pressure. The resulting yellow solid was purified by reverse-phase HPLC (10-100% MeOH in H_2O over 10 min; t_R = 9.6 min) to yield a white solid (12 mg). ESI-LRMS (+) *m/z* 840.6 $[M+H]^+$; ESI-HRMS (+) calcd for $[C_{26}H_{48}N_5O_8P_3S^{154}Gd]^+$ 837.1645, found 837.1657; r_{1p} = 1.9 mM^{-1} s^{-1} (H_2O, 60 MHz, 310 K).

75. [Dy.L^7]

An analogous procedure to that described for the synthesis of **[Gd.L^7]** was followed using ethyl 2-({5-*tert*-butyl-2-[(4,7,10-tri{[ethoxy(methyl)phosphoryl]methyl}-1,4,7,10-tetraazacyclododecan-1-yl)methyl]pyridin-4-yl}sulfanyl)acetate (230 mg, 0.29 mmol) and $DyCl_3.6H_2O$ (142 mg, 0.38 mmol), to yield a white solid (80 mg). t_R = 9.5 min; ^1H NMR (400 MHz, $CDCl_3$) δ -75.8 ($C(CH_3)_3$ major), -78.1 ($C(CH_3)_3$ minor); ^{31}P

NMR (162 MHz, $CDCl_3$) δ 249.5 (major), 208.2 (minor); ESI-LRMS (+) *m/z* 846.9 $[M+H]^+$; ESI-HRMS (+) calcd for $[C_{26}H_{48}N_5O_8P_3S^{160}Dy]^+$ 843.1689, found 843.1703.

76. [Dy.L^7-glucosamine]

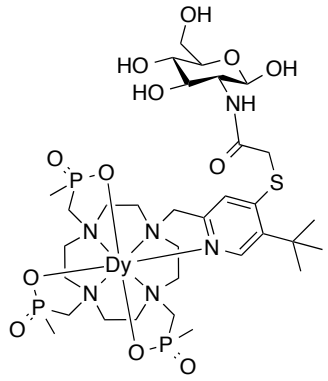

To a stirring suspension of the dysprosium(III) complex of {[4-({5-*tert*-butyl-4-[(2-ethoxy-2-oxoethyl)sulfanyl]pyridin-2-yl}methyl)-10 {[ethoxy(methyl)phosphoryl]methyl}-7-{[hydroxy(methyl)phosphoryl]methyl}-1,4,7,10-tetraazacyclododecan-1-yl]methyl}(methyl)phosphinic acid, **[Dy.L^7]** (10 mg, 0.012 mmol) in anhydrous DMF (0.3 mL) was added DIPEA (4 μL, 0.024 mmol) and after 30 min, HATU (7 mg, 0.018 mmol). The solution was left stirring for 30 min at rt before glucosamine hydrochloride (4 mg, 0.018 mmol) was dissolved in a minimum amount of H_2O (0.1 mL) and added to the reaction mixture. The mixture was left stirring at rt for a further 18 h, before being concentrated under reduced pressure. The crude material precipitated by dropping onto stirred dry diethyl ether (15 mL) and was isolated by centrifugation. Further impurities were triturated with MeCN, before the solvent was removed under reduced pressure. The crude yellow solid was purified by reverse-phase HPLC (10-100% MeOH in H_2O over 10 min; t_R = 11.6 min) to yield a white solid (4 mg). ^{1}H NMR (400 MHz, D_2O) δ -75.9 ($C(CH_3)_3$ major), -76.8 ($C(CH_3)_3$ major), -78.5 ($C(CH_3)_3$ minor), -79.3 ($C(CH_3)_3$ minor); ESI-LRMS (+) *m/z* 1007.6 $[M+H]^+$; ESI-HRMS (+) calcd for $[C_{32}H_{59}N_6O_{12}P_3S^{160}Dy]^+$ 1004.238, found 1004.237.

77. [Dy.L^7-chitosan]

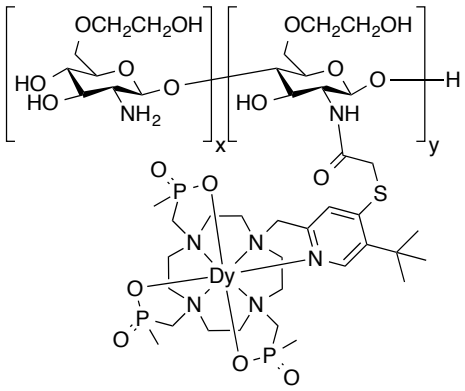

The dysprosium(III) complex of {[4-({5-*tert*-butyl-4-[(2-ethoxy-2-oxoethyl)sulfanyl]pyridin-2-yl}methyl)-10 {[ethoxy(methyl)phosphoryl]methyl}-7-{[hydroxy(methyl)phosphoryl]methyl}-1,4,7,10-tetraazacyclododecan-1-yl]methyl}(methyl)phosphinic acid, **[Dy.L^7]** (10 mg, 0.012 mmol) was dissolved in anhydrous DMF (0.3 mL) to which DIPEA (11 μL, 0.06 mmol) and HATU (14 mg, 0.036 mmol) were added. The mixture was stirred at rt for 30 min under argon, before glycol chitosan (1.5 mg, MW ≈ 6.5 kD) dissolved in H_2O (0.1 mL) was added. The mixture was left stirring at rt for a further 18 h, before the solution was diluted with H_2O (5 mL) and dialysed against Purite water for 48 h (0.5 - 1 kD MWCO), with the bulk solvent water refreshed periodically. The solvent was removed under reduced pressure, before the residue dissolved in H_2O and dialysed for a second time (2 kD MWCO) for a further 48 h. The solution was lyophilised to yield a white solid (3 mg, crude). ^{1}H NMR (400 MHz, D_2O) δ -75.2 ($C(CH_3)_3$ major), -76.4 ($C(CH_3)_3$ minor), -77.8 ($C(CH_3)_3$ minor).

6.3 References

1. A. E. Merbach and E. Toth, *The chemistry of contrast agents in medicinal magnetic resonance imaging*, Wiley, New York, Chichester, 2001.
2. A. Beeby, I. M. Clarkson, R. S. Dickens, S. Faulkner, D. Parker, L. Royle, A. S. de Sousa, J. A. G. Williams and M. Woods, *J. Am. Chem. Soc., Perkin Trans. 2*, 1999, 493–504.
3. O. Reany, T. Gunnlaugsson and D. Parker, *J. Chem. Soc., Perkin Trans. 2*, 2000, 1819–1831.
4. Z. Kovacs and A. D. Sherry, *J. Chem. Soc., Chem. Commun.*, 1995, 185–186.
5. Z. Kovacs and A. D. Sherry, *Synthesis-Stuttgart*, 1997, 759–763.
6. P. K. Senanayake, N. J. Rogers, P. Harvey, K.-L. N. A. Finney, A. M. Funk, J. I. Wilson, R. Maxwell, D. Parker and A. M. Blamire, *Magn. Reson. Med.*, 2016, DOI: 10.1002/mrm.26185.

Appendix

A.1 Summary of Complexes

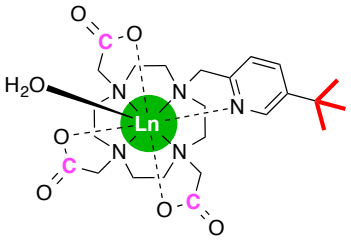

[Ln.L^1(H$_2$O)]

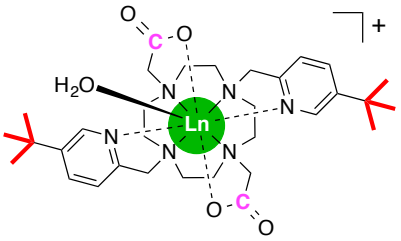

[Ln.L^2(H$_2$O)]

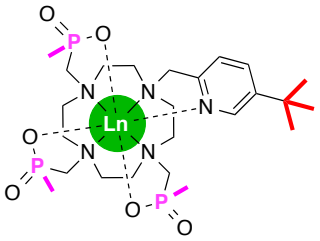

[Ln.L^3]

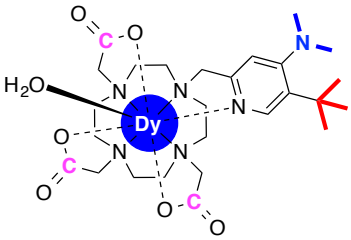

[Dy.L^4(H$_2$O)]

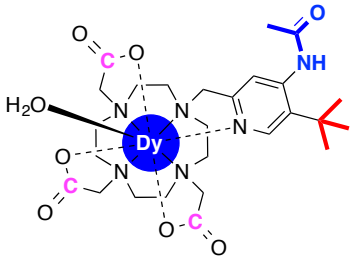

[Dy.L^5(H$_2$O)]

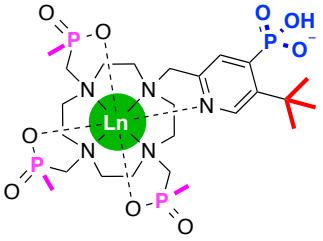

[Ln.L^6]

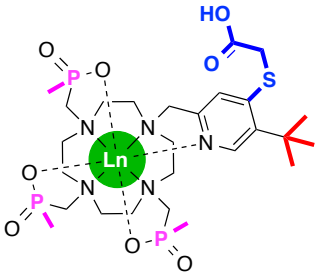

[Ln.L^7]

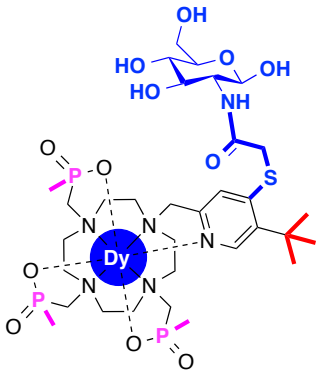

[Dy.L^7-glucosamine]

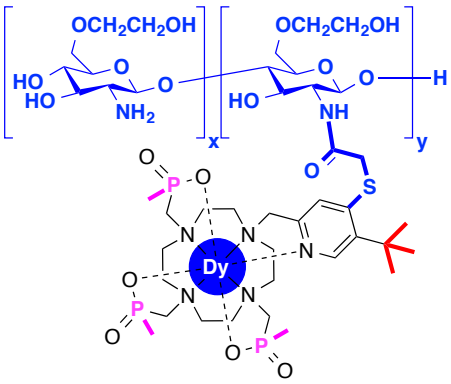

[Dy.L^7-chitosan]

A.2 List of Publications

1. P. K. Senanayake, N. J. Rogers, K.-L. N. A. Finney, P. Harvey, A. M. Funk, J. I Wilson, D. O'Hogain, R. Maxwell, D. Parker, A. M. Blamire, *Magn. Reson. Med.,* 2016, DOI: 10.1002/mrm.26185.
2. N. J. Rogers, K.-L. N. A. Finney, P. K. Senanayake, D. Parker, *Phys. Chem. Chem. Phys.*, 2016, **18**, 4370-4375.
3. A. M. Funk, K.-L. N. A. Finney, M. A. Fox, A. M. Kenwright, N. J. Rogers, P. K. Senanayake, D. Parker, *Phys. Chem. Chem. Phys.,* 2015, **17**, 16507-16511.
4. A. M. Funk, K.-L. N. A. Finney, P. Harvey, A. M. Kenwright, E. R. Neil, N. J. Rogers, P. K. Senanayake, D. Parker, *Chem. Sci.,* 2015, **6**, 1655-1662.
5. P. Harvey, A. M. Blamire, J. I. Wilson, K.-L. N. A. Finney, A. M. Funk, P. K. Senanayake, D. Parker, *Chem. Sci.,* 2013, *4*, 4251-4258.